Freie Universität Berlin

Time- and angle-resolved photoemission spectroscopy on bidimensional semiconductors with a 500 kHz extreme ultraviolet light source

zur Erlangung des Grades eines
Doktor der Naturwissenschaften
am Fachbereich Physik
der Freien Universität Berlin

Michele Puppin

Berlin 2017

This work has been performed between December 2010 and June 2017 in the Max-Planck Research group *Structural and electronic surface dynamics* headed by Dr. Ralph Ernstorfer, associated to the department of Physical Chemistry (headed by Prof. Dr. Martin Wolf) at the Fritz Haber Institute of the Max Planck Society.

Berlin, June 2017

Erstgutachter: Dr. Ralph Ernstorfer

Zweitgutachter: Prof. Dr. Martin Weinelt

Datum der Disputation: 29. September 2017

ABSTRACT

This thesis describes the development of an experimental apparatus for time- and angle-resolved photoemission (tr-ARPES) at high repetition rates. The first part of the work describes a new, high-repetition rate, extreme-ultraviolet (EUV) light source and the second part, studies the excited-state dynamics in 2H-WSe$_2$, thereby demonstrating the experimental capabilities of the machine. tr-ARPES follows the evolution of the electronic structure in non-equilibrium: EUV photon energies grant access to the whole Brillouin zone and high repetition rates improve statistics and mitigate detrimental space-charge effects. Femtosecond EUV pulses are obtained in a highly-nonlinear process called high-harmonic generation (HHG), which requires energetic driving pulses to produce a good flux. Commonly adopted Ti:Sapphire lasers have a limited scalability in average power, resulting in limited EUV flux above 100 kHz. In this thesis, this limit is overcome by developing a 500 kHz optical parametric chirped pulse amplifier (OPCPA). A high power picosecond Yb:YAG laser is used to amplify 1.55 eV pulses with an energy of 30 μJ and a duration below 20 fs, representing an order of magnitude improvement from the past technology.

A single harmonic is selected for photoemission: this is simplified by the higher spacing of neighboring harmonic in the case of UV-driven HHG. The OPCPA is frequency doubled (3.1 eV) and tightly focused in a high-pressure argon gas jet. An EUV optical setup selects the 7th harmonic at 21.7 eV, preserving a temporal resolution close to 50 fs. HHG efficiency and linewidth scale favorably in the UV: a photon flux of more than 10^{11} photons/s is achieved, with an energy resolution of 110 meV.

tr-ARPES experiments were performed on the layered semiconductor 2H-WSe$_2$. First, the conduction band is mapped throughout the Brillouin zone, 100 fs after an excitation well above the material's single-particle band gap. The evolution of the excited state is followed, revealing the microscopic energy relaxation pathways and the band gap renormalization effects.

In addition, pumping the system at an excitonic resonance, many-body effects are addressed. The peculiar band-structure of 2H-WSe$_2$ allows one to observe simultaneously resonant and non-resonant two-photon photoemission features, modeled by optical Bloch-equations. The energy and shape of the resonance differs from the single-particle conduction band, suggesting that excitons are created. Inter-valley electron-phonon scattering is identified as a possible mechanism of exciton decay to optically-dark states, which occurs on a sub-20 fs time-scale.

KURZFASSUNG

Diese Arbeit beschreibt die Entwicklung eines experimentellen Aufbaus für zeit- und winkel-gelöste Photoemission (tr-ARPES). Im ersten Teil wird eine extrem ultraviolette (EUV) Laserquelle mit einer hohen Wiederholfrequenz beschrieben. Die Untersuchung der ultraschnellen Elektronendynamik im angeregten Zustand von 2H-WSe$_2$ mit diesem neuen Experiment wird im zweiten Teil berichtet.

Mittels tr-ARPES lässt sich die Evolution der elektronischen Struktur in Nicht-Gleichgewichtszuständen verfolgen: EUV-Photonenenergien ermöglichen den Zugang auf die gesamte Brillouin-Zone, und eine hohe Wiederholfrequenz reduziert Raumladungseffekte. Femtosekunden EUV-Impulse werden durch Hohe-Harmonischen-Erzeugung (HHG) erzeugt. Dieser Prozess erfordert energetische Laserpulse, um einen guten Photonenfluss zu erzeugen, welche bisher nicht mit Ti:Saphir-Lasertechnologie bei Repetitionsraten über 100 kHz erzielbar sind. In dieser Arbeit wurde diese Grenze durch die Entwicklung eines 500 kHz optischen parametrischen chirped-Puls-Verstärkers (OPCPA) überwunden. Laserpulse mit einer Photonenergie von 1.55 eV, einer Pulsenergie von 30 μJ und einer Dauer unter 20 fs werden mit einem Yb:YAG Pikosekundlaser mit hohe Leistung verstärkt.

Für die Photoemissionexperimente muss eine einzelne Harmonische isoliert werden: hierzu wurde HHG mit ultravioletten Laserpulsen, der zweiten Harmonischen des OPCPA-Ausgangs, betrieben, welche mit einer kurze Fokuslänge in einem Hochdruckgasstrahl fokussiert werden. Der Abstand zwischen benachbarten Hohen-Harmonischen ist dadurch 6.2 eV, und die 7. Harmonische mit einer Photonenergie von 21.7 eV wurde mit hohem spektralen Kontrast isoliert. Ein Photonenfluss von mehr als 10^{11} Photonen/s und eine Energieauflösung von 110 meV wird erreicht.

Mit dieser neuen Laserquelle wurden tr-ARPES-Experimente an dem Halbleiter 2H-WSe2 durchgeführt. Zunächst wurde die Struktur der angeregten Zustände des Materials 100 fs nach einer Anregung mit 3.1 eV Photonen in der ganzen Brillouin Zone vermessen. Die zeitliche Entwicklung der angeregten Zustands-Population wurde Energie- und Impuls-aufgelöst verfolgt. Damit lassen sich auf mikroskopischer Ebene sowohl Energiedissipationspfade als auch dynamische Änderungen der Elektronischen Struktur aufgrund von Renormalisierungseffekten direkt beobachten.

Das Material würde zudem in einer exzitonischen Resonanz optisch angeregt, um Vielkörpereffekte zu erforschen. Resonante und nichtresonante Zweiphotonphotoemissionen wurden gleichzeitig beobachtet und durch optische Bloch-Gleichungen modelliert. Die Energie und Form des angeregten Zustands nach Anregung der exzitonischen Resonanz unterscheidet sich von dem Einzelteilchen-Leitungsbandzustand. Das wird als Signatur von Exzitonen in tr-ARPES interpretiert. Intervalley Elektron-Phonon-Streuung wird als möglicher Mechanismus des Exciton-Zerfall zu dunklen optischen Zuständen identifiziert.

CONTENTS

INTRODUCTION

1.1 MOTIVATION AND AIM OF THE THIS WORK

Electro-magnetic radiation is our main probe of the internal structure of matter. When light interacts with a solid, the macroscopic response is the result of many-body interactions between the constituent quanta: the microscopic understanding of this complex interplay is one of the cornerstones of solid-state physics.

The payoff of century-long struggles to solve this problem, are groundbreaking applications at the intersection of photonics and electronic. Opto-electronic devices, such as solar cells, LEDs, lasers, fiber optical communication technology shapes our everyday life.

To tackle the overwhelming theoretical problem of describing many-body effects in matter is often convenient to divide the problem into various subsystem: the electrons, the lattice and the spins. The coupling of different subsystems is often weak enough to treat them in the perturbative limit: powerful ab-initio theories such as density functional theory, are routinely adopted to study the electronic structure of matter along these lines. However, when light brings a many-body system out-of-equilibrium, the relaxation dynamics follows complex pathways where all the couplings have to be considered: we are still far to describe from first-principles what happens in this case. The timescales of the fundamental scattering mechanisms involved span several order of magnitude starting from few femtoseconds.

Our ability to create light pulses lasting a time comparable to the fundamental microscopic motions is an invaluable tool for our understanding of the problem. On the other hand, the availability of such femtosecond light sources is a driver to develop new technologies where information is processed on the ultrafast timescale.

Several excitations in materials could be exploited to build devices. Foreseeable applications are not simply based on the charge state of the electrons, but also on its spin [1], the band topology [2], or novel quantum numbers, which could be broadly grouped under *pseudo-spins* [3, 4].

Transition-metal dichalcogenides (TMD) are a perfect example illustrating these trends. TMDs are a broad-class of compounds which grows in a layered structures [5]: they have been studied since decades as they can exhibit exotic electronic properties, stemming from their bidimensionality [6].

It was eventually discovered that isolated single layers of these materials could be produced and studied [7]. In particular, atomic-thick semiconductors approaching the ultimate limit for electronic miniaturization have been isolated. The lack of inversion symmetry of a single-layer has profound consequences: circularly polarized radiation can produce spin-polarized electronic populations, localized in specific valleys of the conduction band [8], this *valley* degree of freedom, is an example of pseudo-spin. Layers of chemically different 2d materials can even be stacked to generate heterostructures [9], where the *layer* degree of freedom is now part of the functionality [4]. In such heterostructure, the dwell-time of a photo-generated carrier within a single layer is less than 100 fs [10], below the carrier-phonon relaxation times.

In bidimensional materials, light-matter interaction is also modified [11]: the absorption of a photon generates an electron-hole pair, which, thanks to Coulomb interactions, might form a bound-state called exciton. The screening of the electric field by the surrounding medium is very different in a bidimensional system, giving rise to strongly bound excitons or excitonic molecules, formed by three or more electrons and holes. The formation of these many-body states and their interplay with the pseudo-spins have to be understood in-depth, both for practical and fundamental reasons.

Experimental probes capable of following the carrier evolution in such systems are thus strongly desirable. Ideally, these probes should be able to directly observe a valley-specific population in reciprocal space. In other words, there is the need of an experimental technique combining femtosecond temporal resolution with energy and momentum resolution.

1.1.1   *Time resolved-spectroscopies and related technology*

The spirit of time-resolved spectroscopies is to observe the loss of order as a function of time and the subsequent relaxation after an impulsive optical perturbation (called *pump*). As soon as it is driven out of equilibrium, the system tends to recover its original ground state: this occurs via scattering events between the fundamental constituents. The timescales involved range from few femtoseconds, for instance in the case of electron screening and electron-electron scattering, increasing toward several tens to hundreds of fs in the case of nuclear motions. After the optical pump, the system is investigated by a second *probe* pulse, delayed by a well defined amount. The experiment is repeated for a range of delays: all the snapshot are then brought together to reconstruct a *stroboscopic* movie of the system's response.

As the majority of femtosecond laser sources operates at visible to near-infrared (NIR) frequencies, it is most common to study the

transient reflectivity or absorption changes (and hence the dielectric function) in this spectral range. Optical spectroscopies, however, cannot provide any information on where in reciprocal space the scattering events occur, in other words the optical response results form an integration over the momentum components fulfilling optical selection rules. Also, due to the long wavelengths, optical probes cannot provide microscopic insights into the atomic arrangement. As a matter of fact the microscopic scattering mechanisms under study are momentum-dependent, and at the same time lattice and electronic structure are fundamentally entangled. Hence, novel techniques combining time and momentum or spatial resolution are highly desirable.

Nowadays, new time-resolved spectroscopies are being developed following two main directions. The first direction is to use of probe light pulses of different frequencies, or electrons pulses of different energies. The second direction is to act on the pump photon energy, addressing specific modes of the system resulting in different relaxation pathways. All these approaches relies on converting the VIS-NIR frequencies of a femtosecond light source to the desired range (VUV to MIR) or on synchronizing a femtosecond light source with a probe of different nature, such as femtosecond electron pulses or x-rays produced by a free-electron laser. Frequency conversion processes, owing to intrinsically low efficiencies, compel intense and energetic driver pulses. The maximum measurement repetition rate, ν_r, is determined by the time required from the sample to return to equilibrium, which depends on the excitation fluence (radiant energy per unit area) and on the material parameters. For many materials, experiments are performed with a fluence in the range between tens of $\mu J/cm^2$ to tens of mJ/cm^2, ν_r then lies in a range between few kHz to the MHz. One of the challenges in the field is to develop novel femtosecond lasers, capable of achieving the optimum duty cycle for maximizing the signal-to-noise ratio.

1.1.2 *Thesis aim: a novel femtosecond source for tr-ARPES and proof-of-concept experiments.*

The main topic of this thesis is the development and commissioning of a novel femtosecond light source for time- and angle-resolved photoelectron spectroscopy (tr-ARPES). In this technique the probe pulses have sufficient photon energy to photo-emit the sample's electrons, which are then measured in an analyzer capable of detecting both the electron's kinetic energy and emission angle. Thanks to momentum and energy conservation (Equation 1 and Equation 2) the emitted electrons retain information about the binding energy E_B and crystal momentum of the initial state $k_{\parallel}$:

$$E_{kin} = h\nu - |E_B| - \phi_{sample},\qquad(1)$$

$$k_\parallel = \frac{\sqrt{2 m_e E_{kin}}}{\hbar} sin(\theta), \tag{2}$$

where E_{kin} is the photoelectron's kinetic energy, $h\nu$ is the photon energy, ϕ_{sample} is the sample's work function, m_e is the electron mass and θ is the angle of emission relative to the surface normal. The binding energy is typically referenced to the Fermi level, where $E_B = 0$ and increases for more strongly bound states below the Fermi level, where $E_B > 0$. One of the great appeal of the technique compared to optical spectroscopies is that it combines momentum and time resolution, allowing to observe specific locations of the Brillouin zone, an introduction to this spectroscopy will be given in this chapter, in Section 1.3.

A photon energy exceeding the workfunction ϕ_{sample} of the sample is a fundamental prerequisite: as typically $\phi_{sample} > 5$ eV, the minimum photon frequency are in the deep-ultraviolet (DUV $\lambda \lesssim 200$ nm). Moreover the kinetic energy of the photoelectrons determines the escape angle from the sample surface: high-momentum states can only escape the surface if they have a sufficient kinetic energy. From eq. 2 and 1 it is apparent that high photon energies are required for accessing higher momentum states. Energies above 10 eV grant access to the whole Brillouin zone of most materials: this spectral range is called extreme-ultraviolet, in short EUV, and covers the range 10.25 eV - 124 eV (121 nm - 10 nm)[1]. Owing to high absorption, EUV pulses cannot be generated in bulk materials with high photon fluxes: the alternative approach is a non-linear interaction with a gas. By focusing a laser in a gas to peak intensities in excess of 10^{14} W/cm^2, a process called high-order harmonic generation can take place.

In this regime, the electric field of light competes with the intra-atomic potential and tunnel-ionization becomes possible. The ionized electrons, quiver coherently with the driving light and have non-zero chance to recombine with the parent atom, releasing the excess energy gained in their motion as a photon. This radiation comes as a set of odd-order harmonics up to a certain cut-off energy in the EUV range. In the temporal domain, this corresponds to a train of bursts of sub-femtosecond duration contained in the driver pulse temporal envelope. The inherent synchronization and the short pulse duration makes high-harmonics ideally suited for pump and probe experiments. The drawback of this approach lies in the very low conversion efficiency (typically worse than 10^{-5}) and the very high peak intensity needed, which typically limits experiments to laser amplifiers operating at repetition rates up to 10 kHz. It must be noted that light sources designed for this purpose and operating at to 50 kHz - 100 kHz have already been demonstrated [12, 13] and static HHG-photoemission experiments have been performed up to 4 MHz [14].

---

[1] ISO 21348 Definition

As mentioned in the previous section, the excitation density poses a limitation (see section 1.6.2) on the maximum repetition rate at which tr-ARPES experiments can be performed. For an ideal data acquisition system, the count rate (expressed in counts/s) is independent on the repetition rate, and depends only on the average power of the probe. This means that in principle a 1 Hz laser providing 10^8 photons per pulse is equivalent to a 1 kHz laser with 10^5 photons per pulse. However, one important factor has been neglected: due to the charged nature of photoelectrons and the short duration of the photoelectron pulse, Coulomb interactions limit the amount of usable photons per pulse above which the PES spectrum is distorted beyond use. This effect is known as *space-charge* and will be describe in Section 1.6.1: a very important point is that to minimize space-charge effects the number of photoelectron per pulse have to be minimized. This means that for a given experiment is always better to work at the maximum repetition rate which the sample can tolerate.

The most widespread femtosecond lasers are based on Ti:Sapphire: upscaling this technology toward the desired repetition rate, while preserving the necessary peak intensity is extremely challenging. First, this imply that an increasingly higher optical power of tens of Watts has to be dissipated in the amplifier crystal, imposing the complication of cryogenic cooling. Second, there is simply a lack of commercially available pump lasers suited for the task. In the past decade, big progress has been made on high-power lasers based on Ytterbium doped glass fibers or solid state Yb:YAG lasers. This novel class of laser can reach kW level average power with picosecond pulse duration [15–17]. This suggests an alternative path: by making use of optical parametric amplification (OPA) in a non-linear crystal, such sources can be used to amplify femtosecond pulses. Thanks to the completely different physics of OPA compared to a conventional laser, it is now possible to scale the repetition rate of single-pass HHG to the MHz level while having sufficient flux for time-resolved experiments [18]. The main result of this work is a photoemission setup operating at 500 kHz, capable of achieving a temporal resolution below 50 fs in proof-of-concept experiments on transition metal dichalcogenide semiconductors. To achieve this, an optical parametric chirped pulse amplifier (OPCPA) was developed, based on a combination of Yb fiber and and Yb:YAG slab amplifiers. The OPCPA has been described in a publication [19] and will be presented here in more detail.

1.1.3 *Thesis structure*

The first part of this thesis (Part i) is devoted to the description and characterization of the newly developed light source: after reviewing the fundamentals of OPA, the description and characterization of the laser will be presented in Chapter 2. To increase the photon energy

of the developed NIR laser to the EUV a setup capable of HHG was developed: this will be subject of Chapter 3. The chapter focuses also on the development of the experimental beamline, where a single harmonic at 21.7 eV is isolated and refocused on an ultra-high vacuum ARPES chamber. The second part (Part ii) of the thesis is finally devoted to experimental tr-ARPES results. The experimental ARPES chamber is described in Chapter 4, together with the characterization of the source for tr-ARPES experiments. In the last chapter, tr-ARPES is applied to study the transition metal dichalcogenide 2H-WSe$_2$. This layered material already in his bulk form can show valley- and layer-specific physics [20]. First, a novel application of tr-ARPES is demonstrated, thanks to the increased rate of data acquisition. By populating the conduction band of the semiconductor with a 3.1 eV UV pulse, it will be shown how it is possible to map excited states across the Brillouin zone of the material: these states are unaccessible by static photoemission. The experimental data will be compared with density functional theory (DFT). Last, the excitonic physics in the system will be explored, resolving exciton formation and decay to optically-dark states.

1.2 ANGLE-RESOLVED PHOTOELECTRON SPECTROSCOPY

Angle-resolved photoemission (ARPES) is a well-established experimental technique based on the photoelectric effect. ARPES experiments and theory are subject of numerous review publications [21] and books [22–24], here the main results will be summarized. An appealing feature of ARPES is the possibility of mapping the Fermi surface or other relevant electronic band-structure features in reciprocal space: in this respect one can regard ARPES as a sort of momentum-space microscopy. Moreover, by achieving high resolution, it is possible to study many-body interactions which appear as renormalization effects in the band-structure of materials.

By shining photons of sufficient energy on a crystalline surface, photoelectrons are emitted along well defined angular directions, determined by their single-particle initial state $|\psi_i\rangle$ and modulated by matrix elements, in turn determined by the experimental geometry, the light polarization and the sample's symmetry. The electron kinetic energy is measured by an electron energy analyser; if the analyser has a small angular acceptance, or if it operates in a mode where the photoemission angles are measured simultaneously, the three components of the photoelectron momentum $\vec{K}$ in vacuum are completely determined by the equations (3).

$$K_x = \frac{1}{\hbar} \sqrt{2mE_{kin}} \sin\theta \cos\phi, \tag{3a}$$

$$K_y = \frac{1}{\hbar} \sqrt{2mE_{kin}} \sin\theta \sin\phi, \tag{3b}$$

$$K_z = \frac{1}{\hbar} \sqrt{2mE_{kin}} \cos\theta. \tag{3c}$$

The angles θ and ϕ are defined in Figure 1, where the experimental geometry used in this thesis is depicted. In the setup, the angle between the incoming radiation (linearly polarized in this work) and the energy analyser is fixed. The sample is mounted on a manipulator capable of rotations along 3 axes. The sample frame of reference is typically chosen such that the z-axis coincide with the surface's normal; the choice of the x and y axis is arbitrary and is convenient to align them to high-symmetry directions on the surface. In this frame of reference, the direction of the outgoing electrons is determined by the polar and azimuthal angles θ and ϕ. The electron energy analyser employed in this work is an hemispherical electron energy analyser[2]. In such a device, the kinetic energy dispersion of the photoelectrons is realized by the electrostatic field of a spherical capacitor. The photoelectrons are collected by a first set of electrostatic lens and refocused on an entrance slit. In the lens the electrons are decelerated (or accelerated) by a fixed amount so that the kinetic energy of interest, travels along a circular trajectory at the center of the hemispherical capacitor with a defined pass energy. The electrons finally hit an imaging detector, composed by a micro-channel-plate (MCP) electron multiplier, followed by a phosphor screen to convert the electronic cascade into photons, which are finally imaged on a CCD panel. Electrons of different kinetic energies are spatially-separated on the detector along the radial direction (axis KE in Figure 1). Electrons entering the analyser with different angles along the slits long axis are instead displaced along the α axis. This allows for efficient parallel detection of multiple emission angles and kinetic energies. The collected image on the detector corresponds to an energy versus momentum intensity distribution curve.

The measured $\vec{K}$ and E_{kin} are related to the initial state momentum $\vec{k}_i$ and binding energy E_B by the conservation rules of equations (1) and (2). The two relations are, however, insufficient to completely determine the initial state, as they don't provide information for the $\vec{k}_\perp$: to determine this momentum component it is necessary to know the final state $|\psi_f\rangle$, this will be explained in greater detail in the next section.

---

2 Specs Phoibos 150
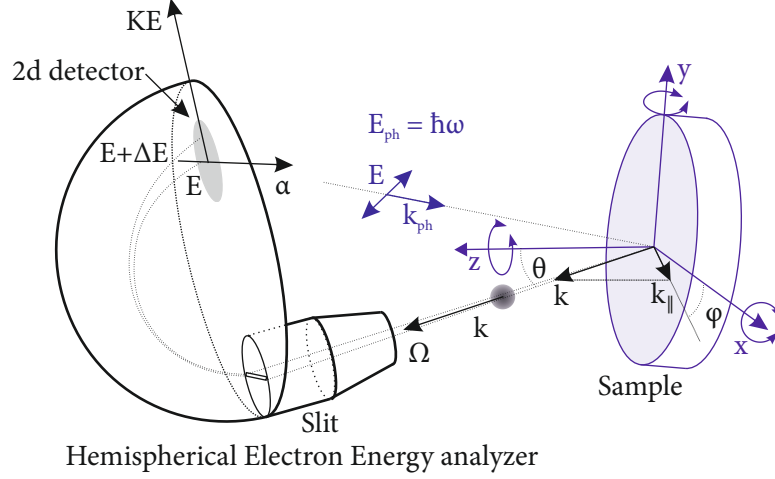
Figure 1: The experimental geometry for ARPES adopted in this work. The incoming EUV light is p-polarized, $\mathbf{k_{ph}}$ is the photon wavevector, E_{ph} photon energy; $\mathbf{k}$ is the photoelectron wavevector, and $k_\parallel$ is the projection parallel to the surface, E is the pass-energy of the analyser. The z-axis is oriented along the surface normal, which defines the photoemission angle θ.

1.2.1 *The three step model of photoemission*

The three step model is one of the first theoretical pictures used to describe the photoemission process and it is still widely used because it provides an intuitive picture. As shown in Figure 2 the photoemission process can artificially divided in three distinct steps:

1. Photoexcitation of the electron

2. Transport to the surface

3. Penetration through the surface

1.2.1.1 *Step 1: excitation in the solid and nearly free-electron approximation*

In the simplest picture, the photo-excitation is described as an optical transition between two single-particle Bloch states. The initial state $|\psi_i\rangle$ has momentum $\vec{k}$ and energy E_i; the final state $|\psi_f\rangle$, has an energy E_f and momentum $\vec{k}_f$. The photoemission cross-section will be treated in more detail in section 1.2.2. The energy conservation relation imposes $E_f - E_i = \hbar\omega$ where ω is the photon's angular frequency. The simplest choice for $|\psi_f\rangle$ is a nearly-free electron state. The photon momentum $\hbar k_{ph}$ for an EUV energy of 20 eV is about 0.01 Å^{-1} which is negligible compared to a typical Brillouin zone size: for example for a typical lattice parameter $a = 5$ Å of Si one has $\frac{2\pi}{a} \approx 1.25$ Å^{-1}. For a strictly free electron final state the energy and
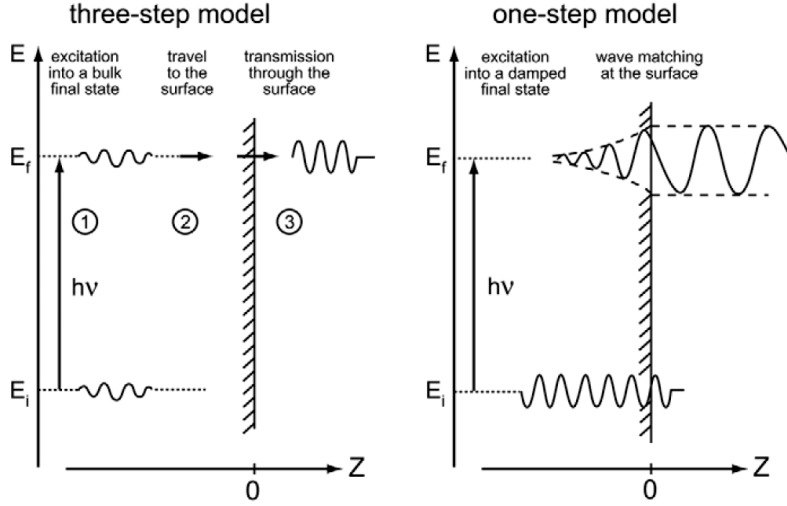
Figure 2: The three-step model compared with a single-step model, from reference [22].

momentum conservation cannot be simultaneously fulfilled due to the different photon and electron energy-momentum dispersion relations. This highlights the role played by the periodic lattice potential: in a nearly-free electron final state (i.e. a free electron perturbed by a weak periodic potential [25]) the extra momentum necessary to fulfill momentum conservation is provided by a reciprocal lattice vector $\vec{Q}$. The process is illustrated in Figure 3(a): the optical transition is approximately vertical in a reduced zone scheme, but the extended zone scheme provides a more intuitive picture of the parallel momentum conservation. The energy of the final state in this approximation can be written as:

$$E_f(\vec{k}_f) = \frac{\hbar^2 \vec{k}_f^2}{2m_e} - |E_0|,$$

(4)

and the momentum conservation relation is:

$$\vec{k}_f = \vec{k} + \vec{G}.$$

(5)

The treatment of the photoelectron final state as nearly-free becomes increasingly justified for higher kinetic energies, when the lattice potential become comparatively negligible; however the approximation might break down for low kinetic energy photons, such as the one produced by crystal-based laser sources around 6 eV.

1.2.1.2 *Step 2: transport to the surface and surface sensitivity*

During its travel toward the surface the photoelectrons strongly interact with the rest of the system, experiencing inelastic scattering and
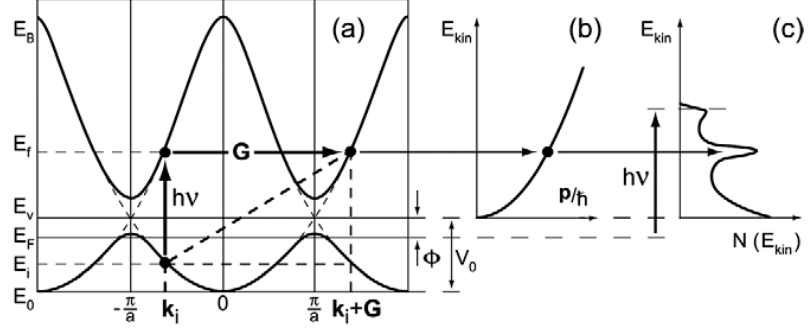
Figure 3: The photoemission kinematics, adapted from reference [21]. a) Is the first photoemission step: a direct optical transition withing the solid. Here **G** is a reciprocal lattice wavevector, necessary to conserve momentum. V_0 is the inner potential a ϕ is the workfunction. E_i initial state energy, E_f final state energy, E_F Fermi level, E_V vacuum level, E_B photoelectron energy in the bulk. b) The free electron final state in vacuum has a wavevector $p/\hbar$. c) The photoelectron spectrum.

energy losses. This generates a tail of inelastically scattered photoelectrons at lower kinetic energies. Due to these strong interactions, the photoelectron escape depth is generally very short, which translates into a strong surface-sensitivity for the technique. The electron mean-free-path roughly follows an universal curve [26], which shows that the EUV photon energy range exhibits the largest surface sensitivity.

This second step highlights two important aspects for this work: the first, is an important experimental requirement of a having a surface clean from contamination, therefore ARPES experiments has to be conducted in ultra-high vacuum conditions (UHV), this will play an important role in the design of the experimental beamline in chapter 3. Second, in the experimental interpretation is always important to remember that the measured (surface) properties do not necessarily reflect the bulk behavior of the material (see chapter 5)

1.2.1.3 *Step 3: transmission through the surface and photoemission kinematics*

The photoelectron traveling in the solid has to overcome the surface potential energy barrier $V_0 = |E_0| + \phi$ (see Figure 3) and escape in vacuum toward the detector. The bulk Bloch nearly-free final state $|\psi_f\rangle$ with momentum $\vec{k}_f = \vec{k}_{f,\parallel} + \vec{k}_{f,\perp}$ has to be matched to the free electron final state in vacuum with momentum $\vec{K} = \vec{K}_\parallel + \vec{K}_\perp$. As a consequence of the translational symmetry along the surface (x-y plane) the parallel momentum component is conserved:

$$\vec{k}_{f,\parallel} = \vec{K}_\parallel. \tag{6}$$
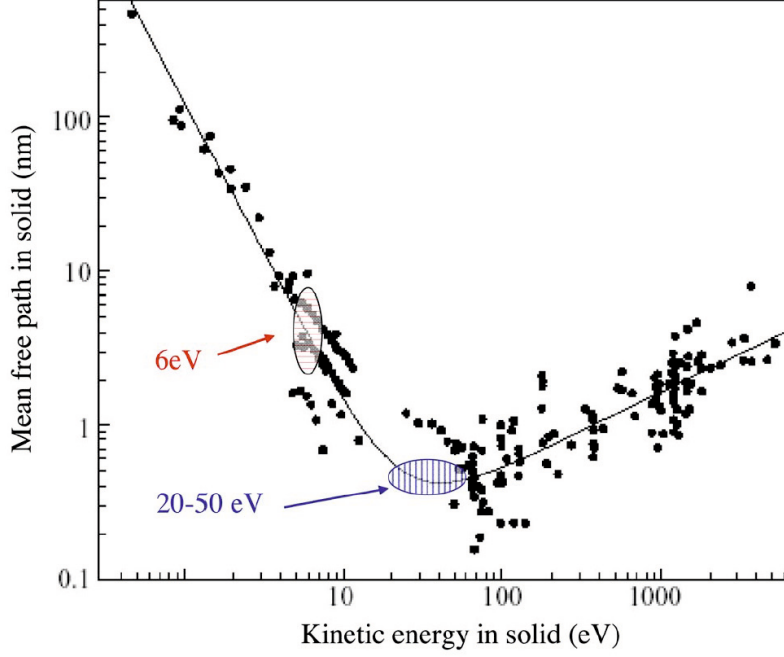
Figure 4: Electron escape depth from reference [27]: highlighted are the regions 20-50 eV, typical for EUV based ARPES and the 6 eV region typical for laser based ARPES.

The translational symmetry in the perpendicular direction is broken, therefore $\vec{k}_{f,\perp}$ is not a conserved quantity. To determine $k_{i,\perp}$ one can make use of energy conservation $E_f = E_{kin} + \phi$, together with eq. (2) and obtain the following relations:

$$k_{\parallel} = \frac{1}{\hbar}\sqrt{2m_e E_{kin}} sin(\theta), \tag{7}$$

$$k_{\perp} = \frac{1}{\hbar}\sqrt{2m_e(E_{kin}\cos^2\theta + V_0)}. \tag{8}$$

Despite the approximations made, equation (7) has proven to work remarkably well for a number of systems and is commonly employed. Since the surface potential step V_0 is experimentally unknown, the best way of determining it is to first determine the lattice parameter along the surface normal and then match the experimental data to the expected periodicity, using V_0 as a fit parameter.

The parallel momentum relation (Equation 7) implies that the electron is refracted to higher angles upon crossing the surface, as shown in Figure 5. This has some very important consequences, when dealing with laser-based photoemission. As mentioned in the Section 1.1, it is difficult to convert the frequency of the laser sources to the EUV range and often the energy is limited to about 6 eV. For practical reasons, the maximum angle accessible in a setup similar to the one employed in the thesis is of the order of 45°. For a typical workfunction

of 4.5 eV and for an electron at the Fermi level, this gives the following limits for the accessible momentum space: $k_\parallel(6 \text{ eV}, 45°) = 0.44$ Å^{-1} while $k_\parallel(20 \text{ eV}, 45°) = 1.42 \text{ Å}^{-1}$. The border of the first Brillouin zone (FBZ, typically $\approx 1.25 \text{ Å}^{-1}$) can therefore be reached only by EUV photons.
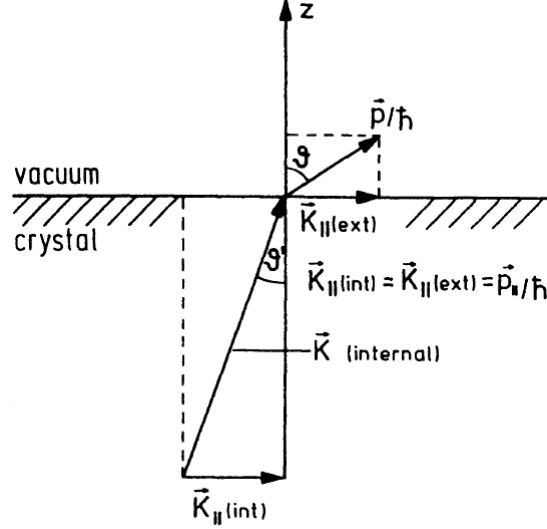
Figure 5: Parallel momentum conservation at the crystal surface, from reference [22]. $\vec{K}$ is the wavevector inside the solid, $\vec{p}/\hbar$ is the wavevector outside the solid. The parallel components $\vec{K}_{\parallel,int}$ and $\vec{p}_\parallel/\hbar$ are conserved. z is the direction of the surface's normal and θ and θ' are the internal and external photoelectron angle respectively.

The three-step model provides an intuitive picture, which grasps many of the fundamental aspects of photoemission. Further refinements of the theory, treat photoemission as a single, coherent step (see Figure 2). In this case the surface effects have to included and the optical transition occur to a final state which for $z \to +\infty$ behaves as a free wave, but has a non vanishing bulk component, damped away from the surface to account for the escape depth. A frequently used class of final states are the so called time-reversed LEED (Low Energy Electron Diffraction) states [22].

1.2.2 *Photoemission cross section, matrix elements and correlations*

So far the presented treatment of PES has neglected most many-body effects - besides the phenomenological mean free path in step 2 - and took into account only the kinematics of the photoemission processes. To properly account for the measured signal, several other aspects have to be taken into account. First, one has to realize that the photoemission signal intensity is modulated by matrix elements effects which depend on the symmetries of the states involved in the transition, on the scattering geometry and on the light polarization. Due to

this matrix elements, it is often difficult to interpret the signal intensity as simple population of the measured bands. Second, signatures of many-body interactions in the initial state can be in many cases extracted from the PES signal. To show this effects, in this section an expression of the photoemission transition rate will be presented. By treating the light field as a perturbation, the transition probability w_{if} can be calculated with the Fermi golden rule:

$$w_{if} = \frac{2\pi}{\hbar} \left| \langle \Psi_f^N | H_{int} | \Psi_i^N \rangle \right|^2 \delta \left(E_f^N - E_i^N - h\nu \right). \tag{9}$$

Equation (9) describes an optical transition between two N-electron states, where $|\Psi_i^N\rangle$ is the N-electron initial state and the N-electron final state $|\Psi_f^N\rangle$ contains a photoelectron propagating away form the surface. Given w_{if}, the photoemission intensity can be calculated by summing over the possible initial and final states:

$$I(\vec{k}, e_{kin}) = \sum_{i,f} w_{if}. \tag{10}$$

The interaction Hamiltonian is treated as a perturbation to the N-electron Hamiltonian describing the system (which can be thought of a semi-infinite crystal). In the dipole approximation H_{int} can be written as:

$$H_{int} = \frac{e}{2m_e c} \left(\vec{A} \cdot \vec{p} + \vec{p} \cdot \vec{A} \right) \approx \frac{e}{m_e c} \vec{A} \cdot \vec{p}. \tag{11}$$

The last approximation in Equation 11 amounts for neglecting so called surface photoemission effects [22]. Besides the use of perturbation theory and the dipole approximation, there were so far no approximations in writing equation (9). However, the problem in its current form is quite difficult to solve. One needs to first solve the unperturbed N-body Hamiltonian describing the system, including a proper description of the surface, in order to determine the possible initial and final states. Finally the response of the N-1 electron system to the creation of photo-electron and photo-hole has to be taken in account. All this tasks are especially hard for strongly correlated systems where many of the commonly used theoretical approximations break down.

1.2.2.1 *The sudden approximation*

In order to treat the problem it is convenient to factor out from the N-body states the photoelectron wavefunction, separating it from the remaining N-1 electrons. As soon as the photo-hole and photo-electrons are generated, the remaining N-1 electrons will react by screening

the charges. A common simplification in this respect, is the sudden approximation: in this case one assumes that the photoemission process is instantaneous, i.e. that the photoelectron is removed instantaneously generating a sudden, step-like change in effective potential. The higher the kinetic energy of the photoelectron, the better justified is this approach, there are however studies that show that even at 6 eV this picture does not break down [27]. In this approximation one can factor out from the N-electron states $|\Psi_f^N\rangle$ and $|\Psi_i^N\rangle$, the single-electron state involved in the transition.

$$|\Psi_{f,m}^N\rangle = \mathcal{A} |\phi_f^{\vec{k}}\rangle |\Psi_{f,m}^{N-1}\rangle,\qquad(12)$$

$$|\Psi_i^N\rangle = \mathcal{A} |\phi_i^{\vec{k}}\rangle |\Psi_i^{N-1}\rangle.\qquad(13)$$

In eq. (13) $\mathcal{A}$ is an anti-symmetrization operator to satisfy the Pauli exclusion principle. In the final state, the index m indicates that in general the photoemission process leaves the residual N-1 electrons in a set of eigenstates of the new Hamiltonian after the sudden change in potential. The photoemission intensity (eq. (10)) can be rewritten as:

$$\begin{aligned}I(\vec{k}, e_{kin}) &= \sum_{i,f} |\langle \phi_f^{\vec{k}} | H_{int} | \phi_i^{\vec{k}} \rangle|^2 \sum_m |\langle \Psi_{f,m}^{N-1} | \Psi_i^{N-1} \rangle|^2 \\ &\quad \times \delta(E_{kin} + E_{m,f}^{N-1} - E_i^N - h\nu),\qquad(14) \\ &= \sum_{i,f} |M_{i,f}^{\vec{k}}|^2 \sum_m |c_{m,i}|^2 \delta(E_{kin} + E_{m,f}^{N-1} - E_i^N - h\nu).\end{aligned}$$

The first element in eq. (14) is the one-electron dipole matrix element $M_{i,f}^{\vec{k}}$, responsible for the photoemission selection rules. By a symmetry analysis, it is possible to predict such selection rules in many practical cases: this is reviewed in the work of Moser et al., where the interested reader can find further informations [28]. The second part of the equation can be interpreted as follows: if correlations in the wavefunction can be neglected for most of the coefficients, then $|c_{m,i}|^2 \approx 0$. In this case one recovers the one-particle picture and the ARPES spectrum will consists of a single delta-like peak. If instead correlations becomes important, satellites peak will appear in the spectrum (so-called shake-up states), for example in the photoemission from molecules vibronic peaks will become apparent. In the framework of many-body system, a different language and mathematical formalism is used, which will be described in the next section.

1.2.2.2 *Spectral function and quasi-particles*

In many-body theories, the Green function's formalism is one of the most powerful and commonly used tools. In this contest, the effects of many body interactions on a single electron are calculated in term of a

so-called self-energy correction $\Sigma(\vec{k}, \omega) = \mathbb{R}e(\Sigma(\vec{k}, \omega)) + i\, \mathbb{I}m(\Sigma(\vec{k}, \omega))$ to the Green function G of the electron. In a non-interacting system with a single-particle energy $E_0(\vec{k})$, the green function G_0 can be written as:

$$G_0(\vec{k}, \omega) = \frac{1}{E - E_0(\vec{k}) - i\epsilon}, \tag{15}$$

where ϵ is an infinitesimal normalization constant. In the interacting case, theory corrects the Green function by mean of the complex self-energy:

$$G(\vec{k}, \omega) = \frac{1}{E - E_0(\vec{k}) - \Sigma(\vec{k}, \omega)} \tag{16}$$

One important result is that it is possible to compare the theory results quite directly with the photoemission data, provided that some conditions are met, as will be discussed in section 1.2.3. Following reference [22], one can rewrite the photoemission intensity in the following way:

$$I(\vec{k}, e_{kin}) = \sum_{i,f} |\langle \phi_f^{\vec{k}} | H_{int} | \phi_i^{\vec{k}} \rangle|^2 A(\vec{k}, \omega) = \sum_{i,f} |M_{i,f}^{\vec{k}}|^2 A(\vec{k}, \omega), \tag{17}$$

where the spectral function is related to the system's single particle Green function by the relation:

$$A(\vec{k}, E) = \frac{1}{\pi} \mathbb{I}m(G(\vec{k}, E)). \tag{18}$$

$A(\vec{k}, E)$ describes the probability of removing an electron with energy E and wavevector $\vec{k}$ from the system below the Fermi energy E_f. In the non-interacting case one has:

$$A(\vec{k}, E) = \delta(E - E_0(\vec{k})). \tag{19}$$

This is equivalent to eq. (14) with all the $|c_{m,i}|^2 = 0$, except the ground state: in this case one expects Dirac-delta-like peaks at the single particle energies.

$$A(\vec{k}, E) = \frac{1}{\pi} \frac{\mathbb{I}m(\Sigma(\vec{k}, E))}{(E - E_0(\vec{k}) - \mathbb{R}e(\Sigma(\vec{k}, E)))^2 + \mathbb{I}m(\Sigma(\vec{k}, E))^2}. \tag{20}$$

In the limit of weak interactions ($\mathbb{I}m(\Sigma(\vec{k}, E))$ small), the spectral function can be separated in two components, with a relative ratio

Z_k which in this framework are called coherent and an incoherent component [21]:

$$A(\vec{k}, E) = \frac{Z_k}{\pi} \frac{\Gamma_k}{(E - E_1(\vec{k}))^2 + \Gamma_k^2} + A_{inch}. \tag{21}$$

The electron is modified by the many-body interactions: it can still be thought as a particle, but *dressed* by the excitation, also called a *quasi-particle*. The fist (coherent) component of the spectral function has a Lorentzian shape: the linewidth $\Gamma_k = \mathbb{I}m(\Sigma(\vec{k}, E = E_0(\vec{k}))$ represents the finite lifetime and depends on the imaginary part of the self-energy. The quasi-particle has a *renormalized* energy and mass $E_1(\vec{k}) = (E_1(\vec{k}) + \mathbb{R}e(\Sigma(\vec{k}, E = E_0(\vec{k})))$ which depends on the real part of the self-energy. The incoherent component appears as an tail at lower energy to the main quasi-particle peak, caused by the inelastic scattering of the quasi-particle, in analogy, for example, with the vibronic peaks in a molecular photoemission spectrum. The incoherent tail is not structureless and depends on the details of the underlying many-body interactions. The calculations of self-energy corrections are a complicated task and can often be performed only on model systems: one of the very attractive features of ARPES is that it gives the opportunity to take a glimpse at the many-body interaction in complex strongly-correlated matter.

1.2.3 *Photoemission lineshape analysis*

In the previous section, the connection between ARPES and many body physics was highlighted: the lineshape reflects the renormalization effect on the quasi-particle lifetime and is related to the imaginary part of the self-energy; whereas the deviation from the bare particle dispersion and energy relates to the real part. In order to extract this kind of information from the spectrum, however, also the effects of the lifetime of the final state (the photoelectron) have to be taken in account, which was so far neglected. This lifetime is related to the scattering processes which might occur to the photoelectron as it leaves the solid i.e. step 2 in the 3-step model. This effect can be modeled by considering a complex wave-vector for the escaping photoelectron [22]:

$$k_\perp = k_\perp^{(1)} + i k_\perp^{(2)}, \tag{22}$$

here, $\lambda = (k_\perp^{(2)})^{-1}$ is the escape depth of the photoelectron. This can be inserted in the matrix element of equation (17):

$$I(\vec{k}, e_{kin}) = \sum_{i,f} \frac{|\tilde{M}_{i,f}^{\vec{k}}|^2}{(k_{i,\perp}^{(1)} - k_{f,\perp}^{(1)})^2 + (k_{f,\perp}^{(2)})^2} A(\vec{k}, \omega). \tag{23}$$

It is apparent from this equation that the finite escape depth enters as a Lorentzian-like broadening of the measured signal. This is also related to the relaxation of momentum conservation rules perpendicular to the surface, which means that several initial states with distinct $k_\perp$ will contribute to the intensity at a given photon energy.

Intuitively, one can think in the following way: as a result of the reduced mean free-path, the unscattered photoelectrons come mostly from the surface, the initial state position is hence well determined in the z direction (small Δz); from the Heisenberg indeterminacy relation, the complementary momentum indeterminacy increases correspondingly $\Delta k_\perp > 1/\Delta z$.

It is not possible to distinguish between the two lifetime broadening effects in general. Luckily, there are particular conditions where the bare initial-state line-shape can be measured: to show this, one can follow the simplified derivation of reference [29], where both initial and final state have a Lorentzian width, respectively Γ_i and Γ_f. The measured width Γ_m can be written as:

$$\Gamma_m = \frac{\frac{\Gamma_i}{|v_{i,\perp}|} + \frac{\Gamma_f}{|v_{f,\perp}|}}{|\frac{1}{v_{i,\perp}}(1 - \frac{mv_{i,\parallel}\sin^2(\theta)}{\hbar k_\parallel}) - \frac{1}{v_{f,\perp}}(1 - \frac{mv_{f,\parallel}\sin^2(\theta)}{\hbar k_\parallel})|}, \tag{24}$$

in this equation, $\hbar v_{i,\perp} = \partial E_i/\partial k_{i,\perp}$ and $\hbar v_{f,\perp} = \partial E_f/\partial k_{f,\perp}$ are the group velocities in the initial and final band, respectively. One can see from eq. (24) that $\Gamma_m \to \Gamma_f$ when $\Gamma_i \to 0$. In this case, the initial states has a long life-time (for example for states very close to the Fermi level): the dominant contribution to the width comes from the final state. On the other hand if $v_{i,\perp} \to 0$ one has $\Gamma_m \to \Gamma_i$: in this case the measured linewidth reflects the initial state single-particle lifetime. The condition $\partial E_i/\partial k_{i,\perp} \approx 0$ is fulfilled if the initial states is inherently bidimensional, for example this is the case for surface states or for some states in layered materials with very weak interlayer coupling. This last case is very important as low-dimensional materials tend to exhibit strong-correlations: the width measured by ARPES can in this case be related to the underlying many body effects.

The finite momentum- and energy-resolution plays a very important role on the ability of resolving the aforementioned effects in the band-structure. Measurements are affected both by momentum and energy broadening: to include these effects, the theoretical intensity has to be convoluted by the experimental energy and momentum resolutions, indicated as $R(E)$ and $Q(\vec{k})$.

$$I_{exp}(\vec{k}, E) = \int dE' d\vec{k}' I(\vec{k}', E') R(E - E') Q(\vec{k} - \vec{k}') \tag{25}$$

The advances in electron analysers and the development of third-generation light sources and high-resolution laser-based sources contributed to the advent of high E-k-resolution ARPES in the past decades. A present-day state-of-art laser source [30] can produce up to 2×10^{12} photons per second at 11 eV and enables photoemission with energy and momentum resolutions better than 2 meV and 0.012 Å^{-1}, respectively. A newly developed synchrotron beamline (beamline I05 at the Diamond synchrotron radiation source in the United Kingdom), offers broadly tunable radiation with optimal high-resolution performance between 18 eV $<$ hν $<$ 240 eV. In this range, a flux of up to 10^{12} ph/s is obtained (peak flux at 120 eV) with a resolving power of $E/\Delta E = 25000$.

The flux at about 20 eV, useful for a comparison of our light source, is 1.5×10^{11} ph/s with resolution of 0.1 meV. For a fair comparison with the typical energy resolutions of HHG-tr-ARPES however, one have to worsen the energy resolution to about 100 meV. In this artificial conditions one can estimate a flux of 1.1×10^{13} ph/s. On the other hand the duration of synchrotron pulses is on the order of tens of picoseconds, three orders-of-magnitude longer than the time resolution achievable with time-resolved photoemission (tr-ARPES). The concepts used for describing *static* ARPES, will still apply for tr-ARPES, which is the subject of the next section.

1.3 TIME-RESOLVED PHOTOEMISSION

In a *dynamic* or time-resolved photoemission experiment, the light source operates in pulsed mode, typically with pulse temporal-widths ranging from tens to several hundreds of femtoseconds. The experiment is performed by shining two light pulses on the sample, a *pump* pulse is used to drive the system out of equilibrium, a *probe* pulse arrives at well defined temporal delay and is responsible for the photoelectric transition. By changing the delay and repeating the experiment, a temporal evolution of the perturbed system can be recorded. Every delay point can be essentially considered as an independent photoemission experiment. The time-resolution of this pump and probe technique is given by the temporal cross-correlation of the pulse's temporal-widths; for simplicity both pulses will be treated as Gaussians with a width given by their full-width at half maximum (FWHM). In this introductory section, some of the novelty and applications of tr-ARPES will be shortly summarized. By gaining femtosecond time-resolution it is possible to study the relaxation mechanisms of complex systems. The timescales and the energy-scales of typical interactions in condensed matter are summarized in figure 6.
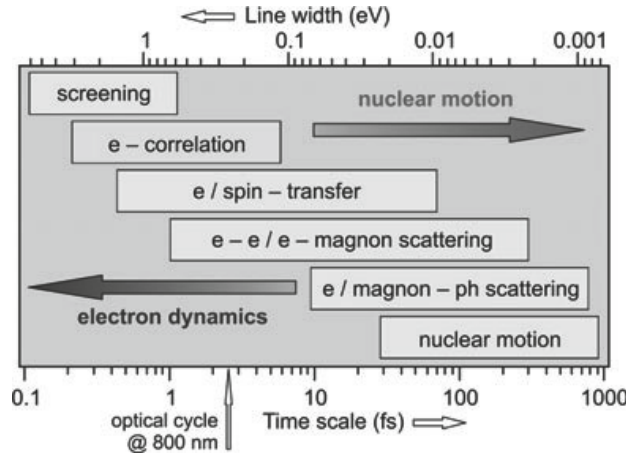
Figure 6: Time-scale and corresponding line-widths of various elementary processes in matter, from reference [31]

The quasi-particle dynamics span time and energy-scales covering several decades, depending on the particular interaction: the fastest processes are related the charge screening, which occurs on time-scales determined by the plasma frequency (ω_p) of the system. For metals this can reach the sub-femtosecond regime or *attosecond* regime [32]. Electron-electron correlations are at the basis of electron localization observed in the Mott metal to insulator transition: one therefore ideally expect that the temporal dynamics in such cases could exhibit transients as short as few femtoseconds [33]. Electron transfer processes across interfaces, for example from a bulk state to a surface or to a image potential state, occur on timescales well below 100 fs: studying the temporal evolution of these surface states, screening phenomena can also be studied [34]. It is worth noting that on these short time-scales, due to the coherent nature of the laser light, light-matter interaction has to be treated via optical Bloch equations, to account for coherent evolution of the interacting states [35]. This is particularly true for weakly interacting states at surfaces, while for system with stronger interactions (for example metal bulk states) decoherence is so fast that these effects are hard to observe and often negligible. Electron-electron scattering events dominate the relaxation of a perturbed system in the first few hundreds of femtoseconds, followed by the scattering with phonons which instead persists in the picosecond regime. For magnetic systems, the collective spin motions (magnons) must be included in the picture, as they can scatter both with electrons and phonons. This range of timescale (fs-ps) which is the most widely studied by tr-ARPES.

One of the most important relations to keep in mind for tr-ARPES is the so-called time-bandwidth product. The pulse width in the time domain is inversely proportional to the spectral bandwidth (see 2.2): from eq. (1) follows that this bandwidth is directly transferred to the

experimental energy resolution $R(E)$. When investigating the fastest dynamics, it is physically impossible to achieve simultaneously a high spectral resolution. On the other hand, as suggested in Figure 6, processes with a very fast dynamics will have a correspondingly broad line-width.

1.3.1 *Two-photon photoemission and tr-ARPES*

It is useful to distinguish two experimental situations: in the first one, the photon energy of both pump and the probe is lower than the sample's workfunction. In this case, direct photoemission from either the two pulses is not possible and only *nonlinear* photoemission is possible: the lowest order of this nonlinear process is known as two-photon-photoemission (2PPE).

The probed states are in this case unoccupied states with energy lying between the Fermi energy and the vacuum level, transiently populated by either one of the two pulses. This field is more well-established than tr-ARPES and gives important information on the dynamics of hot-electrons on metal surfaces [36], the lifetime and dephasing mechanisms of surface Shockley states and image potential states [35, 37], and can be used to study electron-transfer processes in molecular adsorbates on surfaces [38].

The second case, considered by this work, is the one where at least one of the two pulses has a photon energy exceeding the workfunction. In the case of tr-ARPES even without a pump the direct photoemission signal is always present. The probed states are the occupied states between $\hbar\omega - \phi_{sample}$ and ϵ_f, together with transiently populated states below the vacuum level. The latter is essentially 2PPE: the operated distinction between 2PPE and tr-ARPES is arbitrary in this respect. It is worth noting that while in 2PPE experiments one typically uses optical excitation densities F = 1-10 μJ/cm^2, the excitation densities used so far in the case of tr-ARPES experiments have been typically F $>$ 0.1 mJ/cm^2 [31]. In time-resolved experiments probing the occupied states, one studies small variations of the direct photoemission signal, this translates in an overall lower signal to background ratio.

1.3.2 *tr-ARPES experiment and observables*

tr-ARPES uses angle-resolved detection to gain momentum resolution (it has to be noted that often also 2PPE experiments can be performed with momentum-resolution). A schematic of the experiment is shown in Figure 7.

This is nothing more than the already described ARPES experiment, now performed with VUV-EUV pulses and a perturbing pulse at controlled delay. The pump pulse wavelength can fall in a wide
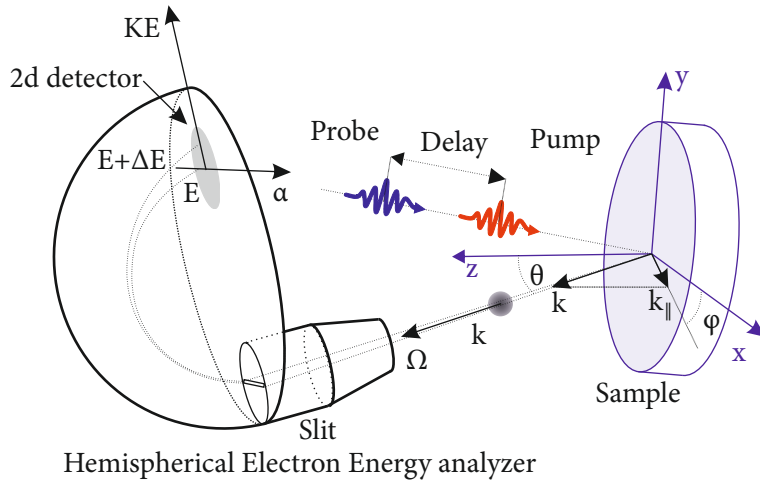
Figure 7: The tr-ARPES geometry: here a pump pulse in red is followed by the probe pulse in blue. An ARPES experiment is performed for multiple values of the temporal delay.

range, from the MIR to the DUV (between 20 μm- 200 nm) or photon energies between 6-6000 meV (Section 1.6). In practice, readily-available NIR wavelengths around 800 nm, the fundamental frequency of the Ti:Sapphire laser, are the most widely used. In a typical tr-ARPES experiment one induce a perturbation of the ground state of the material of interest. The response of some specific spectral-function feature and their relaxation, ar then followed as a function of pump and probe delay. These features can be the binding energy, the line-width, or the intensity of coherent and incoherent quasi-particle peaks. The perturbation is almost always accomplished by populating states unoccupied under equilibrium conditions (see Section 1.4). It is often difficult to disentangle the population dynamics from to the dynamics of the underlying bare-band-structure. In tr-ARPES is possible to observe states inaccessible by direct photoemission. As it will be shown in section 1.5.4, these unoccupied states can be mapped and their relaxation can be followed in real time.

1.4 PUMP INTERACTION MECHANISMS AND ULTRAFAST SCATTERING PHENOMENA

There are several ways in which the pump can interact with the system. Most commonly, the pump induces a direct optical transition between occupied and unoccupied electronic states. In this category fall for example the excitation of carriers across the bandgap of a semiconductor or the excitation of hot-electrons in the conduction band of a metallic sample. In both cases, the generate hot electron-hole-pair population relaxes his excess energy via several microscopic scattering channels. The electrons can scatter among themselves and with the other degree of freedom, for example phonons, magnons etc.

Energy and momentum conservation determine the available phase space for scattering, and hence the scattering rate in various situations. For example, in a material possessing a band-gap, the electron relaxation times are typically slower compared to metals, due to the reduced amount of states around the Fermi level. It sometimes useful to classify scattering processes between quasi-elastic or inelastic [33], depending whether the energy loss (or gain) experienced by the electron is below the instrumental resolution or not. For example scattering with an acustic phonon will lead to a small change of energy for the electron (quasi-elastic) and the main change will be in the electron's momentum.

Immediately after the photo-absorption, the excited electrons have a non-thermal distribution, therefore cannot be described by the Fermi-Dirac statistic. Depending on the specific problem, the excited carriers might be localized in specific position of the Brillouin zone, i.e. at a specific momentum. In the first few hundreds of femtoseconds, electron-electron and electron-phonon scattering acts to bring the system away from this highly non-equilibrium state towards a thermal distribution, typically with a high electronic temperature. Electron-phonon scattering events heat the lattice, which has a higher specific heat. Both forms of scattering also redistribute momentum, populating different regions of the unoccupied band structure. The electron-phonon scattering can be often be regarded as quasi-elastic, therefore more scattering events are required to relax a given amount of energy as compared to purely electronic mechanisms and the process has inherently slower effective observed time-constants. After several picoseconds, the temperature in the electronic and lattice sub-systems equilibrates. The dynamics of these quasi-thermal processes can be related to an effective electron-phonon coupling, which can be studied by these means: some examples are presented in Section 1.5.1. The nearly-instantaneous perturbation by the optical excitation can as well trigger a coherent motion of the lattice modes, as described in Section 1.5.2.

The second excitation mechanism is the direct photon absorption by an infrared-active vibrational mode of the sample. In this case the observables are the indirect modifications on the spectral function due to the coupling of the excited mode to the electrons. This excitation scheme is often referred as *phonon-pumping*: due to the typical low energies of the phonon excitations in solids, this has so far been limited to few studies [39], since it is technically challenging to convert the laser frequency in this spectral regions.

Finally, the last interaction mechanism consists in the so-called *photon-dressing* of the initial state or the final state. Here, replicas of the band structure appear in the measured photoelectron spectrum during pump and probe temporal overlap: this mechanisms will be explained in more detail in section 1.5.3.

Richard Haight is generally acknowledge as the pioneer of the field: his studies mainly concentrated on dynamics on semiconductor surfaces and are summarized in reference [40]. Smallwood et al. reviewed some of the most recent advances in the technique [41], and classified the tr-ARPES studies essentially in four categories: incoherent and coherent dynamics, dressed-states and mapping of the unoccupied structure. This division will be followed here and some relevant examples will be highlighted, useful to understand part ii of this thesis.

1.5.1   *Incoherent non-equilibrium dynamics*

In this context, incoherent dynamics refers to the lack of a coherent oscillatory- response of the photo-excited system to the impulsive excitation. This is the most common case and one can typically observe the electron population relaxation or the response of the spectral function.

In one of the first studies of tr-ARPES on cuprates superconductors, the hot electron thermalization was followed in the time domain and fitted to a set of coupled differential equation including the dynamics of electrons, strongly coupled phonons and a phonon bath (extended two-temperature model) [42]. From this kind of analysis, an averaged electron-phonon coupling in the system can be extracted. After this seminal work, many other studies on cuprates were carried on (for a review see reference [41]): one relevant example is reference [43] showing how time-dependent studies of the self-energy can be performed in tr-ARPES.

Another example is the one of $1T$-TiSe$_2$, a transition-metal dichalcogenide exhibiting a charge density wave (CDW) phase transition at low temperature. Here, the low temperature phase is characterized by a back-folded valence band at high-momenta, absent in the high temperature phase. To reach the band location at the Brillouin zone border a HHG-based tr-ARPES setup was employed. A time-resolution below 35 fs was exploited to show that the response of the CDW feature does not show any bottlenecks in its time constant, which was interpreted as an indication that the mechanism behind the CDW formation is purely electronic [44]. The optical excitations does not transfer population directly from the CDW band, which is influenced mainly by the different screening conditions after perturbation: $1T$-TiSe$_2$ is therefore an example where population dynamics and spectral function intensity can be separated. tr-ARPES results on other CDW system are summarized in reference [45].

1.5.2 *Coherent non-equilibrium dynamics*

A sudden pump excitation can trigger the coherent motion of a lattice mode (or in general a mode coupled to the electronic system), provided that the pulse duration is shorter than 1/4 of the mode period. This time is considered the minimum time to start such a coherent lattice motion. The coherent response is often coupled to very specific quasi-particle bands: the appearance, dephasing and decay of coherent oscillations can be used to study the coupling of the mode to the single-particle states. An important example is the case of the *tri-telluride TbTe₃* [46]. In this CDW system the band-gap responds in an oscillatory fashion to the optical perturbation, highlighting the role of lattice coupling in the formation of the CDW. A similar coherent response in the spectral function of the CDW gap was also demonstrated in the case of 1*T*-TiSe₂ [47]: this is an example of how, by adopting a different pump wavelength one can observe in the same system both coherent [47] and incoherent dynamics [44]. Other examples of coherent dynamics were observed in the Mott-insulator *TaS₂* [48], in Pnictides superconductors [49, 50], and thin films of FeSe on SrTiO_3 [51].

1.5.3 *Dressed states*

Photon-dressing of either the initial or the final-state has been observed in photoemission. The latter case, is the most commonly reported, and is also called laser-assisted photoemission (LAPE). LAPE is related to the absorption or the emission of photons at the energy of the pump laser by the free electron final state, mediated by the surface. Experimentally, LAPE signals appears as replicas (or side-bands) of the main photoemission transition. Its peak amplitude in time is the most precise definition of temporal overlap between pump and probe, this *time-zero* might not always be otherwise clearly defined in the experiment. Following the analysis of references [52, 53], for a given pump electric field amplitude $\vec{E}_0$, frequency ω_{ir} and photoelectron momentum $\vec{p}$, it is possible to calculate the relative strength of the n-th ($n = \pm1, \pm2, ..$) sidebands compared to the main line:

$$A_n \approx J_n^2\left(\frac{\vec{p} \cdot \vec{E}_0}{\omega_{ir}^2}\right),\tag{26}$$

J_n is a Bessel function. For the first side-band, and for the typical intensities used in tr-ARPES one can approximate:

$$A_1 \propto \frac{IE_{kin}}{\omega_{ir}^4},\tag{27}$$

where I is the laser intensity and E_{kin} is the photoelectron kinetic energy. The temporal intensity of LAPE signal, can be taken as a measure of the cross-correlation between the pump and the probe beam. It is also clear that the observation of this kind of dressed state is more difficult for low photon energy probes and is strongly enhanced using shorter wavelength pump.

Photon dressing of the initial state has been observed in topological insulators using an infrared pump [54]. In this case one talks about Floquet-Bloch states: this second case can be experimentally distinguished from the first one as overlapping sidebands can interact and band-gaps open in the spectrum. These side-bands are the result of a periodical perturbation of the Hamiltonian, which can be described using Floquet theory. An appealing feature is the possibility to realized coupled light-matter states, existing only out-of-equilibrium, which can be controlled by the driving laser field. For a more extensive description the reader is referred to the work of Mahmood et al. [55].

1.5.4 Unoccupied band structure mapping

Time-resolved photoemission spectroscopies have the ability to populate and probe unoccupied states of matter. For example, in semiconductors excited by a pump photon-energy sufficiently larger than the band-gap, one can populate and observe the conduction band. The carrier excess energy is relaxed by scattering events which transiently populate bands at different momenta and finally accumulate at the conduction band bottom. Here the carriers dwell for longer time before finally recombining at equilibrium. By probing the system at intermediate times, the conduction band can be mapped in reciprocal space thanks to this transient occupation.

Another experimental technique providing access to unoccupied bands is inverse-photoemission (IPES) [22]: here one shines electrons of a well defined energy on the surface, while recording the emitted radiation. The cross-section for the process is however considerably lower as compared to direct photoemission (PES), the ratio between the two cross-sections is [56]:

$$r = \frac{\sigma_{IPES}}{\sigma_{IPES}} == \left(\frac{\lambda_{el}}{\lambda_{ph}}\right)^2. \tag{28}$$

$r \approx 10^{-5}$ for the VUV photon energies at which IPES experiments are typically performed. An experimental disadvantage compared to direct photoemission is the lack of efficient parallel detection schemes, which imply long acquisition times. An important distinction between the IPES and PES measurement is that the final state is different: in IPES one has a N+1 electron final state in the solid, whereas in

PES an N-1 one. Therefore a direct comparison between the two measurements is not possible. Unoccupied state mapping by tr-ARPES is essentially a two-photon photoemission experiment. An elegant examples of this approach was demonstrated for $BiSe_2$ in ref [57]. Here a degenerate 6 eV pump / 6 eV probe was adopted, allowing to observe unoccupied states up to the vacuum level. Higher photon energies grant access to the conduction band at higher momenta: this has been already shown for semiconductors in the transition metal dichalcogenide family [58–61]. In this thesis an advance of this method will be presented in Chapter 5: thanks to the higher photon flux and repetition rate, this scheme can be combined with angular scanning of the tr-ARPES signal. By doing this, it is possible two extract a three-dimensional map of the conduction band, and compare the findings with density functional theory and with inverse-photoemission.

1.5.5 *Quasi-particle lifetimes and tr-ARPES decay rates*

Often, one is interested in characterizing the ground state of a complex material: is it possible to extract equilibrium information from tr-ARPES data?

In a static ARPES experiment, the equilibrium spectral function is probed, whereas in time-resolved experiments a out-of-equilibrium state is induced by the pump. Out-of-equilibrium, the fundamental interactions might be significantly altered, masking the equilibrium quantities. A theoretical analysis form Sentef et al. [62] showed how the equilibrium self-energy can be used to describe the relaxation dynamics in tr-ARPES. This analysis, valid in the limit of weak excitations and low temperatures, suggests a method for measuring the equilibrium electron-phonon coupling in tr-ARPES. For this comparison one should extract the single-particle lifetime τ_{sp} from tr-ARPES: τ_{sp} is related to the imaginary part of the self energy $2Im(\Sigma) = \hbar/\tau_{sp}$, which can be calculated by theory.

Observing the decay of signal intensity in a tr-ARPES experiment for a given state, one does not directly measure the single particle lifetime, but rather a population lifetime τ_{pop}. An open question for the interpretation of the data, is whether this population lifetime can be directly compared to the fundamental single-particle life-times. τ_{sp} can be measured independently by the linewidth of high-resolution ARPES peaks in many important cases (Section 1.2.3).

Along these lines, Yang et al. systematically compared the ARPES quasi-particle life in a cuprate superconductor with the tr-ARPES-derived population relaxation times [63]. The comparison reveal discrepancies of up to two orders-of-magnitude, showing how the population and the single-particle lifetimes are generally non-equivalent, even in the very small perturbation regime. This was taken as an in-

dication that the electron-phonon coupling alone cannot explain the relaxation, and other scattering channels must contribute in this case.

It is of great interest to find special cases where tr-ARPES directly measures the quasi-particle lifetime and quantitatively compare the data with ab-initio calculation. This might be simpler for materials without strong correlations and with simpler ground states: in this case, ab-initio methods can be used to calculate a realistic self-energy. In the last chapter of this thesis (Section 5.4.7), the lifetime of 2H-WSe$_2$ will be compared with ab-initio calculations of the electron-phonon coupling, revealing a reasonable agreement with the experiment.

1.6 PRACTICAL ASPECTS OF TR-ARPES

In the final section of this chapter, some experimental aspects of tr-ARPES will be reviewed, highlighting the important requirements for the light source developed in this thesis (Part i). A driving force for the development of tr-ARPES experiments is the availability of suitable laser sources for producing the femtosecond pulses at high photon energy and at high repetition rate. As shown in the previous sections, VUV photon energies are required for direct photoemission, while EUV energies allow to reach the complete Brillouin zone zone. The importance of high repetition rates is in the reduction of space-charge-induced spectral distortions: the space-charge problem will be discussed in more detail in Section 1.6.1.

After the first observation of EUV high-order harmonics from a 350 fs KrF* laser (248 nm) [64] and from a picosecond Nd:YAG laser (1064 nm) [65] , it was realized that the radiation could be used for time-resolved spectroscopies. In this first demonstrations, the laser operated at repetition rate of few Hz, non-ideal for tr-ARPES. Dye laser technology, by providing broader gain bandwidths, allowed to reach shorter pulse durations and hence higher conversion efficiencies. The first implementation of tr-ARPES on surfaces appears in the work of Height [40] using such lasers at a repetition rate of 100 Hz.

After the nineties, the fast development of Ti:Sapphire lasers routinely provided powerful femtosecond pulses, determining a wider diffusion of laser-based ultrafast spectroscopies. In particular, both low-order harmonics produced in the perturbative regime [66] and high-order harmonics in the non-perturbative regime [67] were demonstrated in gases using Ti:Sapphire lasers, now with repetition rates above 1 KHz. The application of Ti:Sapphire technology to EUV photoemission is reviewed by Bauer [68].

Parallel to these EUV photoemission experiments, an increasing amount of tr-ARPES studies at VUV energies, were performed at repetition rates of hundreds of kHz and with energy resolution in the sub-100 meV regime. In this case, the frequency conversion was at-

tained in non-linear crystal, thereby limiting the maximum energy to $\approx$ 7 eV, due to lack of suitable nonlinear optical materials. This crystal-based tr-ARPES, owing to the superior energy resolution and better statistics, has become a mature-technique, adopted in many laboratories. The opportunity of extending the energy range while maintaining the high repetition rate has attracted increasing attention in the past years. By boosting the HHG conversion efficiency in several ways, several Ti:Sapphire-based high-repetition-rate sources for photoemission were demonstrated [12, 13]. These sources were applied for static photoemission experiments [14] and for tr-ARPES [61].

A second, more radical approach, is to change the adopted laser technology, overcoming the past limitations by increasing the available average power. In this work it will shown how OPA technology allows to bridge the technology gap between high-repetition-rate crystal-based tr-ARPES and high-energy HHG-based tr-ARPES experiments.

1.6.1 *Space charge*

In time-resolved PES, an electron wavepacket of duration comparable to the probe pulse is emitted in vacuum. The initial charge distribution is strongly localized in the vertical direction: if the average number of photoelectrons per pulse is greater than one, Coulomb-repulsion starts to become important and the electron trajectories and velocities are modified. The measured photoelectron peaks result broadened and shifted in energy and at the same time the angular distribution is distorted. While the way to avoid space charge effects all-together is to limit the incident flux to be in the limit of a single photoelectron per pulse, this approach is not always possible. In tr-ARPES, one is most often interested in a subset of the sample's bands, typically close to the Fermi level. Most of the photo-emitted charge is coming from other allowed transitions and secondary electrons: if one would limit the emission rate to a single photoelectron per pulse, the count-rate on the detector would be orders of magnitude lower, resulting in longer integration times. The effect is worsened at higher photon energies, as the window of allowed transitions is increased and deeper levels participate to the emission. A limited space charge can be accepted as long as the experimental resolution ($\Delta E_{charge} \ll \Delta E_{resolution}$) is not hindered and the energy shifts are moderate (few meV). This is particularly true in time-resolved experiments where the energy resolution is already necessarily reduced by the short temporal resolution. Several studies have quantified the effect of space charge in different regimes. For the case of femtose-

cond pulses, Passlack et al. [69] derived the following equation for the energy resolution broadening ΔE_{kin}:

$$\Delta E_{kin} \approx \left(\frac{m_e e^2}{\pi \epsilon_0 r_0} \right)^{\frac{1}{2}} v_0 \sqrt{N} \qquad (29)$$

In this equation m_e is the electron mass, ϵ_0 is the vacuum dielectric constant, r_0 is the EUV spot radius, v_0 is the group velocity of the photoelectron wavepacket and finally N is the number of photoelectrons in the pulse. As the amount of photoelectrons per pulse increases linearly with the number of probe photons per pulse, $\Delta E_{kin} \propto v_{rep}^{-1/2}$. Equation (29) shows how, by approaching the single electron per pulse
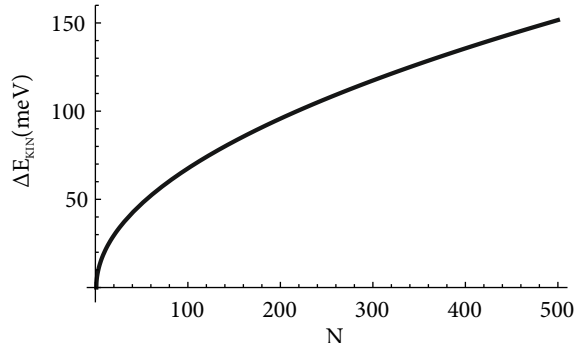
Figure 8: Calculated energy broadening from space charge, using Equation 29. N is the number of photoelectrons per pulse.

The case of picosecond pulses deviates from this and has been treated in reference [70].

1.6.2 Sample relaxation

tr-ARPES experiments are performed by averaging results over time using a train of pulses produced by a mode-locked femtosecond laser: such a pulse train is illustrated in Figure 9. Every pulse has a duration τ_{pulse} and is separated from the next one by the duty cycle of the laser $T_{rep} = 1/v_{rep}$, where v_{rep} is the repetition rate of the light source.

In order for the experiment to provide a meaningful picture of the dynamics of the ground state, it is necessary for the system to achieve full recovery after photo-excitation. Therefore, for the relaxation time $T_{relaxation}$ the inequality $T_{relaxation} < T_{rep}$ must hold. So far only the non-thermal and quasi-thermal dynamics in the first few tens of picoseconds have been introduced: after these short time-scales, equilibrium is not yet reached and new relaxation processes occur. An overview of the scattering processes and the respective timescales in the case of semiconductors are shown in Figure 10 and Figure 11, respectively.
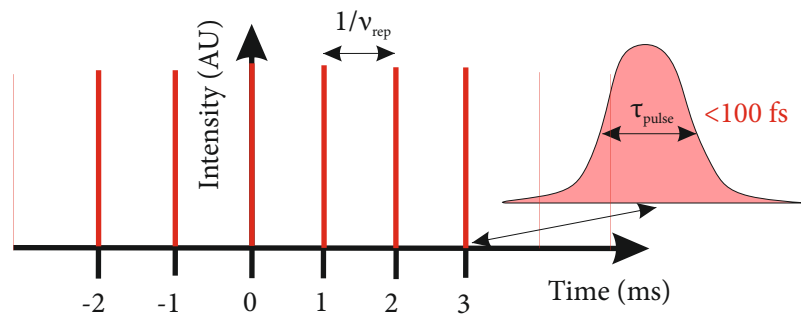
Figure 9: The pulse train of a femtosecond laser, the pulse duration FWHM is τ_{pulse} and the repetition rate is ν_{rep}.
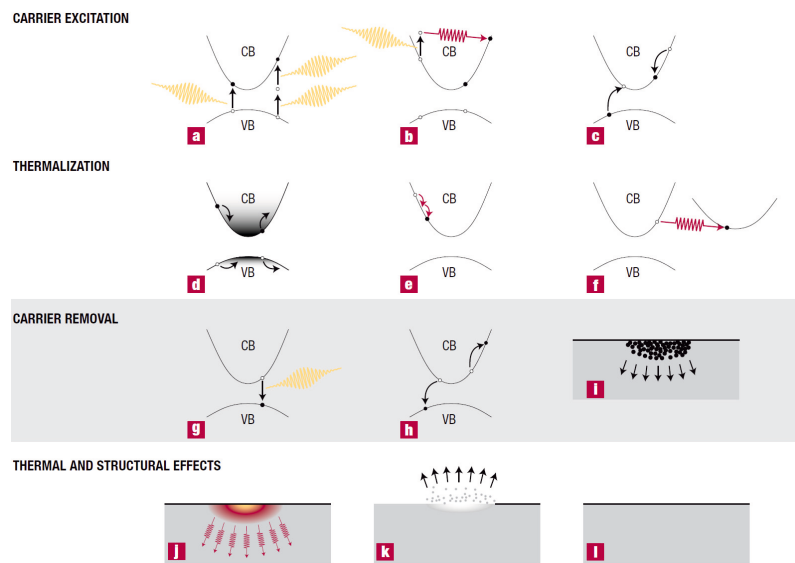
Figure 10: Scattering events and relaxation mechanisms in a semiconductor, from reference [71]. a) Single- and Multi-photon absorption. b) Free-carrier absorption, mediated by a phonon. c) Auger or impact ionization. d) Carrier-carrier scattering and distribution thermalization. e) Intra-valley carrier-phonon scattering. f) Inter-valley carrier-phonon scattering. g) Radiative recombination. h) Non-radiative Auger recombination. i) Diffusion of excited carriers. j) Thermal diffusion. k) Ablation. l) Resolidification and condensation.

Immediately after photo-absorption (Figure 10-a,b), free carriers are created in the system and scattering events (Figure 10-d,e,f) act to bring back the system energy distribution to a thermal one. The total amount of carriers is not a constant and effects as impact ionization (Figure 10-c) might promote additional carriers to the valence band [71]. After the initial thermalization, an excess of free carriers and an excess of energy in the lattice (heath) have still to be removed from the excited area. The main mechanisms for carrier removal are radiative recombination, non-radiative recombination (Auger recombination) and carrier diffusion (Figure 10-g,h,l). Provided that the excitation density is below the damage threshold (i.e. no irreversible changes of the sample are produced), the main thermal relaxation mechanism to be considered is heat diffusion (Figure 10-j). The timescales of all these processes, as a function of the carrier density, are summarized in Figure 11 for GaAs: in the case of a bulk semi-conductor they extend up to the μs regime, showing that the maximum repetition rate which can be tolerated, is in the order of hundreds of kHz for high fluences. In general, besides being fluence-dependent the timescales are material-dependent, hence depend on materials properties such as carrier mobility, and heat diffusion coefficients. In general one can expect a metallic system to exhibit faster relaxations as compared to semiconductors and a bulk material to relax faster than a layered material: the maximum repetition rate depends on the specific problem, but typically ranges from several kHz to few MHz. A final aspect which should be mentioned is sample heating: for a given an excitation density, a high-repetition-rate source deposits a larger amount of energy per unit time on the whole sample. If the thermal conductivity and the cooling power of the sample holder are not sufficient, a constant temperature increase of the sample might also occur.
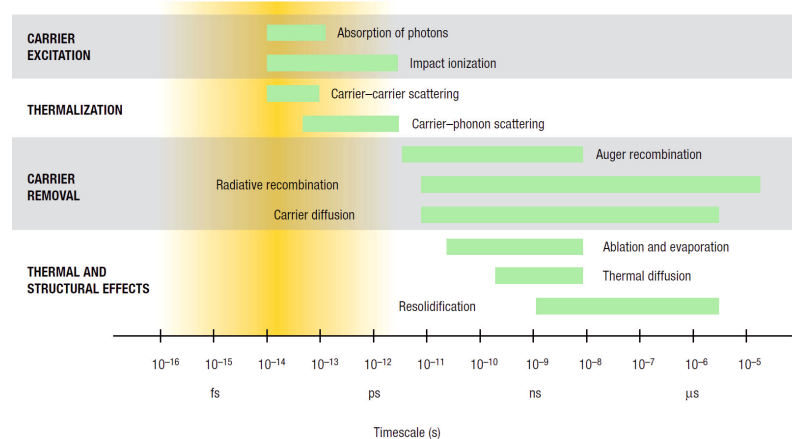
Figure 11: Timescales of relaxation for GaAs, from ref [71]. The green bars show time ranges for excited carrier densities between $10^{17} - 10^{23} cm^{-3}$.

As the excitation density increases, multi-photon photoemission from the pump pulses might take place. The additional photoelectrons contribute to the overall space charge and might even dominate the direct photoemission contribution. This is particularly true for higher pump photon energies. Pump-induced space charge effects where studied in detail by Oloff et al. [72]. The effects of pump-induced space charge are additional broadening and shifts of the photoemission peaks. The magnitude of the shifts scales linearly with the pump photo-electron linear density; the scaling with intensity follows a power law $\propto I^n$, where n is the lowest number of photons necessary to overcome the workfunction. Due to the different propagation speed of the probe photoelectrons and the low-energy pump photoelectron cloud, the shifts are time-delay dependent, being maximum at zero delay and decaying at longer times. The observed behavior is asymmetric between negative delays (probe pulse arrive before the pump) and positive delays: for positive delays the probe photoelectrons are first repelled by the pump electrons which took off first, then, thanks to their higher speed, they take over the pump charge cloud and are accelerated toward the detector. The dynamics involved are relatively slow compared to many case of interest, but still not negligible. The experimental results of Oloff, for a UV pump energy of 3.16 eV are shown in figure 12.
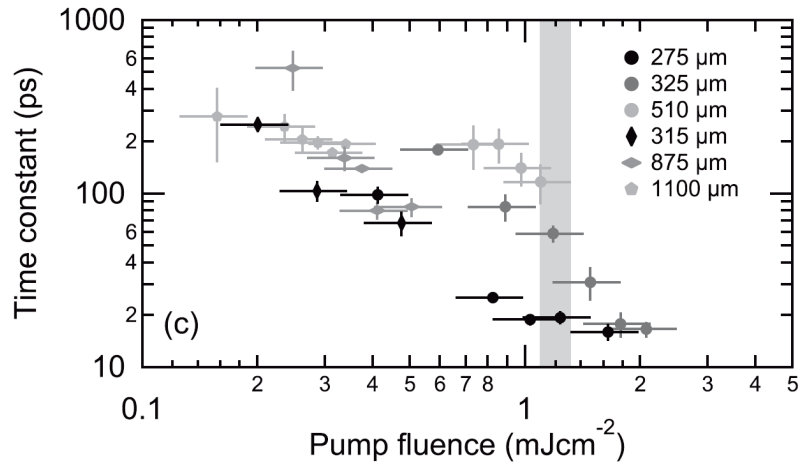
Figure 12: Pump space charge dynamics for positive delays, for a pump energy of 3.16 eV and various pump spot sizes, from ref [72].

The dynamics can be simulated by a mean-field model, taking in account the pump image charge in the sample. The rationale is that, when analyzing long-delay dynamics, special care has to be taken: either one has to limit itself to excitation densities where pump-space charge is negligible, or numerical simulation can be used to disentangle the real and space charge-induced dynamics.

1.6.4 *ARPES hardware*

This last section describes the main features of a tr-ARPES experimental setup, and summarizes the characteristic of different setups found in the literature. Figure 13 sketches the fundamental components of a tr-ARPES setup. The hearth of the system is a femtosecond laser: most of the current setups employ Ti:Sapphire amplifiers with sub-100 fs pulse duration and repetition rates higher than 1 KHz and with a wavelength centered in the NIR, at about 800 nm or 1.55 eV. The output pulses are split in two arms: a pump arm and a probe arm. By sharing a common origin, (*optical synchronization*) the timing jitter between pump and probe is at a few-femtosecond level, and only depends on optical path length fluctuations. This inherent synchronization is an advantage of table-top systems when compared to storage ring facilities or free electron lasers (FELs), where jitter between the pump laser and the FEL radiation worsen the temporal resolution. Delay-control on a femtosecond level is achieved with a high precision mechanical stage, typically with resolution of few hundreds of nanometers.
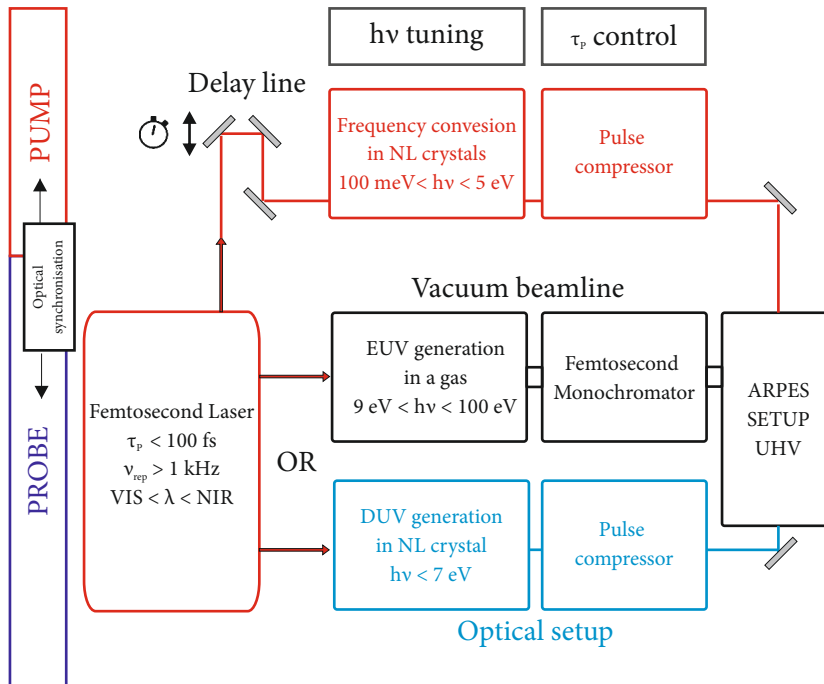
Figure 13: Conceptual scheme for a tr-ARPES experiment, comparing crystal-based and HHG-based setups.

In the probe arm, two approaches are commonly followed to convert the frequency to the DUV/EUV. Either the non-linear conversion is performed in a crystal [73–76] or in a gas [67, 77–79, 13, 80–82] .

In crystal-based tr-ARPES, the maximum achievable photon energy is about 7 eV: here, the limiting factor is the lack of suitable nonlinear crystals supporting *phase-matching* beyond this level. In order to reach the desired photon energy two nonlinear conversion steps are

needed, with a typical overall-efficiency on the order of 10^{-4}. One typically has to reduce the flux of the source to limit space charge [75]: a situation which can be referred as *space-charge-limited* source. Non-linear frequency conversion and the related phase matching will be explained in more detail in the Chapter 2. The DUV beam is separated from the fundamental radiation either by employing non-collinear interaction geometries (spatial separation) or in a angular dispersive element within the pulse compressor. Such pulse compressor follows the DUV generation setup, and is used to minimize the pulse broadening due to transmission though optical elements, such as the focusing lenses and the window of the UHV ARPES chamber.

Gas-based tr-ARPES is technically more complex as the EUV radiation is strongly absorbed in air. EUV generation is performed in a vacuum chamber containing a *gas target* (see Chapter 3 for more details). The laser pulses, typically more powerful than the crystal-based setups, are incoupled in the chamber and focused in the gas target, to intensities up to 10^{13} W/cm^2 fot the perturbative regime, or on the order of 10^{14} W/cm^2 in the case of high-harmonic generation. EUV radiation is propagating collinearly with the driver radiation and several odd harmonics of the driver laser might be simultaneously present. A single harmonic has to be selected while preserving the intrinsic femtosecond duration of the pulses. The conversion efficiency is on the order of 10^{-6}, therefore the strong fundamental radiation background has to be suppressed to avoid parasitic multi-photon photoemission. Moreover, the gas load has to be minimized via a differential pumping gradient, to avoid contamination of the UHV ARPES chamber.

The harmonic selection is performed in two ways: the most straightforward is the use of EUV multilayer mirrors [67, 13, 81] designed for having a high reflectivity for a single harmonic. In the EUV range all materials are strongly absorbing: the efficiency of multilayer optics in this range is low (typically $\lesssim 10\%$). Mirrors are used in combination with thin (hundreds of nm) metal foils to completely suppress the fundamental wavelength and part of the harmonic spectrum, depending on the metal's photoemission cross-section. Temporal pulse broadening effects are in this case limited. The main complication is to achieve a good contrast between neighboring harmonics, which often requires the use of several, lossy, mirrors. The drawback in this case is the lack of tunability of the source: this limits the experimental access to state with different $k_\perp$; at the same time unfavorable matrix element might hinder some experiments. The use of grating-based monochromator is complicated by pulse-broadening effects, mainly due to the pulse front tilting (the arrival time of the light pulse changes along the transverse direction of the beam) induced by the light diffraction. Special designs have to be implemented to minimize the effects in single grating setup [83] or in double-grating configuration

[84]. The design is further complicated (but this is not specific of tr-ARPES) from the fact that the optics have to operate in grazing incidence geometry to provide sufficient reflectivity in the EUV range. Thanks to the appeal of such a source tunability, several tr-ARPES experimental setup with single [78–80, 82] and double grating [77] configurations have been demonstrated, with resolving powers of up to 100.

The overall transmission of these two harmonic-selection approaches is comparable and on the order of about 10%. By driving the HHG with the fundamental of a Ti:Sapphire a monochromatic flux up to $10^{11} ph/s$ and energy resolution of $\approx 200 meV$ can be achieved on the sample [82]. This flux, although already comparable with what is achieved with ARPES beamlines (see section 1.2.4), cannot be fully used. Due to the low repetition rate, high space charge is reached well before exploiting the true capabilities of the source.

It has been realized that, in HHG with an UV driver-wavelength [85, 13], both the efficiency for the lower-order harmonics and the energy resolution can be enhanced. The advantage of using a shorter driver-wavelength are multiple: first, the overall efficiency is increased by up to two order-of-magnitude [13]. Second, the frequency spacing of the harmonics is increased, making the selection of a single harmonic an easier task. Third, due improved phase-matching, an intrinsically narrower bandwidth is produced (these effects will be explained in more detail in Chapter 3). The repetition rate of the tr-ARPES beamlines described ranges from 1 kHz to 100 kHz. For the case of static photoemission a compact HHG-based setup operating at 4 MHz has also been demonstrated [14, 86, 87]. The flux of these light sources drops above 50 kHz due to an unfavorable scaling of average power for Ti:Sapphire lasers. For example, reference [13], presents a setup based on a Ti:Sapphire cryo-regenerative amplifier with 12 W average power and 50 fs pulse duration while reference [60] uses a modified commercial regenerative amplifier delivering 45 fs pulses at 100 kHz, with an average power of 1 W. Table 1 and Table 2 summarizes the parameters of the existing tr-ARPES light sources, for HHG-based and crystal-based solution, respectively. The table includes as a comparison also the parameters of the OPCPA-based setup described in the next chapters.

reference	hν (eV)	ΔE (meV)	Δt (fs)	Flux (ph/s)	ν_r (kHz)
[40]	10-50	N.D	N.D.	N.D.	0.54
[67]	41.85	800	N.D.	8×10^6	1
[78]	20-50	900-390	28-60	1.6-0.9 $\times 10^{10}$	1
[77]	20-36	400-600	N.D.	10^{10}	10
[79]	10-100	150	100	3.6×10^7	10
[85]	22.3	150	32	10^{11}	1
[81]	22.1	170	13	10^{10}	1
[13]	22.3	72	N.D.	3×10^{11}	50
[60]	23.25	N.D.	80	9×10^8	100
OPCPA	21.7	130	40	$> 10^{11}$	500

Table 1: HHG-based tr-ARPES light sources

reference	hν (eV)	ΔE (meV)	Δt (fs)	Flux (ph/s)	ν_r (kHz)
[73]	6.2	60	N.D.	N.D.	1
[75]	6.28	70	65	1×10^{13}	250
[74]	5.93	23	310	2×10^{12}	1-(5.4×10^3)
[76]	6.05	50	85	N.D.	100
[88]	5.92	10.5	240	N.D.	250
OPCPA	6.3	100	50	$> 10^{12}$	500

Table 2: Crystal-based tr-ARPES light sources

The final experimental aspect concern the pump pulses: the wavelength of the pump pulse in most setup is restricted to the fundamental harmonic (FH) of the driver laser, or its second and third harmonics (SH, TH). Ideally however, the probe wavelength should be tuned to address specific resonances of the sample. The sample itself imposes fundamental limitations on the maximum fluence which can be adopted at a given repetition rate. Such limit is reached when multi-photon-photoemission from the pump results in resolution losses and spectral shifts, or when the sample does not relax between successive pulses. This limit can be easily achieved by the harmonics of the driver laser, however it is hard to achieve high fluences at longer-wavelengths (NIR-MIR).

Continuous pump-frequency tunability between 200 nm and 20 μm is reported in reference [78]. This is achieved using a commercial frequency conversion setup[3] which exploits a very high pulse power (780 nm, 7.7 mJ, 30 fs).

The conversion efficiencies in the MIR are low: for 10 μm one has an overall efficiency on the order of 1.3×10^{-3}, after several cascaded

---

3 HE-TOPAS

nonlinear conversion steps. For a given power, producing similar wavelengths for a high-repetition rate systems is even more challenging and one would expect even lower efficiencies.

Tunability in the visible range is more readily achieved via optical parametric amplification: several high-repetition-rate sources are equipped with tunable VIS pump pulses [60, 76]. An independent pulse compressor for the pump exists in several setups, for example [79].

1.6.5 *Conclusion*

In this introductory chapter the major features of tr-ARPES experiments have been illustrated. In order to combat space charge, repetition rates of several hundreds of kHz are desirable, together with fluxes exceeding 10^{11} ph/s to optimize data-acquisition-rate. This performance are easily reached by VUV crystal-based sources, however, due to technical limitations, they are yet unavailable for gas-based EUV sources. The latter are desirable for accessing the whole Brillouin zone of material.

The aim of this thesis is to bridge this technology gap and develop a space-charge-limited EUV source operating at hundreds of kHz. The development of a laser system beyond Ti:Sapphire is the subject of the next chapter, followed by the design and test of the high-harmonic generation experimental beamline.

Part I

THE LIGHT SOURCE

2

HYBRID YTTERBIUM FIBER-SLAB OPTICAL CHIRPED PULSE AMPLIFIER

2.1 INTRODUCTION

Light pulses with duration below one picosecond are commonly referred as *ultrashort* pulses (Section 2.2). The pulse duration, defined here as the temporal full-width at half maximum of the light-field intensity, is one of the most important parameters when dealing with time-resolved spectroscopies such as tr-ARPES: the temporal resolution of the experiment is the width of the cross-correlation between the pump and the probe pulses, and has to be shorter than the process investigated, which in a condensed matter system can last few femtoseconds (section 1.3). Today's state-of-the-art laser technology has broken into the femtosecond regime, thanks to well-established Ti:Sapphire chirped pulse laser amplifiers which reliably provide femtosecond pulses centered at a photon energy close to 1.5 eV (section 2.3).

While this photon energy is bound to the laser's gain material, different photon energies are needed for many spectroscopies, including tr-ARPES (section 1.1.2). A route to overcome this limitation and produce femtosecond pulses at different wavelengths is the use of nonlinear optical interactions (section 2.2.1). In nonlinear optics, the physical limitations of the gain medium are replaced by less stringent constrains, given by *phase matching* (section 2.4.1). A wider photon energy range is achievable, which spans a range from the THz to the EUV.

In particular, photoelectron spectroscopies rely on the availability of femtosecond DUV to EUV pulses. The known laser gain media in this energy range are based on excimers, unfortunately, the level structure of these unstable molecules limits the pulse duration to hundreds of femtoseconds. As an alternative, free-electron lasers are becoming an established source of short EUV pulses. The drawback in this case is the limited access to these large-scale facilities. A laboratory-scale, table-top source for tr-ARPES has to rely on nonlinear frequency conversion to produce femtosecond EUV pulses.

The pulse energy divided by the pulse duration is the pulse power, which is a good order-of-magnitude measure of how easy is for a light pulse to trigger a nonlinear response of matter. EUV photons can be generated starting from the near-infrared (NIR) in a process called high-harmonic generation (HHG, Chapter 3). HHG relies on atomic ionization by very strong electric fields: to produce a usa-

ble EUV flux for photoemission experiments, a pulse power of several hundreds of MW is desirable. This is currently attainable with Ti:Sapphire lasers at a repetition of few tens of kilohertz: ideally too low for many tr-ARPES experiments (section 1.3). Further scaling in average power of Ti:Sapphire lasers is very complex (section 2.3.2), however, another class of ultrafast lasers is better suited to reach very high average powers: Ytterbium lasers (section 2.3.3). The gain bandwidth of Ytterbium laser amplifiers cannot directly compete with the on of Ti:Sapphire lasers. This problem can be circumvented by a second order nonlinear-optical interactions (section 2.4), known as *optical parametric amplification* (OPA).

In an optical parametric amplifier, the optical power of a laser can be transferred to a weaker broadband pulse. By using special noncollinear phase-matching techniques (section 2.6), the bandwidth of the process can surpass the one attainable in conventional laser amplifiers. Moreover, it is possible to achieve wavelength and bandwidth control by acting on the spectral phase of the amplified pulse (section 2.7). Such an amplifier is called *optical chirped pulse parametric amplifier*, OPCPA in short, and will be the central subject of this chapter.

At the hearth of the system that will be presented, there is an ultrafast Ytterbium laser, based on a combination of an Ytterbium fiber amplifier and an Yb:YAG slab amplifier (section 2.7.4). The bandwidth of the Ytterbium fiber laser is frequency broadened in a process known as *white-light generation* (section 2.7.2) which produces a relatively weak spectral *supercontinuum*, covering the visible range and seeding the OPCPA. The average power is then raised to the final value of more than 20 W thanks to the picosecond Yb:YAG slab amplifier, used to pump the parametric amplification process. As this second laser is seeded by the fiber laser, the white light pulses are optically synchronized to the pump (section 2.7.1). This hybrid amplification scheme (section 2.7.1.4), ensures good long-term power and spectral stability. Section 2.7.6 is devoted to a thorough characterization of the OPCPA performance and to its wavelength and bandwidth tunability. The OPCPA output is recompressed to less than 20 fs, with a final energy of more than 30 μJ at 500 kHz. These gigawatt pulses can be easily focused to intensity exceeding 10^{14} W/cm^2 and are capable of high-harmonic generation.

2.2 ULTRASHORT LASER PULSES

This section provides a minimal mathematical background to describe ultrashort pulses: the definitions presented in the following sections will be used throughout the thesis to estimate the effects of linear propagation of ultrafast pulses in dispersive materials. A temporally narrow pulse exhibits a broad spectrum in the frequency domain: while propagating through matter, due to the frequency-

dependent complex refractive index $\tilde{n}(\omega)$, different frequencies travel at different phase velocities and are attenuated by different amounts. The light pulse, initially short, spreads in time, reducing its intensity. In practice, the ultimate goal is to know - and possibly control - the pulse's time duration throughout the optical system, achieving minimal temporal spread where nonlinear interaction have to be realized or when a pump and probe experiment investigates ultrafast dynamics in matter. For simplicity, one can first assume that the electric field has a plane wave spatial dependence, linearly polarized along the x axis, and propagating along the z direction:

$$\mathbf{E}(x,y,z,t) = \mathcal{E}(t)\sin(kz + \Phi_0)\hat{\mathbf{x}}. \tag{30}$$

This is a good approximation in the case of a collimated laser beam: in order to describe the temporal behavior of the light pulse, one can restrict the analysis to the temporal function $\mathcal{E}(t)$. The mathematics can be simplified by introducing several auxiliary quantities [89, 90]:

$$\mathcal{E}(t) = A(t)exp(i\left[\omega_0 t - \Phi(t)\right]) + c.c. \tag{31}$$

Here one defines a central *carrier frequency* of the pulse ω_0, which modulates a temporal envelope function $A(t)$. $A(t)$ is assumed to vary slowly in time as compared to the carrier frequency ω (formally one talks about a *slowly varying envelope approximation* , $|\partial A/\partial t| \ll \omega_0|A(t)|$. The complex electric field amplitude is defined as:

$$\tilde{E}(t) = A(t)\exp(i\Phi(t)), \tag{32}$$

where the quickly-oscillating carrier factor is dropped. The optical intensity, also called *irradiance*, is defined as the radiant power per unit area and is related to the envelope by the following relation:

$$I(t) = \frac{\epsilon_0 c}{2}|\mathcal{E}(t)|^2, \tag{33}$$

$$A(t) = \sqrt{\frac{2I(t)}{\epsilon_0 c}}. \tag{34}$$

It is common to define the pulse duration as the full-width at half-maximum of the function $I(t)$. In the frequency domain one defines the complex spectral amplitude as the Fourier transform of the real field $\mathcal{E}(t)$.

$$\tilde{E}(\omega) = \int_{-\infty}^{\infty} \mathcal{E}(t)e^{-i\omega t} \tag{35}$$

Since $\mathcal{E}(t)$ is a real function, the negative frequency part of $\tilde{E}(\omega)$ does not contain extra information ($\tilde{E}(-\omega) = \tilde{E}^*(\omega)$) and is typically neg-

lected when plotting the spectral amplitude. By extracting the amplitude and phase of the complex spectral amplitude one writes:

$$\tilde{E}(\omega) = \sqrt{S(\omega)} \exp(-i\phi(\omega)), \tag{36}$$

$$S(\omega) = |\tilde{E}(\omega)|^2, \tag{37}$$

$S(\omega)$ is proportional to the spectral intensity measured with a spectrometer, and $\phi(\omega)$ is the so-called *spectral phase*.

The temporal and spectral distribution of a signal are not independent of each other: for given a temporal width, the spectral width must be greater than a certain limit, set by the so-called time-bandwidth product. The following relation holds in general [90]:

$$\langle t^2 \rangle \langle \omega^2 \rangle \geq \frac{1}{4}, \tag{38}$$

where $\langle t^2 \rangle$ and $\langle \omega^2 \rangle$ are the *second-order moments* of the temporal and spectral distributions:

$$\langle t^2 \rangle = \frac{\int_{-\infty}^{\infty} t^2 |\tilde{E}(t)|^2 dt}{\int_{-\infty}^{\infty} |\tilde{E}(t)|^2 dt}, \tag{39}$$

$$\langle \omega^2 \rangle = \frac{\int_{-\infty}^{\infty} \omega^2 |\tilde{E}(\omega)|^2 d\omega}{\int_{-\infty}^{\infty} |\tilde{E}(\omega)|^2 d\omega}. \tag{40}$$

The knowledge of either $\tilde{E}(\omega)$ or $\tilde{E}(t)$ yields to a complete knowledge of the pulse. Depending on the encountered problem, one of the two representation might yield to easier results.

The pulse propagation in a lossless optical material can be completely determined by the knowledge of the refractive index as function of frequency, $n(\omega)$. This comes from an approximate solution of the wave equation (eq. (51)) in the frequency domain [90]. The temporal pulse envelope moves across the medium at a speed given by the group velocity v_g, related to the function $k(\omega)$:

$$\frac{1}{v_g} = \frac{\partial k(\omega)}{\partial \omega}. \tag{41}$$

The spectral amplitude of the electric field, after propagating across a length z of a dispersive material with refractive index $n(\omega)$ becomes:

$$\tilde{E}(\omega, z) = \tilde{E}(\omega, 0) \exp\left(-\frac{i}{2}\frac{\partial^2}{\partial \omega^2}k(\omega)\omega_0^2 z - \frac{i}{3!}\frac{\partial^3}{\partial \omega^3}k(\omega)\omega_0^3 z - ..\right), \tag{42}$$

$$k(\omega) = \frac{\omega}{c}n(\omega), \tag{43}$$

The temporal envelope can be easily determined by inverse Fourier transform. Equation (42) shows that to include the effects of material dispersion on the pulse propagation it is sufficient to calculate the first few derivatives of the wavevector $k(\omega)$. The second and third derivative, respectively known as *group velocity dispersion* (GVD) and *third-order dispersion* (TOD) suffice in most cases, unless dealing with pulses approaching the few-cycles regime (one optical cycle for an 800 nm carrier frequency is about 2.7 fs). In this extreme case, a knowledge of the phase across the whole spectrum is necessary to describe the pulses.

It is common practice to approximate the spectrum as a Gaussian with a given bandwidth and use this simple mathematical form to estimate the pulse duration upon propagation. In this case one has:

$$S(\omega) = S_0 \exp\left(-\frac{\omega^2}{2\sigma_\omega^2}\right). \tag{44}$$

In the case of a constant spectral phase, it is straightforward to derive the temporal intensity via Fourier transformation:

$$I(t) \propto \exp\left(-\frac{\sigma_\omega^2 t^2}{2}\right) = \exp\left(-\frac{t^2}{2\sigma_t^2}\right). \tag{45}$$

The FWHM pulse duration of a Gaussian pulse is related to the parameter σ, and one has $\tau_p = 2\sqrt{2\ln 2}\,\sigma$; the FWHM spectral bandwidth Δ_ω is related to τ_p by the uncertainty relation $\tau_p \Delta_\omega = 1/2$, which attains the minimum possible value in the general inequality (38), for the case of a Fourier-limited Gaussian pulse. Figure 14 shows the temporal and spectral amplitudes of a Gaussian pulse, before and after propagation through 5 mm of fused silica, a commonly used optical material.

So far the spatial dependence of the field has been described by simple plane-waves: in actuality a laser emits an highly-directional and collimated beam, which can be focused to high intensities. When dealing with a focused beam, the spatial light distribution is better described by a Gaussian beam [91]. Assuming that the electric field spatial and temporal components are not coupled, an ultrashort laser beam can be described by the product of a Gaussian beam and a Gaussian temporal envelope. This approximation breaks down for broadband pulses as it neglects the frequency dependence of diffraction. Still, in many practical cases, the spatio-temporal Gaussian pulse can be used to calculate the peak intensity. In the waist plane of a diffraction-limited Gaussian beam, and for a Fourier-limited Gaussian temporal envelope, the peak intensity can be expressed as [92]:

$$I(r,t) = \frac{2P_0}{\pi w_0^2} e^{2(r/w_0)^2} e^{-4\ln(2)(t/\tau)^2}. \tag{46}$$
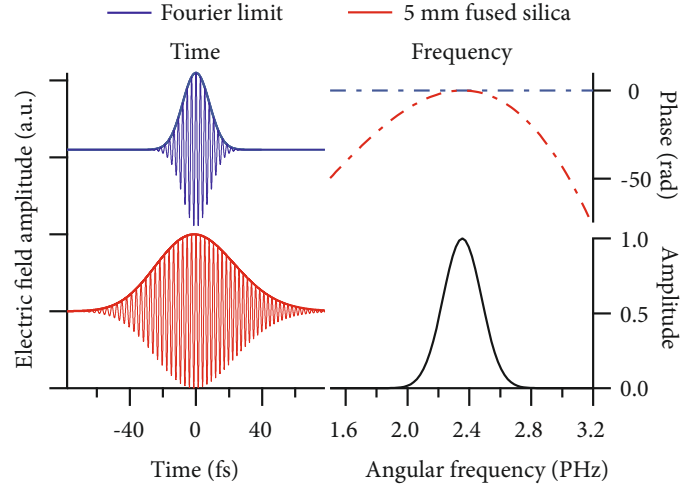
Figure 14: Left side: a Fourier-limited femtosecond pulse in the time domain, the thick blue line is the temporal envelope, while the thin line is the oscillating electric field amplitude underneath. The red trace describes the same pulse after traveling through 5 mm of fused silica. Right side: frequency-domain description of the pulses, showing the spectral phase (top) and spectral amplitude (bottom). The latter is unchanged upon chirp, the pulse chirp results in a non-linear spectral phase (dot-line traces).

Where r is the radial distance from the beam axis, τ is the FWHM pulse duration and w_0 is the Gaussian beam parameter (corresponding to the $1/e^2$ radius of the intensity profile). The pulse power P_0 appearing in this equation can be calculated from the pulse energy ϵ and the pulse duration τ using the following relation:

$$P_0 = \sqrt{\frac{4 \ln 2}{\pi}} \frac{\epsilon}{\tau}. \tag{47}$$

The optical fluence (radiant energy per unit area) is obtained from the instantaneous intensity in Equation 46 by integration over time:

$$F(r) = \frac{2\epsilon}{\pi w_0^2} e^{2(r/w_0)^2}. \tag{48}$$

The peak intensity of the pulse obtained from equation (46) corresponds to twice the pulse power divided by the mode area:

$$I(0,0) = \frac{2P_0}{\pi w_0^2}. \tag{49}$$

In a similar fashion, the peak fluence is twice the pulse power divided by the mode area:

$$F(0) = \frac{2\epsilon}{\pi w_0^2}. \tag{50}$$

2.2.1 *The wave equation and nonlinear polarization*

The demonstration of the first ruby laser dramatically increased the accessible nonlinear optical interactions: a laser beam can be focused more easily compared to a conventional light source, moreover by concentrating the field in a shorter time duration, even moderate pulse energies result in strong electric fields and high optical intensities. This is specially true in the case of ultrashort pulses, where in a temporal window of few femtoseconds, an energy of few microjoule can produce peak intensities of several gigawatt. As a result, light can drive non-linearly the response of matter, generating new light waves at different frequencies. This will be exploited throughout this thesis to generate ultrashort laser pulses and to convert light pulses to shorter wavelengths. The interaction of an electric field with matter can be described classically by the wave equation:

$$\left(\frac{\partial^2}{\partial x^2} + \frac{\partial^2}{\partial y^2} + \frac{\partial^2}{\partial z^2} - \frac{1}{c^2}\frac{\partial^2}{\partial t^2}\right)\mathbf{E}(x,y,z,t) = \mu_0 \frac{\partial^2}{\partial t^2}\mathbf{P}(x,y,z,t). \quad (51)$$

The medium polarization, driven by the electric field, act as source term. When a high-intensity optical field $\mathbf{E}$ interacts with matter, the resulting polarization field $\mathbf{P}$ depends non-linearly on the applied field. As a result, the polarization term radiates at different frequencies compared to the driving field. It is common to divide the polarization into linear and non-linear terms:

$$\mathbf{P} = \mathbf{P}^L + \mathbf{P}^{NL}. \quad (52)$$

The first term describes conventional linear optical effects, such as refraction, dispersion and so on; the second is related to the nonlinear effects. The nonlinear polarization $\mathbf{P}^{NL}$ depends on the optical intensity, the wavelength and on the material properties: it is often sufficiently well described by a perturbative expansion in powers of the electric field amplitude $\mathbf{E}$ [93].

$$P^{NL}(t) = \varepsilon_0[\chi^{(2)}\mathcal{E}^2(t) + \chi^{(3)}\mathcal{E}^3(t) + ..]. \quad (53)$$

Depending on the exponent of the electric field, one speaks of second-order interactions, third-order, and so on: higher-order interactions are typically several orders of magnitude weaker than the previous orders. The interaction strength is determined by the optical susceptibility $\chi^{(n)}$, which becomes increasingly smaller as the order n increases. Equation (53) is in a more general case a vector relation and $\chi^{(n)}$ is a tensor of rank n. The expansion is based on the idea that the electric field can be treated perturbatively in the Hamiltonian describing light-matter interaction. The intensity of optical fields generated by n-th order effects scale as I^n times the nonlinear susceptibility $\chi^{(n)}$: as soon as this intensity dependence breaks down, one speaks of *non-*

perturbative regime. An example of this breakdown is the phenomenon of high-harmonic generation, which will be described in more detail in the next chapter(Section 3.1).

The first term of the expansion, describes *second-order* nonlinear effects: the induced polarization is proportional to the square of the electric field. If $\mathcal{E}(t)$ is the sum of two plane waves with frequency $\omega_1 > \omega_2$, the resulting $P = \varepsilon_0(t)$ oscillates also at the sum-frequencies $\omega_{sf} = \omega_1 + \omega_2$ and difference frequency $\omega_{df} = \omega_1 - \omega_2$. Second-order interactions will be explored in detail in Section 2.4: thanks to the development of optical materials with high damage threshold and strong response to the applied field, second-order interactions are the most efficient way of converting the photons of a pulsed laser source to different frequencies via processes known as *sum-frequency generation* and *difference-frequency generation*. A striking example is the generation of the second-harmonic of a laser, a particular case of sum-frequency: two photons of the driving electric field are annihilated and a photon at twice the frequency is created. By making use of suitable crystals, efficiency on the order of $\approx 70\%$ have been demonstrated between NIR wavelengths around 1 μm and visible 0.5 μm photons [94]. For an efficient nonlinear interaction, the maxima of the phase fronts of the interacting waves have to coincide over a macroscopic distance. Achieving this *phase-matching* condition is of uttermost importance in nonlinear optics.

In third-order interactions, four photon beams interact exchanging energy and momentum. An example of third-order processes are so-called *self-phase-modulation* and *self-focusing* effects, both the effect can be described by an effective intensity-dependent refractive index:

$$n = n_0 + n_2 I. \tag{54}$$

In this case, all the four interacting photons are taken from the same fundamental beam, and phase matching is automatically satisfied [93]. Although smaller in magnitude when compared to second order-effects, these self-action effects (*Kerr effect*) are important because they are far more common than the former. Third-order interactions are symmetry-allowed in all materials, whereas second-order interactions are canceled in inversion-symmetric media. The *phase matching* of these self-processes don't require particular strategies: they tend to accumulate when a very intense optical pulse propagates for long distances. The intensity-dependent refractive index has two main consequences: spatially, the change of intensity across the laser mode act as an effective lens (*Kerr-lensing*), leading to self-focusing of the beam. The second effect, related to the temporal variation of the intensity, leads to self-phase-modulation of the pulse: the central frequency of the pulse is modified and new spectral components are created. An excessive self-phase modulation may lead to pulse distortions during light amplification, which ultimately limit the pulse power achievable in a

laser. On the other-hand, self-phase modulation can be exploited to broaden the spectrum of a laser. The process of white-light generation in an insulator (section 2.7.2) exploit the Kerr effect in both ways: a balance between Kerr-lensing and the defocussing effect of free carriers induced in the material give rise to *filamentation*. The beam size stays constantly small for a long propagation distance compared to the depth of focus: due to the high-intensity, new optical frequencies are efficiently generated (efficiencies are $\approx 10^{-3}$). These new frequency components can potentially lead to shorter optical pulses.

Beyond third-order processes, as the interaction order is increased, the efficiencies become increasingly lower. This complicates the generation of EUV photons: at a fundamental photon energy of 1.5 eV the lowest order above a photon energy of 20 eV is the 14th. Very high order processes are usually observed in gases, where some transparency for EUV photons is retained and where higher intensities can be applied without irreversible photo-damage[1]. Toward the end of the eighties, at optical intensities higher than 10^{13} W/cm^2, the process of high-order harmonic generation was first observed [64, 65]. The perturbative description of nonlinear optical interactions breaks down and the intensity scaling of harmonic generation no longer follows the expected I^n power law. After more than thirty years of studies, non-perturbative high-harmonic generation (HHG) is well understood and light sources for spectroscopy based on HHG are widespread. The maximum reported conversion efficiencies for high-harmonic generation are on the order of 10^{-5}. Strong losses are also inevitable in the EUV photon range when transporting the beam to the sample. Realizing a working tr-ARPES experiment is therefore a demanding task in term of the driving laser source, which has to combine high average power with high pulse power.

2.3 CHIRPED PULSE AMPLIFICATION IN SOLID STATE LASERS

Ultrashort-pulses can be generated by a mode-locked laser oscillator [90]. A lasing medium is enclosed in a resonant optical cavity where amplification can occur for several longitudinal modes. If by some mean many of these modes are made to oscillate in phase, mode-locking occurs and a short pulse circulates in the cavity. In the temporal domain the laser output consists of a train of pulses, separated by a period T_c, determined by the travel time of the pulse in the laser cavity. The maximum frequency bandwidth is determined by the *gain bandwidth*, which is an intrinsic property of the optical transition where lasing occurs and of the lasing medium [96]. Ultrafast oscillators operating in the femtosecond regime require gain bandwidths of several THz, which were first achieved in liquid solutions of Dye molecules. The pulse energy of an oscillator is usually not sufficient

---

1 see reference [95] for an overview on optical parametric processes in gases

to drive the strongest nonlinear interactions and further laser amplification stages must be employed. The repetition rate is decreased and higher energies are extracted from a second medium with a population inversion. Two technological milestone marked the advent of today's ultrafast laser technology: the invention of chirped-pulse amplification and the development of lasers based on Ti:Sapphire crystals.

2.3.1 *Chirped-pulse amplification*

Chirped pulse amplification (CPA [97, 98]) is a method to increase by orders of magnitude the achievable pulse power in a laser amplifier. As a pulse grows in energy, its increasingly higher power drives non-linear effects in the amplifier's optical components, distorting the pulse temporal shape and ultimately leading to optical damage. To quantify nonlinear self-effects, it is customary to define a dimensionless coefficient, the B integral, which is the integrated nonlinear phase acquired by the pulses due to self-phase modulation (see eq. (54)) :

$$B = \frac{2\pi}{\lambda} \int n_2 I(z) dz \tag{55}$$

It is clear from equation (55) that B is minimized as the intensity is reduced. In CPA, the pulses are temporally stretched: for the same output energy, the pulse power is strongly reduced and nonlinear effects are minimized. The technique of CPA was originally devised for microwave power-electronics in radar applications. In this optical counterpart, an suitable *pulse stretcher* introduces a controlled amount of group delay dispersion, followed, after the amplification, by a *pulse compressor* introducing the same amount of dispersion but with a reversed sign, in order to recover the original pulse duration.

It is possible to introduce large amounts of normal dispersion by propagating the optical pulses through very long paths in a transparent material. The first demonstration of the technique used a 1.4 km-long optical fiber for this task [97]. Materials with opposite (anomalous) dispersion aren't in general available, moreover, a large B-integral would be accumulated if the high-energy amplified pulses had to travel through large amounts of material for re-compression. Negative dispersion can be artificially produced using diffraction gratings [99]. After diffraction, different wavelengths are propagate at different angles: in a grating compressor one exploits the difference in optical-path-length to introduce a controlled amount of group-delay-dispersion. Angular dispersion also results in *spatial chirp* (the central frequency varies across the laser beam) and *pulse front tilt* (the arrival time of the pulse fronts changes across the beam). To remove these two spatio-temporal distortions, four successive diffracti-

ons from identical and parallel gratings are required. To simplify the setup, the beam is typically back-folded along the same path after the second grating. Dispersion tuning is obtained by changing the distance between the two gratings. A similar concept is exploited in a *prism compressor* [100], however the amount of dispersion introduced by prism-based setups is significantly lower for the same size. For example a 30 fs pulse at 800 nm is stretched to a duration on the order of 50 ps by two 600 lines/mm gratings two meter apart, whereas a two meter-long prism compressor based on quartz prism increases the pulse width to about 0.3 ps. Martinez showed how a grating-based setup could be also used to introduce positive dispersion: the grating stretcher [101] is a compact device (≈ 1 m) which introduces similar amounts of dispersion of a very long fiber. The calculations of the dispersion effects in stretcher/compressor pairs in this thesis were performed with the freely available software lab2[2].

The application of CPA to the amplification of ultrashort pulses faces several problems: the broader the pulse bandwidth, the more difficult is to re-compress the pulse with high fidelity. In order to obtain a clean pulse, free of pedestal and other temporal structures before the main peak, high-order phase distortions introduced by the stretcher-compressor unit have to be corrected [102]. The additional phase due to transmission through the optical materials in the amplifier also play an important role and has to be accounted. As the power (both average power and peak power) and the bandwidth are upscaled, also the size of the gratings have to be accordingly increased: this means that very homogeneous optical gratings of considerable size have to be produced, increasing cost and complexity. The diffraction efficiency η_d also plays a very important role: the total transmission of the compressor is $T = \eta_d^4$. For broadband pulses, carefully optimized metal gratings exhibit a diffraction efficiency comparable to the reflectivity of the bare substrate (≈ 95 %) over the broad pulse spectrum [103]: this translates to a maximum transmission $T \approx 80$ %.

For narrower bandwidths, (on the order of 10 nm) transmission or dielectric gratings with higher diffraction efficiency can be produced [104]. In this case, an overall compression efficiency well-above 80 % can be obtained. A frequency-narrower pulse is also considerably less sensitive to higher order phase distortions, which can often be neglected for picosecond pulses. In this work a home-built grating compressor was developed for CPA of a picosecond Ytterbium laser: the setup will be described in greater detail in Section 2.7.5.4.

---

2 LAB2-A virtual femtosecond laser laboratory, B. Schmidt, M. Hacker, G. Stobrawa, T. Feurer, `http://www.lab2.de`

2.3.2 *Power scaling of Ti:Sapphire ultrafast lasers*

Ti:Sapphire is the solid state material with the broadest gain bandwidth known, covering the 660-1180 nm region [96] with about 230 nm FWHM [102]. Pump absorption is rather efficient in a region around 0.53 μm, where powerful diode-pumped Neodymium lasers are available. The replacement of the liquid dye gain medium with a solid state one was a greatly improved the reliability of femtosecond lasers, leading to widely-adopted commercial products. The diffusion of these new systems was not straightforward as it required the development of suitable mode-locking technologies. Mode-locked dye lasers relied on the low saturation fluence of the gain medium to initiate passively mode-locking in a process based on gain depletion [105]. The saturation fluence, J_{sat}, is a measure of the optical fluence at which the energy stored in the upper level starts to be insufficient to support an exponential growth of the signal intensity. In a medium with a stimulated emission cross section σ_{em}, it can be calculated as follows [96]:

$$J_{sat} = \frac{h\nu}{\sigma_{em}}. \tag{56}$$

Solid-state materials have greater saturation fluencies, preventing the application of the same mode-locking strategies of dye lasers. The breakthrough came with the discovery of Kerr-lens mode-locking, which is based on a coupling between cavity modes induced by self-focusing effects. The newly-available Ti:Sapphire oscillators not only improved the energy and pulse duration considerably, but also provided a very reliable seed for Ti:Sapphire chirped-pulse-amplifiers. The shortest laser pulses which have been directly obtained from a Ti:Sapphire oscillator have a duration of less than 5 fs ([106]).

The saturation fluence in Ti:Sapphire is $\approx$ 0.9 J/cm^2, which is combined with a very high damage threshold (8-10 J/cm^2) and a high thermal conductivity $\approx$ 46 W/mK at 300 K. In comparison, the saturation fluence of dye lasers is on the order of few mJ/cm^2, making the amplification of high power pulses more difficult. Most of the high-power high-repetition-rate ($\geqq$ 1 kHz) table-top CPA Ti:Sapphire amplifiers share a common architecture [102]. First, a femtosecond pulse train is generated in a mode-locked oscillator: the repetition rate is usually on the order of 100 MHz, with pulse energies of nanojoules and durations around 10 fs. The pulses are then stretched to 40-200 picoseconds in a grating stretcher and further amplified. Depending on the available pump laser several passes through an amplifier crystal are required to reach the saturation fluence and deplete the pump energy, the gain per pass is usually in the 2-100 range. Amplification can be performed in a regenerative amplifier: a fast optical shutter (an acoustic-optical or electro-optical modulator) in-couples the stret-

ched pulse in an optical cavity and out-couples it after several tens of round-trips through a Ti:Sapphire crystal. Low-gain per pass is needed to suppress amplified spontaneous emission from the cavity. This scheme enables high optical-optical conversion efficiencies (up to 40% [107]) but the multiple passes through the modulator material increase the linear and non-linear phase accumulated. Another approach, sometimes following a regenerative pre-amplifier, is to use a multi-pass configuration where the beam is folded several times in the crystal. The efficiency can be up to 30 % for a high-power, low-gain amplifier stage. Finally, the pulses are compressed in a grating-based compressor. The pulse duration which can be ultimately achieved is in the range 25-50 fs, depending on the total gain, on the amount of uncompensated phase and on possible spectral cuts by the finite aperture of the stretcher-compressor optics. Amplification affects the pulse duration by an unavoidable *gain-narrowing*: the spectrum narrows significantly when the original ultra-broad oscillator pulse undergoes order-of-magnitude amplification in a non-uniform gain profile. Nowadays, an optimized 1 kHz commercial amplifier can reliably deliver about 20 W (20 mJ) with 25 fs pulse duration[3], whereas commercially-available amplifiers in the 10-50 kHz range[4] reach an average power of 10 W.

The highest average power amplifier demonstrated to date exhibit an output of 40 W at 10 kHz [107]. The compressed pulse width was in this case about 40 fs, with a compressor throughput of 26 W. As reported by the authors, thermal distortions in the grating compressor limited the beam quality, leading at best to $M^2 \approx 1.8$ at 20 W, when using air-cooling. At higher repetition rates, toward the hundreds of kHz, regenerative amplifiers employing continuous-wave pump lasers have been demonstrated [108]. In this case, a power of about 3.5 W in a range between 500 kHz and 1.7 MHz (7-2 μJ) was demonstrated for 40 fs pulses; a higher seed energy was is in this case necessary, imposing the adoption of a cavity-dumped femtosecond oscillator as a seed.

The upscaling in power for high-repetition-rate Ti:Sapphire amplifiers is limited by several factors: on the technological side, suitable pump lasers are not easily found. The most common pump lasers are Q-switched Neodymium lasers, intra-cavity frequency-doubled to ≈ 0.53 μm, with a pulse duration of several nanoseconds. In the 10 kHz range these nanosecond green lasers are commercialized with average powers of hundreds of watts[5], however at high repetition rate the power drops to about 50 W in the 50-500 kHz range and to about 20 W for continuous-wave lasers. Even assuming a high conversion efficiency of 40 %, at 500 kHz the maximum output of an hypothetical amplifier (not compressed) is around 20 W. It is worth mentioning

---

3 Legend Elite Cryo, Coherent, `www.coherent.com`
4 Wyvern, KM labs, `http://www.kmlabs.com`
5 DM-527 Series, Photonix `http://photonix.com`

that more complicated (and expensive) laser designs, based for example on the Nd:YAG innoSLAB technology can produce about 200 W of power with nanosecond duration at 0.53 μmat 150 kHz [6], another alternative is the use of thin-disk lasers[7]. To the best of the author knowledge, such lasers where never tested for such an application.

Another intrinsic technical problem is the construction of a suitable pulse compressor: the broad bandwidths impose the use of metal gratings to achieve good efficiency, which so far seems to be practically limited to about 20 W of average power in table-top systems [107]. Different approaches, based on down-chirped amplification, could potentially solve the issue: here the pulses are stretched with negative dispersion and afterwards re-compressed by transmission through a transparent optical material [108]. The gain narrowing effects, together with the phase accumulated during the CPA, hardly allow for sub-25 fs pulses at a 20 W power level.

Although all these aspects play an important role, the biggest challenge for reaching the highest powers in solid-state lasers is thermal management. In order to produce population inversion in a laser gain material, a three- or four-level level configuration is exploited. In a four-level system for example (see figure 15, panel a)) the pump excites a population in an upper-level which quickly decays by collisions into the longer-lived upper level of the laser transition. When emis-
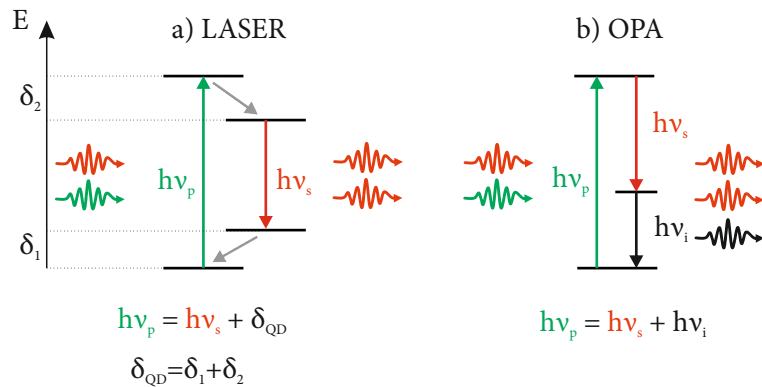

Figure 15: Comparison of Light Amplification by Stimulated Emission of Radiation (LASER) and Optical Parametric Amplification (OPA). δ_{QD} = quantum defect; the index s,p,i stand for signal, pump and idler respectively

sion is stimulated and population is transferred to the lower laser level, the population has to quickly decay to the ground state, favoring the population inversion. In both steps some energy is dissipated

---

6 Innoslab1, Edgewave, `http://www.edge-wave.de`
7 Trupulse, Trumpf lasers, `http://www.de.trumpf.com`

in the host material. The photon energy difference between the pump and amplified photon is called quantum defect:

$$q = h\nu_{pump} - h\nu_{laser} = h\nu_{pump}\left(1 - \frac{\lambda_{pump}}{\lambda_{laser}}\right). \tag{57}$$

The quantum defect energy has to be removed to minimize the temperature increase of the laser medium. The refractive index of a material varies as a function of the temperature (thermo-optical effect): due to the non-uniformity of the thermal load, a temperature gradient is typically established within the crystal. These so-called *thermal-lensing* effects have to be considered when designing the laser and might considerably affect the beam quality. It is important to mention that all the previous examples of very high-power Ti:Sapphire employed sophisticated cryogenic cooling mechanism for the amplifier crystal: this exploit a favorable increase in thermal conductivity of the material at low temperatures. Unfortunately, the gain bandwidth is reduced by the correspondingly lower vibrational broadening. The reported cryo-cooling power for the highest power system is on the order of 200 W [107]: scaling the same concept to higher powers has yet to be demonstrated.

In figure 15, panel b) the level scheme of an optical parametric amplifier (OPA) is compared to the conventional four-level system: in an OPA the pump photon energy is entirely divided between the amplified beam and an auxiliary beam, called the idler, which is generated in the process (Section 2.5). Optical parametric amplification, can support very high gain bandwidths and even shorter pulses than Ti:Sapphire (Section 2.6). Provided that the crystal is transparent for all the three wavelengths, there is no energy deposited in the crystal and no cooling is needed, even when dealing with pump beams with hundreds of watts. Although the process can be rather efficient ($\approx$ 20% a the Ti:Sapphire wavelength), the difficulty is that OPA is a nonlinear effect requiring high intensity for good efficiency. This is not easily achieved with nanosecond pulses because the fluence needed to achieve such high intensity is often beyond the damage threshold of the nonlinear material (Section 2.5). For picosecond pulses however, this constrain is loosened, making OPA a more viable approach.

Compared with conventional pump lasers for Ti:Sapphire, the generation of picosecond-high energy pulses is considerably more complex and often requires CPA. The beam quality of the pump is quite closely transferred to the amplified beam in parametric amplification: this means that a nearly diffraction-limited pump has to be used to compete with the beam quality of a Ti:Sapphire laser (on the order of $M^2 = 1.5$ or better). A shift of femtosecond technology toward optical parametric amplifiers had therefore to wait the availability of suitable high power picosecond lasers.

2.3.3   *High power Ytterbium ultrafast lasers*

High-power picosecond Ytterbium lasers have applications in micro-machining: picosecond pulses lead to better-defined material ablation compared with longer pulses, and high power ensures a high-throughput production. This application lead to a rapid adoption and advance of such lasers in the past decade. Gain media based on Ytterbium ions present several advantages for the construction of high-power laser amplifiers. The absorption band of Ytterbium, typically between 940-980 nm, match well with the emission of commercially-available InGaAs laser diodes: these efficient and reliable semiconductors lasers reach powers of several kW in the form of stacked diode bars. Ytterbium has one of the most favorable quantum defects between all the known solid state laser materials. When the host medium is YAG, the lasing is centered around 1.030 μm, which translates in a quantum defect below 10%. As a comparison, Neodymium lasers emit around 1.064 μm and can be pumped by GaAs laser diodes emitting around 800 nm: the thermal performance is significantly worse, with a defect on the order of 25%. Ti:Sapphire amplifiers, emitting around 0.8 μm and pumped by the second harmonic of diode-pumped Nd lasers, have an even higher defect, on the order of 30% [96]. The amplification linewidth of an Yb:YAG crystal, which is the host medium with the best thermal and optical quality for high power operation, is on the order of only 1-2 nm, which is still able to support pulses below one picosecond.

Thanks to this favorable properties, it was possible to demonstrate nearly diffraction-limited mode quality with kilowatt-level average power and sub-picosecond pulse duration [16, 17, 15]. To reach such power levels, the most critical aspect is to achieve a good thermal management for the quantum-defect heat. At the same time, one must compensate thermo-optical effects which distort the mode profile, preventing diffraction-limited single-mode beams. Three main types of chirped-pulse laser amplifiers have been developed for this scope: fiber, slab and thin disk laser amplifiers [109, 110].

To reach a saturated amplification, a minimum seed power is needed, often well-above a typical oscillator: suitable pre-amplification stages are required and different amplifier geometries might be adopted at different stages of amplification. For example, the laser system adopted in this work is based on a fiber laser followed by a slab amplifier: the laser will be described in greater detail in the Section 2.7.4); here the main characteristics and specific advantages of each of the three amplifiers will be quickly summarized. The common idea behind these high-power amplifiers is to improve the thermal characteristic by adopting a favorable geometry for very effective cooling of the gain medium.

A fiber laser can be though as the ultimately long crystal rod having the most convenient surface to volume ratio, allowing for a very efficient heat extraction. The radiation propagates in the core of a glass fiber, guided by total internal reflection at the interface of a cladding layer (step-index fiber). The amplification occurs in fiber sections enriched with the desired dopant ions. Diffraction limited output for this type of laser is achieved when the propagating radiation is in the fundamental transverse spatial mode of the fiber (single-mode propagation in the LP_{01}, the fundamental linearly-polarized mode). The waveguide-nature of the amplifying medium allows to virtually neglect thermal effect on the beam quality which is power-independent. The light is confined in a small area (with a typical mode diameter of about 10 μm), therefore high intensity is achieved for distances much longer compared to free-space counterparts: this helps achieving high gains and good optical-optical conversion efficiency which can be higher than 80% [111]. The core diameter of a step-index fiber, determines whether only the fundamental mode propagates or not: larger cores allow higher order modes to propagate. The pump radiation is produced by inherently non-diffraction limited high power diodes: to achieve good guiding of the pump radiation, the diode radiation is confined in a larger diameter outer cladding (pump cladding), concentric to the inner-core; the reduced overlap between the pump and the gain medium is compensated by the long length over which the absorption can occur. Fiber lasers represent a very viable approach for reaching high CW powers and simultaneous high beam quality in a compact and environment-insensitive setup, however the small cross-section of the fiber core and the long medium potentially results in unwanted high B-integrals. Up to some hundreds nJ, is possible to build femtosecond amplifiers where all the components are spliced together and the propagation only occurs in fibers, resulting in a monolithic and environment-insensitive laser. Above this level, CPA becomes challenging in these system and the possibility of achieving multi-μJ pulse energies using conventional fibers is hindered.

So-called *photonic-crystal* fibers can circumvent this problem: with single mode diameters of several tens μm is possible to reach mJ operation with practically-achievable stretching factors on the order of 1 ns [16]. Photonic-crystal fibers are micro-structured fibers with periodically spaced holes in the region surrounding the core: for particular values of the spacing and of the diameter of the holes, the fiber becomes *endlessly single-mode* [112]. In this case one the higher modes leak through the sieve-like structure and are unable to propagate, allowing diffraction-limited operation with a larger mode size. A power of several ten watts with pulse energies in the multi-μJ range are easily achievable with a stretched pulse duration on the order of 100 ps. In the range of hundreds of watts, photonic fibers run into multi-mode

instabilities, limiting further scalability. On the CPA side, the stretching required to reach the mJ level is at least one order of magnitude higher compared to the other amplifier geometries. Finally, it is important to mention that the gain bandwidth of Ytterbium:glass fiber system is considerably broader than the one of Yb:YAG, supporting in principle pulse duration as short as 30 fs [111]: for amplified system 250 μJ pulses with 120 fs pulse duration have been demonstrated. At this peak powers, an alternative route for producing ultrashort pulses becomes viable: this approach is based on post-compression after broadening into gas-filled hollow-core fiber [113]. At 50% transmission, this method has overall a better efficiency compared to OPA, but is inflexible in terms of frequency tunability. Nonlinear-compression-based EUV light sources are currently promising cost-effective solution for high repetition rate HHG [114].

Fiber lasers represent probably the ideal solution to produce ultrashort pulses at moderate power levels below 100 W. The higher B-integral makes the further scaling less attractive relative to other amplifiers, nonetheless mJ pulses at kW level are possible [16]. In this thesis a fiber amplifier system was developed in collaboration with the university of Hanover and Venteon laser systems (Section 2.7.5). The system is used both as a pre-amplifier for a slab amplifier and as a driver for a broadband white-light generation (Section 2.7.5.3).

2.3.3.2 *Slab amplifiers*

Slab amplifiers tackle the thermal management problem by shaping the crystal in a thin slab (typically on the order of 10x10x1 mm^3) sandwiched between two heat sinks. Compared to a rod-like geometry, thermo-optical aberrations in a thin slab are reduced by a factor 30 [109]. A successful, commercially-available design is the *innoSlab*[110], illustrated in figure 16. The pump radiation of high power diode bars (up to about 1 kW per laser crystal can be used), after suitable homogenization and relaying, is focused in a line inside the crystal, defining a pump absorption plane parallel to the heat-sinks This establishes a one dimensional heat flow along the thinner dimension of the crystal and produces a well-defined cylindrical thermal lens. The beam passes several time across the pump plane, without overlap with the previous passes and covering the most of the pumped region to optimally extract the energy deposited by the pump laser diodes. The beam bounces back and forth on two end-mirrors (unstable resonator), and is finally out-coupled passing close to the end mirror edge after several passages. The two cylindrical end-mirrors expand the beam in one direction at every passage, leaving the intensity constant after (the gain per passage is of the order of 10). The resonator length (given by the two end-mirror distance) is matched to the cylindrical thermal lens arising in the crystal. The amplified beam is very asymmetric, being magnified several times in a single direction: a set

of cylindrical and spherical telescopes reshape the beam to correct for astigmatism and ellipticity of the beam, restoring a nearly diffraction-limited beam. In the direction of the beam expansion (horizontal in figure 16), a slightly worse beam parameter M_h^2 is typical, especially at very high powers. Up to 660 W can be extracted in a single amplifier and the power can be boosted above 1 kW placing two stages in tandem [15]. The big advantage, compared to fiber lasers, is the moderate B-integral: the laser can operate even without CPA reaching 100 μJ and can reach the mJ level with a fraction of the chirp of a fiber laser. When compared with fiber lasers, this comes with an increased complexity and a lower pointing stability, associated with free-space propagation. In addition, the pulse duration is not as good, because of the lower amplification bandwidth of the Yb:YAG crystal, which support a Fourier limit of about 700 fs. State-of-the-art commercial system can be carefully engineered and offer mode quality and stability comparable to fiber amplifiers. In this thesis a commercial innoSlab
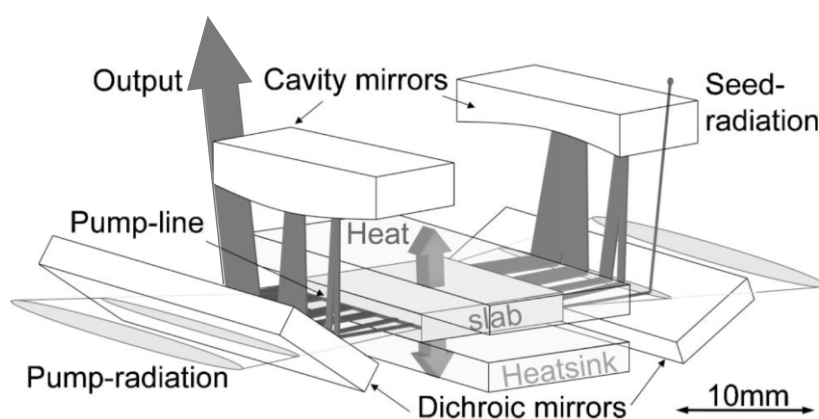

Figure 16: Schematic of the unstable resonator of a slab amplifier, adapted from reference [15].

system[8] [115] was adopted to produce the pump radiation for the OPCPA (Section 2.7.5.4).

2.3.3.3 *Thin disk lasers*

The third category of high-power Ytterbium amplifiers is based on the thin disk geometry. The overall amplifier can be thought as an active mirror: an extremely thin Yb:YAG crystal, is fixed on a heat-sink. A mirror coating is embedded at the back side of the Yb:YAG crystal, reflecting the beam after every amplification pass. The thermal flow is one-dimensional, in the same direction of the beam amplification, with minimal thermo-optical effects. This kind of amplifier was not used in this work and is mentioned here for completeness: a more in-depth description can be found in several reviews [116, 117]. When compared to the previous two amplifier geometries, the thin-disk has

---

8 Amphos 200, Amphos gmbh

the lowest optical nonlinearity. Thin-disk amplifier can compete on any parameter with fiber and slab lasers and are the most promising in scalability in the multi-10 kW range. Due to the low gain per pass, typically several tens of reflections are needed in regenerative amplification setups to reach the multi-100 W regime. This makes the synchronization of thin-disk-based OPCPAs more complex, as will be illustrated in Section 2.7.1. A promising strategy is to use this kind of laser to boost the power output of an already-existing high-power source: this hybrid solution has been suggested as an optimal route to reach the multi kW regime [110] and demonstrated [118] in view of pumping OPCPAs.

2.4 $\chi^{(2)}$ effects and phase matching

In this section elements of the theory of second order nonlinear optical interactions will be introduced: the resulting phenomena of optical parametric amplification is the physical basis of the operation of the laser system developed in this work. The nonlinear polarization (equation (53)) can be expressed more conveniently in the frequency domain and generalized including the vector nature of the interacting waves: in general $\chi^{(n)}$ are n-th rank tensors. The i-th Cartesian component of the second order nonlinear polarization, generated by two fields of frequency ω_1 and ω_2, can be written as [119]:

$$P_i^{(2)}(\omega_3) = \epsilon_0 D^{(2)} \sum_{j,k} \chi_{ijk}^{(2)}(-\omega_3; \omega_1, \omega_2) E_j(\omega_1) E_k(\omega_2), \qquad (58)$$

where $D^{(2)} = 1$ if $\omega_1 = \omega_2$ or $D^{(2)} = 2$, otherwise. The non-linear polarization can be exploited to convert the frequency of a laser field, or to transfer energy between different laser fields to build a so-called *parametric amplifier*. The even-order susceptibilities are automatically zero for inversion-symmetric media. For applications, it is desirable to exploit non inversion-symmetric crystals with high nonlinear optical coefficients. The crystals must posses a high optical quality, intended as a combination of transparency and high damage threshold. One of the most widely adopted nonlinear crystals is β-barium borate or BBO [120, 121]: its transparency ranges from the deep-UV to the near-infrared (see figure 17) and is combined with one of the highest nonlinear optical coefficients. In this work this will be the only nonlinear crystal adopted, so its properties will be described in some detail.

As shown in equation (58), the second-order susceptibility in general mediates the interaction of three wave of frequency ω_1, ω_2 and ω_3. Two specific cases are worth mentioning: if $\omega_1 = \omega_2 = \omega$, the resulting wave is either the second harmonic $\omega_3 = 2\omega$ (*second harmonic generation*) or a DC field $\omega_3 = 0$ (*optical rectification*). The former effect will be exploited to convert the near infrared 1.030 μm wavelength
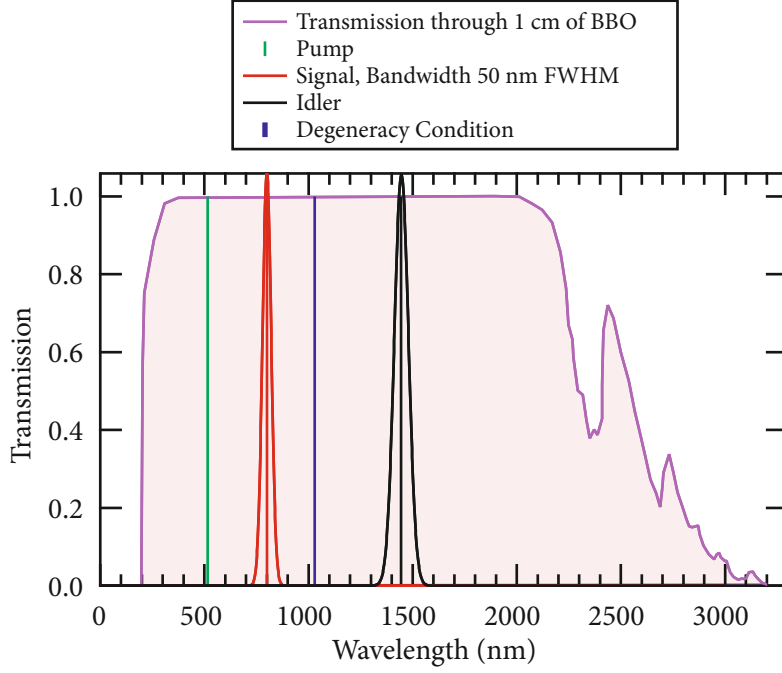
Figure 17: Transparency range of a BBO crystal: over-imposed are the spectra of a 800 nm signal with 50 nm FWHM and of its corresponding idler at 1450 nm.

of Ytterbium lasers to 0.515 μm. In the case of narrow-bandwidth (few nm linewidth), picosecond pulses, conversion efficiencies exceeding 50% can be reached. The general case of $\omega_1 \neq \omega_2$ results either in the generation of a wave at the *sum-frequency* $\omega_3 = \omega_1 + \omega_2$ or at the *difference-frequency* $\omega_3 = \omega_1 - \omega_2$. All together, these processes are known as three-wave-mixing processes. The easiest approximation of the wave equation (paraxial approximation), which describes three-wave mixing in a material, for the case of plane waves $A_i exp(-i(k_i + \omega_i t))$ is the following [122]:

$$\frac{dA_i}{dz} = -i\frac{d_{eff}\omega_i}{cn_i}A_s^* A_p exp\left(-i\left(\Delta k\right)\right) \tag{59a}$$

$$\frac{dA_s}{dz} = -i\frac{d_{eff}\omega_s}{cn_s}A_i^* A_p exp\left(-i\left(\Delta k\right)\right) \tag{59b}$$

$$\frac{dA_p}{dz} = -i\frac{d_{eff}\omega_p}{cn_p}A_i A_s exp\left(i\left(\Delta k\right)\right) \tag{59c}$$

Here the three frequencies have been replaced with a new notation ω_p, ω_s and ω_i, and are known as *pump*, *signal* and *idler* waves, which is the nomenclature adopted in the framework of optical parametric amplification (OPA). Nonetheless, they can be used to describe any three-wave mixing process, by a proper selection of the boundary conditions and frequencies. ω_p is by definition the beam at the highest

frequency, whereas there is no general rule for the frequencies of idler and the signal wave. It is common to call *idler*, the wave which at the beginning of the mixing process has zero amplitude $A_i(z = 0, t = 0) = 0$. The energy conservation of the process imposes:

$$\hbar\omega_p = \hbar\omega_s + \hbar\omega_i \tag{60}$$

The process of sum-frequency generation involve the absorption of two photons via a virtual state and the emission of a higher-frequency photon; conversely, difference frequency generation involves the absorption of a photon and the emission of two as depicted in figure 15.

An analytic solution of equation (59) exists in the *undepleted pump* approximation. This assumes that the amplitudes of the high-intensity waves driving the interaction are not considerably reduced, or in other words that the conversion efficiency η is low. For three-wave-mixing processes, it can be shown that the efficiency is $\eta \propto sinc(\Delta k L/2)$ [119]. In this formula, L is the interaction length and $\Delta k = k_p - k_s - k_i$ is the phase mismatch of the interacting plane waves, which has to be minimized for the process to be efficient. This is the so-called *phase-matching* condition, which closely reflects the microscopic momentum conservation for the interacting photons:

$$\hbar k_p = \hbar k_s + \hbar k_i \tag{61}$$

The phase-matching condition $\Delta k = 0$ can be rewritten as:

$$n_p = \frac{n_i\omega_i + n_s\omega_s}{\omega_p} \tag{62}$$

The condition (62) cannot be fulfilled in normally-dispersing, isotropic media. Assuming, as it will be the case for the OPA process considered here, $\omega_p > \omega_s > \omega_i$, one has in the normal dispersion case $n(\omega_p) > n(\omega_s) > n(\omega_i)$. Luckily this inequality does not always hold in an anisotropic crystal.

2.4.1 *Critical phase matching*

One of the most adopted phase-matching strategies make use of the anisotropy of the nonlinear optical medium. The lower symmetry of a nonlinear crystal also translates into birefringence: the refractive index of the medium depends on the polarization of the propagating wave [91]. In the simplest case, the crystal has a single *optical axis*: linearly polarized waves with the electric field orthogonal to the optical axis (*ordinary waves*) have an index of refraction (*ordinary refractive index*, n_{op}) distinct from the ones having the electric field parallel to

the axis (*principal extra-ordinary wave*, $n = n_{ep}$). For the intermediate the refractive index $n_{ep}(\theta_m)$ is determined by the relation:

$$\frac{1}{n_{ep}^2(\theta_m)} = \frac{sin^2(\theta_m)}{n_{ep}^2} + \frac{cos^2(\theta_m)}{n_{op}^2} \qquad (63)$$

Here θ_m is the angle between the optical axis and the propagation direction of the extraordinary-wave. By properly choosing the polarization and the crystal orientation, it is possible to achieve phase matching for the three-wave-mixing processes. BBO is a *negative uniaxial* crystal ($n_{ep} < n_{op}$): assuming that both the idler and the signal wave are ordinary polarized waves (*type-I, oo → e, phase matching* [119]) the phase-matching condition can be recast as:

$$n_{ep}(\theta_m)\,\omega_p = n_{os}\omega_s + n_{oi}\omega_i. \qquad (64)$$

One can solve for the phase-matching angle θ_m obtaining:

$$\theta_m = asin\left[\frac{n_{ep}}{n_{ep}(\theta_m)}\sqrt{\frac{n_{op}^2 - n_{ep}^2(\theta_m)}{n_{op}^2 - n_{ep}^2}}\right]. \qquad (65)$$

Knowing the refractive index of BBO, expressed as a Sellmaier's equation [121], it is possible to calculate the phase-matching angle for the desired interaction. Figure 18 illustrates the results for two important cases, the SHG of 0.8 μm and the SHG of 0.515 μm.

2.4.2 *Effective nonlinear optical coefficient*

Under critical phase-matching conditions, the geometry of the interacting waves is known and the polarization of the waves is fixed: in this case equation (58) is simplified by performing the summation and introducing an *effective* nonlinear optical coefficient d_{eff}. Assuming that the energies of the interacting photons are away from resonances (which is often true in the case of VIS-NIR wavelengths), d_{eff} does not depend on ω in first approximation. The nonlinear polariza-
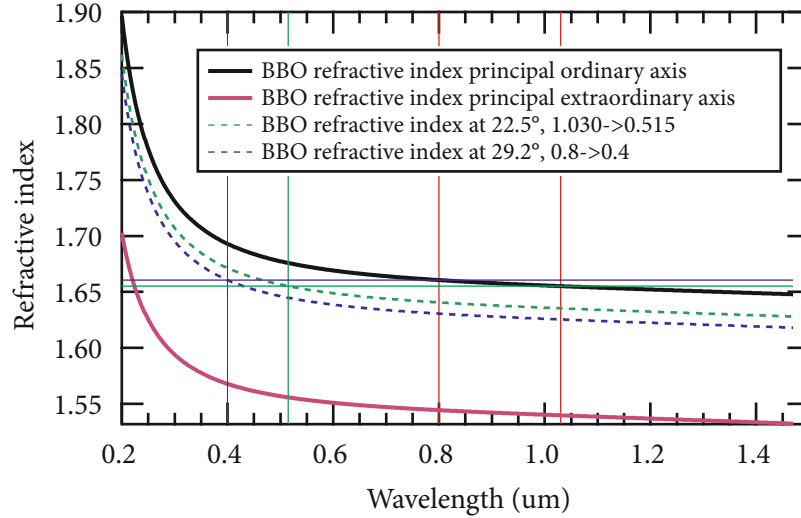
Figure 18: Illustration of critical phase matching for second harmonic generation in BBO. Two wavelengths are considered: 1030 nm and 800 nm. In black the ordinary optical index for BBO as a function of frequency, in purple the extraordinary. At a propagation angle of 22.5° the extraordinary refractive index (dotted green line) at 515 nm is the same as the ordinary for 1030 nm. At 29.2° (dotted blue line) the same hold true for 400 nm and 800 nm.

bility of BBO is proportional to the following tensor [123], expressed in units of pm/V:

$$
d = \begin{pmatrix} d_{11} & d_{12} & d_{13} & d_{14} & d_{15} & d_{16} \\ d_{21} & d_{22} & d_{23} & d_{24} & d_{25} & d_{26} \\ d_{31} & d_{32} & d_{33} & d_{34} & d_{35} & d_{36} \end{pmatrix} =
$$

$$
\begin{pmatrix} 0 & 0 & 0 & 0 & 0.08 & 2.2 \\ 2.2 & -2.2 & 0 & 0.08 & 0 & 0 \\ 0.08 & 0.08 & n.d. & 0 & 0 & 0 \end{pmatrix}.
$$

Given the phase-matching angle one can calculate the d_{eff} of BBO using the following relation, valid for type I phase matching [93] :

$$
d_{eff} = d_{31} sin(\theta_m) - d_{22} cos(\theta_m) sin(3\phi), \tag{66}
$$

here θ_m and ϕ determine the orientation of the optical axis relative to the propagation axis: as shown in Figure 19, for a given phase-matching condition the ϕ angle which maximizes d_{eff} is chosen. In the case of type I phase matching, ϕ is chosen for convenience to be 90° (although a slightly higher value could be obtained at $\phi = 30°$). The nonlinear crystal's faces are then cut at this specific angles, ensuring phase matching for normal-incidence waves. The phase-matching angle for DFG with a pump-wavelength of 0.515 μm (second harmonic
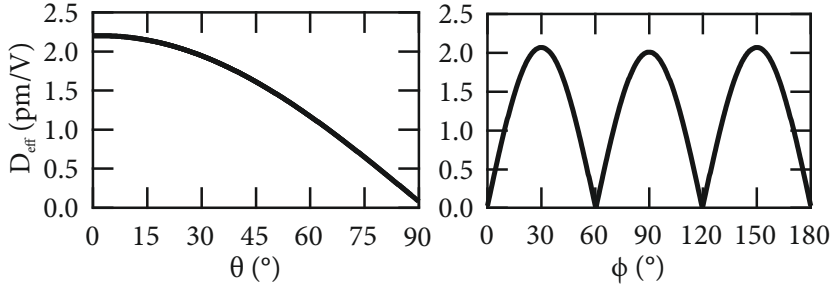
64

Figure 19: Calculated effective non-linear optical coefficient for BBO (D_{eff}). The D_{eff} decreases for increasing crystal propagation angle θ. At a fixed θ, the crystal is cut at ϕ angle which maximizes the D_{eff}, for type-I phase matching, 90°.
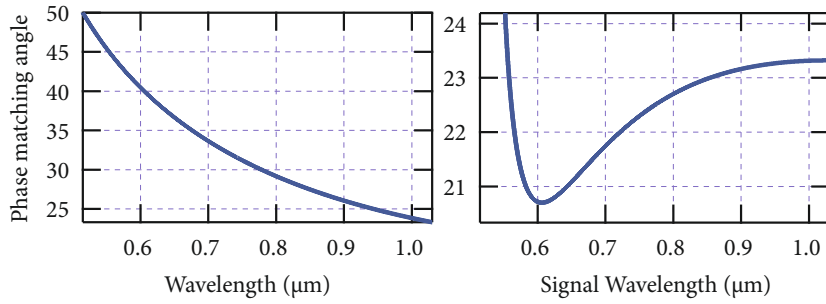

Figure 20: Calculated type I phase matching angle in BBO for SHG (left) and DFG for a pump-wavelength of 0.515 μm (right), as a function of the signal wavelength.

of an Ytterbium laser) is calculated in Figure 20 as a function of the signal wavelength . The theory described in this section was used to calculate the phase-matching angles and the nonlinear coefficients for the relevant cases treated in this thesis and are summarized in table 3.

Type	λ_s (μm)	λ_i (μm)	λ_p (μm)	θ_m (°)	d_{eff} (pm/V)
SHG	1.030	1.030	0.515	23.4	2.01
SHG	0.8	0.8	0.4	29.2	2.00
DFG	0.8	1.446	0.515	22.7	2.02
SHG	0.780	0.780	0.390	30	1.99
SFG	0.390	0.780	0.260	45.9	1.84
SFG	0.260	0.780	0.195	69.2	1.24

Table 3: Calculated phase-matching angles θ_m and effective nonlinear optical coefficient d_{eff} for several processes, at the signal, idler and pump wavelength λ_s, λ_i, λ_p.

The possibility of amplifying light by means of difference frequency generation was soon realized in the history of nonlinear optics [124]. When describing optical parametric amplification, the wave equation (59) can be cast in a more illustrative form, known as Manley-Rowe relations, expressing the coupled equations in term of the optical intensities $I_j, j = s, i, p$

$$I_j = \frac{1}{2}\epsilon_0 c n_j \left| A_j(z) \right|^2 \tag{67}$$

$$\frac{1}{\omega_s}\frac{dI_s}{dz} = \frac{1}{\omega_i}\frac{dI_i}{dz} = -\frac{1}{\omega_p}\frac{dI_p}{dz} \tag{68}$$

The Manley-Rowe relations describe the energy flow between the interacting waves in a three-wave-mixing process: the flow has two possible directions, either the pump is depleted in favor of the idler and signal waves or vice versa. In the first case, relevant for optical parametric amplification, the initial conditions are a strong pump beam at the shortest wavelength and a weak signal beam. The pump photons are lost to multiply the photons of such weak signal. In the process, idler photons are also generated, conserving energy and momentum. This auxiliary beam is what makes OPA essentially different compared to amplification in a laser: the excess energy is never stored in the crystal as there is no population in real states of the system. Provided that the crystal is transparent for all the three interacting waves, no energy is dissipated as heat. Detrimental thermal lensing effects are therefore considerably relaxed, enabling in principle easier scaling to high average power when compared with Ti:Sapphire. The missing ingredient to assess if an OPA can produce sufficient gain and gain bandwidth to compete with existing Ti:Sapphire technology.

To get insights in this direction some of the basic theoretical results will be discussed. The final goal is to use OPA for producing sub-30 fs pulses at high average power (≈ 20 W), the central wavelength for the OPA is chosen to be 0.8 μm for direct comparison with Ti:Sapphire lasers. The pulses produced from an Ytterbium laser cannot be directly used as a pump for the interaction, as their 1.030 μm wavelength is too long. The second harmonic of the laser at 0.515 μm is well suited for this task. The idler wave has in this case a wavelength of 1.45 μm still in the transparency range of BBO (figure 17). The coupled wave equation admits a simple analytical solution, valid for the following conditions:

- negligible pump depletion, i.e. $dI_p/dz = 0$
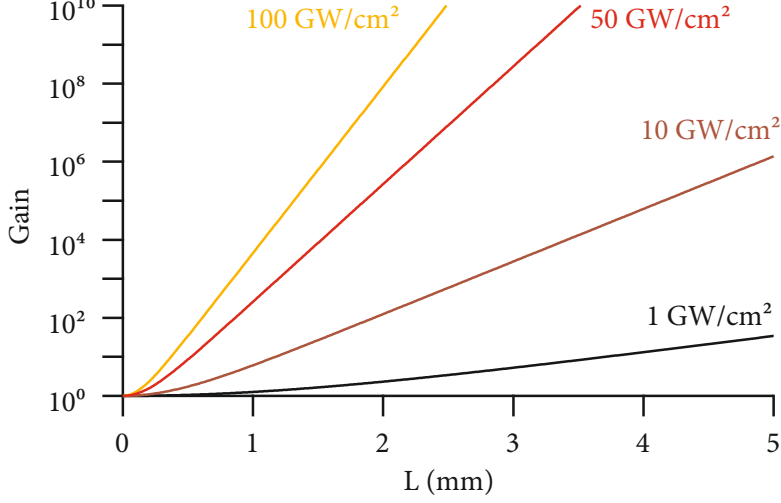
- negligible initial idler intensity $I_i = 0$

Figure 21: Calculated small-signal gain in BBO, from Equation 71, for different pump intensities, as a function of the crystal length L and in phase-matched conditions ($\Delta k = 0$).

In this case (*small-signal gain*), the solution becomes [122]:

$$I_s(L) = I_{s0}\left[1 + \frac{\Gamma^2}{g^2}sinh^2(gL)\right] \qquad (69)$$

$$I_i(L) = I_{s0}\frac{\omega_i}{\omega_s}\frac{\Gamma^2}{g^2}sinh^2(gL) \qquad (70)$$

The following g and Γ parameters were introduced:

$$g^2 = \sqrt{\Gamma^2 - \frac{\Delta k^2}{2}}, \qquad (71)$$

$$\Gamma^2 = \frac{\omega_i\omega_s d_{eff}^2\left|A_p\right|^2}{n_i n_s c^2} = \frac{2\omega_i\omega_s d_{eff}^2 I_p}{n_i n_s n_p c^3} = \frac{8\pi^2 d_{eff}^2 I_p}{n_i n_s n_p \lambda_i \lambda_s \epsilon_0 c^3}. \qquad (72)$$

It is easy to calculate the gain of an optical amplifier from equation (69), the results are shown in figure 21, as a function of crystal length and pump intensity.

In our specific case, the seed radiation for the signal is produced using white-light generation (Section 2.7.5.3): a power on the order of ≈ 1 mW is produced around the signal wavelength. The gain for achieving a power on the order of 10 W is $G > 10^4$. In the plot crystal lengths below 5 mm are shown: this is well below the maximum thickness of commercially available BBO of ≈ 25 mm. It is anticipated here that the crystal length has to be considerably shorter than the pulse splitting length (Section 2.5.2) which is the distance after which the pump and the signal (or the pump and the idler) don't overlap
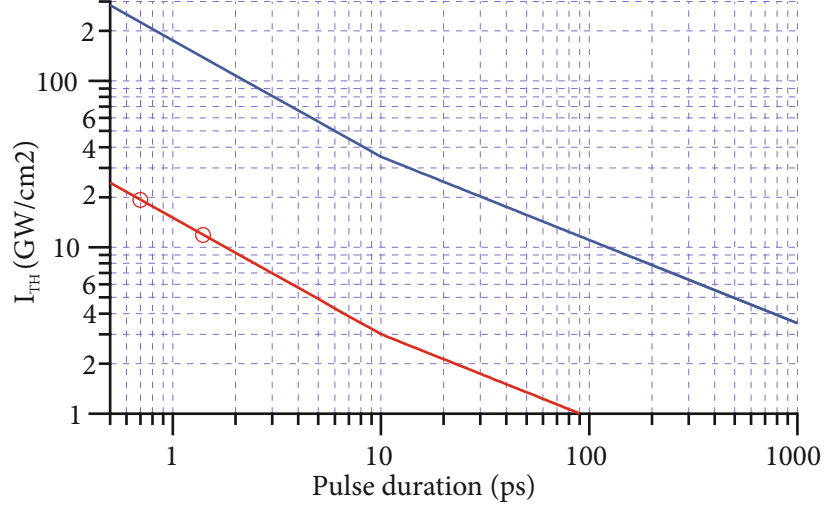
Figure 22: Threshold intensity I_{TH} for damage in BBO, as a function of the pulse duration. The blue line is the damage of the bulk-material, the red is the specified damage threshold for the optical coating. The two dots indicate the damage threshold for 700 fs and 1.2 ps.

in time anymore. In the case of interacting pulses with picosecond duration, this length is shorter than 10 mm. By limiting the maximum thickness at 5 mm, from this simple analysis its apparent that to achieve a sufficient gain in a single amplification stage a minimum pump intensity $\gtrsim 10 \text{ GW/cm}^2$ has to be achieved.

This intensity has to be compared with the damage threshold of the employed nonlinear crystal. In this respect, an important parameter is the duration of the pulse: typically the laser fluence at which damage occurs is lower for shorter pulses. The threshold was experimentally determined to scale as the square root of the pulse duration τ for pulses longer than few ps[125]. For shorter pulses, this threshold fluence scales as $\tau^{0.3}$ [126]. For a given fluence F, the peak intensity $I_{peak} \propto F/\tau$, so overall the threshold intensity scales a $\tau^{-0.5}$ above 10 ps and as $\tau^{-0.7}$ for ps to sub ps pulses. The threshold intensity for BBO damage a 0.532 μm is 7 GW/cm^2 for pulses of a duration of 250 ps [127]: the estimated damage threshold is plotted in figure 22, assuming that the $\tau^{-0.7}$ scaling also holds between 10 and 1 picoseconds.

Pulses longer than 100 ps cannot provide sufficient parametric gain in a short crystal: picosecond and sub-picosecond pulses are instead suitable for reaching hundreds of GW/cm^2. The Ytterbium amplifier used as a pump in this thesis provide ≈ 700 fs pulses, at a wavelength of 1.03 μm. In this case, the theoretical damage threshold exceeds 200 GW/cm^2, however other aspects limit the maximum intensity. BBO is hygroscopic, therefore it is typically coated to avoid damage from moisture: to limit the reflection losses, the coating is designed to be anti-reflective for the pump wavelength (or a combination of multiple wavelengths). The damage threshold of a BBO coated for
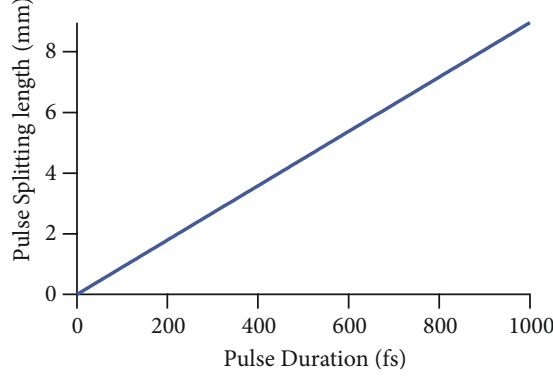
Figure 23: Pulse splitting length originating form temporal (or longitudinal) walk-off in BBO between the pump and the idler beams, for signal, idler and pump wavelengths at 0.8, 1.450 and 0.515 μm respectively.

0.532 μm from a BBO manufacturer (Castech) is specified to be > 0.3 GW/cm^2 for 1 ns long pulses: the corresponding damage threshold is also plotted in figure 22, showing that in a coated crystal much shorter pulses become necessary to achieve the required gain. The estimated pump intensity used for the amplifier in this work was ≈ 35 GW/cm^2, this ensures long-term-stable operation over several hours, but is very similar to the estimated value for the damage threshold, indeed resulting occasional crystal damages.

2.5.1 *The longitudinal walk-off*

The plane-wave theory used so far is not generally appropriate for describing the interaction of short pulses: in this case the wave equation has to be modified to include pulse propagation effects [122]. An important quantity which arises from this analysis is the so-called *pulse splitting length*, written as follows:

$$l_{jp} = \frac{\tau}{\delta_{jp}}, \quad j = s, i \tag{73}$$

The pulse splitting length is the distance after which, due to group velocity mismatch, the interacting pulses (idler or signal) no longer overlap temporally inside the crystal. This longitudinal walk-off limits the maximum length of the crystal which can be used for a single amplification stage. In the case of signal, idler and pump at 0.8, 1.450 and 0.515 μm respectively, the group velocities are $v_p = 1.76 \times 10^{-4}$ mm/fs, $v_s = 1.78 \times 10^{-4}$ mm/fs and $v_i = 1.79 \times 10^{-4}$ mm/fs. The limiting factor is therefore the mismatch between the idler and the pump. The walk-off length, as a function of the pulse duration of the interacting waves, is shown in figure 23.
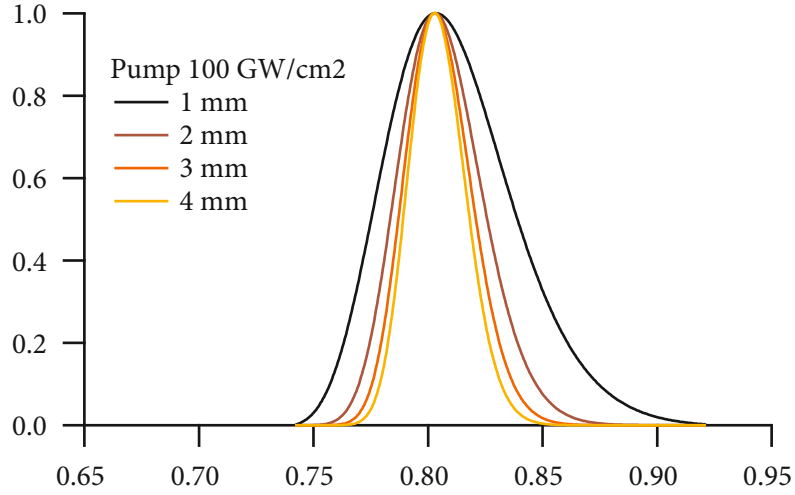
Figure 24: Calculated gain as a function of wavelength mismatch, for various BBO thicknesses, occurring when broad-band pulses are amplified. The interaction considered is $0.515\,\mu m \rightarrow 1.450\,\mu m + 0.800\,\mu m$

Two pulse durations were used in this work for the pump, 700 fs and 1400 fs: the pulse splitting length in this case is 6.3 mm and 12.5 mm, respectively. This values are an upper limit of the crystal length for a single amplification stage. As soon as the crystal length becomes comparable to the pulse splitting length, the solution provided by equations (69) are not accurate and for achieving quantitative agreement with experiments, numerical solutions of the wave equations are necessary. In this thesis crystal lengths of up to 4 mm were tested for the NOPA stage, therefore the simplified analysis presented here is not expected to quantitatively describe the NOPA process, nonetheless it is useful to introduce the basic concept and considerations for the amplifier design.

2.5.2 *Phase-matching bandwidth in an OPA*

In order to generate femtosecond pulses, the amplification gain bandwidth is an important parameter: assuming phase-matching angle $\theta_m = 22.7\,°$ for the interaction $0.515\ \mu m \rightarrow 1.450\ \mu m + 0.800\ \mu m$, the small-signal gain equation (69) can be used to estimate the effect of wavelength detuning from the phase-matching condition.

Figure 24 shows the normalized gain curve as a function of crystal length: the width of the gain profile becomes increasingly narrow as the crystal thickness is increased. The gain narrowing effect limits the achievable pulse duration after amplification. The bandwidth for an OPA processes can be estimated from equation (69) in the following way: if for a given pump frequency ω_p the phase matching is achieved $\Delta k\,(\omega_s, \omega_i) = 0$ for a signal frequency ω_s, for a small variation $\omega_s +$
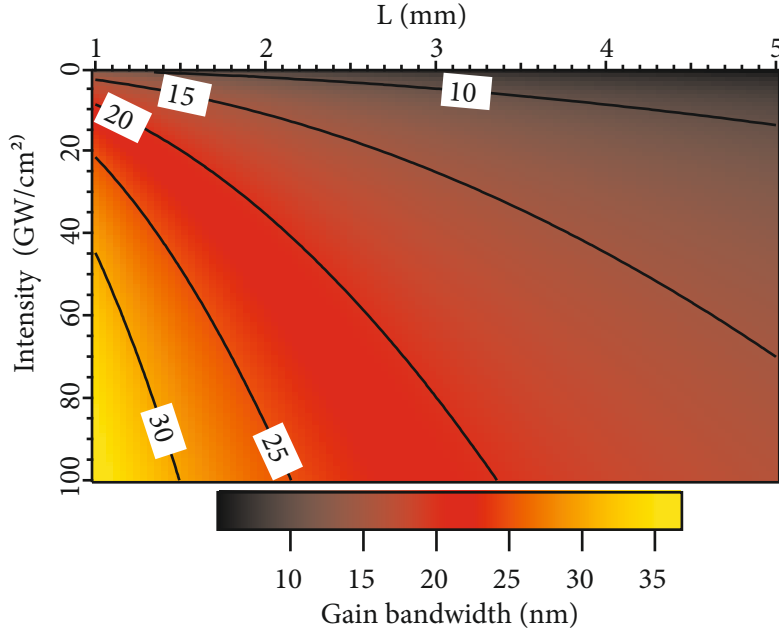
Figure 25: Amplification bandwidth for the $0.515\,\mu m \to 1.450\,\mu m + 0.800\,\mu m$ process, as a function of pump intensity and of crystal thickness. The various lines represent the contours of an indicated constant bandwidth.

$\Delta\omega$ the wavevector mismatch can be written to the first order in $\Delta\omega$ as

$$\Delta k \approx -\frac{\partial k_s}{\partial \omega_s}\Delta\omega + \frac{\partial k_i}{\partial \omega_i}\Delta\omega = \left(\frac{1}{v_{gi}} - \frac{1}{v_{gs}}\right)\Delta\omega. \tag{74}$$

The wavevector mismatch is proportional to the group velocity mismatch between signal and idler waves. In the large gain approximation $G \gg 1$, the FWHM of the phase-matching bandwidth can be written as:

$$\Delta v \approx \frac{2\,(ln2)^{1/2}}{\pi}\left(\frac{\Gamma}{L}\right)^{1/2}\frac{1}{\left|\frac{1}{v_{gi}} - \frac{1}{v_{gs}}\right|}. \tag{75}$$

Equation (75) can be used to plot the gain bandwidth of the OPA process under scrutiny:

Given the damage threshold and the gain derived in the previous sections, a gain on the order of 10^4 can be achieved with a picosecond $0.515\,\mu m$ pump with an intensity on the order of $\approx 10\,\mathrm{GW/cm^2}$, in a crystal thickness of $\approx$ 3-4 mm. The gain bandwidth for an OPA in this conditions is however below 15 nm: this translates in a Fourier-limited pulse duration of about 60 fs, below the design goal of sub-30 fs. The main limitation can be identified as the group velocity misma-
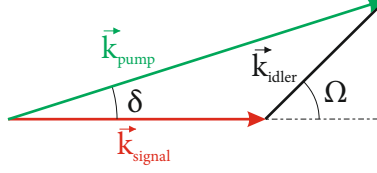
Figure 26: Non-collinear phase-matching scheme: δ is the non-collinear angle between the signal and pump wave-vectors $\vec{k}_s$ and $\vec{k}_p$. The angle between pump and idler $(\vec{k}_i)$ is Ω.

tch between idler and signal. To compensate for the mismatch, it is possible to adopt a non-collinear geometry. This non-collinear OPA or NOPA, maximizes the amplification bandwidth, while simultaneously allowing for efficient, phase-matched interaction.

2.6 NON-COLLINEAR PHASE MATCHING

It is possible to considerably enhance the phase-matching bandwidth of OPAs by employing a non-collinear phase-matching configuration. At an angle α_{nc} the longitudinal group velocity mismatch between signal and idler becomes zero, resulting in nearly achromatic phase matching, with a bandwidth spanning several tens of THz, from the visible to the near-infrared, supporting light pulses containing few optical cycles. The phase-matching relation of equation 76 is a vector relation:

$$\Delta \mathbf{k} = \mathbf{k_p} - \mathbf{k_s} - \mathbf{k_i}. \tag{76}$$

It is still possible to satisfy Equation 76 if the pump and the amplified signal beams form an angle δ in the nonlinear crystal. The condition $\Delta \mathbf{k} = 0$ can be written as:

$$\Delta k_\parallel = k_p cos\left(\delta\right) - k_s - k_i cos\left(\Omega\right) = 0 \tag{77a}$$

$$\Delta k_\perp = k_p sin\left(\delta\right) - k_i sin\left(\Omega\right) = 0, \tag{77b}$$

where Ω is the angle between the generated idler and the pump wavevectors and δ is the angle between the pump and the signal: this geometry is illustrated in figure 26. Close to the broadband phase-matching conditions, the two orthogonal components $\Delta k_\parallel$ and $\Delta k_\perp$ can be expanded to first order for a small frequency variation $\Delta \omega$ [128]:

$$\Delta k_\parallel \approx -\frac{\partial k_s}{\partial \omega_s}\Delta \omega + \frac{\partial k_i}{\partial \omega_i}\cos\Omega\Delta\omega - k_i \sin\Omega\frac{\partial\Omega}{\partial\omega_i}\Delta\omega = 0, \tag{78a}$$

$$\Delta k_\perp \approx \frac{\partial k_i}{\partial \omega_i}\sin\Omega\Delta\omega + k_i \cos\Omega\frac{\partial\Omega}{\partial\omega_i}\Delta\omega = 0. \tag{78b}$$
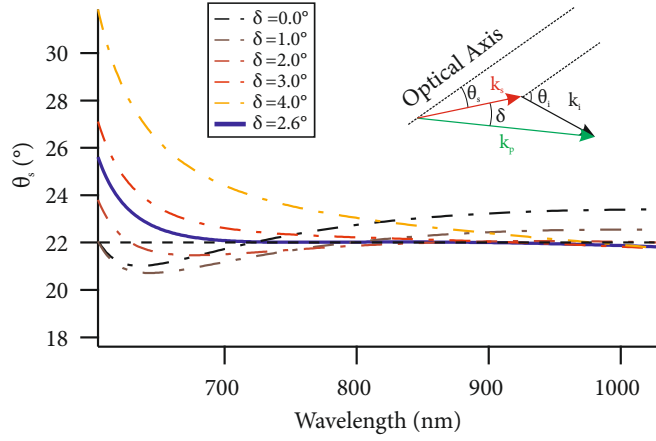
Figure 27: Phase-matching angle θ_s as a function of the wavelength for several non-collinear angles δ. The definition of the different geometrical quantities is given in the panel.

One can easily show that this is equivalent to the following condition for the group velocities of signal and idler:

$$v_{gs} = v_{gi} \cos \Omega \tag{79}$$

The broadband phase-matching condition is achieved when the group velocity of the signal and the projection of the group velocity of the idler along the signal propagation direction are the same. As the idler beam amplitude is by definition zero before amplification, it is more convenient to express the non-collinear phase-matching relation as a function of the signal and pump non-collinear angle δ, which is experimentally accessible. In this case one obtains for the non-collinear angle α_{nc} the following relation:

$$\alpha_{nc} = \arcsin \left(\frac{1 - v_{gs}^2/v_{gi}^2}{1 + 2\frac{v_{gs}n_s\omega_s}{v_{gi}n_i\omega_i} + \frac{n_s^2\omega_s^2}{n_i^2\omega_i^2}} \right)^{1/2} \tag{80}$$

Figure 27 shows the calculated phase-matching angle of the signal as a function of the non collinear angle δ: one can see how for an angle of about 2.6 °, the phase-matching angle becomes independent on wavelength. The idler photons will be generated at an angle $\Omega(\omega_i)$, specified by the phase-matching condition equation (79). This idler beam is therefore angularly dispersed and not readily usable. The phase-matching bandwidth can now be estimated in a similar fashion as what has been done for an OPA (equation (75)); however now the expansion has to be performed to the second order:

$$\Delta v \approx \frac{2\,(ln2)^{1/4}}{\pi} \left(\frac{\Gamma}{L} \right)^{1/4} \frac{1}{\left| \frac{\partial^2 \omega_s}{\partial k_s^2} + \frac{\partial^2 \omega_i}{\partial k_i^2} \right|} \tag{81}$$
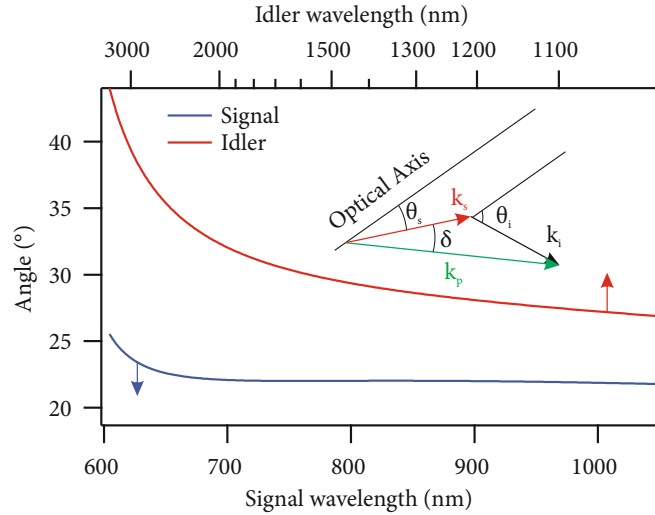
73

Figure 28: Phase-matching angle for a 515 nm pump in BBO, for a non-collinear angle $\delta = 2.6°$, as a function of wavelength: the blue line represent the signal, while the red line is the idler. The idler photons are created at a wavelength-dependent angle θ_i to fulfill momentum conservation. The bottom axis is the signal wavelength and the top axis is the corresponding idler wavelength. The geometry is illustrated in the figure.

The calculated bandwidth for the processes 0.515 μm$\rightarrow$ 1.450 μm+ 0.800 μmis plotted in figure 29: an amplification bandwidth exceeding 40 nm is expected for a 3 mm crystal. This formula, although already suggesting that the non-collinear OPA (nOPA) supports a much wider phase-matching bandwidth, is not accurate in determining the experimentally observed bandwidth as it assumes small energy departures from the central wavelength. A more accurate description requires a proper numerical treatment of the nOPA gain: for instance, in the framework of Ytterbium-based optical parametric amplifiers, simulations show that ultra-broad band spectra covering hundreds of nanometers can be amplified [129, 130], with good agreement with experimental results [131]. For the spectra reported, supporting few cycle pulses, a simple expansion around the central frequency is not a good description for pulse propagation and dispersion calculations: one has to take into account the full ω-dependence of the refractive index and spectral phase.

2.6.1 *The spatial walk-off*

The non-collinear configuration minimizes temporal walk-off effects (also called longitudinal walk-off), enabling broad-bandwidth amplification in longer crystals. It must be kept in mind that the angle between the three interacting waves results in a lateral walk-off in the non-collinear plane. After a certain length, the interacting pulses
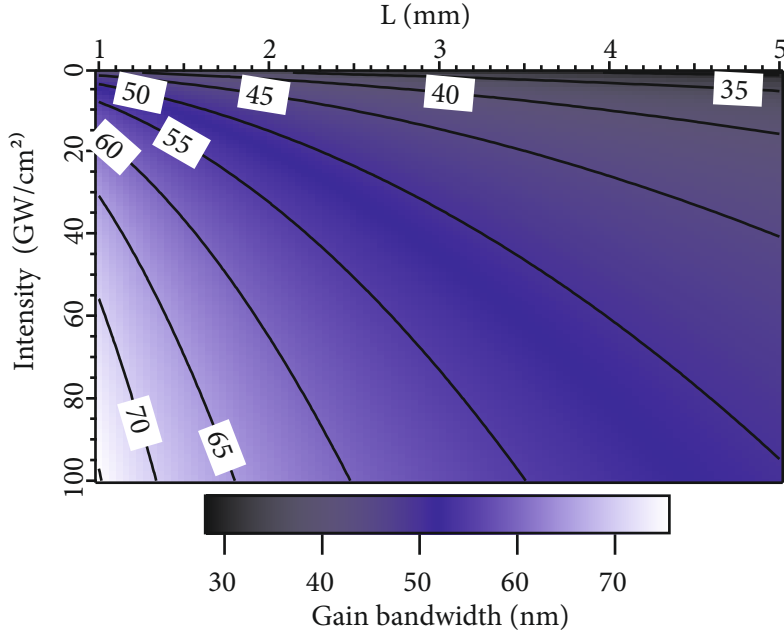
Figure 29: Gain bandwidth of a NOPA, calculated using Equation 81 for the process 0.515 μm$\rightarrow$ 1.450 μm+ 0.800 μmin BBO. The labeled lines represent constant bandwidth contours.

no longer overlap in the region of maximum intensity, giving rise to a mode asymmetry along the direction of non-collinearity. A useful parameter to quantify this effect is the walk-off length, defined as the distance after which the signal and the pump beam are separated by the Gaussian beam parameter w_0 of the pump. The calculated angular walk-off is plotted in figure 31: as expected, the length increases for higher non-collinear angles and is reduced for larger pump spot sizes.

An important aspect of the problem, so far neglected, is that the beam propagations occurs in an anisotropic medium, in our case the nonlinear crystal BBO. The necessary condition for achieving non-critical phase matching, as discussed in section 2.4, is indeed birefringence. The direction of the Poynting vector of an extraordinarily-polarized wave in a birefringent crystal is not parallel to the direction of the wave-vector [91]. The Poynting vector's direction corresponds to the direction of optical energy flow and hence the direction along which the beam propagates, whereas the wavevector $\vec{k}$ is orthogonal to the phase fronts. BBO is a negative uniaxial crystal: in this case a *birefringence walk-off* occurs for the extraordinarily-polarized pump wave (Type I interaction). The Poynting vector has an angle ρ relative to $\vec{k}_p$ in a direction opposite to the optical axis. This gives rise to two inequivalent non-collinear phase-matching configurations, illustrated in figure 30. If the wavevector of the signal wave lies between the optical axis and the pump wave, the angular walk-off between the signal and the pump is further accentuated by the birefringence, one speaks
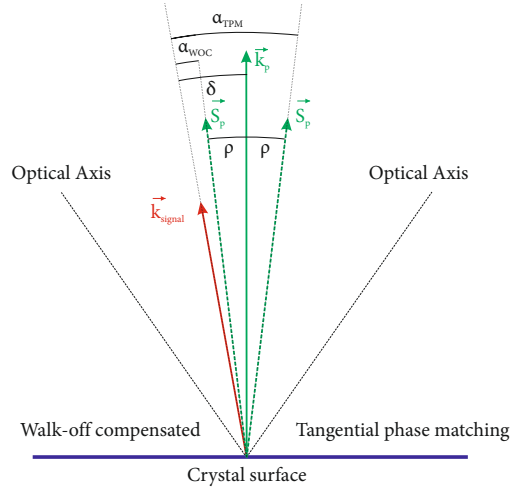
Figure 30: Phase-matching configuration in presence of spatial walk-off. ρ is the walk-off angle, δ is the angle of non-collinearity between the signal wavevector $\vec{k}_{signal}$ and the pump wavevector $\vec{k}_p$. The position of the optical axis in the two configurations is indicated: when the optical axis is located counterclockwise from the pump, one has a walk-off-compensated configuration and vice-versa. α_{WOC} and α_{TPM} are the walk-off angles for the walk-off-compensated and tangential phase matching configuration, respectively.

in this case of *tangential* phase-matching configuration (TPM). On the other hand, when the crystal is rotated by 180°, the so called *walk-off compensated* (WOC) phase-matching configuration is realized. In this case the effect acts to increase the effective interaction length of the process. The walk-off length, corrected for the birefringent effect is indicated in figure 30, for both cases.

For a realistic beam parameter w_0 of about 0.5 mm, the WOC geometry ensures an interaction length above 10 mm, considerably higher than the TPM case. The values are significantly above the thickness of 3 mm required by the bandwidth analysis (Section 2.6), showing that the geometrical effects introduced in the NOPA are not a limiting factor for the configuration under study. Other aspects have to be taken into account when comparing the two configurations, in particular in Section 2.7.3.3, it will be shown that parasitic nonlinear optical processes are different in the two cases.

2.7 OPTICAL CHIRPED PULSE PARAMETRIC AMPLIFICATION

Optical parametric amplification is a powerful tool to convert the frequency of femtosecond lasers, enabling tunable femtosecond pulses from the visible to the infrared [122] and removing the constrains imposed by the laser gain bandwidth. Very energetic and moderately short (down to the picosecond regime) pulses can be produced by
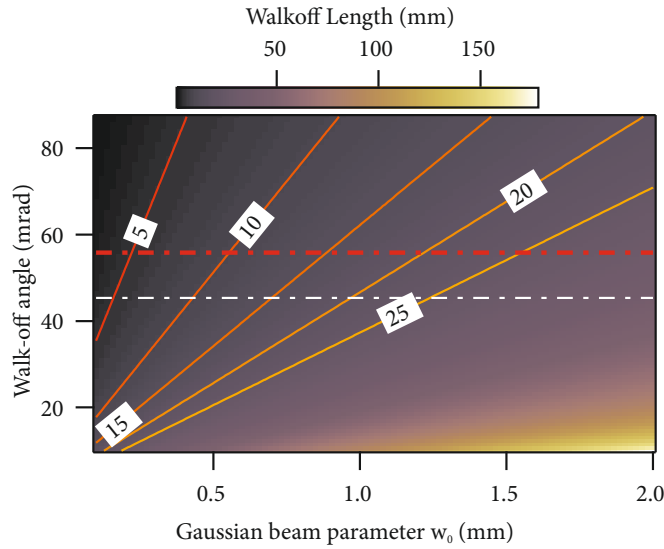
Figure 31: Spatial walk-off as a function of the walk-off angle for different Gaussian beam parameters of the pump beam. The red line-dot trace indicates the tangential phase-matching configuration, the white line-dot trace shows the walk-off for a compensated geometry. The diagonal lines mark contours of a constant walk-off length, indicated in the labels.

chirped pulse amplification of mode-locked Nd and Yb lasers: optical parametric amplification can also be performed with these sources to amplify femtosecond pulses [132]. In this case a narrow-bandwidth source amplify a second, weaker source with a broad-bandwidth. In this way the pulse power can be enhanced, thanks to the shorter final pulse duration.

This extension of OPA is generally called optical parametric *chirped-pulse* amplification (OPCPA): this name is due to an analogy with the technique of chirped-pulse amplification (Section 2.3.1) in conventional quantum amplifiers [133]. Due to the nearly-instantaneous nature of the induced nonlinear polarization, the parametric process is possible only during temporal overlap of the pump and the signal pulses. The signal pulse has a broad bandwidth, supporting a pulse duration in the femtosecond range: in order to achieve an efficient energy exchange, it has to be stretched to match the duration of the pump pulse. Here lies the analogy with CPA: the amplified pulse is chirped in a controlled way before amplification and subsequently re-compressed, although in this case not to reduce the B-integral of the amplifier. The stretching ratio in OPCPA is of few picoseconds, on the order of the duration of the pump pulse, whereas for conventional CPA it amounts to several tens to hundreds of picoseconds.

A conceptual scheme of an OPCPA is depicted in figure 32: the seed radiation produced by a broadband light source is stretched in a stretcher, in this example just by transmission through a dispersive medium; the seed is amplified in a non-linear crystal by the pump ra-

diation, which is produced by a synchronized laser source. The beam interact non-collinearly to ensure broadband phase matching and an idler beam is generated, removing the excess energy from the crystal. The amplified beam is re-compressed in a suitable compressor, for example a prism pair. This very basic OPCPA setup is also the one adopted in this work, and will be described in more detail in Section 2.7.4. Different OPCPAs, besides differing for the adopted pump and seed lasers and their synchronization, might include several amplification stages and adopt different choices for the stretcher-compressor pair, especially for very short pulse durations.
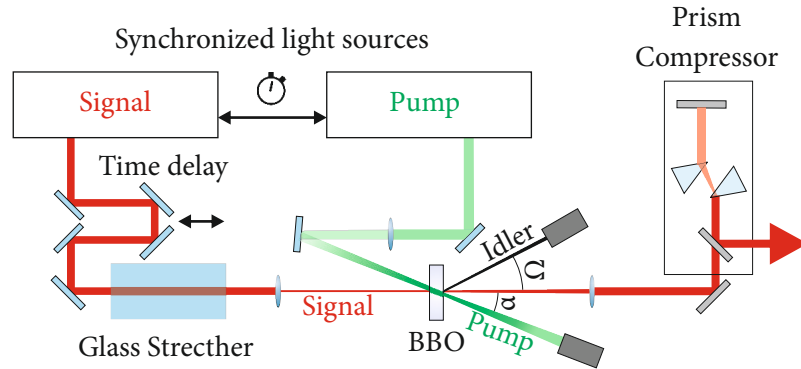

Figure 32: General scheme of an OPCPA. The different parts are explained in detail in the main text. The external angle between pump and signal is indicated as α and the pump-idler angle is Ω.

The nearly-instantaneous temporal gating effect of the pump has several implications which lie at the base of the distinction between an OPCPA and a conventional OPA. Nowadays a typical OPCPA has a pump pulse of several hundreds of femtoseconds (200 fs - few ps) and is used to amplify a pulse supporting 5-30 fs [134, 135]. A conventional OPA typically converts the sub-100 fs output of a Ti:Sapphire laser to produce tunable visible or infrared pulse of comparable duration [122]. Recently, Ytterbium lasers with pulse duration below 300 fs, have become common and this has triggered the development of commercial OPAs and nOPAs based on these systems. In this case, the duration of the chirped amplified pulses lies in between the previous two examples: as the pump pulse duration approaches the duration of the amplified pulse, the distinction between OPA and OPCPA becomes artificial.

OPCPAs are increasingly popular due to their superiority in respect to Ti:Sapphire for several key parameters. Different nonlinear crystals are available allowing efficient amplification across a broader frequency domain, from the near UV [136] to the infrared [137]. This represent a great advantage for several spectroscopic applications where resonant excitation of the system is desirable. The coherent combination of several broadband OPCPAs spanning several octaves of radiation allow to synthesize the shortest controlled light

waveforms [138]. Another field where OPCPAs have opened new possibilities, is the generation of extremely short (down to the attosecond scale) EUV /soft X-ray pulses via high-order harmonic generation (see Chapter 3). In general, several strong-field physics applications can benefit from the shorter pulses that a parametric amplifier can support, since the highest peak powers are instantaneously applied to the matter, before detrimental ionization occurs. The lack of a quantum defect solves the thermal problems not allowing Ti:Sapphire to reach simultaneously high repetition rate and high pulse energy: by adopting adopting OPCPA technology, many experiments can be performed in a fraction of the time. The success of this technology strongly relies on the developments in the last two decades of high-power and high-repetition-rate Ytterbium solid-state lasers, as the ones described in Section 2.3.3. The current state-of-the-art promises to be able to surpass the Ti:Sapphire standards in every parameter (pulse duration, energy and repetition rate), hence representing a new generation in femtosecond laser technology. Dye lasers allowed the first breakthroughs in the world of femtosecond physics, the adoption of Ti:Sapphire amplifiers represented the second era of femtosecond laser technology, greatly increasing pulse power and reliability [105]. OPCPA today represent the third and newest generation of ultrafast lasers [117].

2.7.1 *Synchronization of seed and pump laser sources*

To achieve a stable operation condition in a parametric amplifier, the pump and seed have to be synchronized within a fraction of the pulse duration. The various strategies to achieve such pump-signal synchronization are the subject of this section. In particular, the focus will be put on OPCPAs operating in the visible and near-infrared range and based on Ytterbium pump lasers.

2.7.1.1 *Electronic Synchronization*

When the pump and the signal beams are derived from independent lasers, it is necessary to synchronize the two laser oscillators electronically. The most precise electronic synchronization is achieved by locking the repetition rate of the two laser oscillators to a high-frequency electronic oscillator, therefore requiring the adoption of pricey GHz electronics. The current technology enables root-mean-square fluctuations in the arrival time of the pulses on the order of 100 fs [139], sufficient when working with pulses lasting several tens of picoseconds, but too high for sub-picosecond pulses. An electronically-synchronized OPCPA has the advantage that the choice of the pump laser is relatively decoupled to the seed laser oscillator, which is not the case for *optical synchronization*.

2.7.1.2 *Seeding by Ti:Sapphire broadband oscillators*

To build OPCPAs based on sub-picosecond pump lasers, the pump laser is seeded directly using a fraction of the signal laser. The broadband signal pulses can be provided by a Ti:Sapphire oscillator: the challenge in this case is that the Ti:Sapphire laser line barely covers the amplification bandwidth of the Yb and Nd lasers. Only the broadest oscillators available [106] have a sufficient spectral power around 1 μm to directly seed an Ytterbium laser [131, 140–144]. For more conventional Ti:Sapphire oscillators, a fraction of the pulses have to be frequency shifted to match the Ytterbium gain profile. This can be achieved using a technique called *soliton self-frequency shift*, attainable via nonlinear propagation in a photonic crystal fiber [145]. In both cases, the effective seed energy is rather low: a long optical path in regenerative amplifiers or in fiber lasers might be necessary to rise the pump pulse energy to desired level. This poses the problem of long-term drifts on the relative optical path length which require active delay stabilization [140, 141].

2.7.1.3 *Supercontinuum seeded OPCPAs*

An alternative to Ti:Sapphire seeding is to use an Ytterbium femtosecond oscillator, directly seeding the pump amplifier chain. To reach a sufficient bandwidth the pulses have to be frequency-broadened using nonlinear optical techniques. The weak oscillator pulses can be focused into a large-mode-area micro-structured fiber [146–149] where self-phase modulation over long interaction lengths produces the desired broadening. If this fiber-based spectral *supercontinuum* retains its phase coherence, it can be re-compressed to a duration of few optical cycles. This is not always true due to *soliton fission* [150], an effect which hinders the temporal coherence of the pulse train. It is worth mentioning in this context that also Erbium-based fiber lasers equipped with similar frequency conversion mechanisms are promising for seeding of OPCPAs [128], these systems will not be considered in this work.

Supercontinuum generation is also possible in transparent bulk materials, if higher-power pulses of an amplified femtosecond laser are available. In this case the broadening process is usually called *white-light generation* (WLG, Section 2.7.2). Efficient and stable WLG in bulk materials was for a long time thought to be exclusive of sub-100 fs pulses: further research in the field and the use of different optical materials such as YAG, proved that even picosecond lasers can produce stable broadband spectral continua [151]. This is a tremendous simplification in term of pump-signal stabilization, as part of the pump laser can be split immediately before the OPCPA to produce the seed radiation, virtually eliminating the drift problems. This approach is largely adopted in ultrafast fiber amplifiers, where the pulse duration

is well below 500 fs and a high quality continuum can be produced without efforts [152, 153, 136, 154–156]. For longer pulse durations, typical of Yb:YAG systems (about 1 ps), the approach is still feasible, at a cost of a somewhat increased complexity: in the work of Schulz et al., the authors report that the crystal has to be continuously translated to avoid long-term damage of the crystal [157, 158].

2.7.1.4 *Hybrid seed*

A high-power amplifier can consist of several stages, where the final amplification is sometimes performed in a booster stage, preceded by pre-amplifiers: this is also the case of the Ytterbium amplifier described in this work (see Section 2.7.4), where a picosecond Yb:YAG innoSlab amplifier is seeded by a high-power fiber amplifier. In this case, the overall path length in the power amplifier is only a few meters and an hybrid approach can be successfully implemented [159, 160]. In this case, the fiber amplifier is used to generate a white light continuum, which is then stretched and amplified by the picosecond power amplifier. The pointing stability and the mode quality are better for the fiber system, at the same time the pulse duration is shorter: the generated broadband signal is therefore more stable than the one obtained with the power amplifier pulses [158].

2.7.2 *White light generation in bulk materials*

When a light pulse of sufficient intensity travels through an optical material, nonlinear phase modulation produces new frequency components. The effect can be quite dramatic for high-intensity near-infrared femtosecond pulses, which may produce an extremely broad continuum spanning both the blue and the red side of the original spectrum: this phenomenon of *supercontinuum generation* occurs both in condensed and gaseous media and was intensively studied for its applications as broadband light source [161].

The very short Fourier limit of supercontinuum light is particularly attractive: the broadened light can potentially be compressed to very short pulse durations, provided that temporal coherence is retained in the process. Broadening of high-intensity femtosecond lasers in gases is routinely employed to generate few-cycle pulses, a technique called *nonlinear compression* [162]. Nonlinear compression allows dramatic pulse shortening with relatively good efficiency (on the order of 50 %). In the case of OPA or OPCPA seeding, the broadening is most often performed with pulses of lower power in a bulk transparent material, for which the intensity threshold is reduced. On the other hand such white light generation results in few nJ of white light at most [151].

Supercontinuum generation is a rather complex phenomenon which involves several nonlinear optical effects [163]: a full understanding

of the various broadening mechanisms requires extensive simulations of the pulse evolution in a dispersive, ionized, nonlinear medium, beyond the scope of this thesis.

Qualitatively, the key-component for spectral broadening is self-phase modulation (Section 2.2). Two effects contribute to the time-dependent index of refraction: the optical Kerr effect and the presence of a time-varying plasma density due to ionization of the medium. The overall broadening becomes larger if the pulse propagate at high intensity for longer distances: it is therefore maximized when diffraction is compensated, for instance by propagating the beam in a waveguide or in a fiber. In the case of white-light generation, a phenomenon called *filamentation* is responsible of this long interaction length. Filamentation is the result of an interplay between the Kerr effect and the generated plasma, but this time occurring in the radial direction of the beam. Kerr lensing induces a self-focusing effect which increases the intensity and thereby the level of ionization. The higher plasma density at the beam center, counteracts the self-focusing by *plasma defocusing*. A filament occurs when the beam geometrical parameters are such that a perfect balance between the two effects is achieved, a condition known as *intensity clamping*. The increased length of such filament, compared to the usual depth of focus set by diffraction, is at the base of the extreme bandwidth of the white light.

Thanks to its high damage threshold, sapphire has been the most widely used material for white light generation to seed nOPAs. The development of Ytterbium lasers has pushed the investigation of alternative materials, capable of efficient and long-term stable continuum generation when irradiated with the comparatively longer pulses of these lasers [151, 157, 164]. The material's key parameters for WLG are the damage threshold, the third-order susceptibility, responsible for the Kerr effect, and the band gap, which governs the multi-photon absorption leading to free carriers [151]. In the case of continuum generation with ytterbium lasers, YAG is well established: thanks to the lower band gap compared to sapphire, the threshold for white light is lower and stable continua can be produced either with pulses of duration of few hundreds of femtosecond [151] or with picosecond pulses [157, 164]. The experimental results of WLG in YAG will be presented in Section 2.7.5.3.

2.7.3 *OPCPA bandwidth engineering*

The amplified spectrum is one of the most important parameter of an OPCPA: the desired wavelength-tunability range determines the choice of nonlinear crystals as well as the wavelength of the seed and pump lasers.

The spectral bandwidth is selected during the chirped pulse amplification: due to the temporal gating effect of the pump, the relative

duration of the broadband signal and the pump is what matters in this respect. The duration of the pump laser is usually most often kept as short as possible to maximize the intensity: this allows to reach the same gain with larger spot sizes, minimizing the fluence, simultaneously, the threshold intensity for optical damage increases with pulse duration (Section 2.5). Shorter pump pulses also minimize the overall stretching of the seed, thereby simplifying the compression. The bandwidth of the laser is therefore usually controlled by a suitable chirp management of the seed radiation.
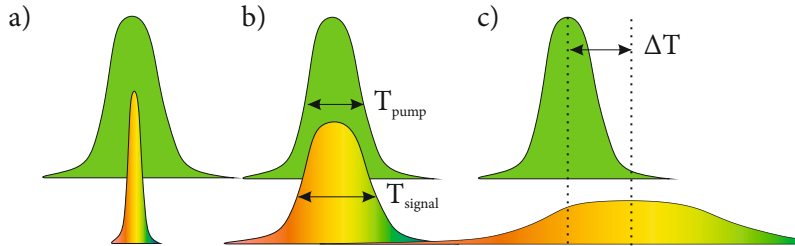

Figure 33: Schematic illustration of optical chirped pulse parametric amplification. The pump temporal FWHM is T_{pump} and the signal duration is T_{signal} a) The signal is compressed relative to the pump; b) the duration of the interacting pulses is matched c) the signal is considerably longer relative to the pump. By delaying the two pulses by ΔT, different frequency components are amplified.

The seed pulse has a bandwidth supporting pulse durations of few femtoseconds: when chirped to a duration approaching the picosecond level, the instantaneous frequency changes monotonically with time, increasing (decreasing) for positive (negative) chirp. If the pump duration is overall longer than the seed (figure 33-a) all the frequency components are within the pump temporal envelope, and the full spectrum undergoes amplification. However, only a small portion of the pump is effectively seeded, resulting in a poor efficiency. In case b) the duration of the pump and the seed is matched: again all the frequency components can be potentially amplified, but now the available pump will be more effectively depleted. In case c) the seed stretch is increased further: only the frequency components below the pump temporal envelope are amplified, resulting in a narrower bandwidth at a certain wavelength.

A situation like b) is desirable when amplifying the shortest pulses and thus fully exploiting the non-collinear achromatic phase matching. Situation c) instead results in flexibility in the selection of the central wavelength and the bandwidth of the OPCPA. By changing the relative delay between the two pulses one can change the central wavelength. The amplified bandwidth can be increased or decreased by changing the amount of chirp in the seed.

The efficiency of the process does not change significantly as long as enough seed photons are present to saturate the gain and deplete

the pump. However, as the stretch grows, increasingly less power per unit frequency seeds the OPCPA, ultimately preventing saturation. If the pump cannot be fully depleted in a single pass, more amplification stages are required: a high power seed helps to simplify the setup by reducing the number of stages.

2.7.3.1 *Parametric superfluorescence*

Another important aspect speaks against low seed power and the corresponding high gain factors: the presence of *parametric superfluorescence*. Vacuum fluctuations of the electric field are always present: these photons can initiate spontaneous down-conversion of the pump into idler and signal photons. These can in turn be further amplified and compete with the seed photons for gain (see for more detail reference [165] and references therein). The random nature of these quantum fluctuations makes the superfluorescence temporally incoherent, therefore resulting in an incompressible temporal pedestal of the duration of the pump pulse, detrimental in several applications. To minimize the amplified superfluorescence is better to split the total gain between several stages. This helps because the divergence of the superfluorescence and the amplified light are different, allowing to remove some of the unwanted superfluorescent by spatially filtering the beam before the final amplification stages [166].

2.7.3.2 *Optimization of OPCPA efficiency*

The simplified theory presented in this work does not account for the pump depletion which occurs when high conversion efficiencies are reached. Numerical solution of the coupled differential equations governing the process are necessary for a more realistic description (for a relevant example on VIS-NIR OPCPA pumped by picosecond Yb:YAG lasers, reference [130] can be consulted). The non-uniformity of the pump profile, both in space and in time, determines a different, time-dependent gain for various frequency components. For example when the frequency components below the temporal maximum are already experiencing saturation, the ones under the wings still undergo high gain.

A more in-depth analysis [167, 168] reveals that there are trade-offs between the conversion efficiency and the achievable bandwidth: a precise chirp control of separate stages and temporal shaping of the pump pulses [169] can be used to optimize the amplification process for maximizing the final peak power. The same considerations hold also for the spatial profile, where again the non-uniformity of the gain and later walk-off effects can reduce the conversion efficiency [170]. Spatio-temporal shaping can indeed increase the conversion efficiency of OPCPAs, however the losses and the complexity of pump shaping optics may in practice overcome the benefits.

The typical efficiencies reported for OPCPAs operating in the VIS-NIR range, pumped by the second harmonic of sub-picosecond diffraction-limited Yb:YAG amplifiers ranges between 15 % [160] to 25 % [171, 144], without recurring to pump shaping.

2.7.3.3 *Parasitic second harmonic generation and thermal effects.*

Several parasitic effects can occur in an OPCPA, especially when extremely high bandwidths have to be realized. These effects are three-wave mixing processes which are also phase-matched during amplification and produce radiation at different wavelengths, competing with the signal growth [129, 131]. In the case of parametric amplification in BBO in the range between 650 nm and 1000 nm, a recognized problem is parasitic second harmonic generation of the signal, which becomes particularly efficient around 900 nm for the walk-off compensated (WOC) phase matching scheme [172]. The parasitic effect can be reduced by selecting a tangential phase matching (TPM) scheme, for which the phase-matching wavelength is red-shifted: broadband amplifiers covering this range have to adopt TPM to limit severe losses and spectral distortions in the NIR. The TPM however limits the usable crystal thickness and generally worsen the mode shape. In the case of narrower bandwidths centered around 800 nm, such as the one considered in this thesis, the two configurations were compared and the WOC configuration was found to give better results with only a modest residual parasitic second harmonic (Section 2.7.6)

Even though OPA is more thermally-efficient than a conventional laser, the average powers of the pump is still exceptionally high, with the possibility to be scaled to the kilowatt level. Residual thermal effects due to the finite transmission of the crystal, the possible absorption of the idler wave and of the parasitic waves is expected to rise the temperature in the crystal non-uniformly. The thermo-optical effect, already before observing distortions due to thermal lensing, disturbs the phase matching. To model the residual absorption of a given nonlinear crystal, a knowledge of the absorption coefficient is necessary. The study of reference [173] reveals that the major role is played by residual absorption of the pump and of the idler wave above 2 μm. In the cited work, a broadband signal covering a range from 600 to 1230 nm was amplified in BBO: the study revealed a temperature increases by more than 150 K for megahertz repetition rate and a 200 W Ytterbium pump laser. By restricting the amplification range above 690 nm, only the pump absorption plays a role: the same study reported a increase of around 50 K in this case. This has to be compared to temperature acceptance bandwidth of the mixing process: this quantity is defined as the temperature change necessary for which the product $L\Delta k$ varies form $-\pi$ to π, where L is the crystal

length and Δk is the phase mismatch[9]. In the case of amplification of 800 nm radiation in BBO this is 39.82 K cm [10].

In the case of a few-millimeters-long crystals studied by reference [173], 50 K are not yet sufficient to disrupt the OPCPA process noticeably. The absorption coefficient for the pump can be several hundreds 10^{-6} cm^{-1}, with some variability depending on the manufacturer [158]. Riedel et al. characterized several crystals and found the lowest absorption coefficient to be 13×10^{-6} cm^{-1}. In this case a marginal temperature increase below 1 K was measured for a 160 W Ytterbium pump lasers and bandwidth of about 240 nm, with the spectrum entirely above the mentioned short wavelength cut-off.

Even when the phase-matching process is not severely disturbed by the temperature increase, a mechanical tensile stress can build up in the crystal and potentially lead to fracture. In the case of BBO this occurs at an estimated temperature of 470 K [173]. In respect of the thermal management, LBO is a better candidate for scaling to high average powers: the limiting power achievable in LBO using a realistically available Ytterbium pump laser of 1.6 kW is about 181 W at 100 kHz with 7 fs pulses [130].

2.7.4 *Laser system overview*

The laser system developed in this thesis has two main design goals: the first is to achieve a high average power, enabling HHG at very high repetition rates. The second goal is to have a tunable bandwidth, giving the choice between high temporal resolution and narrower spectral width, for experiments requiring a better energy resolution. The goal for the temporal resolution was set under 20 fs, below conventional high-power Ti:Sapphire amplifiers. In the narrow bandwidth mode, the target was to achieve a time-bandwidth product comparable to a conventional, high-repetition-rate Ti:Sapphire[11], but at a considerably higher average power. A central wavelength of 800 nm, similar to the widespread Ti:Sapphire laser, was chosen because reliable and cheap optical components are available out-of-the-shelf.

The technology of choice was described in the first part of this chapter: the ultrafast amplifier is an OPCPA, based on an ultrafast Ytterbium laser with an hybrid (section 2.7.1.4) architecture. The frequency/bandwidth tuning is performed using the methodology described in section 2.7.3. The laser system is based on a combination of Ytterbium:fiber amplifier, which has a pulse duration of 350 fs for which the generation of a stable white-light continuum in YAG is well

---

9 this is about 13% larger than the FWHM of the sinc function for the phase-matching bandwidth introduced in Section 2.4

10 SNLO, nonlinear optics code available from A. V. Smith, AS-Photonics, Albuquerque, New Mexico, USA, `http://www.as-photonics.com/snlo`

11 RegA, Coherent, `https://www.coherent.com`

established (section 2.7.2). The high-average-power pump is based on a commercial Yb:YAG innoSlab amplifier [12]. An important requirement for the OPCPA is to achieve stability over the course of several hours, to enable extended HHG-based tr-ARPES data acquisition.
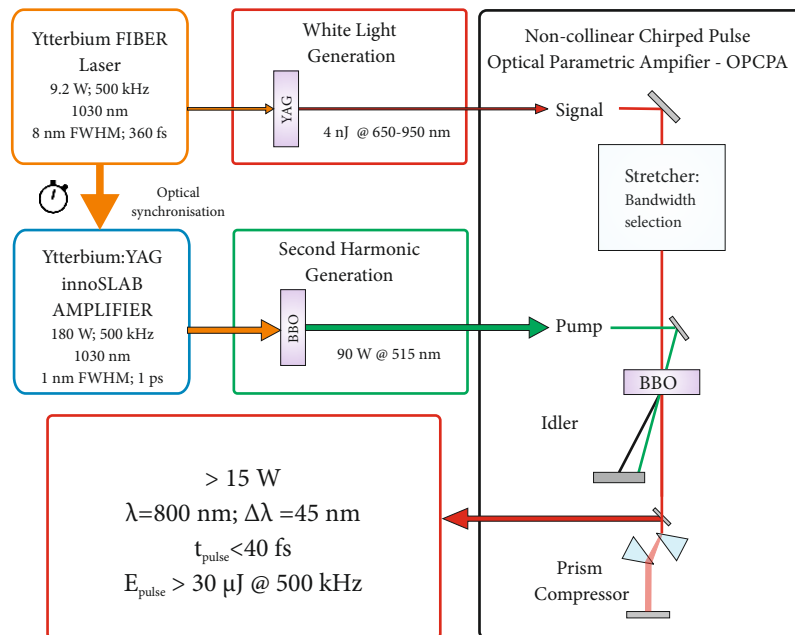

Figure 34: Scheme of the laser system.

The laser system is schematized in figure 34. The fiber laser produces pulses with an 8 nm FWHM bandwidth at an average power of 9.2 W at a repetition rate of 500 kHz. A part of this power is compressed to 360 fs and is used to generate a white-light continuum in YAG. At least 4 nJ of radiation between 650-950 nm seed the OPCPA. The second part of the fiber laser output is further amplified in the innoSlab amplifier: due to the advantageous design of this laser, the CPA can be kept at a minimum level. The output pulses, with about 20 ps pulse duration at an average power of 200 W are re-compressed to 1 ps in a home-build grating compressor and frequency doubled. The result is more than 90 W of 515 nm radiation to be used for pumping the OPCPA. To match the duration of the picosecond pump pulses, the white light is stretched in a glass block: the use of different glass thicknesses allow to tune the amplifier bandwidth. The seed energy is sufficient for using a single stage of amplification, therefore greatly simplifying daily operation. Finally, the pulses are re-compressed in a prism compressor. The final output power exceeds 15 W; when tuned to 800 nm and with a bandwidth of approximately 45 nm, the pulses could be re-compressed to a sub-40 fs pulse duration. The next sections will describe in greater detail the specifications of the Ytterbium

12 AMPHOS 200, Amphos, http://www.amphos.de

Table 4: Requirements for the fiber laser for a repetion rate of 500 kHz: λ_c = central wavelength; $\Delta\lambda$ = FWHM bandwidth; Δt = pulse duration; E_p = pulse energy

Task	λ_c (μm)	$\Delta\lambda$ (nm)	Δt (ps)	Power (W)	E_p (μJ)
White light	~ 1	$\gtrsim 5$	$\lesssim 0.4$	$\gtrsim 0.5$	$\gtrsim 1$
Slab seed	1.030	1.5	> 20	> 1	> 2

laser system and the experimental results. Some of the data presented on this chapter was published in reference [19].

2.7.5 *The Ytterbium fiber laser system*

The fiber laser is based on a master-oscillator power-amplifier (MOPA) architecture: a master oscillator produces weak pulses, which are pre-amplified in conventional fibers before seeding a power amplifier based on a large-mode-area fiber. The laser system operates at a repetition rate of several hundreds of kHz to one MHz and produces a broadband continuum spanning the visible to seed the OPCPA, simultaneously, it is able to seed the innoSlab amplifier. The minimal requirements are summarized in table 4 for a repetition rate of 500 kHz:

2.7.5.1 *All-normal dispersion fiber oscillator*

It is rather difficult to scale the pulse energy of an ultrafast fiber oscillator: high B-integral disturb the intra-cavity pulse evolution, making the design of fiber oscillators rather different than their solid state counterparts [174]. Another challenge comes from the fact that the gain profile of an Yb doped glass fiber is not maximum at the wavelength 1.030 μm which is required to seed the Yb:YAG system.

Driven by the increased demand of femtosecond fiber lasers, research in the field have brought to the development of oscillators operating in the all-normal-dispersion regime (ANDi lasers) which are capable of achieving nJ pulses, with tunable wavelength and bandwidths supporting $\approx$ 100 fs [175]. The nonlinear pulse evolution in such laser is itself part of the design: spectral broadening effects are used together with intra-cavity spectral filtering. This allows to center the wavelength within the gain in Yb:YAG, to produce bandwidths supporting pulse durations below 200 fs and to promote pulse formation. An important feature of these lasers is that they operate in a chirped-pulse regime, therefore their output is not Fourier-limited and require an external compression mechanism to reach the ultimate pulse duration. In our system, a 25 MHz mode-locked Ytterbium fiber oscillator working in all normal dispersive regime provides a spectral bandwidth of 10 nm full width half maximum (FWHM) at a central

wavelength of 1030 nm [176]. The scheme of the oscillator is shown in figure 35: it comprises of a fiber-only part, together with a free-space-propagation section. One of the benefit of an all-fiber design is the alignment insensitivity: unfortunately, due to the lack of suitable components such a solution was not possible. The free-space propagation in the laser oscillator has a length of only about 50 cm, embedded in an actively temperature-controlled, monolithic breadboard of a footprint of about $50 \times 40\,cm^2$. The laser operates 24/7 for several months without need for re-alignment.
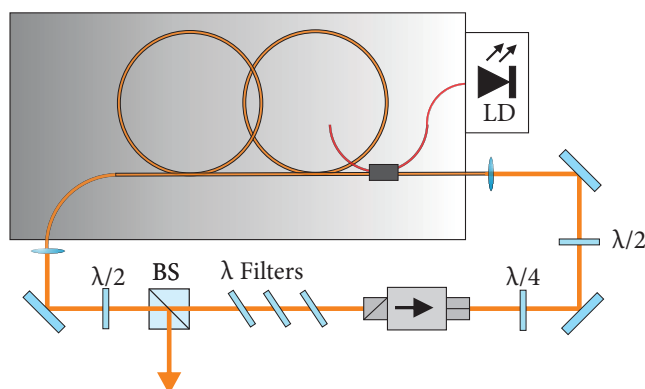

Figure 35: Ytterbium:fiber oscillator, LD is the pump laser diode, $\lambda/2$ half-waveplate, $\lambda/4$ quarter-waveplate, λ filter = birefringent band-pass filter; BS beam splitter

The free-space part of the cavity contains three waveplates (two half-waveplates, labeled $\lambda/2$ in figure 35 and a quarter-waveplate, labeled $\lambda/4$), a polarizing beam splitter used as output coupler, an optical isolator defining the circulation direction of the ring cavity and a wavelength filter (indicated as λ filter in figure 35). These wavelength filters are a combination of birefringent plates of different thickness and a thin-film polarizer, used to reject part of the spectrum based on the different polarization rotation for different wavelengths. The filter is the main component used to set the central wavelength of the laser at 1.030 μm. Mode-locking is achieved by nonlinear polarization evolution: during propagation in the fiber, an intensity-dependent polarization rotation occurs, a polarizer can promote mode locking in a similar fashion of the aperture of a Kerr-lens-mode-locked laser. Self phase modulation and spectral filtering in the wavelength filter participate in the pulse formation too: the self phase modulation produces new frequency components at the wings of the spectrum which are rejected by the λ filter. Due to the high chirp of the pulse, such spectral filtering is equivalent to a temporal gating.

The pump of the laser is a laser diode, which is fiber-coupled to the pump core of the Ytterbium-doped fiber through a wavelength division multiplexer. The oscillator's output power and bandwidth depend on the settings of the waveplates and on the current in the

pump laser diode. Up to 500 mW of output power in mode-locked operation can be achieved, with pulses than could be re-compressed to about 250 fs, measured with an autocorrelation technique.

2.7.5.2 *Fiber amplifier*

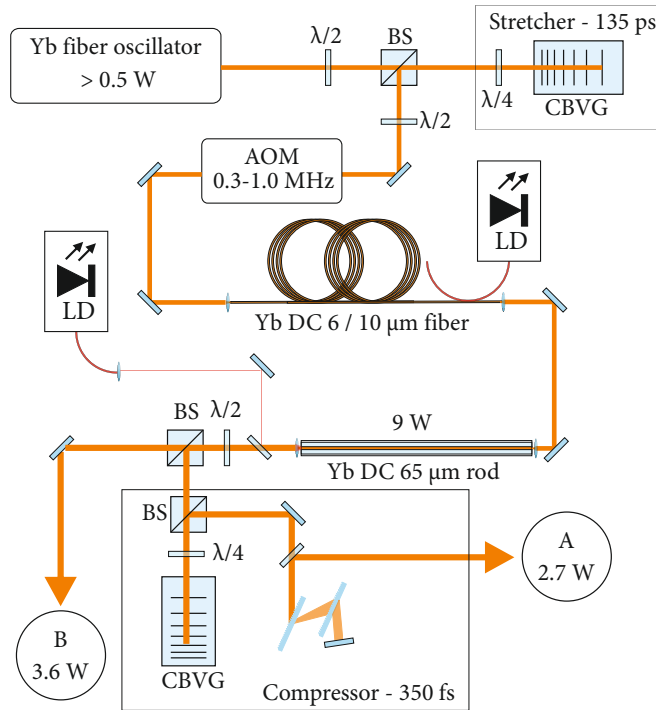The overall scheme of the fiber CPA is shown in figure 36.

Figure 36: Schematic of the Fiber laser. $\lambda/2$ half-waveplate; $\lambda/4$ quarter-waveplate; BS beam splitter; CVBG chirped volume Bragg grating; AOM acusto-optical modulator; LD pump laser diode.

After the oscillator, a fiber pre-amplifier is used to raise the energy and reduce the repetition rate. The stretcher for the chirped pulse amplification is based on a chirped volume Bragg grating[13]. The pulse duration is ≈ 130 ps before amplification. About 40 mW are necessary to seed the dual-stage preamplifier[14]. The pump laser consists of a pair of fiber-coupled laser diodes with up to 10 W CW power each; the amplification is performed in double-clad polarization-maintaining large-mode-area fiber. Active temperature control enables to tune the wavelength of the pump diodes to maximize the absorption by Ytterbium and stabilize the gain. The whole assembly is embedded in a water-cooled aluminium housing. Between the two amplification stages, a fiber-coupled acusto-optical modulator reduces the repetition rate to range between 0.3 and 1 MHz. The final out-

---

13 CVBG, Optigrade 12.55 ps/nm
14 VENTEON | PULSE : THREE PRE-AMP 3

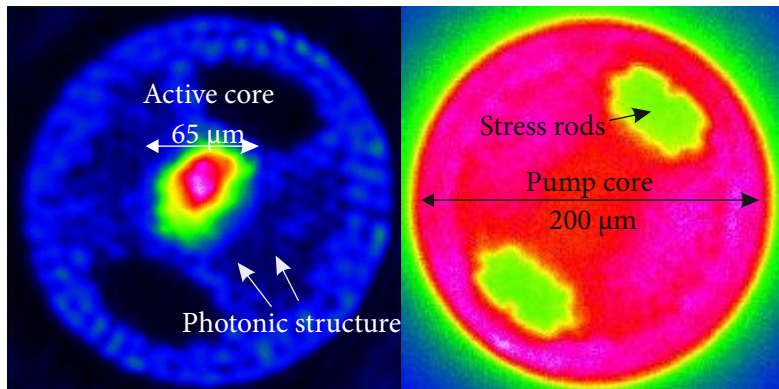put power is above 150 mW in the whole range and the bandwidth, reduced by gain narrowing, is about 7.5 nm.

Figure 37: Left: image of the end-facet of the seeded ROD-type fiber, showing the active core and the photonic structure. Right: entrance face of the ROD-type fiber, showing the pump radiation mode (the fiber is end-pumped) and the stress-rods for polarization maintaining operation.

The main amplification stage consists of a 80-cm-long photonic crystal fiber[15], designed to have a very large mode area of 76 μm, thereby capable of amplifying the pulses to a ten-watts level, without excessive distortion. An image of the output of the fiber is shown on figure 37: on the left side, the seed radiation in the active core is imaged on a CCD camera. Around the core, a photonic structure given by periodic holes ensure single-mode operation and diffraction-limited output for this large mode size. On the right-hand side, the same image is taken for the pump radiation, highlighting the pump core, overlapping with the active core. The fiber is end-pumped by a laser diode with up to 50 W power. A pre-amplifier power of 136 mW is sufficient to saturate the gain of the last amplification stage and an average power up to 10 W is reached at a pump power of 23 W. After amplification the spectral bandwidth is about 7 nm FWHM centered at 1030 nm.

The output of the ROD-type laser is split: the first part is used to seed the slab amplifier (see section 2.7.5.4). The rest of the output is sent into a two-stage compressor: first, a CVBG of the same dispersion rate of the stretcher, but of opposite sign, compensates most of the chirp. As the pulses have travelled several meters of fibers, and due to the fact that the oscillator output was originally chirped to several picoseconds, this is not yet sufficient to achieve full compression. The second part of the compressor consists of a transmission grating in a four-pass geometry, which reduces the pulse duration to 360 fs (inferred from intensity autocorrelation). The overall compressor transmission is about 50%: this leaves a compressed output of

---

15 NKT, DC 285/100 PM-Yb-ROD

about 2 W (4 μJ), sufficient for the generation of a stable white-light continuum, as will be shown in the next section.

2.7.5.3 *White light generation results*

The short pulses of the fiber system are well suited for white light generation in YAG (see section 2.7.2). To establish the optimal conditions for white light generation, several crystal thickness (4, 8, 16 and 20 mm) and different focusing geometry were compared. The goal of the study is to find the best compromise between long-term stability and sufficient efficiency to seed the OPCPA. If the white light power is sufficiently high, it is possible to saturate the OPCPA gain in a single amplification stage, thereby decreasing the complexity and potentially improving the overall stability.

The setup consists of an iris followed by respectively 75, 100, 200 mm focal-length plano-convex lenses, the beam diameter ($2w_0$) at the curved front face of the lens was approximately 2 mm. The crystal is installed on a translation stage, a 1030 nm high-reflective dielectric mirror is used to remove the driving wavelength; the transmission of the separator is flat across the visible range until a cut-off at about 940 nm. The power and the spectrum of the white light were measured simultaneously, using a power meter and a fiber spectrometer. During the experiment, for every optical fluence the position of the crystal is re-optimized to achieve the best total power yield. By closing the iris, it is possible to fine-tune the focusing conditions [151], however this simultaneously introduces interference effects and reduces the power. In order not to introduce such an uncontrolled effect, in this comparison the beam was always left unclipped. The effects of the iris were tested and did not yield sizeable improvements.

At a peak intensity of about 330 GW/cm^2, the crystal degrades after a few seconds: the intensity was therefore limited well below this value. To achieve long-term stability, with virtual no degradation over days, it was possible to use a fluence of up to 200 GW/cm^2 in our laboratory conditions. Several studies report that continuously moving the crystal [157, 158] improves the lifetime, so also fluences above 200 GW/cm^2 where considered in the comparison. Figure 38 compares the spectra of typical white-light supercontinua in a 4 mm and a 20 mm YAG crystal, for an input pulse energy of 1.4 μJ and at repetition rate of 500 kHz. The spectrum extends between 500 and 920 nm; the long wavelength cut-off is determined by the spectral filter used to remove the fundamental: the conversion efficiency in this spectral range is on the order of 10^{-3}. The filter most-likely introduces the peak-like structure around 515 nm, which is not relevant for the OPCPA as it is outside the amplification bandwidth. It is not clear if the ripples seen around 900 nm are due to oscillations in the filter reflectivity or to the white light generation process itself, but the fact that they appear already close to the threshold power for white light generation

and that their position is fixed, points toward the first option. The spectrum was normalized to the power measured with a calibrated power meter. The fiber spectrometer response was tested comparing direct sunlight with a reference solar spectrum, the factory calibration was accurate within 10% in the range of interest.
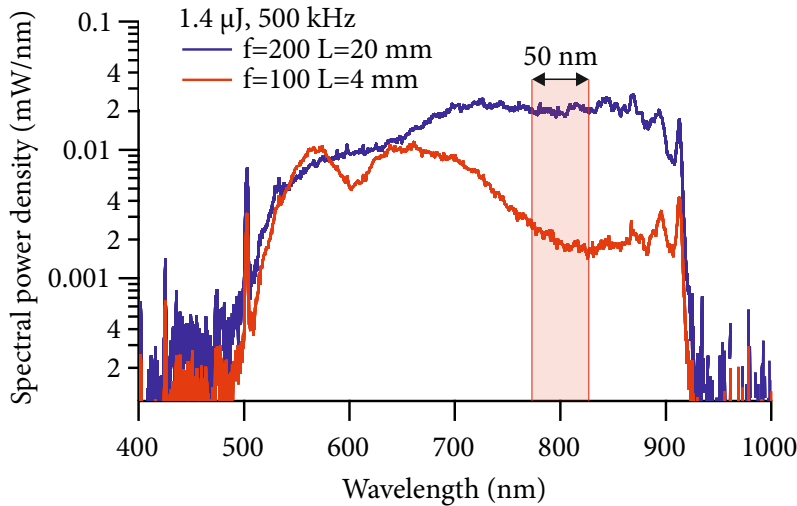

Figure 38: Spectral power density for the white-light measured in two configurations indicated in the figure. The red shaded region represents a window of 50 nm around 800 nm, used for calculating the effective-seed power.

For our application, the spectral area around 800 nm has a particular interest. In the following section, the absolute power within this region was also extracted from the calibrated spectra as a reference. As the input power is increased, multiple competing filaments develop in the crystal, resulting in spectral interference, power instability and in a reduced mode quality. This is shown in Figure 39 for a 20 mm crystal and 200 mm focal length, the beam diameter $2w_0$ at the lens was approximately 2 mm: above a power of 1200 mW (2.4 μJ) strong spectral modulations arise indicating multiple filaments.

The results are summarized in Figure 40, reporting the total white light power as a function of incident power for the different focal lengths and crystals; on the right hand side of the same figure the power in a window of 50 nm around 800 nm is extracted form the spectra. For all the investigated parameters the total output power tend to increase as the incident power increases. For the shorter focal length the output is quickly saturated when the crystal length is increased: there is no significant improvement in total power by using crystals above 4 mm for focal lengths of 100 mm or below, however as can be seen in 40, there is an overall spectral shift toward the NIR spectrum around 800 nm for longer crystals. At 200 mm focal length, the white light generation still saturates for crystals longer than 16
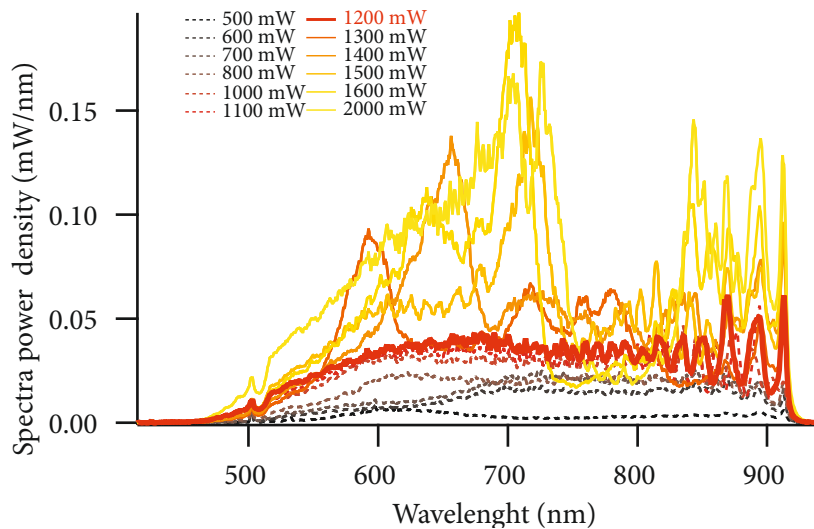
Figure 39: White light spectrum for increasing power of the fiber amplifier: above a threshold of about 1.2 W (2.4 μJ), red thick line, strong spectral modulations arise. This effect is understood as interference between multiple filaments. The spectra have been measured using a 20 mm thick YAG crystal and using a 200 mm focal length

mm; longer focal length were not tested, however, it is plausible that a longer focal length might still improve the yield. The presence of multiple filaments for longer crystals, as can be seen in figure 39 is highlighted by the discontinuity in the total power around 1300 mW; for a 16-mm-long crystal the multi-filament behavior occurs only at the highest fluence investigated. The highest efficiency, before the onset of multiple filaments, was recorded with the longest crystal at a focal length of 200 mm and 1200 mW power. In this conditions, the white light has an energy of more than 20 nJ, and a seed of 3 nJ for an 800-nm OPCPA. This is more than enough for saturating a single stage OPCPA based on a 4 mm BBO crystal, when operating at bandwidth of 50 nm FWHM: the seed power finally used was around 2 nJ at 800 nm for stable longe-term operation.

2.7.5.4 *Picosecond pump laser*

The picosecond pump laser consists of an Yb:YAG innoSlab[16] (see section 2.7.5.4): the laser was seeded by the uncompressed output of the fiber amplifier. Experimentally, about 3.6 W are sufficient to seed the innoSlab amplifier, which has an output power exceeding 200 W at 500 kHz repetition rate; the spectrum is centered at 1030 nm with a FWHM of 1.6 nm. The very high powers involved require special care for long-term stability: water-cooled beam dumps where employed whenever possible to catch any high-power beam (such as

---

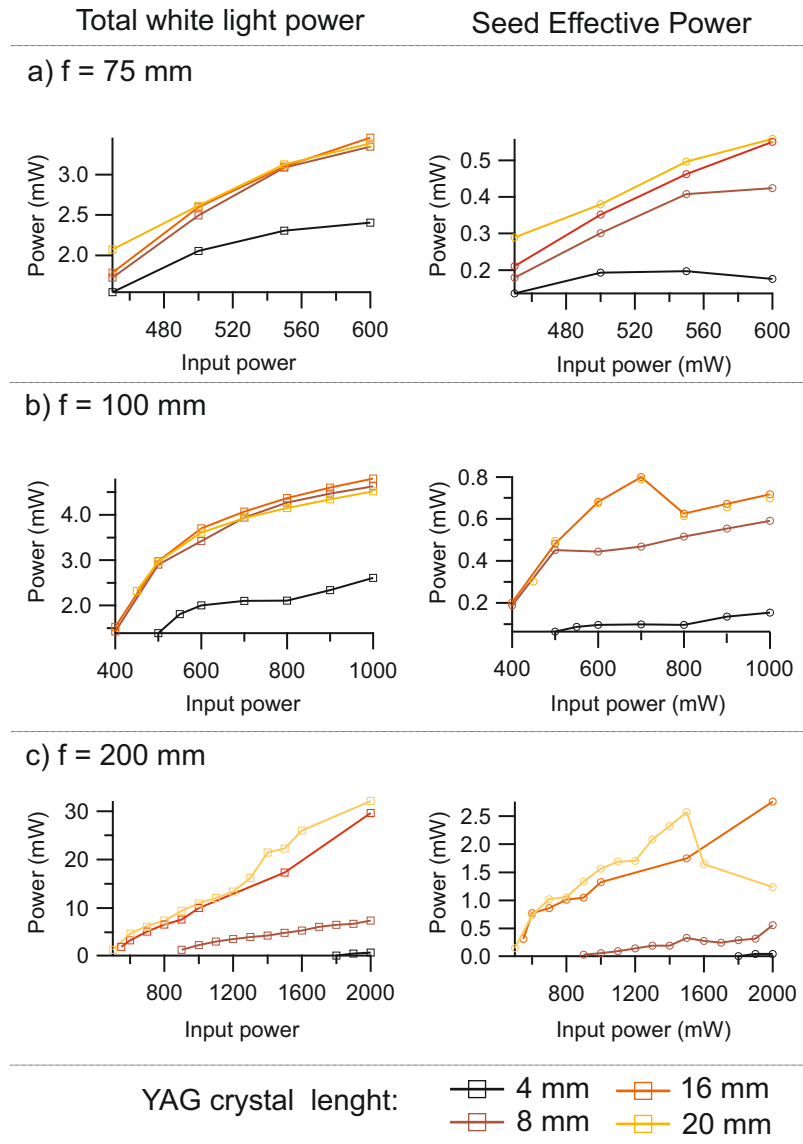16 AMPHOS 200, Amphos, http://www.amphos.de

Figure 40: Systematic measure of white-light total power (left column) and effective seed power (right column) for the focal lengths of 75 mm, 100 mm and 200 mm (line a),b),c) respectively). For every configuration, four different YAG crystals where tested, with thicknesses of 4, 8, 16 and 20 mm.

the depleted pump beams) and any residual reflections from optical components; moreover an active beam stabilization unit was developed to compensate slow drifts of the pointing over time, thereby ensuring optimal overlap between pump and signal in the OPCPA.

The chirp of the seed pulses is about 12.5 ps/nm: this translates into an output pulse duration of about 20 ps after amplification in the innoSlab. Two home-built Tracey compressors [99] were developed for the laser: the first implementation is based on dielectric transmission gratings with 1000 lines/mm[17]. The pulse compression in this case was about 1.25 ps, with a transmission close to 75%. An upgrade was successively installed, employing newly-developed high-reflective dielectric gratings[18] with a measured diffraction efficiency of more than 98% and 1600 lines/mm. This upgrade increased the total transmission to 96%. In this second case, due to a more compact and easy-to-align setup, and possibly thanks to the reduced thermal effects in the compressor, the pulse duration was measured to be as short as 0.7 ps. Up to 190 W were frequency doubled in a 1-mm-thick BBO crystal (the details of the crystal's cut angle are given in table 3) with 55% efficiency, in line with similar results found in literature [177]. The resulting 105 W average power[19], at a wavelength of 515 nm, were used for pumping the OPCPA.

2.7.6 *OPCPA characterization*

Thanks to the high-power white light, optical parametric amplification was performed in a single stage: the overall setup is schematized in figure 34.

The seed and the pump beams are overlapped non-collinearly for achromatic phase matching in a BBO crystal ($\theta = 24.3°$, internal angle 2.4°, Type I). A minimum seed power of 2 mW (0.1 mW in the 800 ± 25 nm spectral region) was necessary to saturate the OPCPA power. The seed was generated in a 20-mm-thick YAG crystal, focusing the compressed output of the fiber laser with a plano-convex lens of 200 mm focal length. The typical seed power was 6.3 mW (1 mW or 2 nJ in the 800 ± 25 nm spectral region): no degradation of the YAG crystal was observed over more than one year of operation. Several tests were performed to find the optimum pump spot size and crystal length. A pump FWHM of 815 μm (4σ diameter = 1340 μm) and 4-mm-thick BBO[20] gave a good compromise between high gain, no detrimental self-focusing effects and long-term stability. The typical lifetime of the crystal is several days of continuous operation, depen-

---

17 LightSmyth Tech.
18 AMO
19 82.5 W were measured with the first compressor in a 2-mm-thick BBO crystal.
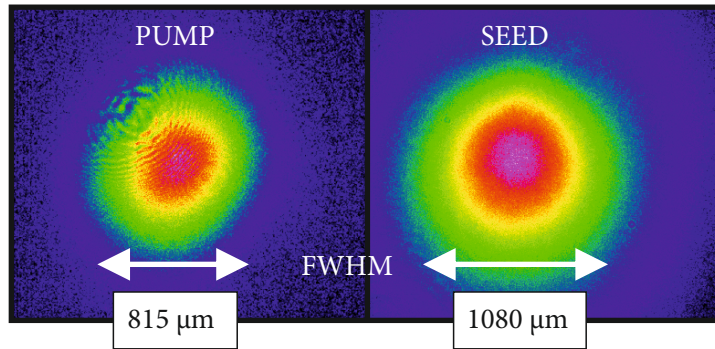20 Dual-line 800/515 nm anti-reflective coating, Castech

Figure 41: Measured FWHM of the pump and seed mode for optimized operation of the OPCPA.

ding largely on the quality of the coating. The intensity in this case[21] is about 35 GW/cm^2. The seed pulses are stretched by transmission through approximately 60 mm fused silica glass: an amplified bandwidth of 145 nm (-10 dBc) was obtained for 1.2-ps-long pump pulses. By improving the compression, the very same settings lead to an amplified bandwidth of about 60 nm (-10 dBc) as illustrated in Figure 42.

The different results are easily explained in a time domain picture: in figure 43, the temporal pulse shape of the spectra of figure 42 was calculated using the Sellmaier equation for the dispersive materials in the beam path, the same calculation was performed for a white light spectrum. The result are compared with two Gaussian pulses with the same time width of the pump. The temporal width of the stretched pulses is in good agreement with the pump duration, illustrating how temporal gating by the pump controls the OPCPA spectrum (Section 2.7).

The spot size of the white light was varied to optimize the conversion efficiency, the optimal white light spot had a FWHM of 1080 μm, the optimum mode ratio was therefore 0.75 seed/pump[22]. An maximum average power output of 28 W was measured for the amplified signal. This corresponds to a pump-to-signal conversion efficiency of 25% in the single-stage OPCPA. A slight change of the phase-matching angle of the BBO is observed with increasing pump power. The phase-matching drift stabilizes within a few minutes and is likely caused by thermal effects. Therefore, the phase-matching angle is finally optimized after thermalization. It was hard to reproduce the maximum power output on a daily basis due to several factors, mainly related to damage of the optical coatings exposed to the 0.515 μm beam; the situation was improved by reducing the power of the

---

21 To achieve the same intensity with the old compressor, a FWHM spot size of 575 μm was adopted [19]

22 For the long pulses the results were pump FWHM 575 μm; seed 650 μm, with a ratio closer to 0.9 [19]
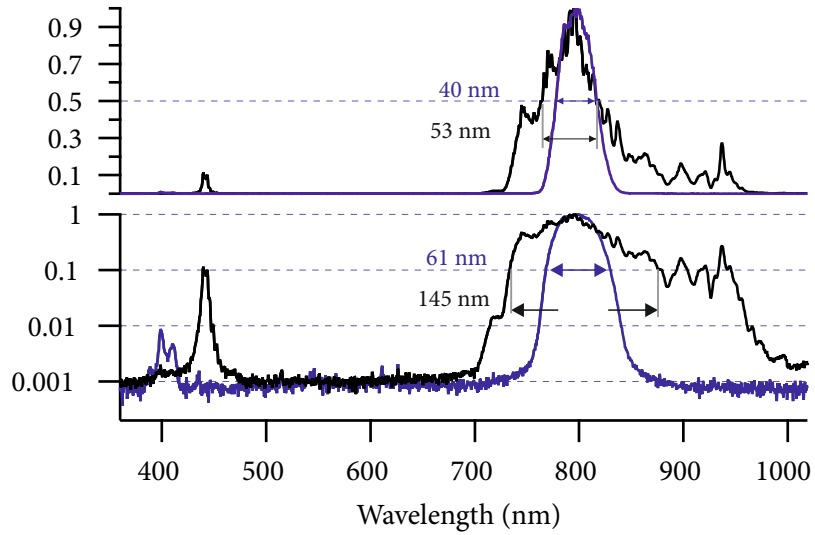
Figure 42: Spectrum of the OPCPA for two pump pulse durations: 1.2 ps (black line) and 0.7 ps (blue line). The upper-plot has a linear intensity scale, normalized to the peak of the spectrum: the indicated width is the FWHM. The lower plot present the same data on a logarithmic scale, used to compute the -10 dBc width. The parasitic second harmonic is resolved at shorter wavelengths.
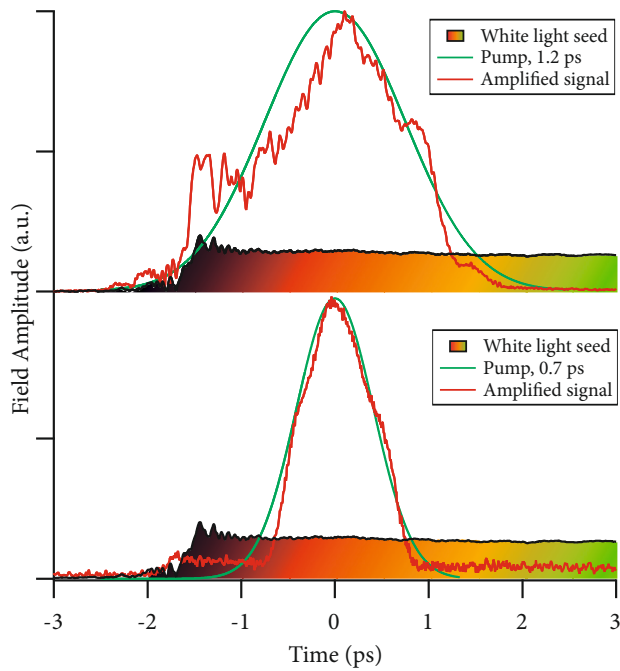

Figure 43: Simulated temporal envelopes of the interacting OPCPA pulses. The amplified signal is plotted in red for a 1.2-ps-long pump pulse (top) and for 0.7 ps (bottom). The pump pulses are represented by Gaussian pulses having the experimental temporal FWHM (gree curves). The white light seed temporal profile is plotted with a rainbow shading.

amplifier to 180 W, which lead to a reproducible power of about 22 W.

A walk-off-compensated configuration was adopted for achieving the best beam quality, the mode profile is shown in figure 44 b); in this configuration a modest parasitic second harmonic was present in the spectrum. In the case of broader bandwidths (black curve in figure 42) the second harmonic was more noticeable due to the stronger components in the longer wavelength side (see section 2.7.3.3): using a dichroic mirror, out of an output of about 18.3 W, 260 mW were measured to be parasitic second harmonic. For the narrower spectrum (blue curve in figure 42) 1% can be considered an upper estimate of parasitic second harmonic. Tangential phase matching was also tested, but resulted in a reduced power output, likely due to lateral walk-off effects in the 4-mm-long crystal.

The beam quality was checked at a central wavelength of 750 nm, for an average power of about 19 W. The near field spot profile is shown in panel b) in figure 44. The beam quality was measured using the $D4\sigma$ method and a calibrated beam profiler[23]. A nearly diffraction-limited quality of $M_x^2 = 1.12$ was obtained in the plane defined by the non-collinear wavevectors of pump and signal waves, in the orthogonal direction the mode quality was $M_y^2 = 1.28$. The measured values agree well with the M^2-value of the pump laser of 1.10 and 1.36 for the x and y directions, respectively [19].

2.7.6.1 *Wavelength tunability and pulse compression*

One of the most attractive features of OPCPAs is the wavelength and bandwidth tunability: the non-collinear phase matching allows broadband phase matching down to about 650 nm for a pump with a wavelength of 515 nm. In Figure 44, the wavelength tunability of the system is reported, in the case of 1.3 ps pump pulses: the output power is above 15 W when tuning the central wavelength in the range 680 nm - 900 nm .

The highest output power of 19.7 W is achieved around 750 nm, close to the seed WLG maximum used for the tuning experiment (shaded gray curve in figure 44). Tuning the system toward the near-infrared increases the bandwidth due to lower material of the fused silica glass stretcher in this spectral range. In order to achieve a comparable bandwidth around 900 nm, an additional 50-mm-long glass block of fused silica was added, which also reduced the average power to 15 W due to the lower seed level. The spectrum was tuned around 790 nm and recompressed to sub-20 fs in a Brewster-cut fused silica prism compressor. Frequency-resolved optical gating [89] (FROG) was used to characterize the compressed pulse duration: this
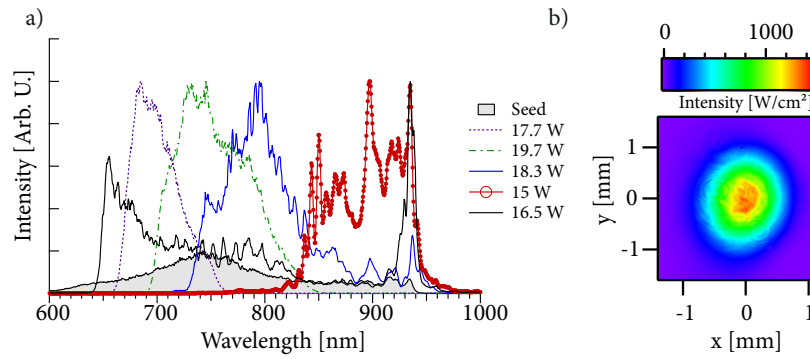
---

23 Spiricon BGS-USB-SP620

Figure 44: a) Spectrum tuning of the OPCPA with a 1.2 ps pump pulse, the average power corresponding to each spectrum is indicated; the seed white light spectrum is the shaded gray area. b) Near-field spot profile, at 790 nm, calibrated in intensity from the measured power.

measurement allows to retrieve the spectral phase of ultrashort pulses, fully characterizing the pulse shape.

An home-built FROG setup was set up in order to measure pulses shorter than 20 fs. The beam was split in two paths using a pellicle beam-splitter to minimize phase distortions; each pulse replica is overlapped in a 25-μm-thick BBO crystal to generate a non-collinear second harmonic. The setup is equipped with metallic mirrors only, ensuring broadband reflectivity and no additional spectral phase. The second harmonic spectrum is measured as function of the replica's delay: the resulting FROG traces are used to retrieve the spectral phase. Pulses as short as 16.8 fs FWHM where measured; the results are shown in Figure 45. Due to the uncompensated higher-order phase, the pulse is approximately 10% longer than the calculated Fourier limit of 15 fs. The final compressed output power is 15 W, at a repetition rate of 500 kHz with a peak power exceeding 1 GW. No thermal effects were observed from the prism compressor. By changing the insertion of the second prism in the compressor, it was possible to obtain pulse durations below 20 fs in the whole wavelength tuning range, besides the red-tuned spectrum at 900 fs, which had a frog trace of 22 fs, likely due the different amount of dispersion in the stretcher. The OPCPA can achieve a comparable output power for broad optical spectra supporting few-cycle pulses: by shortening the FS stretcher to 10 mm, an output with a bandwidth of approximately 300 nm (-10 dBc) at an average power of 16.5 W is demonstrated, as shown in figure 44. The resulting M-shaped spectrum supports a Fourier-limited pulse duration of 5.4 fs. In the case of the narrower-bandwidth spectrum obtained with the 0.7-ps-long pump, a commercial FROG[24] has a sufficient bandwidth to measure the pulse duration.

---

24 Swamp optics, Grenouille 8-20-USB

In this case the results is 30 fs, with a retrieved bandwidth of 39 nm FWHM, in good agreement with the measured spectrum.
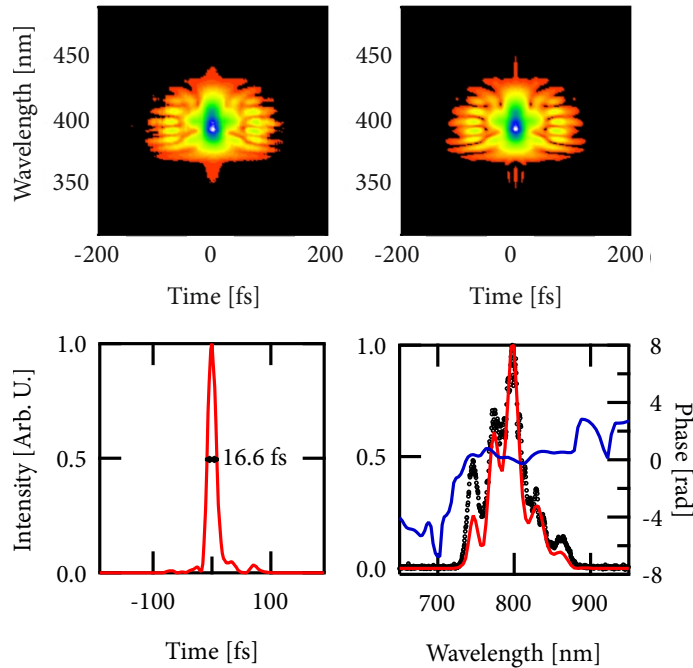

Figure 45: Frequency Resolved Optical Gating (FROG) traces. Top left: measured trace, top right: simulated FROG trace. Bottom left, retrieved temporal envelope with a FWHM of 16.6 fs. Bottom right: retrieved spectrum (red) and spectral phase (blue) compared with the measured spectrum (black dots).

2.7.6.2   *Long term spectral and average power stability*

The overall optical path length for the pump pulses in the slab amplifier and the compressor is less than 10 m: owing to the stability of the InnoSlab design, no active synchronization with the fiber-based seed is necessary. To show this, the long-term average power stability was monitored over a period of 1.5 hours, together with the optical spectrum. The results are shown in Figure 46. For an output of 19 W centered at 730 nm, the average power standard deviation is 0.3%.

The spectrum-centroid standard deviation is on the order of 0.2%. This can be used to give an estimate of the timing jitter between the two arms: figure 47 shows the measured OPCPA output spectrum as a function of the temporal delay. The centroid of the spectrum was extracted for each delay: this follows a linear behavior with a slope of 0.09 nm/fs.

The observed spectral fluctuations imply timing fluctuations between the two arms below 35 fs on average, proving that the adopted hybrid design for OPCPA does not require active synchronization be-
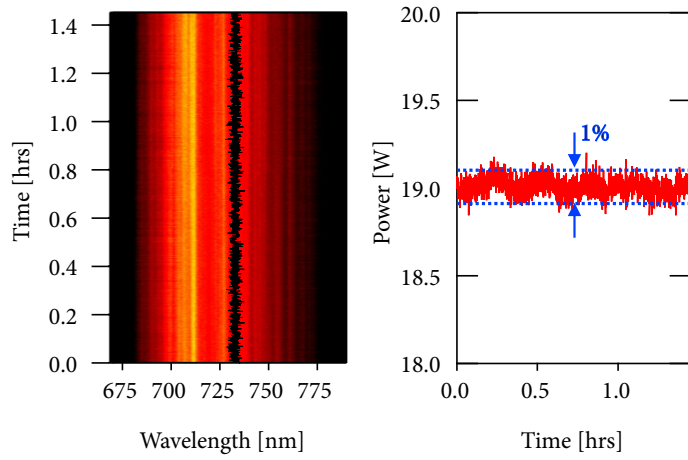
Figure 46: Left: Spectral stability of the OPCPA, tuned to a central wavelength of 730 nm. The black line is the calculated centroid. Right: average power stability as a function of time, the blue dotted lines indicate a 1% relative variation, the calculated standard deviation is 0.3%.

Figure 47: Amplified signal spectrum as a function of pump and seed delay for the OPCPA pumped by a 1.2 ps pump. The centroid is calculated (green dots) and fitted with a line (green line).

tween pump and signal, in contrast with other OPCPA architectures [141].

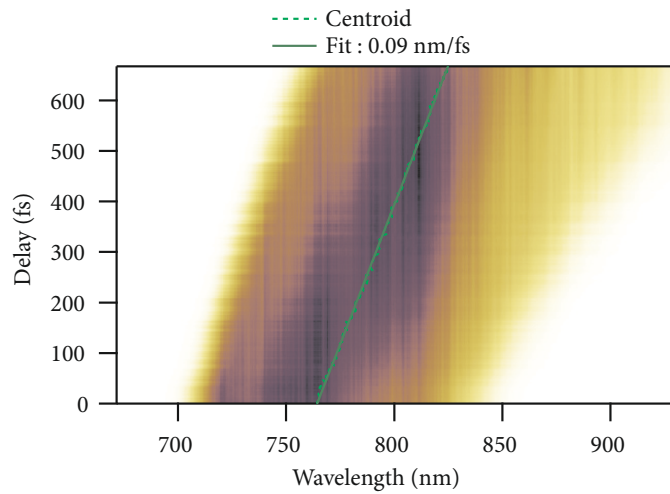### 2.7.6.3 *Conclusions*

In summary, a conceptually-simple high-power OPCPA was demonstrated. The light source is based on optically synchronized Yb-lasers and relies on an hybrid Yb:fiber/innoSlab architecture: the OPCPA is seeded by a broad white light continuum generated from the femtosecond Yb:fiber laser system and pumped by the high-power picosecond Yb:YAG innoSlab amplifier. A pump-to-signal conversion efficiency of 25% is achieved in a single-stage amplifier providing up to 28 W of output power. Long-term power and spectral stabilities are possible, without resorting to active delay stabilization. Sub-20 fs, 30 μJ pulses are obtained with a simple prism compressor. The measured characteristics of the system are suitable for HHG at high repetition rate [12]: this will be the subject of the next chapter, the application of the source to tr-ARPES will be instead demonstrated in the second part of the thesis.

UV-DRIVEN 500 KHZ HIGH-ORDER HARMONIC GENERATION

The femtosecond light source developed in the Chapter 2 can now be put into test for the generation of EUV radiation. In this chapter, a setup for generating and isolating a single harmonic around 21 eV will be presented, preserving a temporal resolution close to 50 fs. The first part of this chapter recap the fundamental theoretical results of HHG (Section 3.1.1), focusing on the problem of optimizing this process with high repetition rate, modest pulse energy and an UV driver wavelength (Section 3.2). These theoretical considerations will be applied to develop the EUV generation setup, which will be described and characterized. In view of the later tr-ARPES experiments, emphasis will be put on the characterization of the single harmonic time-bandwidth properties (Section 3.3). The generated EUV photon flux exceeds 10^{11} photons/s at 500 kHz, with a duration reaching the sub-20 fs regime, ideal for tr-ARPES. The light is delivered to the experimental chamber through a beamline, including diagnostic tools, fundamental for the success of the experiment Section 3.5.

3.1 INTRODUCTION

Powerful femtosecond laser pulses can be tightly focused to very high intensities, creating transient electric fields otherwise not achievable. When the field becomes comparable with the microscopic electrostatic fields in matter, a perturbative description of the interaction fails. To understand if a perturbative expansion of the nonlinear polarization (section 2.2.1, Equation 53) converges, the magnitude of the electric field have to be compared to the relevant microscopic parameters characterizing the system. If one assumes that the light frequency is non-resonant to any quantum transition in the system and disregards bound to free transitions, the ratio between the (k+1)-th and k-th order of the nonlinear polarization can be expressed as [162]:

$$\alpha_{bb} = \frac{\chi^{(k+1)}\mathcal{E}^{k+1}}{\chi^{(k)}\mathcal{E}^{k}} \approx \frac{e\mathcal{E}_0 a_B}{\hbar\Delta}, \tag{82}$$

$\mathcal{E}_0$ is the peak electric field amplitude, e is the electron charge, $\Delta = |\omega_{if} - \omega|$ is the detuning of the laser frequency to the transition between a ground state i to an excited state f. a_B is a generalized Bohr radius for atomic numbers higher than one: $a_B = \hbar/\sqrt{m_e I_p}$. In this expression m_e is the electron mass and I_p is the ionization energy, the minimum transition energy from the least bound state to the conti-

nuum of free states. In order for the series to converge, α_{bb} must be sufficiently small. In the case of transitions to free states, the relevant quantity is the so-called Keldysh parameter γ [162], defined as:

$$\alpha_{bf} = \frac{1}{\gamma} = \frac{e\mathcal{E}_0}{\omega\sqrt{2m_e I_p}} \approx \frac{e\mathcal{E}_0 a_B}{\hbar\omega}. \tag{83}$$

If both $\alpha_{bf} \ll 1$ and $\alpha_{bb} \ll 1$ the perturbative approach used in the previous chapter is valid. In practice, this starts to fail for typical intensities on the order of 10^{13} W/cm^2: above this threshold, the contributions of multi-photon processes of different orders start to violate the I^k intensity scaling law. In this regime, the Coulomb field of light is comparable to the nuclear attraction for the least bound electrons: as a result, ionization by field tunneling become relevant. The electrons, stripped from their parent atom, are driven by the field and produce a non-negligible nonlinear polarization. Among several phenomena arising in this high-field environment, the most important in the context of this work is *high harmonic generation*. HHG is a characteristic radiation produced by field-ionized electrons re-colliding with their parent atoms.

3.1.1 *High-harmonic generation*

High harmonic generation (HHG) was first observed at the end of the eighties, studying the nonlinear interaction of noble gases with newly developed high power pulses from picosecond to sub-picosecond lasers [64, 65]. At high intensities, short-wavelength radiation is generated, corresponding to odd-orders of the driving laser's frequency. Most strikingly, such harmonics do not obey an intensity scaling with order k of the form I^k: instead, the harmonics form a *plateau* of nearly constant conversion efficiency, until a *cutoff energy* is reached. It was immediately realized that such a radiation could be readily applied as a coherent table-top source for scientific applications, in particular for photoelectron spectroscopies [178]. Figure 48 illustrates a prototypical HHG spectrum: a set of equally spaced peaks extends well into the EUV spectral range and terminates in a continuum-like cutoff region.

The harmonics are temporally synchronized to the laser, they are therefore suited for time-domain pump and probe photoemission experiments, provided that a single harmonic can be isolated from the plateau. As the field progressed, an important characteristic of HHG became apparent: the radiation is not produced continuously during the laser pulse envelope but possess time structures appearing with an half-light cycle periodicity. This is reflected in the frequency domain by a 2ω harmonic-spacing. These sub-cycle light bursts are to-date some of the shortest light pulses that can be artificially produced and their isolation and use as a spectroscopic tool is the goal of *attose-*
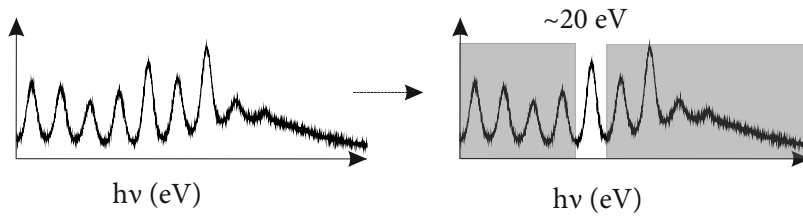
Figure 48: A prototypical high-harmonic spectrum, showing Plateau harmonics and a cutoff region. The spectral selection for a HHG-based tr-ARPES experiment selects a single harmonic of the Plateau, here at $\approx$ 20 eV.

cond science [32]. Not long after the first observation of HHG, a simplified picture, the *three-step-model* succeeded in capturing the main features of the process [179]. Shortly after, Lewenstein introduced a model [180] following the same spirit, but based on formally more correct theoretical grounds. The model provided better quantitative agreement with non-approximated solutions of the time-dependent Schrödinger equation.

The next sections are devoted to describe the basic physic of HHG. Particular attention will be devoted in highlighting the differences arising when HHG is driven by the fundamental ω and generates an harmonic $q\omega$, compared with the situation where the driver is a UV beam of frequency 2ω and generates an harmonic at a comparable energy $\approx (q/2)2\omega$, the comparison is not possible at the exact same harmonic energy as in inversion-symmetric media only odd harmonics are generated.

3.1.2 *The three step model of high-harmonic generation*

The *three-step-model* (also known as *simple man's picture*) divide HHG in an optical-field-induced ionization step, followed by an energy gain of the electron in vacuum under the action of the electric field and finally a recombination step, where the electron recombines with the parent atom, releasing its excess energy through the emission of a EUV photon (Figure 49).

For the simple case of noble gases, the calculation of the ionization rate in the first step can be performed with good accuracy using analytical models. If the Keldysh parameter $\gamma < 1$, the dominant ionization mechanism is optical-field ionization. The instantaneous ionization rate can be calculated as a function of time using the so-called Ammosov-Delone-Kane (ADK) model [181]. As γ approaches unit, also multi-photon ionization processes contribute to the total rate: an alternative model, based on the theory of Yudin and Ivanov [182] and known as *adiabatic ionization model*, is better suited in this case. In the three-step model, while the ionization probability is derived from quantum mechanics, the quivering motion in the electric
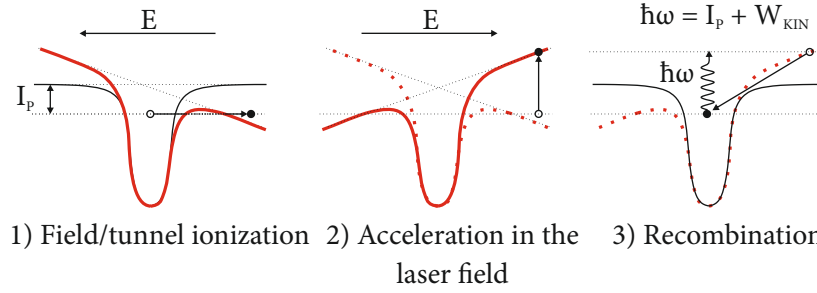
$$\hbar\omega = I_P + W_{KIN}$$

1) Field/tunnel ionization   2) Acceleration in the   3) Recombination
laser field

Figure 49: The three step model: $\vec{E}$ electric field, I_p ionization potential, W_{KIN} ponderomotive electron energy. The black line represents the unperturbed atomic potential as a function of position, the red line is the potential modulated by the strong field. A photon of energy $\hbar\omega$ is generated in the recombination step.

field is described in a fully classical way and neglects the field of the parent atom all-together. For linear polarization, the problem is one dimensional and it is easy to compute the electron's trajectories as function of the phase of the field at the time of ionization, here seen as an instantaneous process [32].

Part of the electrons does not return to the atom and continue its motion in the continuum after the light field ceases, however, some trajectories return at the origin: these are the electrons which might recombine with the atom releasing high-harmonic radiation. This is illustrated in the upper panel of figure 50: depending on the time of ionization, the electrons follows different paths x(t), interacting with the light field $E_L(t)$. The field ionization probability, also indicated in the figure, is maximum at the peak of the electric field amplitude, where most of the electrons are liberated, and quickly decreases away from the turning points. The kinetic energy can be computed as a function of the arrival time: this is expressed in units of the *ponderomotive* energy U_p defined in equation 84 and plotted in the lower panel of figure 50. In the third step of the model, the electrons recombine with the atom emitting photons of energy $\hbar\omega = W_{kin} + I_p$, given by the sum of the ionization potential I_p and the kinetic energy W_{kin}.

$$U_p = \frac{e^2 \mathcal{E}_0^2}{4m\omega^2} \tag{84}$$

The maximum kinetic energy is obtained by electrons traveling for slightly less than a cycle in the field: this trajectory defines the cutoff energy, expressed in equation 85:

$$E_{cut} \approx I_p + 3.2 U_p \tag{85}$$

Electrons arriving before or after this time have a lower energy and their trajectories are respectively called *short* or *long*: for every energy
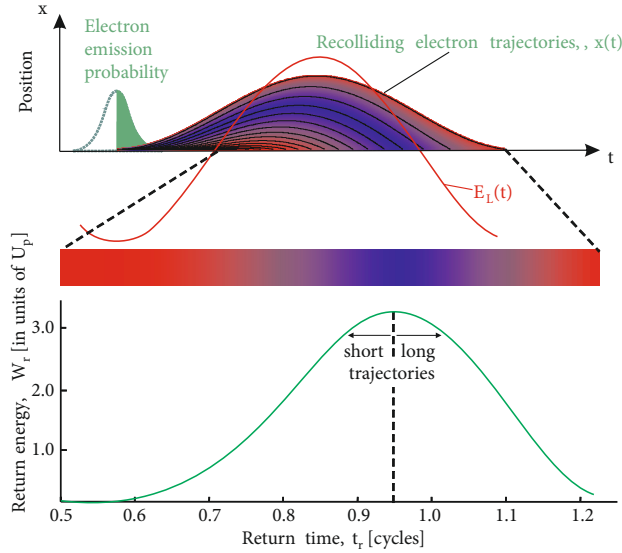
Figure 50: Top: the re-colliding electron trajectories, as function of the electric field $E_L(t)$ phase. The ionization probability (in green) is maximum at the pulse peak. Bottom: the trajectories return energy as a function of return time in units of the optical cycle. The trajectories are classified in long and short, depending if their return time is longer or shorter than the trajectory producing the maximum energy. Adapted from reference [32].

in the harmonic spectrum, except at the cutoff, there are contributions from both long and short trajectories.

The cutoff energy is proportional to the ponderomotive energy U_p: in order to extend the cutoff, either a higher laser intensity has to be achieved ($I \propto \mathcal{E}^2$) or the frequency ω has to be reduced. It is indeed true that the soft X-rays energy range can be reached by focusing mid-infrared ultrashort laser to high intensities in the lightest noble gases (He, Ne) [183]. In most of the experiments where the generation of a high photon flux is the main goal, noble gases are chosen because they can sustain high intensities before the medium is completely ionized: a condition preventing good conversion efficiency, as will be shown in section 3.2.

The presence of peaks in the spectrum at the odd harmonic frequencies has the following intuitive explanation: every half-cycle of the driving field the three-step process repeats, leading to T/2 periodicity (T is the light period). The frequency components at twice the driving frequency 2ω constructively interfere giving rise to peaks in the frequency domain. This is the analogue of the optical frequency comb produced by the pulse train of a mode-locked laser oscillator, just now the pulses have durations in the attosecond range (harmonics are emitted during a fraction of T/2, which is ≈ 1.3 fs at 0.8 μm) and the periodicity is half a cycle.

The process is illustrated in figure 51: from basic consideration of Fourier analysis [85], the bandwidth of an harmonic is inversely proportional to the number of half-cycles contributing to it. If the fun-
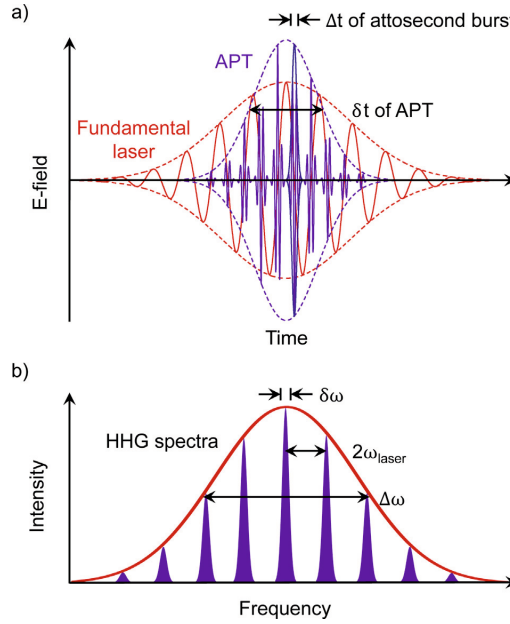

Figure 51: a) Red trace, temporal envelope and oscillation of the fundamental laser. Purple trace, attosecond pulse train (APT) produced during HHG. b) Frequency domain picture: the HHG spectrum has an overall bandwidth $\Delta\omega$ inversely proportional to the time width Δt of the attosecond burst, the harmonics are spaced by $2\omega_{laser}$ and the single harmonic bandwidth $\delta\omega$ is inversely proportional to the APT total duration δt. From reference [85]

damental frequency increases, for the same peak intensity, more half-cycles contribute to the same harmonic, one therefore expects narrower linewidths. This effect was experimentally verified [85, 13] and is of great interest for photoelectron spectroscopy.

A more accurate treatment of HHG is based on the so-called Lewenstein model [180], which approximate the solution of the Schrödinger equation using the *strong-field approximation*, valid when the Keldysh parameter is considerably lower than unity. The Keldysh parameters can be written in term of the ponderomotive energy as:

$$\gamma = \sqrt{\frac{I_p}{2U_p}}. \tag{86}$$

A thorough description of the Lewenstein model and the strong-field approximation will not be presented here (see for example [92]). Simulations based on the Lewenstein model can provide quantitative agreement with the time-dependent Schrödinger equation if $\gamma \ll 1$;

the results improve for photon energies much higher than I_p, as the model neglects the Coulomb force exerted by the left-over atom.

It can be anticipated here that neither assumption is well justified for the parameters used in our experiments, nonetheless the model provide some useful insights in the underlying physics. In a quantum-mechanical description, the harmonic emission is generated by the fast interference between the ground state wavefunction and the wavefunction of the electron liberated in the continuum. Following Lewenstein original treatment [180] the dipole moment can be written in atomic units as:

$$x(t) = i \int_0^t \int d^3\mathbf{p}\, \mathcal{E}cos(t')d_q(\mathbf{p} - \mathbf{A}(t')),$$
$$\times\, d_q^*(\mathbf{p} - \mathbf{A}(t))exp[iS(\mathbf{p}, t, t')], \quad (87)$$

here, $\mathbf{A} = (Ecos(t), 0, 0)$ is the vector potential, p the canonical momentum and q represent the harmonic order. The phase S in the integral is the so-called action integral, defined as:

$$S(\mathbf{p}, t, t') = \int_{t'}^t dt'' \left(\frac{[\mathbf{p} - \mathbf{A}(t'')]^2}{2} + I_p \right). \quad (88)$$

Within this model, it is shown how the main contribution to the action integral are given by the classical trajectories of figure 50, linking the classical picture to the quantum one. An important results provided by the quantum-mechanical picture is that every harmonic acquires a certain phase relative to the electric field, which has to be accounted for, when computing the macroscopic phase-matching properties in the generating medium (section 3.2). The phase of the contribution to the j-th trajectory to the q-th harmonic, can be written as [184]:

$$\phi_j^q = q\omega t' - S(\mathbf{p}, t, t'). \quad (89)$$

This *single-atom* phase is order- and trajectory-dependent: its influence on the phase-matching gives an experimental access to these degrees of freedom, allowing to reinforce selectively spectral components arising from the different trajectories. The intensity scaling for the phase of a given trajectory leads to different far-field properties in the generated harmonic beam: the short trajectories tend to produce better spatial beam quality, more suited for applications [185].

The liberated electron's wave packed experiences quantum diffusion: this is reflected in a reduced dipole amplitude for longer propagation times of the electron in the continuum [180]. Intuitively, this can be understood as a reduced overlap between the ground state and the unbound electron. The practical consequence of this is that the efficiency of HHG increases for a driving field with a shorter pe-

riod. The scaling of efficiency with wavelength was determined to be[1]
[186]:

$$\eta \propto \lambda^{-6.9\pm0.2} \quad \text{NIR, } 0.8 < \lambda < 2.0 \ \mu\text{m} \tag{90}$$

$$\eta \propto \lambda^{-4.7\pm1.0} \quad \text{VIS, } 0.5 < \lambda < 0.8 \ \mu\text{m}. \tag{91}$$

The single atom dipole described is the fundamental source of harmonic radiation, however efficient formation of an EUV beam can only occur if a large number of such dipoles radiate coherently from a macroscopic gas volume within the laser beam. The next section explains the basic physics of such *phase-matching* problem.

3.2 THE PHASE MATCHING PROBLEM FOR HIGH-HARMONIC GENERATION

To obtain an observable macroscopic polarization, the radiation of single atomic dipoles has to add in phase over a sizable volume of the illuminated gas. For this to occur, the driving laser and the harmonic have to be in phase ($\Delta k = 0$) for an extended length: this is the very same principle which allowed high conversion efficiencies for three-wave mixing processes in birefringent non-linear crystals (chapter 2). The situation is however more complex in the case of high-harmonic generation in gases. The harmonics have the same polarization of the driving light and the noble gas itself is isotropic, hence critical phase matching (section 2.4) is impossible. Following the derivation of reference [187, 188, 13], here for simplicity limited to on-axis emission, it is possible to calculate the number of photons in the q-th harmonic produced by a specific trajectory as:

$$N_q \propto \eta(q, \lambda)\xi(q, P) = \eta(q, \lambda) \int_{-\infty}^{+\infty} dt \times$$

$$| \int_{-z_{min}}^{+z_{max}} \sqrt{w(z,t)}\rho(P)(1 - p(z,t)) \times$$

$$exp[-\alpha_q(z)]exp[iz\Delta k_q(z,t)]dz|^2, \quad (92)$$

the factor $\eta(q, \lambda)$ is related to the single dipole response for the particular trajectory and for the driver wavelength: the microscopic recombination probability is contained in this factor, whereas the effect of the extended medium are all separated in the integral $\xi(q, P)$.

The laser beam can be described as a spatio-temporal Gaussian beam, incident on an uniform gaseous region of length L_{med} of density $\rho(P)$ at a pressure P. The integration is performed across the gas region in the range z_{min} to z_{max}, as illustrated in figure 52. The on-axis

---

[1] the efficiency scaling was determined by changing the wavelength while keeping the same peak intensity and the same number of light cycles
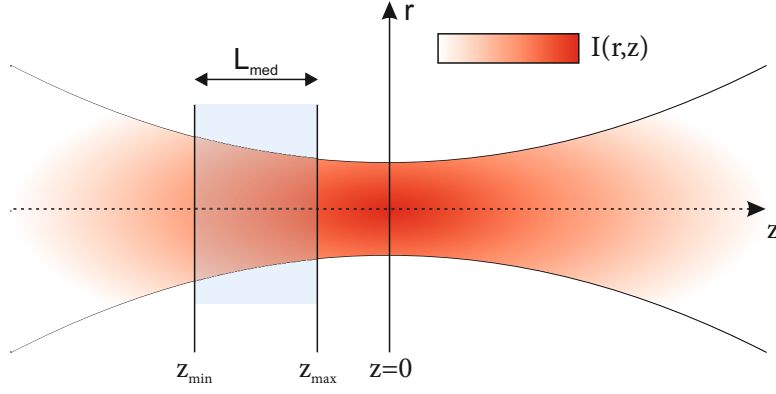
Figure 52: Definition of the HHG focusing geometry for a Gaussian beam with waist at z=0. The gas occupies an uniform region of length L_{med}, between z_{min} and z_{max}.

intensity of the beam can be expressed as:

$$I(z,t) = \frac{I_0}{1+(z/z_R)^2} exp[-4ln2(t/\tau)^2].$$ (93)

The function $w(z,t)$ is the strong-field ionization rate, which can be calculated according to the first step of the model in section 3.1.2. The rate w is completely determined by the function $I(z,t)$: the ionization probability is easily computed as [92]:

$$p(z,t) = 1 - exp\left[-\int_{-\infty}^{t} w(z,t)dt\right].$$ (94)

The presence of the factor $(1 - p(z,t))$ in Equation 92 accounts for the depletion of the ground state which might occur when the ionization is progressively higher. The last terms in the integral represent the re-absorption of the q-th harmonic and the phase mismatch between the driver and the EUV beam. The harmonics energy exceeds the photoionization energy, this means that the medium itself is not transparent and re-absorption limits the maximum signal build-up. Assuming that the harmonic energy is below the ionization energy of the single-ionized atoms produced in the process[2], re-absorption can be written as:

$$\alpha_q(z) = \int_z^{z_{max}} \frac{(1-p(z,t))}{2\sigma_q\rho(P)}dz = \int_z^{z_{max}} \frac{(1-p(z,t))}{2L_{abs}}dz.$$ (95)

In equation 95 the absorption cross-section for the harmonic is σ_q. Finally, the term $exp[iz\Delta k_q(z,t)]$ describes the phase matching between the fundamental radiation at frequency ω and the harmonic $q\omega$. The wavevector mismatch $\Delta k_q = k(q\omega) - qk(\omega)$ has four contributions to

---

2 this derivation neglects the effect of HHG from ionized species, which can in some condition have important contributions [189]

the total phase that must be considered for phase matching. All these terms vary as a function of position and time.

3.2.1 *The single atom phase*

The single-atom phase Δk_a comes from the quantum phase collected during the particular trajectory considered. Besides the field ionization rate w, it is the only non-classical term in the phase matching integral $\xi(q, P)$ and depends in principle on the solution of the TDSE. Luckily, the atomic phase scales linearly with intensity for plateau harmonics [184] as $\phi_j^q = -\alpha_q I$, with the constant $\alpha_q > 0$; the corresponding wavevector mismatch $\Delta k_n = \partial \phi_j^q / \partial z$ can be obtained inserting the term $I(z, t)$ given by eq. 93 [13]:

$$\Delta k_a = \alpha_q \frac{2z}{z_R^2} \frac{1}{1 + (z/z_R)^2} I(z, t). \tag{96}$$

The coefficient α_q can be calculated once for all for the trajectory of interest, avoiding a time-consuming calculation at every step. The atomic mismatch vanishes at the beam focus (z=0), where both trajectories contribute. The coefficient α_q is remarkably larger for the long trajectories: this translates into larger spatial phase modulations across the generation medium. As a result, the far-field properties of the long trajectories are typically worse, leading in stronger divergence of the EUV: to enhance or decrease the relative contribution of the different trajectories is therefore possible to use an aperture to clip the beam. The magnitude of the coefficient α_q increases linearly with harmonic order q, which should be considered when the generation of similar photon energies by different driving wavelengths is compared: the order $q \approx 1/2$ when driving HHG with the second harmonic.

3.2.2 *The neutral medium dispersion*

In the neutral gas the refractive index is different for the driver and for the q-th harmonic, the medium dispersion contributes to the phase mismatch as:

$$\Delta k_n(P) = \frac{q\omega}{c} [n(q\omega, P) - n(\omega, P)]. \tag{97}$$

This phase term can be controlled by changing the pressure in the interaction region: this is one of the most important experimental parameters which can be controlled to achieve phase matching. The

complex refractive index $\tilde{n}$ is related to the medium density ρ and polarizability α through the Lorentz-Lorenz relation:

$$\tilde{n} = n + ik \tag{98}$$

$$\frac{\tilde{n}^2 - 1}{\tilde{n}^2 + 2} = \frac{4\pi}{3}\rho\alpha \tag{99}$$

$$\tilde{n}(\omega) \approx 1 + \pi\rho\alpha \qquad \text{Fundamental} \tag{100}$$

The third relation holds for the driver frequency, and assumes weak polarizability and negligible absorption. The refractive index in the visible range for Argon, the gas used in this work, can be found using the Sellmaier equations of reference [190], whereas for the EUV range, theoretical data from reference [191] can be used to calculate n, starting from $\alpha(q\omega)$. In the EUV range the real part of the refractive index is $n \lesssim 1$, making the overall contribution of the neutral atoms to the mismatch negative.

3.2.3 *The plasma dispersion*

Not all the electron trajectories return with the parent atom and most of the electrons reaching the parent atom don't recombine: the residual ionization of the medium plays a fundamental role in phase matching because free carriers have a different refractive index compared to the neutral medium. The electron-ion plasma do not recombine within the ultrafast duration of the pulse (recombination occur in the nanosecond range): after ionization the plasma density can be approximated as constant on a femtosecond range. The dielectric constant of a free-electron plasma can be written as:

$$\epsilon(\omega) = 1 - \frac{\omega_P^2}{\omega^2} \tag{101}$$

$$\omega_P = \sqrt{\frac{\rho_e e^2}{\epsilon_0 m_e}}, \tag{102}$$

where ω_P denotes the plasma frequency. Overall, the ionized gas results in the following phase mismatch:

$$\Delta k_p \approx \frac{q\omega}{c}\frac{\rho(P)\omega_P}{2\omega^2}\left(1 - \frac{1}{q^2}.\right) \tag{103}$$

Where the approximate expression holds when the frequency $\omega \gg \omega_P$. The plasma-induced mismatch is positive and quickly becomes the dominant term for higher ionization fractions. As it is apparent from the expression 103, the absolute plasma mismatch tends to decrease with the order q, meaning that it is easier to compensate for the ionization-induced mismatch using an UV-driver.

Table 5: The sign of the different Δk contributions, the relative refractive indexes and phase velocities.

Phase	Δk	Refractive index	Phase velocities
Atomic	positive, z>0 negative, z<0		
Neutral	Negative	$n(\omega) > 1 > n(q\omega)$	$c(\omega) < c(q\omega) < 1$
Plasma	Positive	$n(\omega) < n(q\omega) < 1$	$c(\omega) > c(q\omega) < 1$
Geometric	Positive		

3.2.4 *The geometric phase*

To reach high intensities, the beam is often tightly focused: the additional phase of a Gaussian beam, relative to the simpler plane-wave case, becomes important in this geometry. The mismatch due to the so-called Gouy phase is:

$$\Delta k_g = \frac{q}{z_R}\frac{1}{1 + (z/z_R)^2}. \tag{104}$$

For a given harmonic energy, the geometrical mismatch decreases with the driver wavelength because the order q is reduced.

3.2.5 *The total wavevector mismatch*

The resulting total phase mismatch is given by the sum of the previous terms, weighted by the ionization probability:

$$\Delta k = \Delta k_a + (1 - p(z,t))\Delta k_n + p(z,t)\Delta k_p + \Delta k_g \tag{105}$$

The phase-matching condition $\Delta k(z,t) = 0$ is time and space dependent, strongly changing with the ionization of the medium. Moreover, phase matching is order-dependent: the relative weight of the harmonics originating from a single dipole changes in the observable macroscopic HHG spectrum. It is generally not possible to achieve a perfect phase matching across all the interaction volume and for the whole pulse duration. The flux is optimized when $\Delta k(z,t) \approx 0$ over the widest volume of gas and for the longest fraction of pulse possible. The relative signs of the different contributions are summarized in table 5.

A realistic analysis of the phase matching in the general case can only be performed numerically, but some general guidelines can be deduced from the signs of the different components. In the beam focus the atomic dipole phase is zero; assuming that the geometric phase can be neglected (loose focusing), only the plasma and neutral dispersion contribute. The two have always opposite signs: to maxi-

mize the flux for a given ionization level, the gas pressure must be increased. Phase matching is achievable only below a certain critical ionization probability p_{cr} [12, 192].

To produce a certain harmonic, the intensity has to be higher than the cutoff intensity. For high harmonic orders, this condition might be attained only close to the maximum of the electric field envelope. If the ionization by the leading edge of the pulse exceeds already the critical point, it is not possible to phase-match the high order harmonic. This is especially challenging when trying to create photon energies in the soft X-ray regime. A possible solution in this respect is to use longer driver wavelengths [193], for which the ionization rate is lower [182] and the ponderomotive energy higher. A second possible route is to employ light pulses of only few cycles [194]: in this case, the peak of the intensity is reached when the leading edge has not ionized the medium significantly.

To asses the spatial extend of phase matching is common to introduce the *coherence length* $L_{coh} = \pi/\Delta k$, which is the distance over which a phase slip of π has accumulated. As the generating medium absorbs the radiation, a natural question is whether an optimum target size exists for a given coherence length and absorption length L_{abs} (defined in eq. 95). The analysis of Constant et al. [187] reveals that the optimization conditions for eq. 92 of the generating medium obeys the following relations:

$$L_{med} > 3L_{abs} \tag{106}$$

$$L_{coh} > 5L_{abs} \tag{107}$$

3.2.6 *Phase matching in the tight focusing regime*

When a small laser spot has to be used to achieve high intensities, the presence of the geometric phase makes phase matching more difficult: the additional phase has to be compensated by an increased pressure. By moving away from the target, the geometric wavevector mismatch tends to decrease, the atomic dipole phase becomes however different from zero and might improve (worsen) the phase matching, depending if the target is moved before (after) the focus.

In the pursue of high repetition rates, the efficiency scaling of HHG in *tight-focusing* regime was studied extensively [195, 192, 12]. The main result of the analysis is that the efficiency of HHG is invariant in term of scaling of the focusing geometry, provided that the other generation parameters are scaled using certain scaling rules (listed in table 6).

According to these scaling laws, the same efficiency η can be reached with a smaller spot size $w_0' = sw_0$, with $s < 1$. To do so, the pulse energy has to be reduced by a factor s^2, the gas target has to be shrunk and the pressure must be increased ($L_{med}' = L_{med}s^2$ and

Table 6: Coordinate scaling rules for invariant high harmonic generation.

Coordinate	
Scaling factor	$s = w_0'/w_0$
Longitudinal z	$z' = z^2$
Transversal x	$x' = xs$
Transversal y	$y' = ys$

Quantity:		
Wavelenght	$\lambda' =$	λ
Pulse duration	$\tau' =$	τ
Intensity	$I'(x',y',z') =$	$I(x,y,z)$
Medium Length	$L'_{med} =$	$L_{med}s^2$
Medium diameter	$d' =$	ds
Pressure	$P =$	Ps^{-2}
Pulse energy	$\epsilon'_p =$	$\epsilon_p s^2$
Harmonic energy	$\epsilon'_q =$	$\epsilon_q s^2$
Efficiency	$\eta' =$	η

$p' = ps^{-2}$ respectively). In this way the intensity is kept constant and the exact same phase-matching conditions are reproduced. The main challenge when trying to achieve efficient HHG in a tight focusing geometry is to engineer a gas target which can provide high pressures in small volumes, at the same time the target has to be combined with a vacuum environment.

3.2.7 *Plasma defocussing*

Another important effect comes into play when the ionization becomes considerable: plasma defocussing. The radial variation of intensity translates into a non-uniform ionization which defocus the beam. This in turn acts on intensity and phase along the propagation direction, affecting the geometric phase by changing the beam's diffraction.

Indirectly, all the other terms are affected by the different ionization rate, due to modified intensity. The wave equation should be solved numerically adding a defocussing term induced by the field ionization rate [188]; the calculated phase and ionization can then be used in equation 92. The scaling analysis of reference [192] reveals that the limiting factors in HHG conversion efficiency, such as plasma defocussing and gas re-absorption, are also scale-invariant, therefore, besides technical limitations, there is no theoretical hint that a tight-

focusing geometry is intrinsically less efficient than a loose-focusing one.

3.2.8 *HHG using a 2ω driver*

The conversion efficiency of a femtosecond NIR pulses to the UV via second harmonic generation can be very efficient ($\eta_{SHG} \gtrsim 0.3$). In this respect, it is interesting to compare the closest high-harmonics produced by the fundamental $\omega_F = \omega$ with the one produced by the second harmonic $\omega'_F = 2\omega$.

The energy of p-th harmonic in SH-driven HHG is similar to the q-th harmonic of the fundamental, if the condition $p = q/2 \pm 1$ is met, where p and q are odd numbers. There are several benefits of using a second harmonic driver (SH-HHG) which can be summarized as follow:

- Wavelength scaling of the HHG efficiency: from Equation 91, $\eta_{HHG} \propto \lambda^{-4.7 \pm 1.0}$, this represents a factor ≈ 26 for a wavelength of 800 nm.

- Lower q order:
    - reduced geometric phase mismatch (Equation 104)
    - reduced plasma mismatch (Equation 103)
    - more cycles may contribute to the generated signal for similar phase matching conditions, resulting in narrower linewidths as discussed in Section 3.1.2
    - the spacing between neighboring harmonics scales as $2\omega_F$, therefore for SH-HHG the harmonic are twice more spaced. This is an advantage when trying to monochromatize the source (Section 3.4.2)

Improved generation efficiencies for low harmonics (p=7, q=13,15) where demonstrated in reference [13]. The reported conversion efficiency at 0.4 μm is on the order of 5×10^{-5}, which represents nearly a two-order-of-magnitude increase compared to the fundamental. Simultaneously, the generated harmonics indeed exhibit a narrower bandwidth, well below 100 meV for a ≈ 75 fs pulses with 3 nm bandwidth, centered at 390 nm.

In our experiments, both HHG with the fundamental and the second harmonic of the OPCPA were tested. The performance of UV-driven HHG was better and SH-HHG was finally adopted for the tr-ARPES experiments.

3.2.9 *Noble gas choice*

The most important properties of the generating medium are the ionization potential I_p and the intrinsic efficiency for generating an

Table 7: Ionization potential and static dipole polarizabilities for the noble gases, the ionization potential is expressed in eV, the polarizability unit is $[1.6488 \times 10^{-41} \, Cm^2/V]$ from [196]

	He	Ne	Ar	Kr	Xe
I_p	24.6	21.6	15.8	14	12.1
α_{dip}	1.38	2.67	11.1	16.8	26.7

atomic dipole d_{at} which radiates the harmonic. As a rough rule-of-thumb, the static polarizability α_{dip} can be used to compare the different gases. The properties of the relevant noble gases are summarized in Table 7.

Generally the lighter gases are preferred when generating high photon energies because for a given intensity it is harder to ionize them. Since this work will concentrate on the generation of a low energy harmonic at $\approx$ 22 eV, He will not be considered because this photon energy lies below the ionization threshold. The heavier noble gases Xe and Kr have a higher polarizability α_{dip}, but in practice their high cost demands the use of a gas recycling system [60] for long-term operation. Ne, Ar, Kr where tested (Section 3.4.3) and finally Argon was adopted.

3.3 HIGH-HARMONIC AT HIGH REPETITION RATES

The global optimization of HHG flux can be performed by solving equation 92 over a large set of parameters. Here, a more empirical approach was followed, starting from literature results and from the measured OPCPA parameters, several configuration were tested and a setup capable of achieving fully phase-matched high harmonic generation was developed. The pulse energy of the system, in the tens of μJ, outperforms conventional Ti:Sapphire systems by roughly a factor ten in the range of several 100 kHz, however, it is still very modest compared to the mJ-class femtosecond amplifiers for which loose-focusing geometry in employed. The goal is to select and isolate an harmonic around 20 eV: the minimum intensity which have to be reached can be calculated starting from the cutoff law [197].

$$I_t(q) = \frac{2m\omega^2 c\epsilon_0}{e^2} \frac{q\hbar\omega - I_p}{3.17} \tag{108}$$

$$I_0 = \frac{\pi}{2\tau\lambda^2} \frac{E_f}{f_\sharp^2} \tag{109}$$

The parameters for the OPCPA considered in the following sections are summarized in table 8. The threshold intensity and f-number for an order $q = 7$ for SH-HHG and $q = 15$ for the fundamental ($\approx$ 20 eV), are compared using equation 109.

Table 8: Typical laser parameters used for the HHG experiments: λ wavelength (nm) , E energy (eV), ΔE energy FWHM (meV), τ FWHM pulse duration (fs), ϵ_p pulse energy (μJ)

λ (nm)	E (eV)	τ (fs)	ϵ_p (μJ)	$I_t(q)$ ($10^{14} \times W/cm^2$)	$f_\sharp$
800	1.55	30	30	0.393	79
400	3.10	30	10	1.24	51

Assuming a beam diameter $2w_0 = 5$ mm, the equations imply that the focal length should be $f \lesssim 400$ mm for 800 nm and $f \lesssim 260$ mm for 400 nm. In a more realistic case, the beam is not diffraction-limited, and non-compensated dispersion might lead to pulse lengthening, which reduces the intensity. Moreover, good efficiency and narrow bandwidths require the contributions of several light cycles: these two extreme values shows that the expected focal lengths lie well below 500 mm, a typical number for loosely-focused mJ-class Ti:Sapphire amplifiers [79].

In the past years, many high-repetition-rate HHG experiments have been presented, based both on Ti:Sapphire systems and on new Ytterbium lasers. The last part of the section summarizes some of the most important results in the literature.

The highest repetition rates for a Ti:Sapphire-based system where reported by Chiang et al. in reference [87]: here MHz-level static photoemission was also demonstrated. High-harmonic from a regenerative amplifier at 100 kHz where demonstrated [198], and the phase-matching was improved in the work of Heyl et al. [12]. Higher pulse energies, available by cryo-cooled regenerative systems were employed by Chen et al. [199] and by Wang et al. [13] employing the fundamental and the second harmonic, respectively. The latter reported an efficiency of 5×10^{-5}: to the best of the author's knowledge, this is the highest efficiency reported.

One of the first applications of OPCPA technology with a NIR driver for HHG were reported by reference [200] and by reference [18], concentrating on high-photon energies.

Ytterbium fiber lasers can be directly used for HHG, thanks to their sub-500 fs pulse duration: the phase-matching in such systems was studied by Cabasse et al. with an Ytterbium fiber laser at 100 kHz [201], the MHz level was reached by Boullet et al. [202].

The pulse duration of femtosecond Ytterbium amplifiers can be greatly enhanced by the technique of nonlinear compression, reducing it to few-cycle pulses and enabling the production of soft X-rays [203]. A high-power femtosecond fiber laser was broadened to 30 fs and generate harmonics up to 40 eV [204, 205, 114]. With a similar system, phase-matched generation at 70 eV was reported by Rothhard et al. [206]. By nonlinear broadening of a slab amplifier, HHG at 20 MHz

was reported [207]: this is the highest repetition rate for single pass harmonic generation reported.

Further scaling of repetition rate is possible in resonant cavities, enabling access to EUV frequency combs at 100 MHz [208].

3.3.1 *HHG geometry*

For high-flux HHG, the choice of the gas target is very important: for optimal phase matching the pressure and the length of the medium have to be adapted for the focusing geometry (section 3.2.6. The most commonly used gas target geometries are illustrated in figure 53. Three main categories can be identified: the first is the so-called
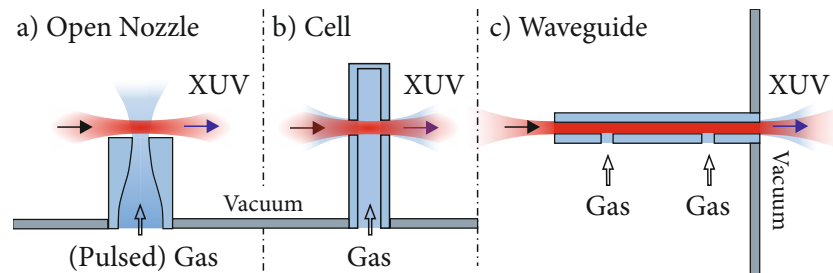
Figure 53: The different gas target geometries for HHG.

free-focus geometry. In this geometry, the beam is focused at the output of a gas nozzle, from which a gas freely expands in vacuum. In this configuration, the supersonic expansion is accompanied by a very fast pressure drop: to achieve a good gas density in the focus, high backing pressures are needed. The great advantage of this configuration is the complete open-space geometry, which translates into a higher tolerance for beam pointing instabilities and drifts.

In the cell geometry (fig: 53 b)) the laser is incoupled into a gas stagnation cell through holes drilled on the side walls. The backing pressure is lower compared to the previous case, however in a tight-focus geometry other challenges have to be faced. The optimum length for the target becomes shorter and reaches the sub-mm range: cells with a small inner diameter have to be produced. The entrance window's diameter need to be minimized in order to reduce the gas load, particularly severe due to high phase-matching pressures. The natural choice are laser-drilled apertures, however, the small depth of focus complicates laser drilling. Beam pointing drifts or mechanical instabilities become critical, due to the high beam average power.

The third possible geometry, uses a waveguide instead of a freely propagating beam: in this case the beam is focused into a hollow-core fiber filled with gas at high pressure and differentially pumped (fig: 53 c)). This method is well developed for kHz lasers and is usually helpful for the generation of high photon energies. Thanks to the added phase of the waveguide mode, is possible to improve the

phase-matching conditions and quasi-phase matching is also possible [194]. This technology is rather unexplored in the case of high-average-power laser where stable damage-free incoupling is more challenging[3].

In our experiments, it was possible to produce harmonic in gas cells consisting of thin glass tubes with walls ≈ 0.5 mm and inner diameters ≈ 1 mm. However, the stability was undermined by the thermal effects in the glass and by pointing instability. On such grounds, the waveguide geometry was not considered and a gas jet was finally adopted. The design of the gas target, together with the strategies for achieving a sufficient pressure for phase matching will be described in the following section.

3.3.2   *The gas target design and characterization*

A gas jet was produced with a convergent nozzle, which consists of a glass tube which smoothly reduces its inner diameter toward a well defined throat. The geometry is illustrated in figure 54, for a throat diameter of 150 μm; the beam is focused as close as possible to the gas outlet, where the atomic density is higher.
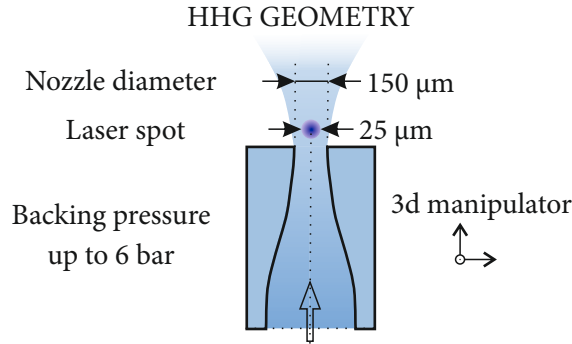

Figure 54: The free-jet geometry adopted in this work, together with typical dimension of nozzle opening and laser spot size.

Nozzles of similar form with throats ranging from 40 μm to 500 μm where tested. It is possible to estimate the on-axis pressure of freely-expanding gas jet from a converging nozzle using the following relation: [209]:

$$\frac{P}{P_0} = \left(1 + \frac{\kappa - 1}{2} M_a^2\right)^{-\frac{\kappa}{\kappa-1}}$$

(110)

---

3 Recent advances in high-power fiber lasers [203] suggest the feasibility of non-linear broadening in hollow-core fibers at hundreds of Watts: a similar setup might be tested also for HHG

In equation 110, P_0 is the backing (stagnation) pressure, measured far away from the converging section of the nozzle, $\kappa = c_P/c_V$ is the ratio of the specific heat at constant pressure and constant volume of the noble gas, for an the ideal monoatomic gas $\kappa = 5/3$. The pressure depends quadratically on the Mach number M_a of the gas, which is the ratio between the gas velocity and the sound speed in the gas. The Mach number can be calculated by solving numerically the gas flow equations. In the case of a converging nozzle, a power expansion fits well the numerical data. The Mach number along the nozzle axis can be expressed in term of the dimensionless parameter $\xi = x/d$ where x is the distance from the nozzle. For values $\xi < 1$, close to the nozzle exit one has [210]:

$$M_a = 1 + 3.337\xi^2 - 1.541\xi^3 \tag{111}$$

Figure 55 a) reports the pressure in the interaction region P_{int}, as function of the backing pressure P_{back} and of the nozzle diameter. The spot size is assumed to be 25 μm and the interaction region is defined as distance of $2w(z)$ with $z = 0.5$ mm to account for the beam divergence and a nozzle outer diameter of 1 mm. The white lines on the figure indicate the 500, 150 and 40 μm nozzle, respectively. Figure 55 b) shows how the pressure in the interaction region P_{int} increases linearly as function of backing pressure P_{back}. Figure 55 c) shows the pressure drop along the nozzle axis as function of distance, for a backing pressure $P_{back} = 1$ bar and a 150 μm nozzle.

In the work of Wang et al. [13], 400 nm pulses of about 50 μJ and ≈ 50 fs are used to achieve phase matching in a Kr glass cell with a pressure of 100 mbar. Using the scaling relations of table 6, our pulse energy yields a scaling factor $s^2 = 1/5$, the phase matching pressure is expected to be 500 mbar in the interaction region. This translates into a backing pressure of 1.2 bar for a 150 μm nozzle, which can be used as a first estimate for the requirements of the gas target.

3.3.2.1 *High pressure gas catch characterization*

Following the previous analysis, the vacuum pumps of the chamber hosting the gas target have to sustain over long time a backing pressure $\gtrsim 1.2$ bar. The HHG chamber is pumped by a water-cooled 700 l/s turbopump[4], backed by a 35 m^3/hr scroll pump[5]: the base pressure of the chamber is around 10^{-4} mbar. The nozzle is glued on a gas line, whose pressure is controlled by an electronic pressure regulator[6] operating up to 6 bars. The maximum pressure specified for the gas line components is 10 bars, a pressure achievable bypassing

---

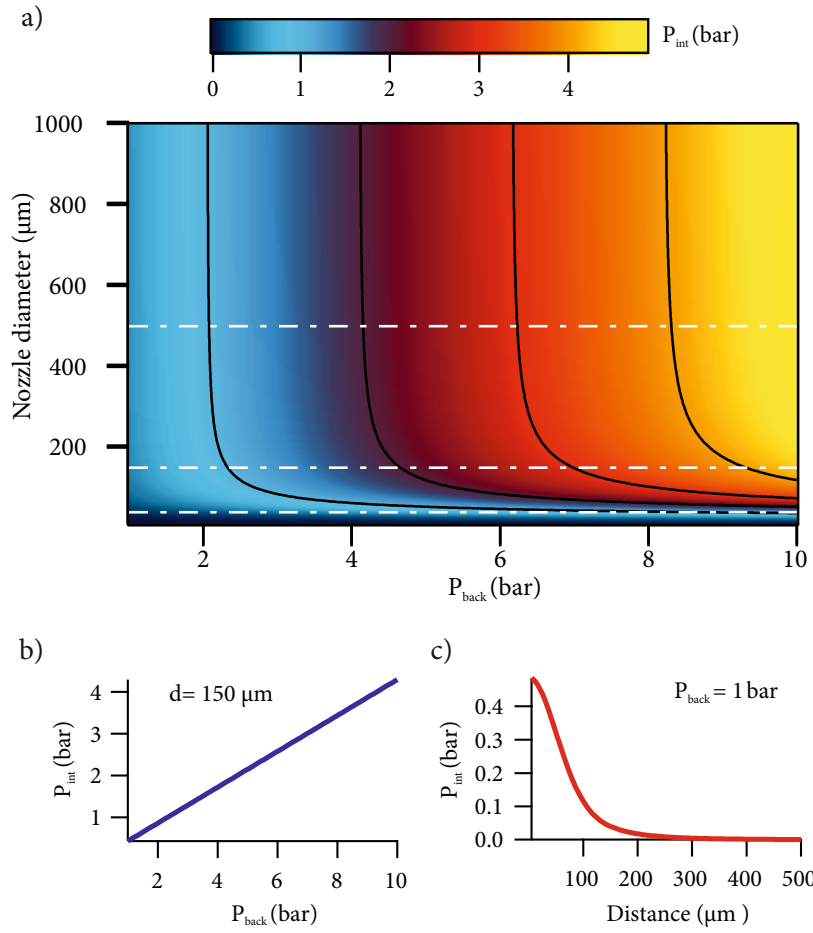4 Pfeiffer HiPace 700
5 Edwards XDS35i
6 MKS

Figure 55: Calculated pressure for an ideal mono-atomic gas expanding from a convergent nozzle. a) Pressure in the interaction region P_{int} as function of backing pressure P_{back} and of the nozzle diameter. The white lines indicate the 500, 150 and 40 μm nozzle diameters. b) Pressure in the interaction region P_{int} as function of backing pressure P_{back}. b) Pressure along the nozzle axis as function of distance for a backing pressure $P_{back} = 1$ bar and a 150 μm nozzle.
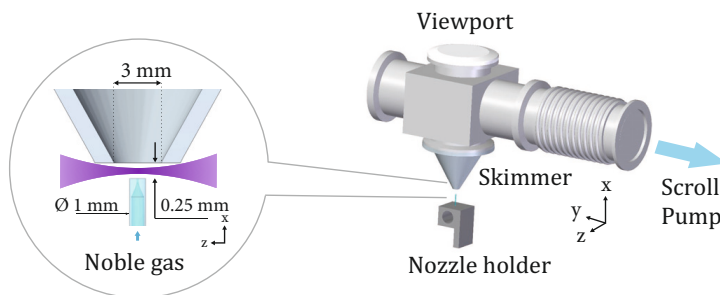
Figure 56: Physical dimensions of the gas-catch, compared with the gas nozzle holder. The clearance necessary for the laser beam is not in scale and is discussed in the main text. The z axis parallel is the beam propagation direction, while x is the vertical direction in the laboratory frame of reference. Adapted from [211].

the regulator. For the test, high purity Argon was used; the heavier (lighter) noble gases are expected to put the pumps under a greater (lower) stress. The turbopump maximum current for long term operation is about 2 Amperes: above this threshold overheating was observed. The current drain of the turbopump and the chamber pressure as function of the backing pressure in mbar is shown in figure 57, blue line.
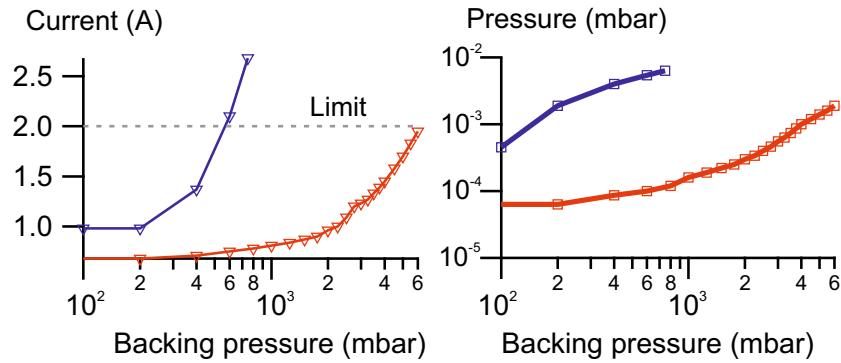

Figure 57: Turbopump current and HHG chamber pressure measured for a 150 μm nozzle as a function of the Argon backing pressure. The blue curve represent the data collected for the nozzle without a gas catch, the data in the red curve was collected with a gas catch at a distance of 100 μm.

The limit current is reached for a backing pressure around 600 mbar, insufficient for phase matching. To overcome this limitation, a *gas catch* was developed and implemented to improve the chamber differential pumping. The gas catch consists of a skimmer facing the nozzle to collect the gas. The skimmer opens in a smaller inner chamber connected to a second scroll pump via a flexible bellow of diameter $\phi = 40$ mm. To center the skimmer aperture and get as close as possible to the nozzle without clipping the beam, the whole assembly is mounted on a three-dimensional manipulator (Figure 56).

The *gas catch* was tested under similar conditions and enables operation of the 150 μm nozzle for backing pressures up to 10 bars: the results are reported in figure 57, red line.

Finally, to characterized the set-up, larger jets provided by a 500-μm-diameter nozzle and a 800-μm-diameter glass tube were also tested. In this case, the limit current is reached at backing pressures of 400 mbar and 300 mbar, respectively (figure 58). According to our previous analysis, this is below the estimated 500 mbar phase-matching pressure: the 500 μm nozzle was nonetheless tested for HHG in the next sections.
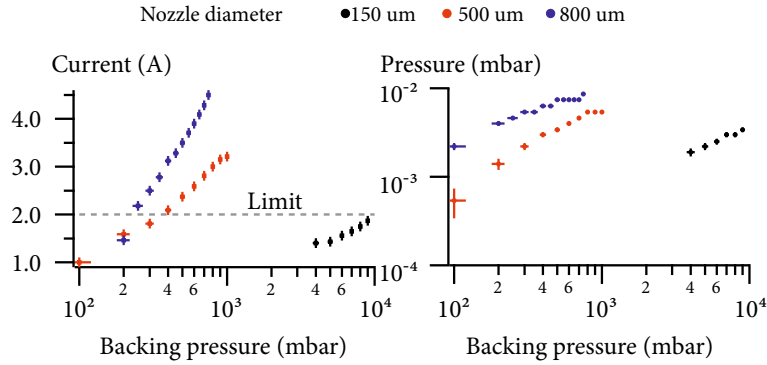
Figure 58: Turbopump current and pressure of the HHG chamber, measured for three nozzles as a function of the Argon backing pressure.

3.4 SOURCE CHARACTERIZATION

The capability of the OPCPA to achieve sufficient peak power was tested in a preliminary HHG experiment with a 800-nm-wavelength driver. In this case, 25 μJ pulses with a duration of about 17 fs (see the FROG results in Section 2.7.6.1) were focused at the output of an Argon gas jet with a 40-μm-diameter aperture. The divergent beam was filtered with a an Aluminum foil with a thickness of 200 nm (Section 3.4.2) before directly illuminating the slit of a VUV spectro-meter[7]. Spectral filtering removes the fundamental radiation and har-monics below $\approx$ 15 eV: the spectrum is shown in figure 59.
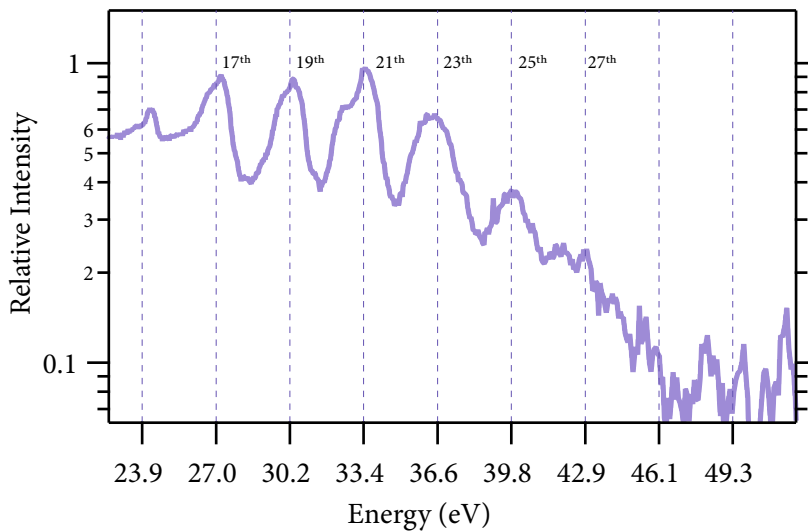

Figure 59: High harmonic spectrum measured using sub-20 fs, driver pulses with 800 nm wavelength, the vertical lines indicate the order of the harmonics.

---

7 McPherson 234/302 equipped with an X-ray camera, Andor iDus 420

Harmonics up to an order q=27 were observed, the strongest harmonic was the 21st at 33.4 eV. The cutoff law suggests a pulse peak intensity of around $1.4 \times 10^{14}\ W/cm^2$, away from the estimated peak intensity of $8 \times 10^{14}\ W/cm^2$ for the focal length of the lens used ($f = 75$ mm). As no particular care was taken to achieve phase matching in the setup (the maximum backing pressure was about 1 bar in this first attempt) this is easily explained by an excessive ionization level at the pulse peak and lack of phase-matching due to tight focusing. It is important to notice how the harmonics are relatively broad and sit on a continuous EUV background: the relative harmonic spacing is around 3.1 eV. The rich structure in this spectrum make the selection of a single harmonic challenging: this will not be the case for a driver with an energy of 3.1 eV, as it will be shown in the next section.

3.4.1 *Source spectrum*

After this initial demonstration, the setup was re-designed for SH-HHG and the high-pressure target of 3.3.2 was incorporated in the HHG chamber, the optical setup is sketched in figure 60.
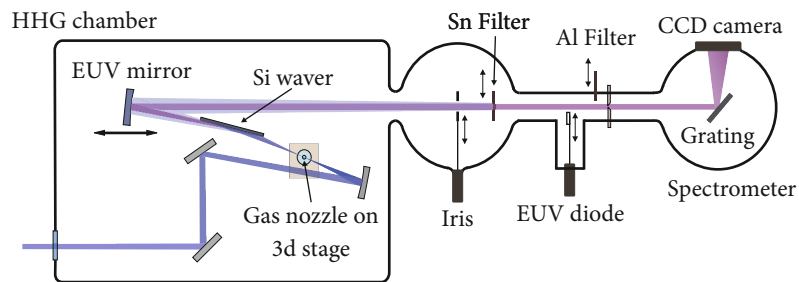

Figure 60: Experimental setup for UV-based high harmonic generation and single-harmonic selection. The absolute flux after monochromatization was measured with an EUV diode and the spectrum is recorded with a grating spectrometer equipped with a CCD detector.

The second harmonic of the OPCPA is generated by loosely focusing the beam with a plano-convex lens of $f = 1000$ mm focal length into a 100-μm-thick BBO crystal (see Table 3 for the phase-matching angle details). The crystal was placed after the focus and translated until an efficiency around 30% was achieved. At this intensity, no long-term damage of the crystal was observed. The second harmonic beam was not recollimated to avoid additional material dispersion. To avoid a long propagation in air, the frequency conversion crystal was placed at $\approx$ 300 mm from the vacuum chamber. In this narrow space, the second harmonic is isolated using two dielectric dichroic mirrors, with a contrast better of 1% each. The beam transmits through a 1-mm-thick CaF_2 window and is directed on spherical

mirror with a f=100 mm focal length and focused on the gas jet. The beam path following the target consists of several optical components to re-collimate the beam and isolate a single harmonic around 22 eV.

3.4.2 *Single harmonic selection*

The high-harmonic radiation propagates collinearly with the UV beam and, when the best efficiency is reached [13], its average power amounts at most for a fraction $\approx 10^{-5}$ of the total photons. For tr-ARPES studies, the fundamental radiation must be suppressed and a single harmonic selected.

Most of the fundamental radiation is absorbed in a Silicon wafer, set at the Brewster angle for the p-polarized 400 nm beam. The theoretical reflectivity, calculated using the Sellmaier equation of reference [212], is plotted in figure 61 a). The Brewster angle is approximately $80°$ and the residual reflectivity, taking into account the $2°$ beam divergence, is approximately 0.5%.

The estimation of the EUV reflectivity is a harder task, as the optical constants are not well studied in this range and the radiation is possibly strongly absorbed on any overlayer on the silicon surface. In the case of a commercial high purity Si single crystal, a passivating SiO_2 layer of about 1 nm is expected [213]. The reflectivity of Si plus 1 nm SiO_2 was simulated for p-polarized 57 nm radiation (the 7th harmonic at 21.7 eV) using the free software IMD [214] and is plotted in 61 a). In this configuration ($80°$ angle of incidence) the reflected power for the driving radiation is below 100 mW, while the reflectivity for the 7th harmonic can be estimated to be above 80%.

After the Silicon wafer, the UV power load is considerably reduced and the radiation is recollimated by a spherical mirror (f=200 mm). The mirror has a multilayer coating[8] designed for reflecting the 7th harmonic. The q-th order EUV harmonic is considerably less divergent (q times less, assuming diffraction-limited propagation) than the fundamental beam, therefore a 25-mm-diameter mirror could still be used without significant losses, even if the wings of fundamental beam were clipped at the mirror borders. The mirror is mounted on a motorized optical mount[9] to adjust the beam pointing, and can be translated along the bead by a linear translation stage, to either re-collimate the beam (distance from the HHG source equal to the mirror focal length) or to re-image the source on the sample for tr-ARPES experiments. The theoretical reflectivity of the EUV mirror is on the order of 30% and is plotted in Figure 61, b). The mirror's coating consists of a Silicon layer, covering a multilayer composed of Cr/Sc/Cr/Si realized on an EUV-grade substrate[10].

---

8 Reflective X-ray Optics LLC
9 Smaract STT-25.4-HV
10 Layertec, flatness $\lambda/20$, roughness < 0.2 nm RMS

For an accurate measurement of the EUV flux and the spectrum, the fundamental has to be completely suppressed: this was done by transmission through free-standing metal foils ($\approx$ 200 nm) either of aluminum or tin. The calculated transmission for the metal foils is shown in figure 61 b). Aluminum acts as a high-pass filter, transmitting energies above $\approx$ 15.5 eV; Tin is instead a band-pass centered around 22 eV and can be used to suppress the 5th and 9th harmonic relative to the 7th.

a) Si wafer reflectivity
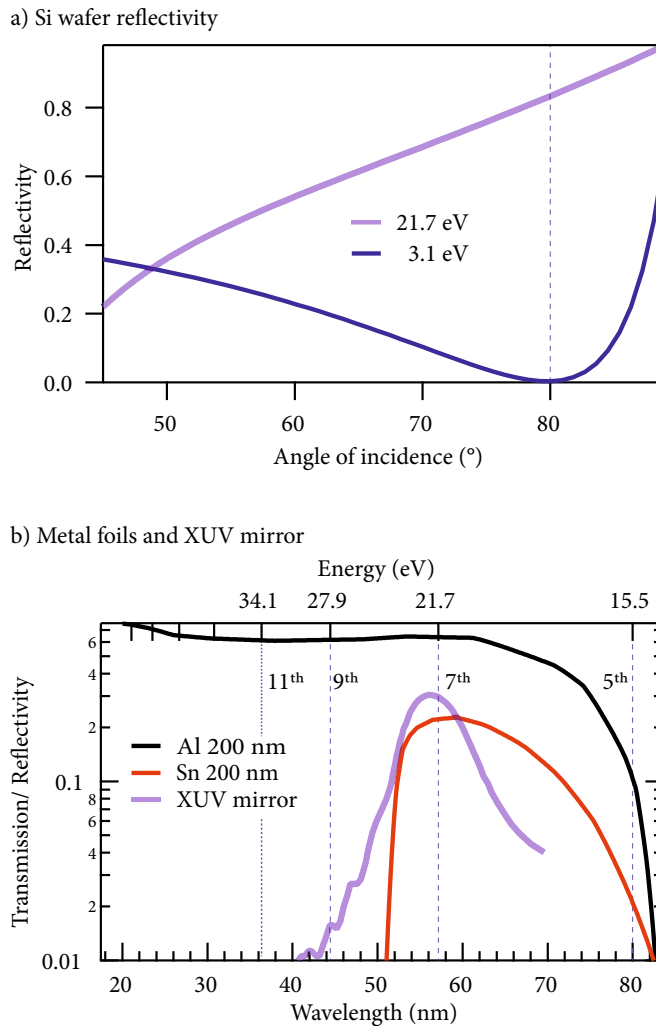

b) Metal foils and XUV mirror

Figure 61: a) Reflectivity of a silicon wafer as a function of the angle of incidence, for 3.1 eV and 21.7 eV p-polarized photons. b) Estimated transmission of 200 nm Al and Sn metal foils, theoretical reflectivity curve of the EUV mirror.

3.4.3 The harmonic spectrum

To characterize the EUV spectrum, the beam was reflected toward an EUV spectrometer equipped with a 2400-lines/mm platinum gra-

ting and an X-ray camera (Section 3.4), as illustrated in Figure 60). A second chamber hosts a motorized iris, followed by a retractable Sn filter. The iris is used to block some of the residual radiation at 400 nm wavelength and to attenuate the EUV beam in the experiments, without changing the harmonic phase-matching conditions. A second Al foil can be placed in front of the spectrometer: it was not possible to measure the spectrum without suppressing the fundamental radiation with a metal foil, due to the high sensitivity of the X-ray CCD camera.

The beam was centered on the spectrometer's slit and the EUV spectrum recorded at a slit aperture of 0.01 mm. The ultimate resolution of the spectrometer with this settings was estimated to be $\gtrsim 0.6$ nm, which translates into $\gtrsim 22$ meV resolution broadening at 21.7 eV. The target pressure and position were optimized to achieve the highest photon flux at the 7th harmonic: the spectrum, filtered with a 200-nm-thick Al foil, is plotted in 62.
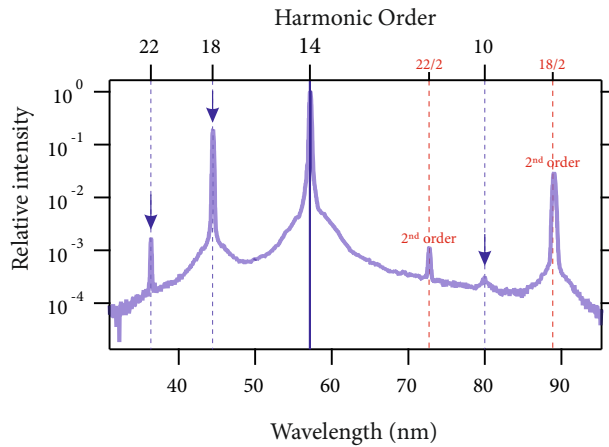

Figure 62: 3.1-eV-driven HHG spectrum in Argon. The spectrum is recorded using a 200-nm-thick Al filter for suppressing the residual fundamental radiation at the spectrometer's input.

The data consists of three images, collected for different grating angles, which were connected by normalizing the intensity of the same harmonic in the regions of overlap between different scans. The wavelength axis was calculated taking into account the spectrometer's geometry and the grating equation: the wavelength is not exactly a linear function of pixel position, however, in the central portion of the camera, the deviations are small. The harmonic order is calculated starting from the OPCPA fundamental, to better compare with the NIR-driven HHG shown in Figure 59, thus only even harmonics are expected in this plot.

The highest observable harmonics is the 22nd (q=11 for the SH-HHG process), unexpectedly some signal at the 11th and 9th order is present. After closer inspection, it is clear that these harmonics are

not generated by residual NIR radiation, but are the second-order diffraction peaks of the 18th and 22nd harmonics. The spectral intensity is normalized to the strongest harmonic, showing that the suppression of the neighboring q=18 harmonic is on the order of 10^{-1}, still insufficient for tr-ARPES (Section 1.6.4). When comparing with 800-nm-driven HHG in Figure 59, it is clear that the UV-generated harmonics are considerably narrower.

The same spectrum after the insertion of a 200-nm-thick Sn foil and the removal of the Al foil is shown in figure 63: this clearly shows the benefits in term of contrast of the bandpass filter. The contrast
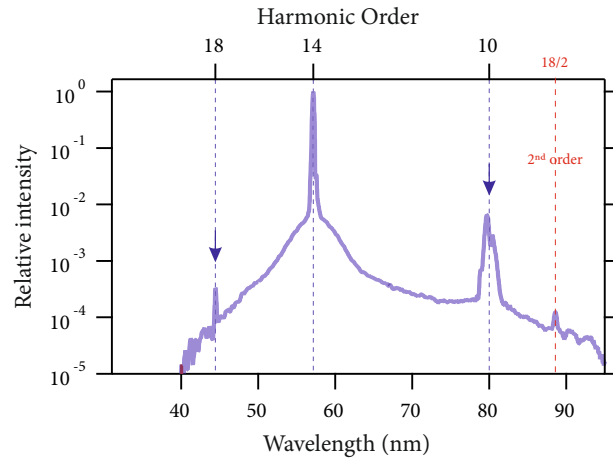

Figure 63: 3.1 eV - driven HHG spectrum in Argon. The spectrum is recorded using a 200 nm-thick Sn filter for suppressing the residual fundamental radiation at the spectrometer's input.

with the 18th is now below 10^{-3}. However, the lower energy nearest harmonic at 80 nm, rises to the percent level, reflecting the higher transmission for this photon energy in Sn. Nonetheless, this second configuration is preferred in tr-ARPES experiments (Section 1.6.4).

The absolute flux of the harmonics was measured with EUV photodiode, mounted on a linear translation stage. The photodiode collects the radiation just before the spectrometer's slit. The current is read by a picoamperometer[11] and converted in photon flux using the factory specifications: the photo diode was not absolutely calibrate with an independent light source. The flux, as a function of the gas pressure, is shown in Figure 64, left panel. The flux peaks above 4 bars at a value exceeding 10^{11} ph/s. A further increase of pressure does not yields an improved signal, indicating that the EUV conversion is absorption-limited.

The spectral resolution at the maximum flux is ≈ 110 meV FWHM (Figure 64, left panel), well above the spectrometer resolution. The right panel of Figure 64, reports the measured contrast for the nearest higher harmonics in this case. The flux measured in this configuration
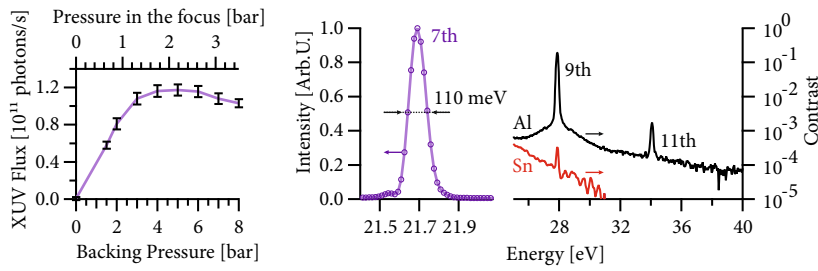
---

11 Keithley 6485

Figure 64: Left panel: monochromatic EUV flux at 21.7 eV at the sample's position. Right panel: Spectrum of the 7th harmonic, corresponding to the flux in the left panel. At higher energies, the residual higher order harmonics are plotted on a logarithmic scale (black line). An additional 200-nm-thick Sn foil improves the contrast to $\approx 10^{-4}$ (red line).

is also the flux at the sample, as there are no other optical components in the beam path. The FWHM of the harmonic was investigated as function of the gas pressure in Figure 65. The bandwidth correspond to a Fourier limit of about 16.5 fs for a Gaussian pulse. The analysis reveals that the FWHM minimum is reached already around ≈ 2 bars. Comparing with the pressure scaling of the flux, one sees that the growth of the harmonic is close to linear already at this pressures. At 1 bar the bandwidth is around 116 meV, showing how the phase matching conditions can indeed influence the energy resolution.
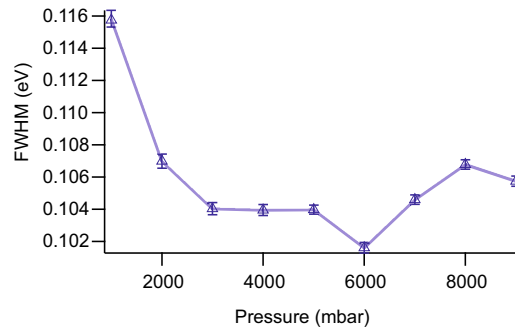

Figure 65: Measured FWHM of the 7th harmonic as a function of the Ar backing pressure. The instrumental resolution is ≈ 20 meV.

3.4.4 Comparison between different nozzles and gases

HHG was tested also in other noble gases: in each case, pressure and nozzle position were optimized to maximize the EUV flux. The relative intensities are listed in table 9. The best results were obtained with Ar, even if Kr was expected to have a stronger single-atom

Table 9: Comparison of the relative flux for the 21.7 eV harmonic with different gases for 150 μm nozzle throat diameter.

Noble gas	Ne	Ar	Kr
Relative flux	0.02	1.0	0.78

Table 10: Relative maximum flux at 21.7 eV for different nozzle throat diameter.

Nozzle throat (μm)	40	80	150	500
Relative flux	1.00	0.74	0.60	0.13

response. It is possible that the higher ionization in this case prevented phase matching at the pulse peak, resulting in shorter coherence lengths. Longer focal lengths could not be tested in the setup due to geometrical constrains. The medium length was changed by trying different nozzles, using the same focusing conditions and Argon as gas target. The nozzle position and pressure were optimized to maximize the flux and the best results are reported in Table 10. Saturation of the EUV flux was observed only for the 150-μm-diameter nozzle: for the 500-μm-diameter nozzle, the turbopump overheated before saturation, whereas for the 40-μm-diameter nozzle the signal was still increasing at the maximum backing pressure withstood by the gasline components (≈ 9 bar). Overall, the flux was on the same order of magnitude and the optimum backing pressure increased for smaller throat diameters, as expected from the analysis of section 3.3.2. The highest flux was observed for the smallest nozzle, indicating that for a medium length of ≈ 100 μm the harmonic re-absorption is already limiting the signal build-up. In practice, in view of the long-term tr-ARPES measurements, a 150-μm-diameter nozzle was preferred as it is more insensitive to misalignment and can be operated at lower backing pressures.

3.4.5 *Spot size characterization*

A good mode quality of the probe beam is important for pump and probe experiments. To characterize the 57 nm beam, the setup was modified to incorporate a micro-channel-plate (MCP) electron multiplier with a phosphor screen. The experimental setup is illustrate in Figure 66: in this case, the spectrometer is removed and replaced by an evacuated tube with the imaging setup. The MCP si connected to a bellow and can be translated along the beam's axis: the final distance between the EUV mirror and the MCP was set at about 2.5 m, to mimic the experimental beamline.
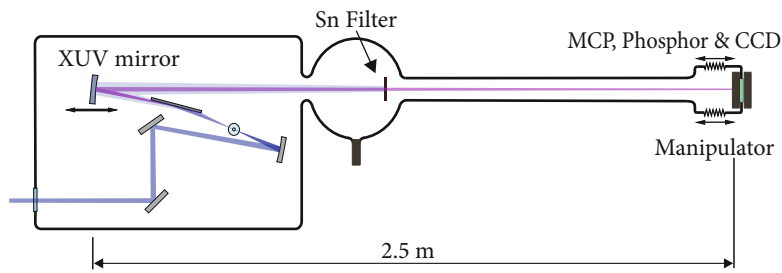
Figure 66: Experimental setup for measuring the EUV beam profile at the sample's position. MCP = micro-channel plate.

The phosphor screen is imaged by an objective on a CCD camera[12]. By translating the EUV mirror along the beam axis, the source is focused on the MCP. The measured mode profile is shown in Figure 67, the image is acquired at maximum EUV flux after passing through a Sn filter to minimize the contribution of neighboring harmonics and to fully remove the fundamental. The FWHM of the spot is about 130 μm, given the magnification factor of the imaging system, the EUV source size is on the order of 11 μm, approximately half the focal spot of the fundamental beam.
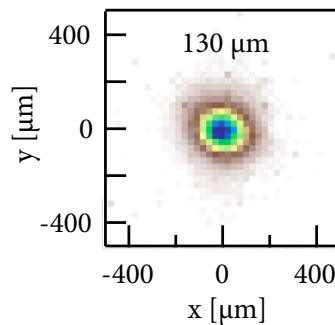

Figure 67: EUV beam profile recorded with the setup in Figure 66 under phase-matched generation conditions. The FWHM of the spot is approximately 130 μm averaged from fits across the transversal x and y direction.

3.5 THE BEAMLINE FOR TR-ARPES.

The EUV source at 21.7 eV, provides a good radiant flux for tr-ARPES experiments. The setup described so far was extended and connected to a surface science chamber, equipped with a manipulator and an electron energy analyzer which will be described in greater detail in the Chapter 4. The beamline, depicted in figure 68, includes the

---

12 Spiricon BGS-USB-SP620

transmissive monochromator and an incoupling chamber for a second laser beam for pump-probe experiments. Diagnostic tools for EUV optimization and alignment were also included.

The OPCPA output is split and 90% of the power is used for SHG. The second harmonic is separated and incoupled in the first chamber (HHG chamber), where the 7th harmonic is created in the high pressure gas jet. The gas catch (removed from the drawing for clarity) is aligned on top of the nozzle using a 3-axis manipulator.

After reflection from the Si wafer and the EUV mirror, the beam arrives to a second chamber (filter wheel chamber), separated from the first by a gate valve with a glass window, to be able to vent the HHG chamber without breaking the vacuum in the rest of the beamline. The base-pressure of this chamber is in the 10^{-8} mbar range, which is increases to 10^{-4} mbar when the gas load is present. This chamber hosts a motorized filter wheel with 5 slots[13], containing additional Sn and Al filters. Before the filter wheel, a manual 3-axis manipulator holds a motorized iris with an encoder[14]. This reproducible aperture to reduce the EUV flux without changing the phase-matching conditions.

The next section of the beamline is used for HHG characterization. After a first (blind) gate valve, a second gate valve hosts a Sn foil, used as a window. A third valve (with a glass window) allows to easily vent the section for replacement of the fragile metal foil in case of damage. After the Sn foil, a linear translation stage is used to slide an EUV diode in the beam to measure the radiant flux on the sample. The same linear translation arm holds a gold mirror without any protective coating. The mirror reflects at 45° the harmonics toward the VUV spectrometer, whose opening slit is preceded by a gate valve to isolate the section and a manual filter wheel for inserting additional foils in the beam if necessary.

The third chamber along the beamline hosts a fixed mirror mount, used to in-couple the pump beam at a low angle from the EUV to avoid experimental time resolution broadening due to pulse front mismatch. The chamber can be baked to reach a base-pressure in the low 10^{-10} mbar range. When the gas load is running and the Sn window is closed, the pressure in the chamber is as low as 10^{-8} mbar. This enables to reach a pressure of some 10^{-11} mbar in the following analysis chamber while measuring.

Just between the last two chambers, a cross joint holds a linear translation stage with a metallic mirror: this can be inserted in the beam path to simultaneously reflect the pump and the residual 400 nm HHG driver, which is still observable if the Sn foil is removed. This allows for ex-situ spatio-temporal overlap of the two pulses, and

---

13 Smaract SFW-6-25.4-HV
14 SID-5714-ID22-S-HV

UHV tr-ARPES Chamber
with Cyrostat & Sample manipulator

10^{-11} mbar

Delay

Hemispherical electron
energy analyzer

Spectrometer

Pick-up mirror

Pump mirror

EUV diode /Au mirror

VAT valve with Sn foil

Filter wheel

Motorized iris
on manipulator

Gas-catch
3d manipulator

Nozzle on 3d
motorized stage

Si wafer

EUV mirror on
translation stage
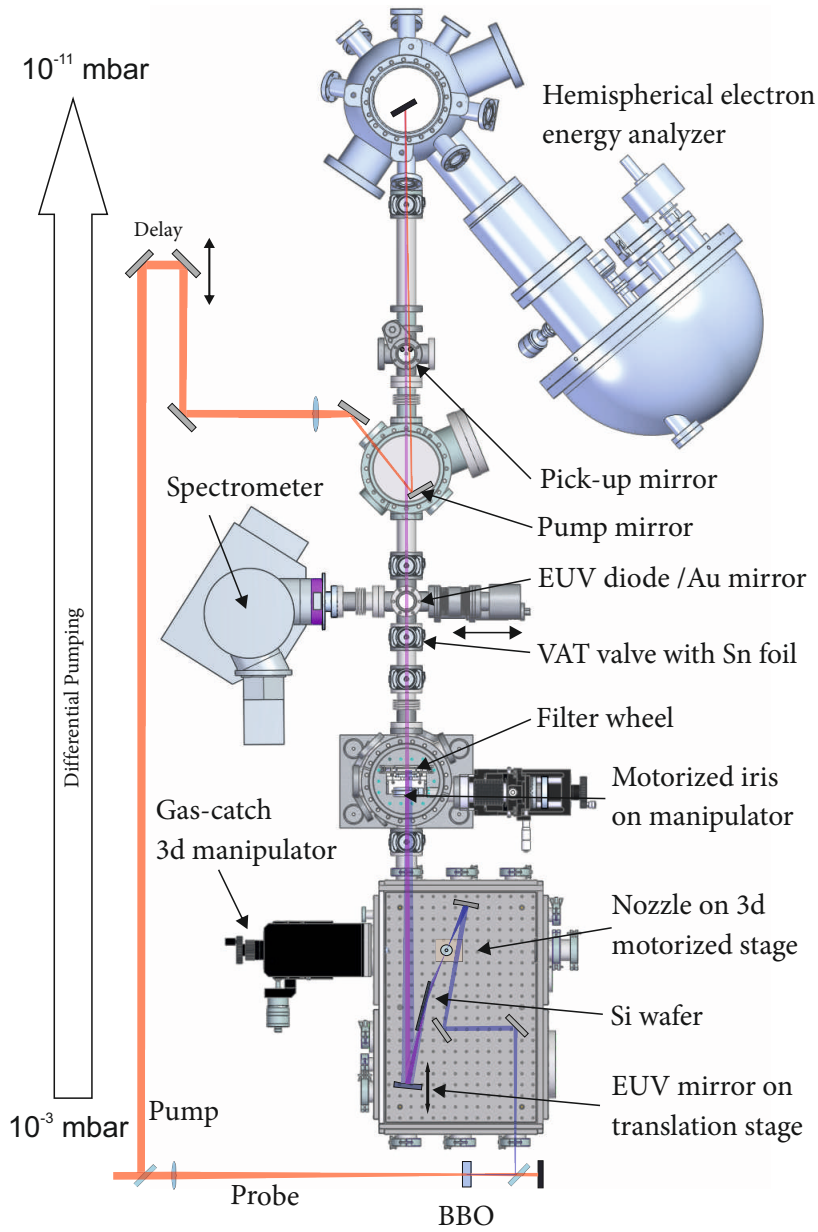
Differential Pumping

10^{-3} mbar Pump

Probe

BBO

Figure 68: The tr-ARPES beamline scheme. The dimensions of the compo-
nent have the correct scaling. The sample-EUV mirror distance is
approximately 2.5 m.

to characterize the pump beam with a beam profiler, an important step in determining the pump radiant fluence.

Part II

TR-ARPES ON TRANSITION METAL
DICHALCOGENIDE SEMICONDUCTORS

4

TIME- AND ANGLE-RESOLVED PHOTOEMISSION
SETUP

The tr-ARPES experiment is performed in a ultra-high vacuum (UHV) chamber equipped with an electron energy analyser[1]. The sample is installed on a manipulator[2] which allows three-dimensional linear positioning and angular adjustments around three axis. The complete UHV system is illustrated in figure 69. The beamline (Section 3.5) is connected to the analysis chamber (in gold in figure 69), at the same height of the analyser entrance. The manipulator, holding the sample during the experiments, can be transferred to an upper chamber (sample storage chamber, in blue), where samples are stored and prepared before the measurements. The samples are inserted in vacuum through a load-lock (figure 69 b)) and are moved to the sample storage chamber using transfer rods. The samples pass through a molecular beam epitaxy (MBE) growth chamber (in green in Figure 69), equipped with evaporators for the growth of thin metal films.
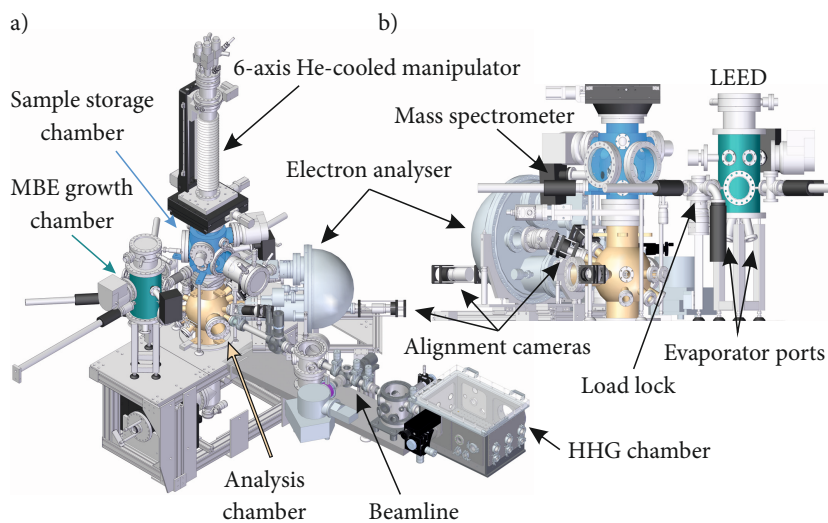

Figure 69: a) Overview of the whole experimental system for HHG-tr-ARPES. b) Detail of the UHV sample-preparation and analysis chamber, courtesy of Chris Nicholson, adapted for this thesis.

The material studied in this work, 2H-WSe$_2$ (Section 5.1), is a layered semiconductor where the atomic planes along one direction are held together by weak van der Waals interactions. To expose a clean uncontaminated surface, the samples are cleaved in the sample storage chamber under UHV conditions with the scotch-tape method.

---

1 SPECS, Phoibos 150
2 SPECS, Carving

The exploded sketch of the analysis chamber is given in figure 70. The pump and the probe beam enter the chamber at a non-collinear angle below 1°. In the beam plane, at 40° from the EUV probe, the electron energy analyser collects the photoelectrons, with an acceptance angle of ±15°. The sample's surface is oriented using the motorized manipulator: three angles determine the orientation of the surface normal relative to the slit plane and allow to select only the photoelectrons coming from a specific cut through the Brillouin zone. These angles of rotation are the polar angle, θ, flip angle β and azimuthal angle ϕ. The direction of rotation are sketched in Figure 70, panel b), for the case of normal emission (sample facing the analyser entry, thereby selecting electrons coming from the Γ point). The whole manipulator can be translated in three directions (x,y,z in figure 70; the x and the y axis form an angle of roughly 45°with the direction of normal emission), allowing to move the photoelectron source spot in the focus of the analyser and achieve maximum transmission with minimal distortion. Moreover, thanks to the precision and reproducibility ($< 10 \ \mu$m) of the movements, it is possible to move the photoemission region across a non-uniform cleaved sample and to easily measure small specimens.
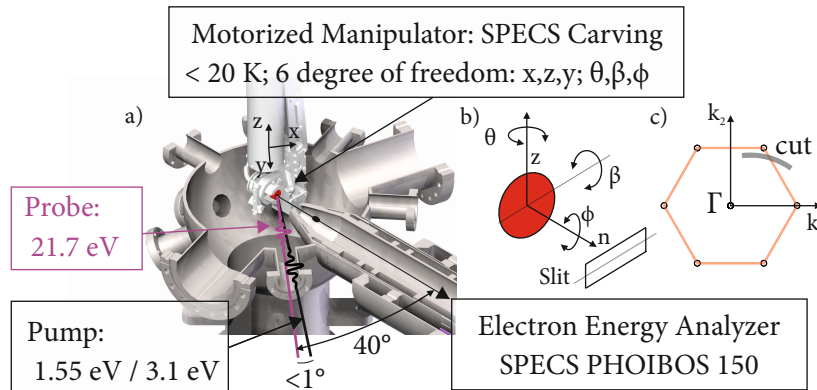

Figure 70: a) Cutaway drawing of the analysis chamber, showing the direction of the incoming pump and probe beams and the measurement geometry. x,y,z are the physical translational degrees of freedom of the manipulator. b) Rotational degrees of freedom of the sample, relative to the analyser slit. c) k-space representation of a cut in the Brillouin zone recorded by the analyser.

A set of electrostatic lenses accelerates the photoelectrons to a well-defined *pass energy*, E_{pass} which is the energy of the central trajectory in the hemispherical electron analyser. The electrons are refocused on an slit, oriented along the plane of the pump and probe beams. The electrons then pass through the hemispherical capacitor, which disperses the energy of the photoelectrons on the vertical axis and preserves the in-plane angular distribution.

The electrons are detected after the exit of the hemisphere, using a combination of two micro-channel-plates (MCP) in a chevron geometry for spatially-resolved electron multiplication. The resulting electronic cascade hits a phosphor screen which converts the signal into visible light, which is imaged by an objective onto a cooled CCD panel[3].

The raw CCD pictures, are binned two by two by the internal camera firmware, before being read by a home-written Labview code. Several sources of background are present: stray light and reflections from the strong photoelectron signals can overlap on weaker signatures; lower energy electrons in the analyser can be reflected in the inner hemisphere and hit the MCP on the same arrival spot of the features of interest. Finally, there is the intrinsic noise from the CCD panel.

The effects of background and of stray signals are particularly detrimental for tr-ARPES: in this experiment one observes small signals above the Fermi level and simultaneously order-of-magnitude brighter occupied-state features.

A grid with an electrostatic bias, set to about 80% of E_{pass}, is inserted in the exit slit to remove most of the low-energy background electrons. After subtracting a dark image, a thresholding algorithm is implemented in the data-acquisition software on every image. In this acquisition mode, a short exposure (typically 25 ms) is selected and pixels below a certain threshold are discarded. This removes a large portion of the stray light, while leaving the signal from true electron counts mostly unaffected. These background subtraction tools allowed a sufficient dynamic range to measure the occupied and unoccupied bands of 2H-WSe$_2$ simultaneously.

Many short-time acquisitions are integrated until a sufficiently good statistic is achieved and the resulting images are finally saved for off-line processing.

4.2 DATA POST-CORRECTION

The image post-processing procedure consists of several steps which are illustrated in Figure 71. The raw image (1) present periodic modulations imposed by the rejection grid. These are removed by spatial Fourier filtering, using a two dimensional Gaussian band-block filter at the spatial frequencies corresponding to the grid modulations. The procedure was tested on photoemission data from a Au(111) surface state, acquired at high-resolution with an Helium lamp, and did not show significant losses of energy and angular resolution. At the image borders (see the top side of the second image in figure 71) some artifacts are introduced, therefore this areas will be always neglected from the analysis.

---

3 PCO sensiCAM

After the filtering, the photoelectron's emission angle and energy are calculated from the pixel position using factory-calibrated ray-tracing functions (2).

The third step is the conversion of the angular distribution in units of the reciprocal space wave vector. The angle between the slits' center and the sample normal has to be determined, starting from the three manipulator angles. In general, every angle of detection corresponds to a (k_1,k_2) pair in the surface Brillouin zone (SBZ). The analyser acquires photoelectrons corresponding to a cut in the SBZ which does not form a straight line for arbitrary (θ,β) pairs (see Figure 70, inset c). When $\beta = 0°$, the surface's normal is in the plane defined by the slits' long direction (this is the case of Figure 70, b) , (k_1,k_2) form a straight line in k-space and the image can be displayed as function of the total $k_\parallel$: this is the case for all the images displayed in the thesis, except from the three-dimensional maps of Section 5.2. In that case, to map the SBZ, several images are collected at different (θ,β) manipulator angles. The dataset is grouped in a three-dimensional matrix which is interpolated on a uniform (k_1,k_2) grid.
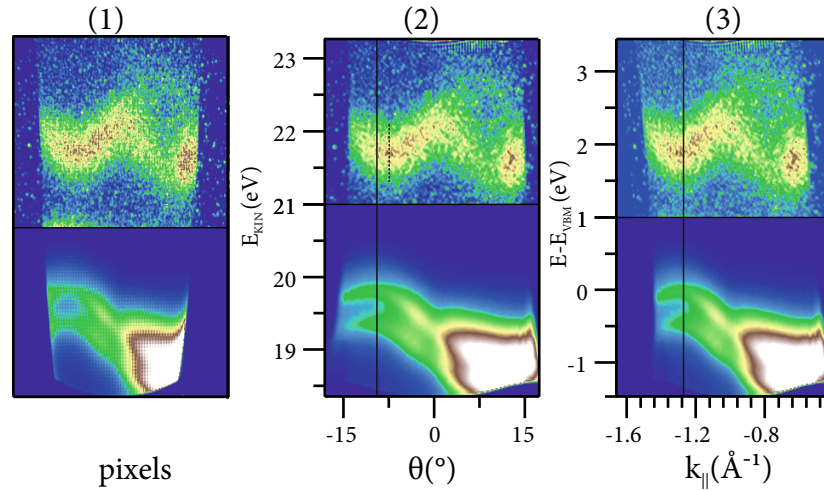

Figure 71: Illustration of the effects of data correction. a) Raw image. b) Angular corrected and filtered image. c) Momentum-corrected image.

4.2.1 Analyser resolution

The analyser lenses were operated in a wide-angular-acceptance mode where multiple angles of emission are detected in parallel. In this mode, the angular resolution at the exit plane of the hemisphere can be estimated from the angular dispersion $d_\alpha = 0.65$ mm/°. The finite size of the source will be in first approximation neglected as the EUV spot diameter is close to the 100 μm spot of the electron source used for factory calibration (Section 3.4.5). All the data shown in this thesis

was taken either with a slit 0.5×20 mm^2 (slit ♯2) or 1×20 mm^2 (slit ♯3) to increase the transmission by a factor of two. Both slits have a length of 20 mm in the non-dispersive direction (parallel to longer side of the slit): this translates in an angle of $\pm 13°$ displayed on the CCD panel (the lens system collects photoelectrons coming from a $\pm 15°$ cone). The ultimate angular resolution in this direction is then limited by the pixel spacing in the CCD camera[4], and is about $0.13°$.

In the orthogonal direction, the angular resolution is determined by the acceptance angle of the slit along its short side: $0.65°$ and $1.3°$ for slit ♯2 and slit ♯3, respectively. For this reason the angular resolution of maps collected by angular scans is generally not uniform.

The instrumental energy resolution is determined by the pass energy and the selected slit, using the relation:

$$\frac{\Delta E}{E_{pass}} = \frac{S}{4R_0} + \frac{\alpha^2}{4} \qquad (112)$$

Here, S is the shortest slit dimension (the energy dispersive direction, orthogonal to the plane of the beams in our setup); $R_0 = 150$ mm is the mean radius of the hemisphere and α is the half-acceptance angle of the slit's shortest side. Using Equation 112, the calculated energy resolution for different slits is shown in figure 72. Given a linewidth of 110 meV, the analyser broadening energies corresponding to 10% and 20% of the linewidth are indicated. The ultimate resolution which can be achieved by the analyser is below 10 meV; however, it is more convenient to accept some resolution broadening to improve the transmission.

4.3 SPACE CHARGE ANALYSIS

The space charge effects depend on the sample photoionization cross section and the photon energy (see Section 1.6.1). At a photon energy of 21.7 eV, photoemission from a wide portion of the material's valence band is energy-allowed. When observing features close or above the Fermi level, many of the photo-emitted electrons are not detected but nonetheless contribute to the total space charge. For this reason HHG-based EUV sources are more prone to space charge when compared to 6-eV-based tr-ARPES.

When higher-energy pump photons are used, the pump itself can generate strong nonlinear photoemission, even exceeding the direct photocurrent from the probe. In this cases the pump-induced space charge is important too and has to be independently characterized.

When measuring 2H-WSe$_2$ the source flux was sufficient to generated thousands of photoelectrons every pulse. The resulting probe space charge will be characterized systematically in the next sections.

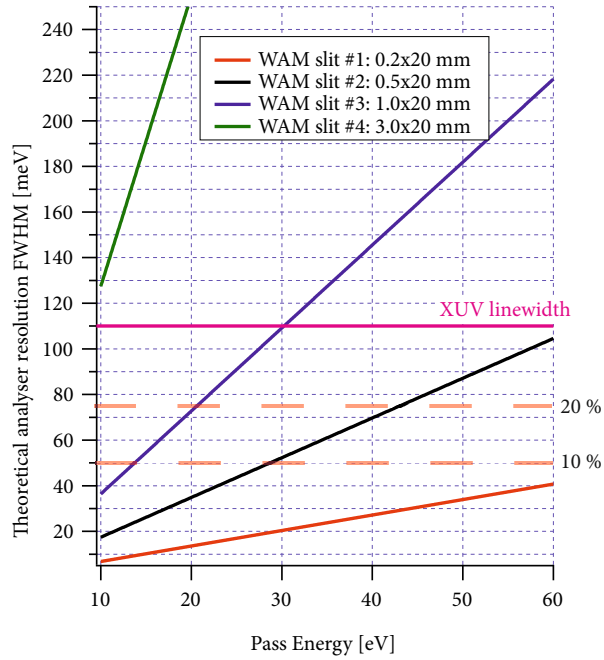4 6.45×6.45 μm^2, binned by a factor 2

Figure 72: Analyser resolution as a function of the pass-energy for different slits in WAM (wide-angle acquisition mode), calculated using Equation 112. The EUV linewidth is indicated, together with the instrumental broadening necessary to worsen the resolution of 10% or 20%, given the probe linewidth.

4.3.1 *EUV-induced space charge in* 2H-WSe$_2$

The K point valence band states in 2H-WSe$_2$ have a bidimensional nature (Section 5.1.2): these states are intrinsically narrow in energy and provide a good reference for space-charge-induced effects. The space charge was measured by keeping the phase-matching conditions for HHG constant and reducing the flux using a motorized iris (Section 3.5), the results are summarized in figure 73.

The upper panel shows two EDCs for two different EUV fluxes. The prominent effects of the space charge are an energy shift and a broadening of the energy resolution.

The total photoelectron yield was estimated by measuring the drain current from the sample using a picoamperometer[5]: from the current, the amount of electrons per pulse can be easily calculated. A Gaussian peak is fitted to the upper valence band, after a Shirley background subtraction [215]. To properly account for the neighboring peak, a second Gaussian was added to the fit. The width and the shift of the top peak are displayed in the two lower panels of figure 73.

The broadening quickly grows until it saturates to about 80 meV, when more than 500 electrons per pulse are emitted. The energy offset continue to increase in the whole investigated range, reaching
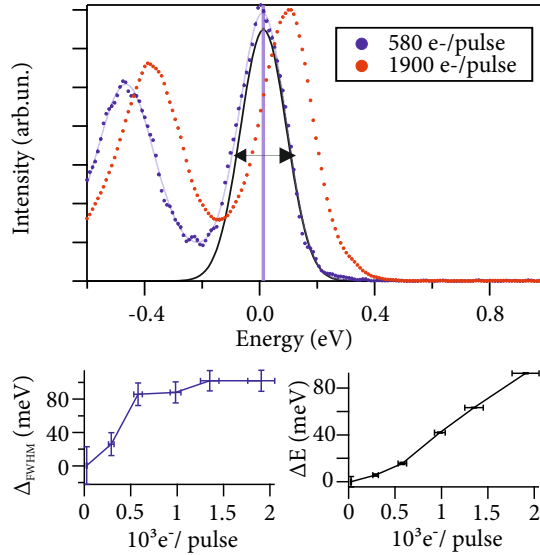
_____

5 Keithley 6485

Figure 73: Effects of the space charge induced by the probe beams. Top graph: photoelectron spectra collected at the K-point in 2H-WSe$_2$ for the indicated average amount of photoelectrons per pulse. Bottom, left: energy broadening of the higher energy peak, as a function of the number of electrons per pulse. Bottom, right: energy shift of the peak as a function of the number of electrons per pulse.

a maximum of 80 meV. In the experiments, a compromise between acquisition time and space charge has to be accepted: typically, the flux was reduced below about $\approx 500\ e^-$/pulse.

4.3.2 *Pump space charge in 2H-WSe$_2$*

A pump photon energy of 3.1 eV will be used to populate the conduction band of 2H-WSe$_2$; the work function of the material is about 4 eV [216], meaning that two-photon photoemission (2PPE) potentially contributes to the space charge. The photoelectron flux as a function of pump fluence is reported in figure 74, the pump and probe are not overlapping in time (the probe arrives 1 ps before the pump) to avoid that the broadening observed is induced by changes in the spectral function of the material (see Section 5.3.1). As in the previous analysis, the valence band's width and position was fitted. Indeed, already at a modest incident fluence of $\approx 100\ \mu J/cm^2$, the pump photoelectron yield is close to $10^4\ e^-$/pulse and surpasses the one of the probe ($\approx 600\ e^-$/pulse).

The photoelectron total yield does not scale quadratically with fluence as expected in a pure 2PPE case and, depending of the sample, the amount of pump-induced photoemission changed significantly. This indicates that surface inhomogeneity and defects contribute to the photoemission: similar effects were already reported for MoS$_2$ in
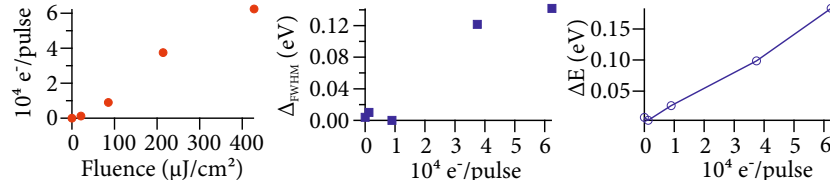
147

Figure 74: Effects of a 3.1 eV photon energy pump in 2H-WSe$_2$. Left graph: number of pump photoelectrons per pulse as a function of the pump fluence. Center graph: energy broadening Δ_{FWHM} at the K point high-energy peak, as a function of the number of photoelectrons per pulse. Right graph: energy shift ΔE as a function of the number of photoelectrons per pulse.

reference [61]. Another possible effect is the sample's re-absorption of part of the photoelectrons, leading to a saturation of the photo-current at higher fluences. As the pump-induced photo-voltage increases, part of the very low kinetic energy photoelectron might be re-captured. The pump space-charge produces shifts and broadens the spectrum, although the effect per photoemitted electron is smaller compared the probe, likely because the pump photoemission cloud has considerably less average kinetic energy than the measured electrons.

The energy broadening stays nearly constant for charges below 10^4 e^-/pulse and becomes ≈ 120 meV above 4×10^4 e^-/pulse. The energy shift constantly increases, exceeding 100 meV above 4×10^4 e^-/pulse. In the experiments, the photoemission current was kept below approx 10^4 e^-/pulse (the corresponding maximum pump fluence changes between different samples, with a typical value of $\approx$ 100-200 μJ/cm^2): at this space charge level the broadening does not affect the experimental resolution and the energy shift is below 30 meV.

4.3.3 Time-resolved mode

When measuring a time-dependent spectrum, the acquisition settings are kept constant while several images are collected as a function of the pump and probe delay. The images are corrected using the procedure of Section 4.2 and joined in a three-dimensional dataset. From the time-resolved data two quantities are extracted: the first are one dimensional *time traces*, representing intensity as function of time in a certain box around a point (E,$k_\parallel$). The second type of dataset consists of energy distribution curves EDC (or momentum distribution curves MDC) as function of time, integrated in a certain range around a $k_\parallel$ value (E value).

To determine the temporal resolution of the experiment, a laser-assisted photoemission (LAPE, Section 1.5.3) signal was analyzed. The corresponding time trace is shown in figure 75. The cross correlation between the EUV and the near infrared is 43 ± 6 fs FWHM. The
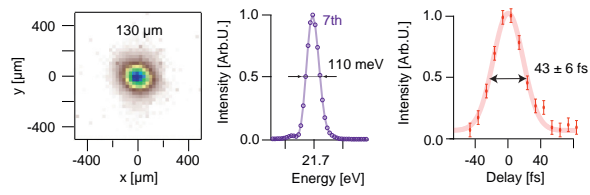
Figure 75: Cross-correlation between the NIR pump and the 21.7 eV probe pulse, measured from a LAPE signal in 2H-WSe$_2$.

NIR pulses FWHM was 35 fs, measured by FROG; this corresponds to a duration of the attosecond pulse train of 25 ± 10 fs, assuming a Gaussian envelope.

TIME- AND ANGLE-RESOLVED PHOTOEMISSION ON 2H-WSE$_2$

After describing the light source and the experimental setup for tr-ARPES, the last chapter of the thesis is devoted to the study of 2H-WSe$_2$, a quasi-bidimensional semiconductor. After a brief description of the physical properties of this material (Section 5.1), two different tr-ARPES experiments will be performed, both exploiting the capabilities of high-repetition rate HHG tr-ARPES.

The first experiment is a demonstration of *excited-state mapping* (Section 5.2): carriers are prepared in the conduction band of 2H-WSe$_2$ by the absorption of 3.1 eV photons. Scattering redistributes the population within few hundreds of femtosecond: during this transient state, the angular distribution of the photoemission from the probe pulses reflects the energy dispersion of the conduction band. EUV photons are required to access the whole reciprocal space Brillouin zone, whereas the high repetition rate combats the intrinsically low signal arising from the low population in the excited states. The mapping data is compared with DFT calculations and the results of different experiments in Section 5.2.1.

The bidimensional nature of 2H-WSe$_2$ (Section 5.1.1) is the origin of several interesting physical properties, among which the presence of strongly bound excitons. This is reflected by strong excitonic peaks in the optical absorption spectrum (Section 5.3).

The carrier dynamic in the conduction band is described in detail for the Σ valley (Section 5.3.1) and the bandgap evolution is followed in time by comparing the valence and the conduction band at the K point in Section 5.3.2. A bandgap renormalization is observed, possibly related to exciton formation.

The second experiment probes the effects of pumping the lowest excitonic feature of the system with the OPCPA fundamental at a photon energy of 1.55 eV. The resonance is associated with the A exciton, which lies $\approx$ 50 meV below the conduction band minima in the K valleySeveral effects can be observed in the tr-ARPES data of the first few hundred femtosecond. Replicas of the valence band appear in the bandgap and the topmost of these replicas overlaps energetically with the A exciton peak. During the pump pulse, the feature evolves in energy and moves upwards toward the A exciton peak center. Simultaneous to these effects, ultrafast scattering occurs between the K point and the Σ point: the time scale of the process is below 20 fs (Section 5.4.3).

The dynamics of the VB and CB were simultaneously observed as a function of fluence, up to a level where the optical excitation is sufficiently strong to drive the transition into saturation (Section 5.4.4).

Initially, the dispersion of the in-gap feature is hole-like, resembling the valence band. On a time scale of few tens of femtoseconds, the feature flattens and flips sign, eventually becoming electron-like as the conduction band (Section 5.4.5). The comparison of the electron-like feature with the conduction band mapped by above-bandgap pumping reveals a difference in energy. This observation suggests that the signal in this case can be associated with a transient A exciton rather than with a single-particle state. The data is in qualitative agreement with a three-level-system model for the two photon-photoemission process, the model is presented in Section 5.4.6.

Finally, the mechanism behind the ultrafast inter-valley scattering is discussed in Section 5.4.7.

5.1 INTRODUCTION: 2H-WSe$_2$.

2H-WSe$_2$ is a member of the transition metal dichalcogenide (TMD) family. This vast class of compounds has the basic formula MX$_2$, where M is transition metal (groups III-XII of the periodic table) and X is a member of chalcogen family (group XVI). The simplicity of the chemical structure is not reflected by TMD's exotic electronic and optical properties, for which these compounds were investigated for half a century [217]. Electrically, TMDs can be metallic, semi-metallic (for example 1T-TiSe$_2$), semiconducting or even insulators: the great variability comes from the degree of filling of the transition metal's d states and the different crystal symmetries. Several TMDs exhibit broken symmetry ground states where lattice distortion and unexpected electric behavior are concomitant: for example, charge density wave and Mott physics are both observable in 1T-TaS$_2$, while 1T-TiSe$_2$ is a proposed excitonic insulator [47, 218].

Group VI (Cr, Mo, W) TMDs are semiconductors which can be thinned down to a single monolayer. Following the discovery of Graphene and of its exceptional properties, these 2d semiconductors have been intensively studied in the past few years: they are at the base of a multitude of proposed electronic and opto-electronic applications, both as monolayers or as atomic-scale heterostructures [219, 220].

The lack of inversion symmetry in the single layer unit cell, together with time-reversal symmetry, imposes that the spin-orbit-split valence bands at K have perfect and opposite spin polarization. This spin texture is reversed for neighboring K points. Circularly-polarized light can selectively excite a spin-polarized carrier population with valley selectivity [221]. This unique spin-valley locking is believed to be at the base of a new paradigm for devices, where charge, spin and valley

degrees of freedoms could be potentially combined into new functionalities [4].

This is not the only exceptional optical property of the semiconducting TMDs: in an isolated monolayer the electron-hole coulomb interaction is screened in a totally different way compared to a bulk material [222]. These excitons, forming after absorption of a photon, exhibit exceptionally high binding energies and rich many-body physics. For example, excitonic molecules such as trions, electron and hole three-body entities, can be observed at room temperature. The excitonic resonance has a very high oscillator strength, which makes light-matter interaction particularly strong in TMDS: for example samples with atomic thicknesses have unusually high absorption (peak absorbance from 0.1-0.3 [220]).

It is possible to realize hetero-structures by stacking monolayers of different TMDs: this artificial crystals promise to integrate multiple functionalities of 2d materials in a single device.

Following these interesting developments, TMDs monolayers where also investigated by tr-ARPES: when compared with optical spectroscopies, ARPES has stricter requirements for sample preparation. The spot size is typically larger (> 100 μm) and the sample has to be in good electrical contact with the experimental ground to minimize charging from the ionizing probe. This rules out the use of transparent dielectric substrates typical of optical experiments. The experiment has to be performed under UHV conditions to minimize surface contamination: these constrains limited the studies to epitaxially-grown samples on conducting substrates such as gold [58, 223] or bilayer graphene [59]. In the first case, the substrate screening is expected to hinder the strong excitonic effects: the study was nonetheless practically relevant to understand the dynamics of photo-excited carriers in contact with a metallic lead. Recent measurements reported valley-selective optical excitation in a single-layer WS_2 on a silver substrate [223]. Graphene bilayer substrates have a comparatively low screening: this allowed to study the photo-induced bandgap renormalization in an heterostructure with a monolayer of MoS_2 on top. The inherent low repetition rate (1 kHz) of the HHG source of these studies, imposed the authors to concentrate mainly on the case of high incident optical pump fluences.

Spin-polarized bands in non-magnetic materials can arise from spin-orbit coupling when the inversion symmetry is broken. This is the case for surfaces, where one talks of *Rashba effect* or for non centrosymmetric bulk materials, where one talks of *Dresselhaus effect*. A TMD monolayer has no inversion points: this is at the base of the reported valley-spin effects. A flipped layer stacking (Section 5.1.1) in the bulk restores inversion symmetry and no spin polarization is expected. This common notion was recently challenged in a theoretical work demonstrating that the spin polarization actually arises by

specific atomic site asymmetries, predicting that spatially localized spin polarization may arise even in centro-symmetric materials [224]. When studying TMDs, an unique feature of ARPES is that, due to the limited escape depth of photoelectrons, the signal originates only from the topmost atomic layers, whereas most of the optical studies are inherently bulk-sensitive. Surface-sensitive spin-resolved ARPES demonstrated that such spin polarization is observable in the topmost layer of 2H-WSe$_2$ [225, 226].

This study paved the way to the study of spin-valleytronic effects also in bulk crystals: tr-ARPES is ideal in this case, being able to resolve ultrafast optical excitations at the surface with momentum resolution (i.e. with valley selectivity). Spin-, valley- and layer-polarized carriers were excited by a circularly-polarized pump and visualized in reciprocal space using a HHG source [20]. Layer-dependent physical properties can be envisaged as another possible mechanism of storing and processing information, naturally embedded in multilayer heterostructures.

Following this vision, understanding the evolution and decay of such polarized currents is of great interest. This motivates further studies, which exploits the newly-developed high-repetition rate tr-ARPES apparatus to better visualize the excited states and map the energy-momentum landscape where these processes take place: these new results will be presented in Section 5.2.

Another interesting aspect is that the screening environment at the surface of a TMD crystal is very different compared to the bulk: this suggest that ramifications of the rich physics of excitons in TMD monolayers could also be observed in tr-ARPES on bulk samples, opposite to conventional bulk-sensitive probes.

5.1.1 *The crystalline structure of* 2H-WSe$_2$.

Among the semiconducting group-VI TMDs, 2H-WSe$_2$ exhibits one of the strongest spin-orbit coupling induced by the heavy tungsten atom. The bulk material has been extensively studied both in theory and in experiments and high-quality, millimeter-size crystals are readily available[1]. Roughly half of the TMDs crystallize in a layered structure whose building block consists of a tri-layer where an atomic sheet of metallic atoms is sandwiched between two sheets of the chalcogen atoms. The structure of such tri-layers is depicted in figure 76, a). When speaking of a TMD monolayer, one refers to this basic unit.

WSe$_2$ belongs to the 2H-polytype: the transition metal is covalently bond to the chalcogen atoms in a trigonal prismatic coordination, resulting in a lack of inversion symmetry for the isolated Se-W-Se monolayer. In the bulk crystal, the overall inversion symmetry is restored thanks to the particular ABAB stacking order where every second

---

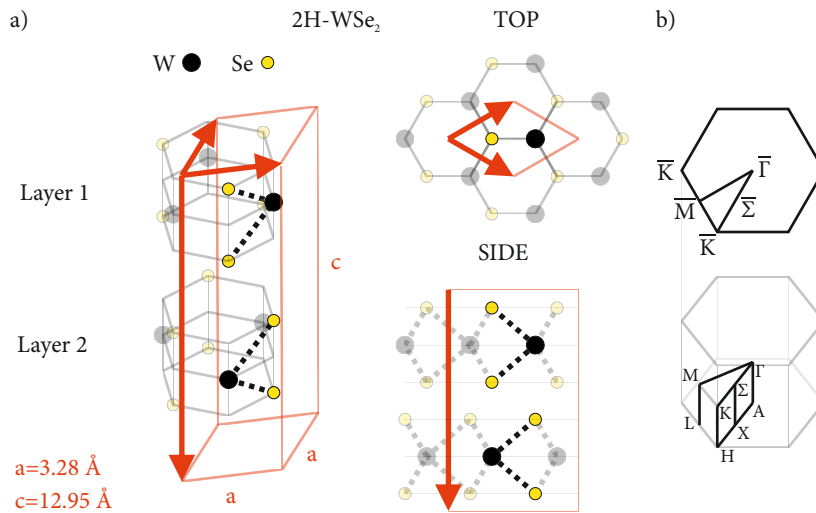1 The samples used in this work where purchased by HQ graphene

Figure 76: a) Real-space lattice structure of 2H-WSe$_2$. The red arrows indicate the unit cell, containing two formula units of WSe$_2$ (thick lines). The trilayer structure and neighboring unit cells are represented as transparent. b) Reciprocal space Brillouin zone and projected surface Brillouin zone. The capital letters indicate the high symmetry points nomenclature adopted in this work.

layer is laterally displaced; the unit cell spans two layers and contains two WSe$_2$ formula units. The lattice is characterized by two lattice costants, a = 3.28 Å and c = 12.95 Å [227]; the thickness of a trilayer (distance between the chalcogen planes) is about 3.6 Å and the interlayer distance is c/2. Successive layers are loosely bound by van der Waals interaction resulting in a strong bidimensional character of the compound. The reciprocal lattice unit cell is shown in Figure 76 b), together with the naming convention adopted in this work for the high symmetry points. The surface-projected Brillouin zone is hexagonal, with a reciprocal lattice unit vector b = 1.74 Å^{-1}. The $\bar{\Gamma}$-$\bar{K}$ distance is 1.274 Å^{-1}.

5.1.2 *The electronic structure of 2H-WSe$_2$.*

The valence band of 2H-WSe$_2$ was investigated by angle-resolved photoemission in the past [228] and was also subject of recent high-resolution ARPES studies [229, 230]. The conduction band along the $\bar{\Gamma}$-$\bar{K}$ was measured with ARIPES (Angle-resolved *inverse* photoemission) [231]. An alternative method to measure the material's conduction band bottom is to artificially move the Fermi level by alkali-metal doping: the bandgap in this strongly doped regime was measured by high-resolution ARPES [232, 233]. After a relative energy alignment, there is generally good agreement when bands calculated by density functional theory (DFT) are overlapped with the occupied states measured by ARPES. The agreement between the experimen-

155

tal and the theoretical band gap is instead poorer (a well-known band problem of DFT in the local-density approximation). When discussing the results of many experiments, the theoretical bandgap is matched a-posteriori to the experimental value.

The literature value of the workfunction of $2H\text{-}WSe_2$ is 4.03 eV [216], in the case of slightly p-doped samples[2]

The material can be considered a good benchmark for excited-state mapping with tr-ARPES as the electronic structure is rather well known and ab-initio calculations are expected to be in good agreement with experiments.

The DFT calculations shown in this work were provided by Hannes Hubener and Angel Rubio[3] and were performed using the PWSCF code of the Quantum Espresso package [234] using the local density approximation (LDA) [235] and norm-conserving relativistic pseudo-potentials, including spin-orbit coupling for the W atoms. Structural parameters were optimised for the bulk configuration and the Brillouin zone was sampled with $12 \times 12 \times 4$ k-points.

The result of DFT calculations along the high-symmetry direction Γ-K are plotted in Figure 77. The k-space cut along which the bands are plotted is indicated on the right side, the k_z component of the wavevector, corresponding to the dispersion direction orthogonal to the layers, has a constant value of $k_z = 0$. The LDA underestimates considerably the band gap: the maximum of the valence band at the K point was chosen as zero of the energy and the over-lying conduction bands were rigidly shifted to match the experimental bandgap in Figure 77.

The uppermost valence bands is characterized by two energy maxima: the first is located at the Brillouin zone center (Γ point). Away from Γ, along the Γ-K direction, a set of two, well-distinguished bands rise toward the second energy maximum, which occurs at the Brillouin zone boundary (K point). The splitting of the two bands originates from the strong spin-orbit coupling and amounts to $\approx$ 500 meV, which compares well to the high-resolution results of reference [230]. The three lowest computed conduction bands are also plotted: the conduction band has two distinct minima (or *valleys*). The first minimum is at the K point: the lowest direct optical transition (direct bandgap) occurs between the K *hill* in the valence band and this K valley. The absolute minimum of the conduction band is located at the Σ valley, half-way between the Γ and the K points. The material has an indirect bandgap occurring between the maximum Γ hill and the Σ valley. While the CB minimum is unambiguously located at Σ point, the assignment in ARPES experiments of the VB maximum between Γ and the K points was controversial [231, 229]. The probable reason for these experimental discrepancies is the remarkable disper-

---

2 The commercial $2H\text{-}WSe_2$ crystals produced by HQ Graphene where p-type, with typical charge carrier densities of $\approx 10^{15}$ cm^{-3} at room temperature.
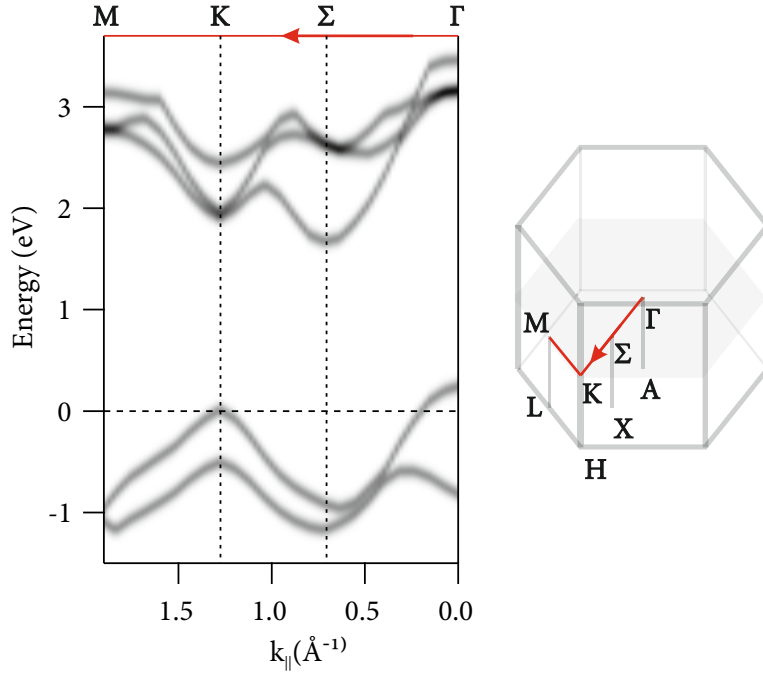3 Max Planck Institute for the structure and dynamics of matter

Figure 77: Calculated DFT bands of 2H-WSe$_2$ along the Γ-Σ-K-M direction of the Brillouin zonefor $k_z = 0$, represented on the left. The conduction bands have been shifted to account for the experimentally-determined bandgap.

sion along the k_z direction for the Γ point bands. Figure 78 shows the calculated k_z-dispersion of the two highest VBs and two lowest CBs, along the high symmetry directions A-Γ-A, X-Σ-X, H-K-H.

Depending on the k-space location, the bands can exhibit considerable dispersion (thick lines), indicating that the bands originate from orbitals with components perpendicular to the layers and that there is also some covalent component in the interlayer cohesive bond which is a signatures of interlayer-coupling and three-dimensional behaviour. This is the case of the VB at the Γ point or the conduction band at the Σ point. The opposite holds true for the valence and conduction bands at the K point, whose k_z dispersion is negligible.

The character of the VB bands and ARPES photoemission matrix elements were investigate in depth in reference [230]. Indeed, it is found that the spin-orbit split valence band at K originates from d_{xy} and $d_{x^2-y^2}$ tungsten orbitals, which are confined in the layer plane. The states at the Γ point have instead a strong Se p_z and W d_{z^2} character.

The determination of the k_z components in an ARPES experiments requires a knowledge of the final state: the plane-wave final state model was discussed in Section 1.2.1. This model was used to fit energy-dependent ARPES data in the work of Finteis et al. [231]: the inner potential was found to be $V_0 = 14.5 \pm 0.5$ eV and the effective $m^* = 1.05 \pm 0.05$, values which will be adopted in this work.
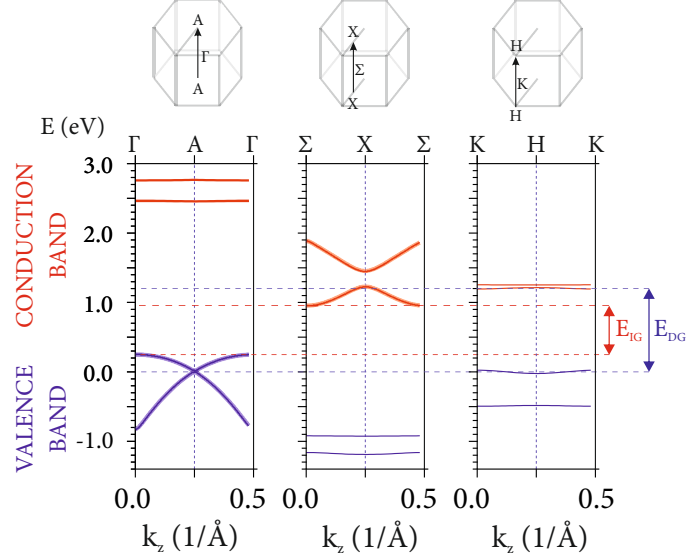
Figure 78: Calculated k_z dispersion along the high symmetry direction Γ-A-Γ (left), Σ-X-Σ (center), K-H-K (right). The LDA-DFT data energy zero was chosen at the average energy of the top valence band at K. The CB was not offset relative to the VB. The indirect E_{IG} (red dotted lines and arrow) and direct E_{DG} bandgaps are highlighted (purple dotted lines and arrow)

Different photon energies probe different position along the A-Γ-A direction: for some energies this band appears to be lower than the H-K-H two-dimensional band. The two band maxima are very close (the energy difference is below 50 meV) and matrix elements effects can in some geometries cancel the contribution from one of the VBs at Γ [231, 229]: this makes the assignment of the indirect bandgap experimentally challenging. The direct (E_{DG}) and indirect (E_{IG}) bandgaps are indicated in Figure 78.

An important consequence of the short escape depth of photoelectrons is that states dispersing in the direction orthogonal to the surface, k_z, are broadened by the indeterminacy in the final state momentum (Section 1.2.3). For this reason the best experimental energy reference are the 2d states at the K point: in this work the zero of energy will be set to the VB maximum at the K point.

The band structure of the material changes when approaching the few-layer limit: states at Γ and Σ are the most affected and there is a remarkable indirect to direct bandgap transition for monolayers, where the Σ valley is at an higher energy than the K valley. The hallmark of this transition is the appearance of strong photoluminescence after optical excitation, indicating that direct radiative carrier recombination can now take place. Such a layer-resolved evolution was measured by combining population of the CB with doping and micrometer-scale ARPES [30, 236].

The ability to observe excited states with momentum resolution is a strong advantage of tr-ARPES (Section 1.5.4). This section will describe an experiment to map the conduction band of 2H-WSe$_2$: several features of the novel light source are used in this study. First, the high repetition rate is fundamental to ensure sufficient statistic at reasonably low pump fluence: as highlighted in Section 4.3.2, the pump-induced space charge become severe already for a fluence $\gtrsim$ 100 μJ/cm^2. The signal from the excited states is typically $\ll 10^{-2}$ relative to the valence band signal: to achieve a sufficient dynamic range to measure the bandgap of the material in a single acquisition, a background suppression method was adopted (Section 4.2). The motorized sample manipulator was used to perform angular scans sampling different portions of the Brillouin zone (Section 4.1). To observe
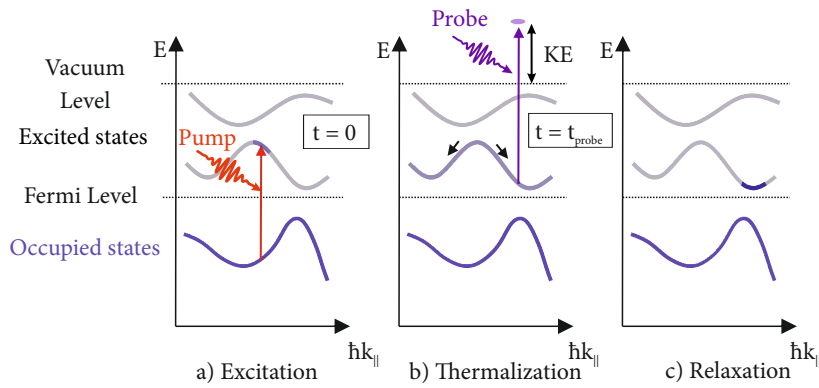

Figure 79: Schematic representation of the excited-state mapping experiment.

the conduction band of the material by means of direct photoemission, it is first necessary to populate it. The basic idea is illustrated in Figure 79: after resonant optical excitation, a non-equilibrium distribution of hot carriers is created in one or more regions of the Brillouin zone (panel a). Electron-electron and electron-phonon scattering processes redistribute energy and momentum as the hot electrons thermalize. This process is very rapid and in the first hundreds of femtoseconds the carriers populate most of the conduction band below the energy of the optical transition. A short EUV pulse can now be used to photo-emit the excited carriers and map the conduction band (panel b).

Energy exchange occurs between the carriers and the lattice: owing to the higher heat capacity of the lattice, the electronic distribution swiftly cools and carriers tend to concentrate at the conduction band's bottom. Electron-phonon scattering contributes to the process at all times and a non-thermal distribution of phonons accompanies the carrier relaxation in the first few picoseconds. As soon as the carriers

are concentrated at the band bottom, the fastest dynamics come to an end as the phase space for further scattering is reduced (panel c).

The experimental setup is schematized in Figure 80. Femtosecond pump pulses with a photon energy of 3.1 eV are obtained from SHG of the driver laser: the temporal resolution in the experiments was $\gtrsim$ 100 fs. Since the second harmonic is generated with a 100-μm-thick BBO crystal, supporting $\approx$ 30 fs pulses, the main source of pulse lengthening are the transmissive optics used in the beam path.
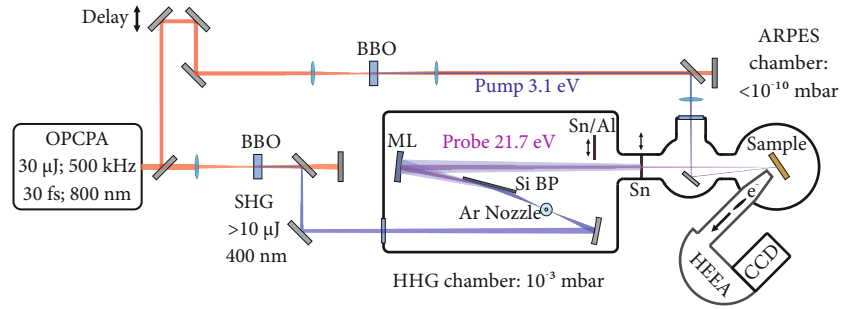

Figure 80: Schematic of the experimental setup for tr-ARPES experiment. SHG: second harmonic generation; BP: Brewster plate; ML: Multilayer mirror; HEEA: hemispherical electron energy analyser.

The sample is excited with a peak fluence of about 200 μJ/cm^2 and the population relaxation is followed in time by the delayed XUV probe[4]. By observing the system 100 fs after photoexcitation with the short XUV pulse, a snapshot of the surface band structure can be measured. The photo-excited band structure is remarkably comparable to the one derived from density functional theory (Figure 77 and Section 5.2.1). The energy analyser was set to acquire simultaneously occupied and excited state's photoelectrons. The same detector and the same energy reference are used for both states: this strategy removes any uncertainty of relative energy-level alignment, which is typical in a comparison between direct and inverse photoemission. An example of the acquired data is shown in Figure 81 a).

The plot corresponds to a line cut along the surface's high-symmetry direction $\bar{\Gamma}$-$\bar{K}$. The lower part shows a reference spectrum before photoexcitation: after the energy is deposited there is a remarkable broadening and a moderate bandgap closure (<50 meV, Section 5.3.2).

At high momenta, two spin-orbit split bands disperse toward the apparent VB top at the K point: as illustrated in Section 5.1.2, these two-dimensional bands have a narrow width, insensitive to the broadening associated with k$_z$-dispersion. The valence band energy max-

---

4 At this fluence some space charge effects were already observable, as observed in Section 4.3.2, however, given the intrinsic broad energy-width of the excited states, compared to the VB, to speed up data acquisition a broadening close to $\approx$ 100 meV was tolerated and 1-mm-wide slit was used.
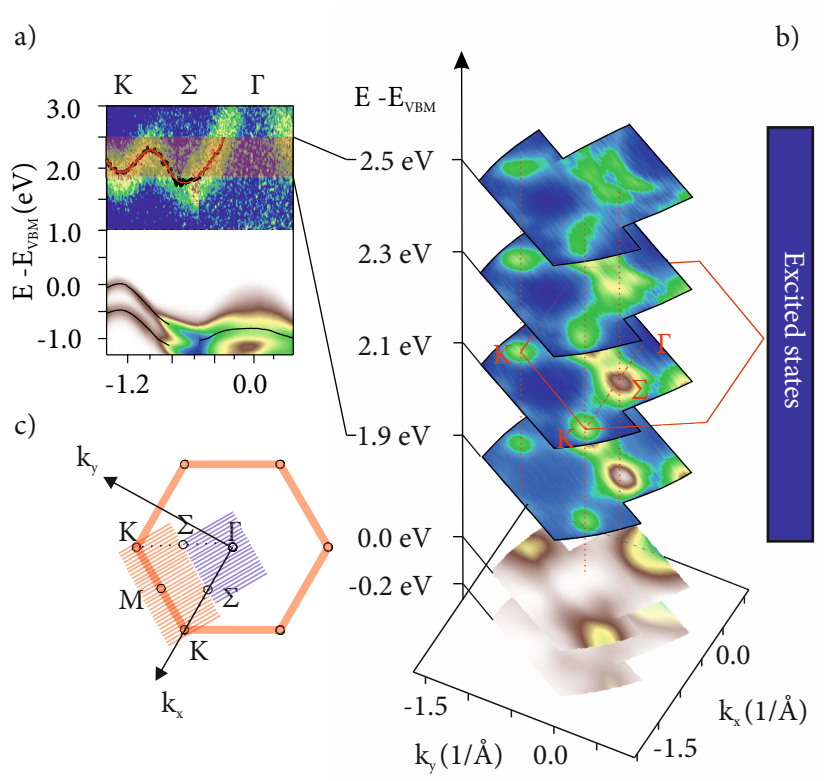
Figure 81: Experimental results of the unoccupied band-structure mapping in 2H-WSe$_2$. a) Line-cut along Γ-Σ-K, showing both valence and conduction band. b) Costant energy maps of the unoccupied states. c) Sampling of the Brillouin zone.

imum at $\bar{K}$ was used as zero reference. There is an apparent discrepancy in the relative position of the Γ to the K point, compared to DFT: this is the consequence of the k_z dispersion and the experimental photon energy of 21.7 eV. The image in Section 5.1.2 consists of two data acquisition at different emission angle, matched in intensity for a clearer display: at the probe photon energy, the photo-emission cone is too wide for the whole Brillouin zone to fit the analyser's angular acceptance.

Above the bandgap, and for a delay of 100 fs (see Section 5.3.1 for the definition of time-zero), the conduction band is visible: in the figure, two different false-color scales where employed for clarity, since the signal of the CB is about two orders of magnitude weaker. Both the K and the Σ valley are visible and the conduction band bottom is located at the Σ point: the sample's surface layers have still an indirect bandgap, as calculated for the bulk.

At this pump-probe delay, a large portion of the conduction band can be observed: it is therefore feasible to attempt an angular scan and combine several acquisitions to get a k-resolved picture of the excited state throughout the Brillouin zone. The reciprocal space sampling is schematized in Figure 81 b): it encloses the path Γ-Σ-K-M-K-Σ-Γ, thereby covering the first unit cell. For two θ angles of the manipulator (see Section 4.1 for the definition of the scan angles), 10° (blue lines) and 30° (blue lines), the β angle was scanned in 1°steps to cover the area of interest. The scan ranges are $(\theta, \beta) = (10°, -20° : 13°)$ and $(\theta, \beta) = (30°, -28° : 28°)$; the acceptance angle along the θ direction is $\pm 15°$.

The results of such a mapping experiment are displayed in Figure 81 c). To produce such a plot it is necessary to properly merge the two datasets and to convert the angular units into reciprocal lattice vector. This kind of analysis is well-established in the ARPES community and a set of pre-existing routines within the software IGOR pro[5] were used for the task[6]. There is a region of overlap between the datasets of approximately five degrees, which was used to re-normalize the two datasets ensuring continuity of the intensity. Due to the slightly different pump fluence for the two scans and the associated space charge, the dataset containing the Γ point was offset in energy relative to each other by about 10 meV. The well-defined energy of the valence bands dispersing toward the K point was used in this case as a reference. The data conversion from angular units to reciprocal lattice wavevectors was obtained re-sampling the data on an uniform k-space grid with the same amount of points. For displaying purposes, and only for the Figure 81 c), the data was slightly over-sampled (about 50% more) and smoothed with a N=2 median filter. For all the other plots no further data treatment was performed.

---

5 Igor Pro, WaveMetrics, Lake Oswego, OR, USA
6 originally developed by Felix Schmitt, Stanford University

The three-dimensional dataset cannot be displayed in a single plot: the exploded view in Figure 81 c) corresponds to several cuts through the datasets, representing intensity distributions at a constant energy or *constant energy maps*. The energy range covers the area from 1.9 eV to 2.5 eV in the unoccupied states, represented by the red transparent area in panel b). The reciprocal space cell is overlaid on the second cut, to indicate the position of the K and the Σ valley. This view reveals how the neighboring Σ valleys are connected at higher energies along the Σ-Σ direction. Simultaneously, the occupied band structure is also recorded: constant energy cuts in a different false color plot represent the top of the valence band. The three-dimensional dataset contains the full information about the k-space structure of the material's bandgap.

5.2.1 *Comparison with density functional theory*

The TMDs bandstructure can be calculated with ab-initio DFT methods: these theoretical results are the key for interpreting experiments lacking the full momentum resolution of ARPES, such as scanning probe and optical spectroscopies. The occupied bands are typically in good agreement with DFT results (Section 5.1.2) and theory can account for the measured band dispersion and the relative energy alignment of the K and Γ point maxima.

Density functional theory simplify the many-body problem of solving the N-electron Hamiltonian by mapping it into a tractable set of single electron equations, the Kohn-Sham equations [237, 238]. In principle, the solution of the equations produces the true ground state energy and electronic density. The complexity of the many-body problem is hidden in the so-called exchange correlation potential, which has to be approximated: at the most basic level this is replaced with a functional of the local electronic density, in short LDA, local density approximation. The numerical solution of the Kohn-Sham equations is done self-consistently and produces a set of Kohn-Sham energies and orbitals, from which the ground state density can be calculated. Taken alone, the KS energies cannot be generally interpreted as the system's single-particle energies (the energy for the removal or the addition of an electron, measured by direct and inverse photoemission in first approximation), nonetheless, they are often in good agreement with experimentally determined band-structures and the practice of using these results is widespread. DFT underestimates systematically a material's bandgap, when the energy difference between the lowest unoccupied and highest occupied KS orbitals is compared to the experimentally-determined values (e.g. by measuring the optical absorption edge). This is the well-known *bandgap problem* of DFT, which would persist even if the exact exchange-correlation potential was known [239].

A more correct description of quasi-particle energies can be obtained at a higher level of theory, correcting DFT using many-body perturbation theory: the most common approach is to use the so-called GW method [240]. This method produces a band-structure which is expected to describe well the quasi-particle energies measured in photoemission (or inverse photoemission), however, it does not describe correctly neutral excitation such as an optically excited state.

To calculate the optical properties of a material, in the form of its dielectric function, the interaction of an electron-hole pair needs to be considered. This can be done with a further refinement, involving the solution of the Bethe-Selpeter equation [241]: at a higher computational cost, BSE calculations predict improved statical optical properties, including excitonic peaks.

In a tr-ARPES experiment one observes the temporal evolution and the relaxation of a solid after an optical excitation. The interaction with an optical field, the creation of electron-hole pairs, the formation of bound excitons, the scattering of carriers with the rest of the electronic system and with the lattice: all these aspects come into play. An ab-initio microscopic description of such a processes is beyond the limit of current theories. There are ongoing strives to extend DFT to describe excited states and temporal evolution in a computationally-tractable manner: *time-dependent density functional theory* or TDDFT is one of the most well-established [242], and it was also recently applied for the description of tr-ARPES [20, 243, 244].

5.2.1.1 *Comparison with the experiment*

The data presented in the previous section is a rather interesting benchmark: how well does the measured bandgap compare with the one determined by other techniques and different theories?

The first step is to compare the experimental results with conventional LDA-DFT calculations (see Section 5.1.2 for the computational details). The simulations, performed on $12 \times 12 \times 4$ grid in reciprocal space, was sampled using the internal packages of the Quantum Espresso package to a $24 \times 24 \times 8$ grid. The resulting KS energies, where re-interpolated on the experimental grid and compared with the data.

The first problem in doing this comparison is the relative energy alignment of the bands: following the arguments in Section 5.1.2, the VB maximum at the K point was used as a reference, both for the experimental data and the DFT bands. The conduction bands were rigidly shifted in energy to match the measured K valley: this operation, in jargon called *scissor operator*, is a crude way of accounting for the bandgap problem. In the theoretical data, two nearly-degenerate conduction bands appear at K (Figure 78): the average energy, including the small dispersion along k_z, was used to align the theoretical band with the experiment.

The second problem is how to handle the k_z dispersion. As shown in Section 5.1.2, the lowest conduction bands exhibit considerable dispersion orthogonal to the layers. Using the free-electron final state parameters from the literature (Section 5.1.2), it is possible to associate every measured point with a well defined k_z, however, the momentum resolution in this direction is generally unknown. The momentum broadening should reflect the short escape depth, following Heisenberg indeterminacy principle one expects $\delta k_z > 1/2\lambda$, where λ is the escape depth, section 1.2.3. Assuming that this depth is on the order of $c/2$[7], half the unit cell in the z direction, the momentum broadening in the orthogonal direction is $\gtrsim 0.08$ Å^{-1}. The size of the reciprocal space Brillouin zone in this direction is 0.48 Å^{-1}: the uncertainty is therefore a considerable fraction of the zone size. It was therefore decided to leave the whole k_z bandwidth on the DFT bands, which are displayed as bundles encompassing the energy dispersion of the KS eigenvalue from which they originate. The comparison was performed on line-cut along the symmetry direction Γ-Σ-K-M. The results are shown in Figure 82.
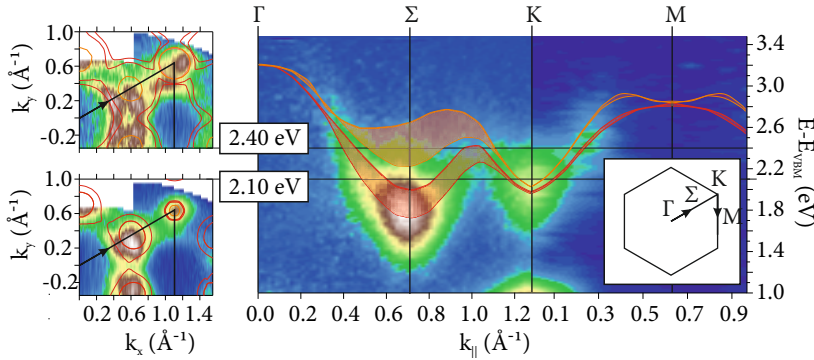

Figure 82: Comparison of 2H-WSe$_2$ excited-state mapping and LDA-DFT calculation. Left: costant energy intensity distributions with the position of DFT bands. Right Γ-Σ-K-M cut through the data, compared with the DFT bands, the shaded regions in the theoretical bands represent the full energy dispersion in the k_z direction. The Γ-Σ-K-M path is indicated on the Brillouin zonein the panel.

On the right panel, the two lowest DFT conduction bands are superimposed with the experimental energy versus momentum intensity distribution. The scissor operator used for the comparison was nearly 800 meV. On the left side, two constant energy maps are plotted with the constant energy contours of the DFT results. The LDA bands are in qualitative agreement with the data: in the case of strongly dispersing bands like the conduction band at Σ (CB_Σ) and the valence band at Γ (VB_Γ), one can use the measured energy and emission angle to

---

7 The assumption is supported by the results of spin-resolved ARPES [229] and time-resolved ARPES [20], where a nearly perfect spin polarization was observed at a comparable probe photon energy.

calculate the corresponding k_z using the free-electron final state model. The k_z are 0.46 Å^{-1} and 0.47 Å^{-1} for CB_Σ and VB_Γ, respectively. The measured band position can be compared with the DFT energies in Figure 78 at these k_z values: after applying a 800 meV offset for the conduction band, the energy difference from the experiment is $\Delta_{VB,\Gamma} = -5$ meV and $\Delta_{CB,\Sigma} = 20$ meV.

5.2.2 *Bandgap comparison between different techniques*

The bandgap of 2H-WSe$_2$ was studied in several works in the literature, both experimental and theoretical. Figure 83 reports the literature value for the direct bandgap determined by optics [245, 246], by comparing direct and inverse photoemission [231], or performing direct photoemission on alkali-atom-doped samples [232, 233]. In this work, we define the bandgap as the difference of the CB and VB centers, extracted from a Gaussian fit of the data. This definition was chosen since the width of the photoemission bands is related to several physical mechanisms, not related to the on-set of band to band transitions (see Section 1.2.2 for a discussion on the photoemission lineshape).

To minimize the influence of space charge and the amount of photo-generated carriers, a second experiment was performed and the fluence was reduced to approximately 70 μJ/cm^2, the estimated photo-doping is $\approx 1.0 \times 10^{13}$ cm^{-2} (see Appendix A). Figure 83 a) shows a line-cut at the K valley, extracted from this mapping dataset. The plot includes also the VB, measured simultaneously. The absolute value of the direct bandgap in 2H-WSe$_2$ is 1.78 eV.

In the case of optical absorption, an analysis of the absorption edge has to be performed to extract the onset of band to band transitions: the optical spectra at the absorption edge is strongly renormalized by excitonic effects (which will be described in greater detail in Section 5.3). In the case of ARIPES, the main complication is to define a common energy reference with the ARPES data used for comparison: Finteis et al. report an error of about 100 meV for the procedure [231]. In the case of atomic dopants, the estimated dopant density was $\approx 2.6 \times 10^{13}$ and the bandgap was defined as the onset of the intensity in the CB feature seen in the ARPES spectra, there is no well-defined peak-like feature in this case [233]. A possible limitation of this approach is that the alkali atoms can induce secondary effects on the band-structure, such as the breaking of the symmetry of the topmost trilayer and the appearance of new replica valence bands at the K point [232].

The graph also reports theoretical results found in the literature, together with the one reported in the previous section: the first column shows the results of DFT at the LDA level, where the diamond marker represents our results, while the triangles are taken from the work of

Roldán et. al. and references cited therein [247]. The second column reports GW-corrected DFT for bulk [248] and for bilayer WSe$_2$ [249]; the last columnt is the A exciton position calculated via the Bethe-Selpeter equation for a bilayer [249]; the bilayer data can be identified in the plot by triangular markers pointing to the bottom.
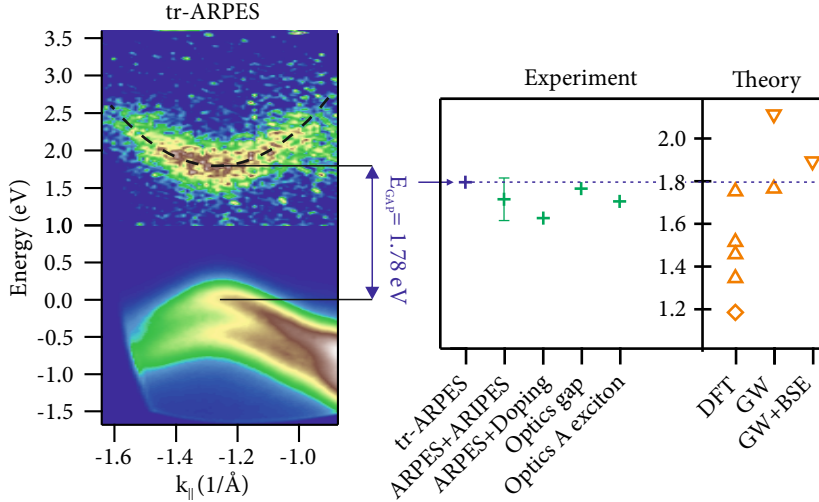

Figure 83: Left: mapping of the K point. Right: comparison of the measured direct bandgap of 2H-WSe$_2$ at the K-point between this work and several experiments and theoretical results. From various references, indicated in the text.

The measured direct bandgap compares well both with the ARIPES and the optical gap, whereas the doping data reports a lower value for the gap, possibly due to the discrepancy in the procedure for determining the gap or for the modification induced by the dopants. The biggest spread in results is observed for the LDA values, which likely depend on the variability of functionals adopted, but in general tend to underestimate the gap. The closest match is given by the GW calculation of Jiang et al. [248], whereas the discrepancy in calculations of He et al. [249] might be due to the fact that the investigated system was a bilayer. The BSE results for the bilayer were included due to the current lack of a proper bulk reference. The bilayer data in Figure 83 illustrates well how the BSE renormalizes the bandgap.

It must be noted that there is a 200 meV disagreement in the measured band gap between the low fluence mapping data and the higher fluence mapping of Section 5.2, the latter being almost 2 eV. A higher fluence alone cannot explain this shift: as it will be shown in Section 5.3.1), the band gap tends to close more for a higher incident flux. Charging effects are expected, in a first approximation, to affect the CB and the VB photoelectrons in a similar way, and should be mostly cancelled out since the energy axis is referenced to the VB position, making this discrepancy of 200 meV hardly explainable.

Values closer to ≈ 1.8 eV were consistently reported for most of the samples in several independent measurements: the 2.0 eV band-gap was not reproducible, pointing either to some systematic error in the analysis or to some specific feature of the sample, for example the measurement could have been performed on a flake produced by the cleaving procedure. The datasets of Section 5.2 and 5.2.1 still demonstrate the feasibility of excited-state mapping. The comparison with DFT of the low fluence dataset yields a reduced scissor operator of 600 meV; the change in orthogonal momentum due to the lower photoelectron's kinetic energy increases the discrepancy with theory at the Σ point ($\Delta_{CB,\Sigma}$) by 8 meV.

The measurement performed so far present a snapshot of the band-structure at fixed time: the comparison of this data with the static calculations rely on the assumption that the excitation does not significantly perturb the quasi-particle bands. At least at a qualitative level, the exited states still resemble the DFT calculations and the measured bandgap is in good agreement with static data. The following sections concentrate on the temporal evolution of these excited states and investigate the renormalization phenomena occurring in the quasi-particle bands.

5.3 CARRIER AND EXCITON DYNAMICS IN TMDS

An optical excitation creates electron-hole pairs: in a semiconducting or insulating environment, the Coulomb interaction between this two oppositely charged quasi-particles is not perfectly screened. This attractive potential, can give rise to bound electron-hole pairs, known as excitons [250]. These bound states appear as resonances in the optical absorption which renormalizes the optical bandgap, reducing it from the value expected from a bare band-to-band transition. In a bulk semiconductor, the exciton binding energies are typically rather weak (e.g. 15 meV for silicon) and the exciton wave-function covers several unit cells: one talks in this case about *Wannier* excitons. Wannier excitons, forming between two bands with masses $m_{VB} = m_h^*$ and $m_{CB} = m_e^*$, can be described in an effective mass approximation. The binding energies follows an hydrogen-like series [251, 252]:

$$E_n = E_{gap} - \frac{\mu e^4}{2\hbar^2 \epsilon^2} \frac{1}{n^2}, \tag{113}$$

where the reduced mass is defined as $\mu^{-1} = m_h^{*-1} + m_e^{*-1}$. The low exciton binding energy, relative to the hydrogen case, come from the high dielectric function ($\epsilon \approx 10$) and the relatively small effective masses ($\approx 0.5 \ m_e$) observed in most semiconductors. Due to these low binding energies, only at the lowest temperature such resonances appear as distinct peaks in the optical spectrum.

The two-dimensional nature of the TMDs enhances these effects: for example, excitons in bulk TMDs[8] have a comparatively high binding energy $\gtrsim 50$ meV [253, 245]. Once reduced to the few layer limit, the screening is so weakened that the exciton binding energies are one order of magnitude higher [222]. Excitons can form at any critical point where the electron and holes group velocities are the same [250]:

$$\nabla_{\mathbf{k}}[\epsilon_{CB}(\mathbf{k}) - \epsilon_{VB}(\mathbf{k})] = 0. \tag{114}$$

The condition is met for direct optical transitions between band extrema (hills and valleys) and more generally where regions of the bands are parallel to each other. Even if the word *bound* is often used to describe excitons, it must be stressed that these quasi-particles are transient in nature, and eventually electron-hole pairs will recombine at equilibrium.

The measured optical absorption for bulk 2H-WSe$_2$ at liquid-nitrogen temperature is shown in Figure 84. The strongest resonances are the so-called A and B excitons, originating from direct transition between the spin-split valence band and the conduction band valley at the K point. The VB splitting is about 500 meV, in good agreement with the observed A and B peak separation (Section 5.1.2).
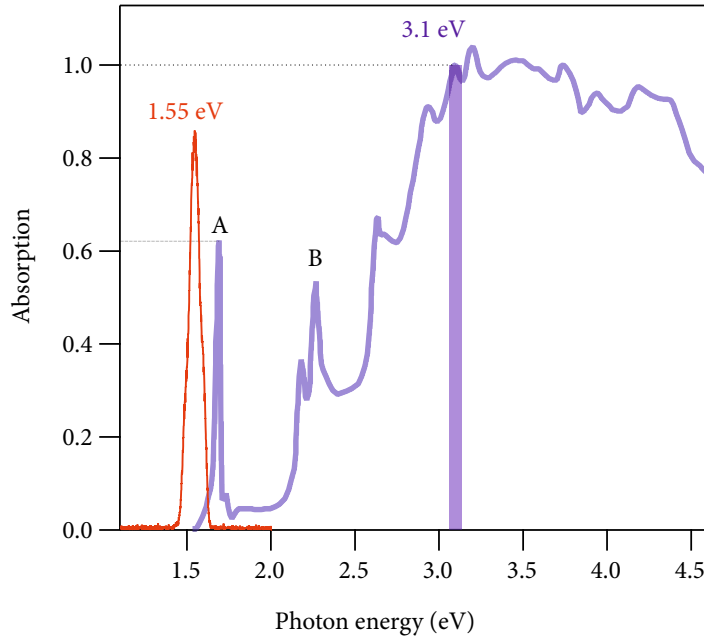

Figure 84: Optical absorption spectrum of 2H-WSe$_2$, adapted from reference [253]. The red line shows the spectrum intensity in arbitrary units of the OPCPA tuned at 800 nm. The blue line indicates the position of the 3.1 eV pump. The data was normalized to the absorption at 3.1 eV.

---

8 The excitonic properties of 2H-WSe$_2$ will be summarized in Section 5.4.1

The A and B excitons can be observed with optical spectroscopies, as they originate from direct optical transitions. These *bright excitons* are in contrast to so-called *dark excitons*, which posses a total momentum $K \neq 0$ and can only decay non-radiatively.

Figure 84 reports the position of the 3.1 eV optical pump used in the previous experiment, together with the spectrum of the fundamental of the laser. The UV pump photons excite electron-hole pairs well above the gap edge: in this case one expects that excitons do not form directly but only after a certain amount of scattering events have relaxed the system to the bottom of the conduction band. Due to the lower sensitivity of tr-ARPES experiments, comparatively higher excitation densities are used, resulting in a non-negligible perturbation of the system: the presence of excited carriers modify the screening properties, dynamically reducing the exciton binding energy. Electron-phonon coupling has also to be taken into account for non-radiative exciton decay via phonon absorption or emission: optical excitation results in a change in the system's phonon distribution, thereby indirectly changing the exciton dynamics. A quantitative simulation of similar processes, including the ultrafast optical excitation was only recently presented in the theoretical work of Selig et al. [254, 255]. In such a simulation, which is not based exclusively on ab-initio methods, one can follow in time the exciton formation and the evolution of free carrier and exciton populations undergoing electron-electron and electron-phonon scattering.

THz spectroscopy allows to distinguish between free-carrier-like behaviour and bound excitons [256]. This is accomplished by measuring the THz probe's waveform, and determining the relative contribution of free-carriers (Drude-like response) and the resonant transitions of the excitonic series. The observation of such transitions do not require an optically bright state: also dark excitons can be probed directly, as long as the total momentum of the exciton is unchanged. THz studies where performed on monolayer WSe_2 (where the 1s-1p transition energy is $\approx$ 170 meV [257]): the results show that there is a non-instantaneous exciton formation time and a different evolution of the free-carriers and excitons [258]. This all-optical technique, unlike tr-ARPES is missing direct informations on the quasi-particle momentum.

5.3.0.1 *tr-ARPES studies of excitons*

Time-resolved photoemission from excitons was already reported: excitons can either be observed after resonant excitation [259], or their formation can follow inter-band excitation after longer times [260]. After ionization by photoemission, the exciton's original hole is left behind and the photoemission spectrum shows a peak below the conduction band, separated approximately by the exciton binding energy. If such an energy difference is comparable with the experimental

energy resolution, one can expect a bound exciton to appear more like a broadening and shift of the conduction band signal toward the lower kinetic energy side. There are however several other contributions to the quasi-particle band shape and position. One is the renormalization of the quasi-particle peak coming from the self-energy of the photo-holes created in the conduction band by photoemission Section 1.2.2.

A second possible effect can be observed when the optical excitations triggers a coherent lattice motion: in this case the energy position of the bands might also follow a temporal evolution. In time-resolved optical experiments, a coherent oscillation of the A_{1g} optical phonon mode was observed, triggered by a NIR pump resonant with the A exciton [261] (see also Section 5.4). According to the calculation reported by the authors, to explain a shift of 100 meV, a lattice distortion of more than 4% along the A_{1g} phonon mode is required.

Finally, the increase in average temperature of the lattice following the excitation is also a source of variation of the bare band position: this is a well known effect and was investigated in $2H\text{-}WSe_2$ by Arora et al. [246]. The authors fitted the following function on the experimental data:

$$E_{gap}(T) = E_0 - \frac{\alpha T^2}{T + \beta}$$

$$\alpha = 3.44 \times 10^{-4} \, eV K^{-1}$$

$$\beta = 170 \, K$$

(115)

Using the fitted parameters, the model predicts approximately a linear decrease above room temperature of 30 meV every 100 K. This shifts might also play a role once a considerable fraction of the electron's energy is transferred to the lattice, after several picoseconds. These effects are all potentially time-dependent and non-trivial to disentangle from each other in the experimental data.

5.3.0.2 *tr-ARPES experiments on bulk TMDs.*

Several photoemission experiments already exists on bulk TMDs and in $2H\text{-}WSe_2$ in particular. One of the first time-resolved photoemission studies was actually performed by the group of Haight on $2H\text{-}WSe_2$ with a 200 fs resolution [262]. A reduction of the CB signal over time was observed and associated with transport of the photoexcited carriers toward the bulk (in this seminal work, no parallel momentum detection was implemented and only few specific positions in the Brillouin zone were investigated). Recently, two studies on $2H\text{-}MoS_2$ were reported, concentrating on the ultrafast dynamics of hot electrons triggered by a pump with 400 nm wavelength[61], or on the fast intra-valley scattering, following resonant pumping of the A exciton [60]. The first work is the most relevant when comparing with the

3.1-eV-induced dynamics: the main focus of the paper was to determine the carrier relaxation times for $2H\text{-}MoS_2$, it was however lacking sufficient statistics to map the excited states. Bulk $2H\text{-}WSe_2$ was measured by Bertoni et al. [20]: the emphasis of this work was on the possibility of valley-selective excitation, using a circularly-polarized pump resonant to the A exciton. The optical absorption at the K point is followed by a fast inter-valley scattering toward the Σ valley: this effect will be explored in a greater detail in Section 5.4.

5.3.1 *Conduction band dynamics, 3.1 eV pump*

The first step of our study concentrates on determining where the optical excitation occurs in the Brillouin zone. Figure 85 reports a set of snapshots of the unoccupied states collected as a function of time along the $\Gamma\text{-}\Sigma$ direction. At early delays the signal is localized close to -0.3 Å^{-1}, at an energy of 2 eV above the valence band maximum at the K point[9]. By integrating a small portion of intensity in this area and fitting the rising edge with a Gaussian pulse, it was possible to define a reference for the pump and probe overlap. The temporal resolution was approximately 100 fs FWHM. A background, particularly visible at high energies in the -100 fs snapshot is coming from a residual contamination of the 9th harmonic, as in this scan a second Sn foil (Section 3.5) was not used.

The collected data shows how, within the pump pulse temporal envelope, the initially confined carriers quickly redistribute across the conduction band as effect of thermalization. Simultaneously, the interaction with the lattice start to quickly dissipate the overall hot electron's energy: already after 1 picosecond, the scattering has relaxed most of the carriers to the bottom of the Σ valley.

5.3.1.1 *Momentum relaxation dynamics*

To have a clearer overview of the temporal evolution of the carrier population as a function of time, two energy-integrated, momentum-resolved datasets were recorded, covering the $\Gamma\text{-}\Sigma\text{-}K$ direction. The results are shown in Figure 86: from this plot it is clear that after the initial redistribution of electrons across the conduction band, for $t < 200$ fs, the electron-phonon scattering start to narrow the momentum distribution, as carriers scatter towards the local minima of the K and Σ valleys. The mapping of the previous section was performed around 100 fs when most of the k-states are populated. Within about 1.5 ps the inter-valley scattering is complete and no intensity is observed at the K point. A line-cut through the data at the Σ point is plotted on the right-hand side of Figure 86 and is fitted with a single

---

9 The VB position at the K point was measured in a previous scan and used to calibrate the kinetic energy measured by the electron analyser.
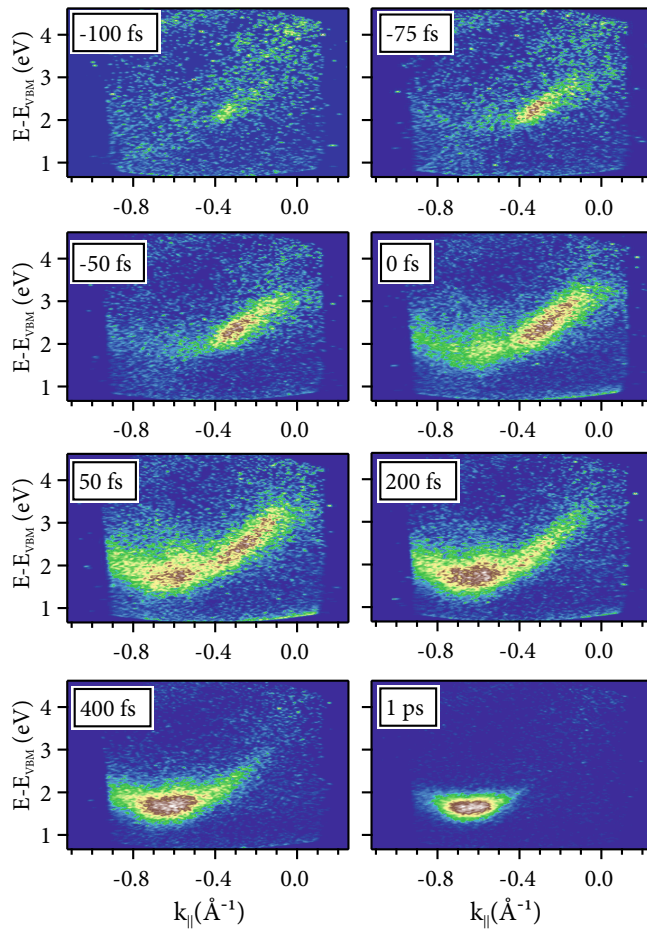
Figure 85: Dynamics along the Γ-Σ direction at short times after excitation, for a 3.1 eV pump photon energy. The optical excitation occurs close to the Γ point, located on the right hand side of the images. The energy is referenced on the maximum of the valence band at the K point.
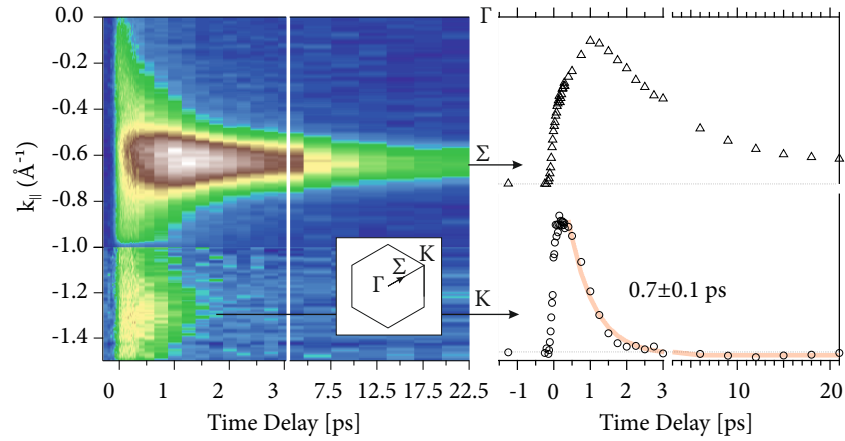
Figure 86: Left hand side: carrier momentum distribution as a function of time delay. The data is collected along the Γ-Σ-K direction indicated in the small box. Right hand side: line cuts of the data, showing the intensity as a function of time at the K and Σ points. The transparent line indicates a fit with a single exponential.

exponential decay, indicating an effective decay time of the intensity at K of about 0.7 ± 0.1 ps. This time does not reflect the lifetime of an electron at the bottom a the Σ valley, as different channels, such as population coming from higher lying states or from the Σ valley partially replenish the K point as it decays. The same trace extracted at the Σ valley shows a more complicated temporal behavior which could not be fitted by a single effective time constant.

5.3.1.2 *Carrier relaxation in the Σ valley.*

By observing the intensity in the left-hand side of Figure 86, it is clear that the total signal is initially increasing and peaks at around 1-2 ps: this is due to the limited observation window which is restricted to a line-cut through the k-space. As electrons cool within the Σ valley contributions from carriers outside the observation window tend to gather at the narrower band minimum. It is rather difficult to interpret the intensity traces extracted from such data: both intra-valley and inter-valley scattering within and outside the observation window should be considered. As a first approximation, an isotropic behaviour was assumed. The total energy within the Σ valley was integrated, increasing the statistical weigth of the points further away from the central position of the band.

The Σ valley was approximated by a parabolic band (see Figure 87 a) centered at about -0.6 Å^{-1}. Within an area of interest delimited by the black curve in 87 a), the intensity $I_{i,j}$ of every (i,j)-th pixel, was multiplied by the energy difference from the band bottom ΔE_j and

by $2\pi k_i$. The total energy within the Σ valley was obtained with the following sum:

$$E(t) = \sum_{i,j} I_{i,j}(t)\Delta E_j 2\pi k_i. \qquad (116)$$

This rough estimate, assumes constant matrix elements, parabolic band shape and neglegts k_z dispersion, implicitly assuming that the tr-ARPES data integrates over the whole three-dimensional Brillouin zone. The results are illustrated in Figure 87 b). The energy relaxation
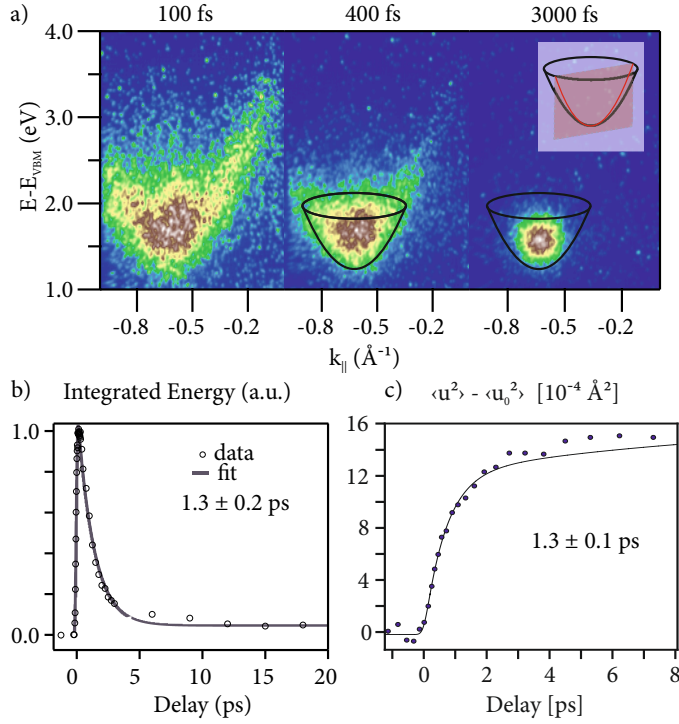

Figure 87: a) Snap-shot of the band-structure at the Σ point at 100 fs, 400 fs and 3 ps with a 3.1 eV pump. In the panel an illustration shows how a single measurement collects only a bidimensional cut along a specific k-direction. b) Energy, relaxation in the Σ valley as calculated with (116). c) Mean square displacement obtained with a femtosecond electron diffraction experiment, courtesy of Roman Bertoni and Lutz Waldecker, Fritz-Haber Institute.

constant extracted with this procedure is 1.3 ps; which is in agreement with the rise time of the Debye-Waller factor of the electron diffraction peak, measured in an independent femtosecond time-resolved experiment (Figure 87 c)). The carrier cooling within the Σ valley seems to be compatible with the increase in lattice temperature in the diffraction experiment.

The photo-excitation transfers a significant population in the conduction band, leaving behind a non-equilibrium hole distribution in the valence band. Figure 88 presents an overview of what occurs along the K-Σ direction, both in the VB and the CB. A visible broade-
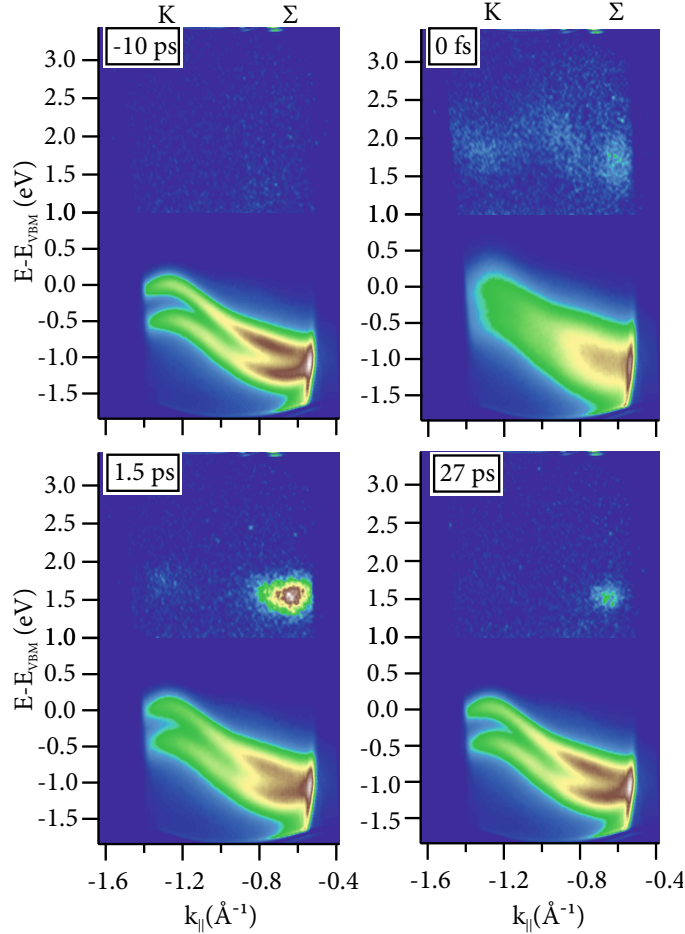

Figure 88: Dynamical response of 2H-WSe$_2$ along the K-Σ direction after a 3.1 eV pump, with a fluence of 380 μJ/cm^2. Each delay shows simultaneously the VB and the CB, using two false color scales, split around 1 eV.

ning in the VB occurs at time zero, making the two original bands almost indistinguishable. Within few picoseconds the bands become separated again, although still significantly broadened. The brodening nearly disappears after some tens of picoseconds, when the carriers are only visible at the bottom of the Σ valley.

The two-dimensional states at the K point are well suited for observing the pump-induced broadening, as they reflect the true quasiparticle linewidth (Section 1.2.3). An EDC at the K point, including both VB and CB is shown in Figure 89. The VB was fitted by two gaussian functions; a Shirley background [215] was used to account for in-
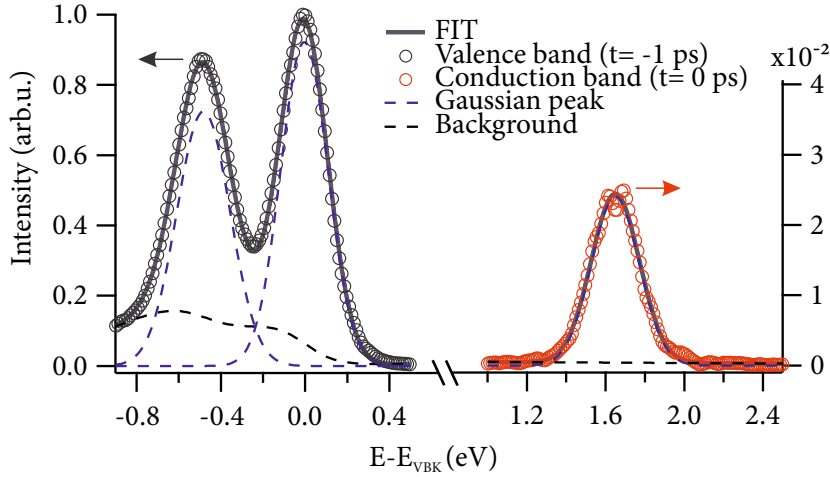
Figure 89: Illustration of the fitting procedure on an EDC collected at the K point. The CB and VB are fitted independently, the fit components are indicated by dotted black lines, whereas the overall fit function is represented by the thick gray line, imposed on the data (circular markers). The vertical intensity scale of the VB (left axis) and CB (right axis) is normalized to the same arbitrary units.

elastically scattered secondary electrons. The fit yields the position E, the area A and the full width at half-maximum FWHM of the VB at the K point as a function of time. All the collected time-resolved traces included delay points well before the pump pulse arrival (t < -1 ps). The unperturbed band was used as a reference: all the energies are scaled rigidly to this value. The area of the topmost VB is also used as a unit of area for the fits performed at later delays. The conduction band is fitted with a single Gaussian, sitting on a linear background. All the fit parameters are left free. The fitted position of the valence band can be subtracted at every step from the CB energy, to obtain the direct energy gap as a function of time: $E_{GAP}(t) = E_{CB}(t) - E_{VB}(t)$.

The results of the fits, are reported in Figure 90. The fluences used were 62 μJ/cm^2 and 380 μJ/cm^2, corresponding to an excited carrier's surface density (electron-hole pairs or excitons) of respectively 4.6 $\times$ 10^{12} cm^{-2} and 2.8 $\times$ 10^{13} cm^{-2} (Appendix A).

During pump and probe overlap the FWHM doubles for a fluence of 380 μJ/cm^2 and the two bands become indistinguishable (see figure 88, at a delay of 0 fs). As a consequence, during this initial times, the fit at the highest fluence might not be completely reliable, as the high error bars seem also to indicate. After the pump and probe overlap, an area loss of approximately 10% is observed, which slowly relaxes to the original value within $\approx$ 25 ps. In the case of the lower fluence the peaks don't merge and the area have only a slight decrease and a similar relaxation time.

At the highest energy densities, the perturbed system exhibits a VB shift limited to few 10s of meV (again, with a possible artifact at time
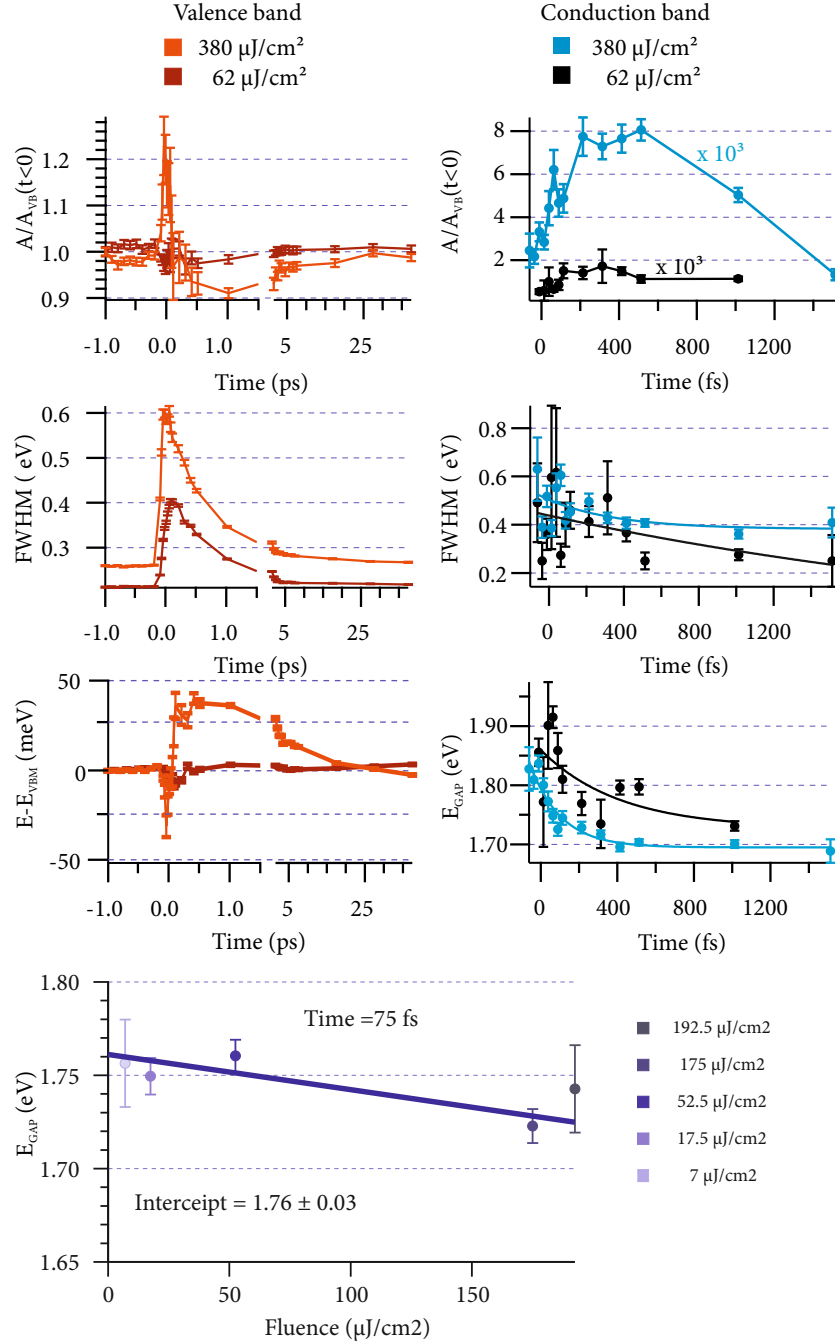
Figure 90: Fit result as a function of time for the valence (left column) and conduction band (right column) at the K point, for two fluences of the 3.1 eV pump. The top row shows the fitted area A, normalized by the area of the valence band before time zero A_{VB} (t < 0). The second row reports the Gaussian FWHM. The third row reports the position of the VB relative to the maximum before time zero E-E_{VBM}; for the CB the plot reports instead the energy gap $E_{GAP}(t) = E_{CB}(t) - E_{VBM}(t)$. The bottom plot reports the behavior of the gap at approximately 75 fs, as a function of the incident pump fluence, together with an extrapolation at zero fluence of 1.76 ± 0.03 eV.

zero, which appears as a gap opening). After temporal overlap the shift is clearly toward lower binding energies and relaxes on similar time scales as the area. The shift of the lowest fluence is below 10 meV throughout the investigated range.

The most striking feature in the VB is the increase of the FWHM, which peaks close to 100 fs and decay at a similar rate as the Σ point energy; the magnitude of the effect increases[10] at the higher fluence. The width of the photoemission peaks, as illustrated in Section 1.2.2, is connected to the imaginary part of the self-energy of the generated photo-hole: after the population transfer, new scattering channels are possible, thereby reducing the lifetime of an hole at the K point.

Both electron-electron and electron-phonon scattering might contribute to the width, and also an overall increase of lattice temperature broaden the peaks. The FWHM follows closely the energy relaxation of the carriers at the Σ valley (Section 5.3.1), which suggest that the broadening is mainly related to an increased phase space for electron-electron scattering.

5.3.2.1 *Evolution of the conduction band*

The right-hand column of the Figure 90 reports the temporal evolution of the signal in the CB. The maximum time investigated was about 1.5 ps, after which the signal was below the detection limit. The area peaks at about 400 fs, reflecting the finite time to transfer population from the area of photoexcitation (Section 5.3.2) to the K point. The fit of the width is rather noisy, especially for the 60 $\mu J/cm^2$, reflecting the low signal. As a guide to the eye, the data was fitted with an exponential decay function. The highest fluence trace appears to have a slightly increased FWHM for all times. The same effect is seen also in the VB fit, even before the pump arrival. This effect can be due to an increased space charge.

The bandgap evolution as a function of time is reported, again using two exponential functions as a guide to the eye. For both fluences, the bandgap starts from a value of ≈ 1.85 eV and then decays toward a value of approximately 1.7 eV.

Several factors might play a role in such bandgap renormalization [263, 264], one being a simple increase of lattice temperature. During the hot electron relaxation, before 1 ps, the lattice still hasn't reached a sufficiently high temperature to explain an effect of more than 100 meV: in the static case, equation 116 predicts such a shift when the jump in lattice temperature is on the order of 300 K. No coherent lattice motions where observed in the tr-ARPES data, so there is no direct evidence that such the down-shift is related to a coherent oscillation. Similar to the case of the Σ valley, one can imagine that what is observed here are the carriers which quickly scatter to the bottom

---

10 The relative offset of the two traces is due to the higher amount of space-charge in this case.

of the band: all the DFT results however point to a two-dimensional nature of the K valley [247] and according to our calculations the k_z band-width is approximately 10 meV (Figure 78). A possible source of uncertainty is the finite integration window's width: by collecting signal from higher lying states at $k_\parallel$ away from the minimum, an apparent down-shift can be expected. The width of the EDC along the Γ-Σ-K direction is 0.02 Å^{-1} and the momentum resolution broadening coming from the finite slit size in the orthogonal direction was calculated to be 0.02 Å^{-1} (Section 4.2.1). The measured band mass from the mapping is 0.4 m_e, consistent with theory: a maximum offset of ≈ 8 meV is thus expected from a similar effect.

The formation of excitons could explain similar shifts: an ionized exciton should appear below the electronic band at about the exciton binding energy [260], which in the case of the bulk A exciton is approximately 55 meV (Section 5.4.1). The electrons at the K point might form several excitons, both dark and bright, depending on the relative momentum of the hole and the electron [254, 255]: the binding energy of all these excitations is not known in detail, although dark excitons where observed in EELS data [265]. One can also expect (Section 5.4.1) the surface excitons to be more tightly bound than their bulk counterpart.

The evolution of the gap with pump fluence was studied in a second experiment: the results are reported in the lower plot in Figure 90. As the bandgap is time-dependent, one must select a specific delay to compare the tr-ARPES bandgap as a funtion of fluence. During the pump and probe overlap, VB broadening make the fit result less reliable; after few hundreds femtoseconds, the CB at the K point is generally too weak to be measured at the lowest fluences. A delay of 75 fs was chosen as a compromise, close to the time used for excited-state mapping of 100 fs. It must be noted that there is some uncertainty during the experiment in defining the time zero by observing the signal rise-time close to the Γ point[11]. The result of this analysis is that the bandgap closes with increasing fluence: the extrapolated zero-fluence gap is 1.76 ± 0.03 eV.

5.3.2.2 *Preliminary conclusions: 3.1 eV pump experiments*

It is useful to summarize the results collected so far, using an excitation above the band gap. First, thanks to high-repetition-rate HHG-based tr-ARPES it is possible to map excited states in reciprocal space. The data is in qualitative agreement with DFT calculations. A detailed map of the K point in 2H-WSe$_2$ reveals a direct bandgap close to 1.8 eV, compatible with other experimental values, once the excitonic effects are taken into account. Second, the dynamical evolution of carriers was followed throughout the Brillouin zone and the energy

---

11 An uncertainty of about 20 fs was found when comparing traces from different experiments at 3.1 eV pump energy.

relaxation timescale in the Σ valley can be well reproduced by time-resolved diffraction results. A similar dynamic can be followed in the broadening of the VB at the K point. The bandgap of the material tends to decrease with time which might be explained by the formation of excitons during the first few hundreds of femtoseconds.

5.4 A-EXCITON DYNAMICS

The final part of the chapter concentrates on experiments where the A exciton peak is resonantly pumped. The evolution of the band structure is followed by tr-ARPES both in the occupied and unoccupied states. Section 5.4.1 describes the main properties of excitons in 2H-WSe$_2$, Section 5.4.2 collects some relevant experimental results on TMDs. The main results are presented in Section 5.4.3, including a detailed pump fluence dependence of the evolution of the VB and CB. A simplified two-photon photoemission model is used to reproduce the main results in Section 5.4.6. Finally the mechanism of intervalley scattering is discussed and related to electron-phonon coupling in Section 5.4.7.

5.4.1 *Excitons in bulk and few-layer WSe$_2$*

The properties of the A exciton were studied in-depth using the Wannier exciton model sketched in Section 5.3. A simplified Lorentz oscillator model can be used to extract from the imaginary part of the dielectric function the exciton contribution on the absorption edge. Beal et al. iteratively fitted the imaginary part of the dielectric function using the following equation [245]:

$$\epsilon_2(E) = \epsilon_0 \sum_{n=0}^{\infty} A_n \frac{E\gamma}{(E_n^2 - E^2)^2 + E^2\gamma^2} + B(E), \qquad (117)$$

$$E_n = E_\infty - Rn^{-2}. \qquad (118)$$

A_n, R and E_∞ are used as fit parameters. The funtion $B(E)$ accounts for the onset of the intraband transitions and ϵ_0 is the background dielectric function, assumed to be constant in the limited range of the absorption edge. The exciton series correspond to a three-dimensional Wannier-Mott exciton, with binding energy Rn^{-2}, where R can be thought as a modified Rydberg constant, and the limit energy E_∞ corresponds to the onset of band to band transitions. The radius and reduced mass in this model are calculated as [245, 266]:

$$r = \frac{e^2}{2\epsilon_s R}, \qquad (119)$$

$$\mu = \frac{2\hbar^2 \epsilon_s^2 R}{e^4}. \qquad (120)$$

Here $\epsilon_s = 7.3$ is an effective[12] dielectric constant. The results are summarized in table 11.

Table 11: A exciton properties in 2H-WSe$_2$, adapted from reference [268]

E_1 (eV)	R (eV)	E_∞	r(Å)	$\mu(m_e)$
1.697	0.055	1.752	18	0.21

The exciton's binding energy extracted from the fit is 55 meV, with a fundamental absorption edge starting at 1.752 eV. The exciton Bohr radius obtained from the model is about 18 Å, to be compared with the inter-layer spacing $c/2 \approx 6.5$ Å of an the intra-layer lattice parameter $a \approx 3.3$ Å. The evolution of the optical resonances going from bulk to monolayer is reported in the work of Arora et al. [246]: the absolute position of the A exciton peak is relatively insensitive to the layer number, however the binding energy of the exciton increases considerably up to several hundreds of meV.

In monolayer TMDs, there are considerable deviations in the energies of higher excitonic states ($n \neq 1$) relative to the conventional hydrogenic case [222]. This effect results from the different screening in two-dimensions: when a hole and an electron confined in a 2d monolayer attract each other, the out-of-plane field lines don't sense the dielectric environment of a bulk material. The potential is non-local: far-away charges are almost unscreened whereas nearby charges, having more field lines in the material, have a screening closer to the bulk case. In most experiments, the monolayers lie on a substrate with a certain dielectric constant, which influences the dielectric environment. Stier et al. studied the evolution of the exciton binding energy and radius of WSe$_2$ monolayers with different capping layers [269]. The exciton binding energy varies from 480 meV, in the case of an uncapped monolayer on a silica substrate ($\epsilon = 2.1$), down to about 220 meV, when an hexagonal boron nitride capping layer is introduced ($\epsilon = 4.5$). The corresponding Bohr radius was determinated to be respectively 8.5 Å and 11 Å, assuming an exciton reduced mass of 0.28 m_e.

Starting from these results, the surface-layer exciton of a bulk crystal could also have an increased binding energy and reduced radius. The monolayer and the bulk case are however not directly comparable as the band structure presents considerable modifications due to the interlayer coupling. In an ARPES experiment, unlike the optical measurements, these surface effects could be enhanced relative to the bulk counterparts. Excitons and dark excitons in 2H-WSe$_2$ were also studied by electron energy-loss spectroscopy [265]: the effective mass of the exciton was reported to be 0.91 m_e.

---

12 The use of an effective dielectric constant comes from the optical anisotropy of the material: $\epsilon_s = (\epsilon_\parallel \epsilon_\perp)^{\frac{1}{2}}$, $\epsilon_\parallel = 4.2$ $\epsilon_\perp = 12.7$ [267].

5.4.2 Ultrafast dynamics in TMDs with exciton pumping

The dynamic of photo-excited carriers in TMDs was extensively investigated: most of the recent optical studies concentrate on monolayer samples [264], often comparing the results obtained with multilayer or bulk samples. Transient absorption microscopy for monolayer and bulk WSe_2 in the low excitation density limit (few $\mu J/cm^2$) was performed by Cui et al. [270]. The system was excited with a 3.1 eV pump and the reflectivity of a 750 nm beam was use as a probe. In the bulk case, the decay of the differential signal had a lifetime of 160 ps, a spatially-resolved analysis revealed an in-plane diffusion coefficient of 9 cm^2/s for pump-induced carriers. In this low-excitation density regime, four-wave-mixing spectroscopy was used to measure the dephasing time for excitons, which is about 420 fs [271] for a bulk sample. The authors identify as the main broadening mechanism, exciton-phonon scattering.

The ultrafast optical response of TMDs under strong optical excitation (>100 $\mu J/cm^2$), was also reported by several studies. In this regime, the generated carriers behave more as an electron-hole plasma until, at the critical Mott density, excitons are suppressed. Strong bandgap renormalization and population inversion was reported by Chernikov et al. in the case of a WS_2 bilayer [272]. In WS_2 monolayers, Sie and coworkers reported the observation of valley-selective optical stark effects, resulting from the interaction of photon-dressed Floquet states and the excitonic resonance [273]. The same authors, using a mid-Infrared pump wavelength, observed a so-called Bloch-Siegert shift in specific K valleys [274]. Jeong studied the layer-dependent transient absorption of WSe_2, using a degenerate pump and probe setup at 750 nm, concentrating on the generation of coherent optical phonons [261]. In particular, in the case of bulk crystals, the prominent observable modes are the A_{1g}, intra-layer mode and the B_{1u}, inter-layer breathing mode. The former intra-layer mode decays into two acoustic modes via anharmonic decay. The Raman spectrum of the material, together with the calculated phonon bandstructure can be found in reference [275].

5.4.3 Experimental results, 800 nm pump

$2H\text{-}WSe_2$ samples where investigated by perturbing the system with the fundamental of the OPCPA: the experimental setup of Figure 80 was modified by removing the BBO crystal and replacing the separator mirrors with conventional high-reflective mirrors. As shown in Figure 84, the spectrum of the OPCPA fundamental (red line) is nearly resonant to the A-exciton peak. An overview of the main experimental results along the Γ-Σ-K direction is presented in Figure 91 b), for

comparison, in panel a) the excited-state mapping of the K point is plotted once more.

The optical excitation at this pump wavelength is localized at the K point; the main dynamics occurs between the K valley and Σ valley. The initial population at the K point undergoes ultrafast scattering to the Σ valley, similar to the case of 2H-MoS$_2$ [60]. The time traces, integrated in the boxes indicated in panel b), are shown in panel c). The red curve is the intensity in the K point, whereas the black line represents the signal rise at the Σ valley. Nearly within the duration of the pump pulse, the population scatters to the Σ valley. The third line corresponds to the intensity measured within the band-gap of the material and is a good reference for the pump and probe autocorrelation, which is approximately 40 fs, similar to what was reported in Section 4.3.3. Using this reference for the autocorrelation, the red trace was fitted with a step function multiplied by an exponential decay and convoluted with a gaussian of fixed width. The fit function used was:

$$\begin{cases} f(t) = C_< & t \leq t_0 \\ f(t) = Ae^{-t/\tau_{K\Sigma}} + C_> & t > t_0 \end{cases} \tag{121}$$

$$g(t) = \int_{-\infty}^{+\infty} dt' f(t') e^{-4ln(2)\left(\frac{t-t'}{\tau_{xc}}\right)^2}. \tag{122}$$

Here $\tau_{K\Sigma}$ is the decay time of the signal at the K point, and τ_{xc} is the FWHM of the cross-correlation. A positive and negative offset were also included to account for the background and for the residual signal at the K point, possibly resulting from backscattering from the Σ point to the K point. The position of the cross-correlation peak was used as a reference for the time zero: it is clear that a small delay between the green and the red traces exists.

The fit results in a cross correlation of $\tau_{xc} = 35 \pm 5$ fs and a scattering time of only $\tau_{K\Sigma} = 16 \pm 2$ fs. The temporal delay between the two signals is approximately 10 fs.

A closer inspection to the cross-correlation-like signal appearing in the gap reveals that it bears some band-like structure, with a hole-like dispersion, similar to the VB. The fitted position of the K hill, shifted by the pump photon energy of 1.55 eV, is indicated by a dashed white line in panel b). The position of the CB obtained from the mapping experiment is marked by an horizontal dashed white line. The position of the observed resonance at time zero does not match the mapped CB, and appears at an energy of $\approx$ 1.65 eV, 150 meV below the conduction band. The signal at the K point is rather clearly downward dispersing, opposed to what was measured by above-bandgap excitation in panel a). A second experiment was performed while cooling the system at liquid nitrogen temperature (70 K). The temporal evo-
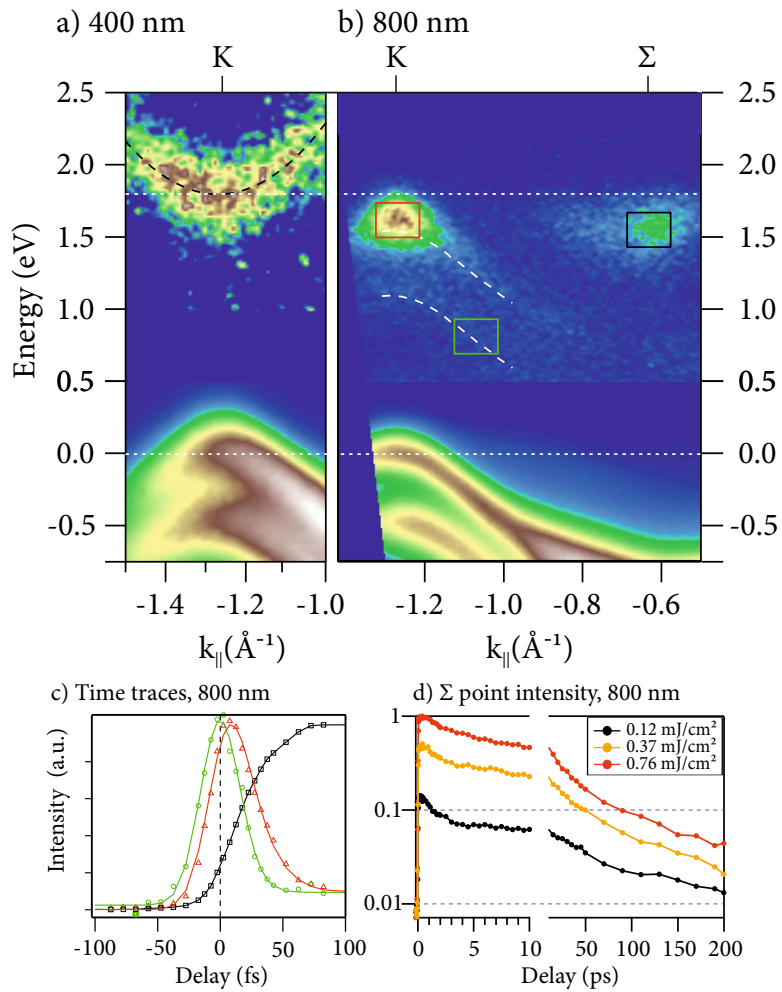
Figure 91: a) Excited-state mapping ot the K point; b) Snapshot of the band structure collected at pump and probe overlap at a pump fluence of 0.76 mJ/cm^2, the horizontal dashed white line indicates the bandgap measured with the mapping experiment about 100 fs after photoexcitation; the white lines within the gap, represents the position of the fitted VB, offset by 1.55 eV. c) Time traces collected from the areas indicated in panel b). The red box, corresponds to the K point, the green box to an in-gap state and the black box to the Σ point; the markers represent the experimental data and the green and red lines are the result from a fit, the black line is a guide to the eye. d) Intensity dynamics at the Σ point recorded up to 200 ps and for the pump fluences indicated in the caption.

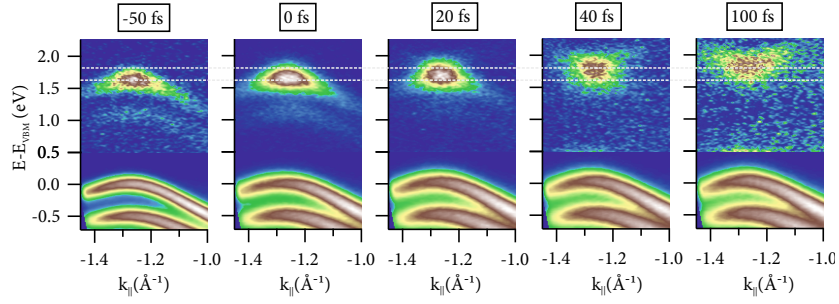lution of the signal at the K pointis shown in Figure 92: in this case the replica bands are more clearly resolved.

Figure 92: Temporal evolution of the K point with a s-polarized 1.55 eV pump, a fluence of 2 mJ/cm^2 and a temperature of 70 K. The two white horizontal lines indicate the initial and the final energy of the feature.

The replica are now more visible and resemble quite closely the shape of the undelying VB. While the replica signal disappears quickly, the signal in the CB is longer-lived and persists even after 100 fs.

The appearance of *replica bands*, might originate either from photon-dressing effects, or it can be explained as non-resonant two-photon photoemission. Photon dressing was already observed in tr-ARPES (Section 1.5.3): two main type of photon-dressed bands exists, LAPE bands and Floquet-Bloch states. LAPE has a remarkable polarization dependence and vanishes when the momentum of the photoelectrons is orthogonal to the pump electric field, which is the case in the s-polarized pump used in the experiment. By rotating the polarization, new intensity components appear in the band-gap, below the Σ point, coming from LAPE from the bright underlying occupied states: this intensity is maximized for p-polarized light. The same behavior is not observed in the replica bands, which are therefore not related to LAPE. The hall-mark of Floquet-Bloch states is a gap opening between overlapping replicas [55]: as there are no regions where the replicas could overlap, this is not observable in our experiments. Another characteristic feature of the Floquet-Bloch states are negative-order replicas of the CB, at an energy reduced by one pump photon [243]. Such replicas should in theory appear in the gap, but also this feature is not observed in the experiment.

Non-resonant, two-photon photoemission from the valence bands should also appear at the energy of the replicas: as it will be shown in Section 5.4.6, a minimal model for describing two-color two-photon photoemission provides a reasonable description of the observed data.

When the in-gap signal is compared to the K valley rise time (Equation 122), there is a remarkable time delay between the two. To further investigate this behavior and its localization in k-space, an extended temporal analysis of the rise time around the K pointwas performed. All the images are binned 2 × 2 and from every pixel of the binned

image a temporal trace is extracted. Every trace is fitted by a Gaussian function to estimate the time at which the signal is maximum. The resulting times as a function of energy and momentum are plotted for two temperatures in Figure 93. At room temperature, panel a), the time-maps show that the closer one looks to the K valley bottom, the more delayed is the rise time, resulting in delays up to $\approx$ 15-20 fs. Lowering the temperature (panel b) in Figure 93) has the effect of opening the band gap by $\approx$ 60 meV, see Equation 116. The exciton's binding energy is not strongly affected by the temperature, but the absolute position of the resonance follows the bandgap [246], meaning that the absorption resonance is shifted away from the replicas. The effect on the time map is that the rise time becomes more uniform across the two bands, laking a clear central maximum at the K point. The feature at lower energy appears narrower in both the pictures: in this representation of the process, this is the result of a dynamical up-shift of the higher-energy feature.
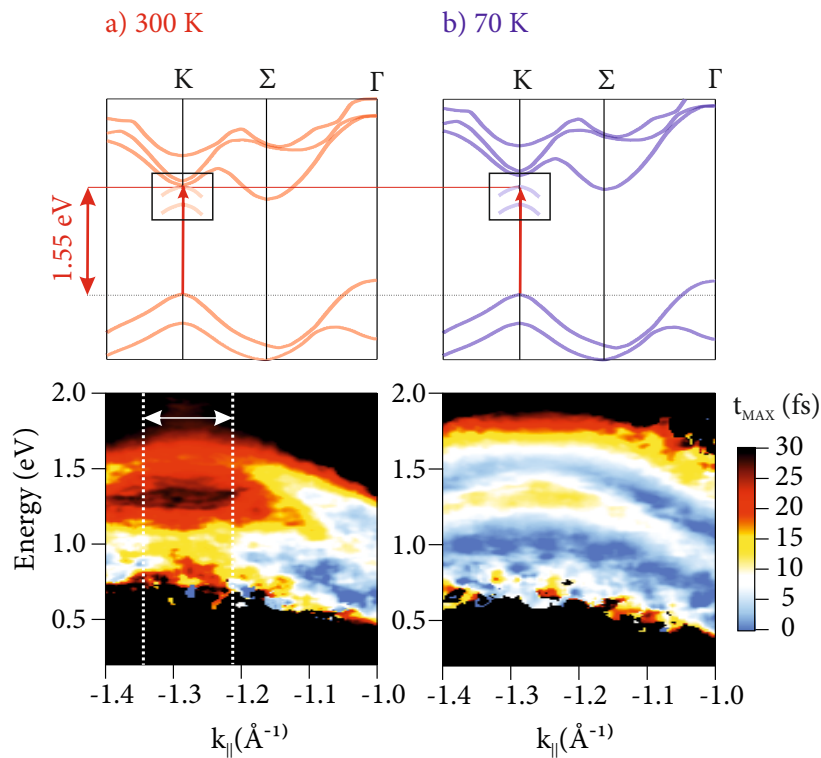

Figure 93: Temporal maximum maps extracted for a) 300 K and b) 70 K and a pump of 1.55 eV, with an incident fluence of 2 mJ/cm^2. The top panels illustrate the schematic bandstructure of 2H-WSe$_2$, together with the position of the replica bands at the K point. The bandgap-opening effect at low temperature results in an stronger detuning from the resonance peak.

The effect can be clearly appreciated in the data shown in Figure 92: here two white dotted lines show the limiting points of this up-shift

at low temperatures, starting from a value around 1.55 eV, the end position is about 1.8 eV. To quantify the effect, a gaussian peak was fitted to the data for every time delay and the energy is reported in Figure 94. The energy is referenced to the VB *before* photoexcitation
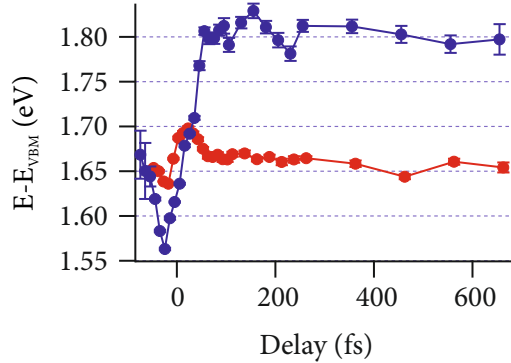

Figure 94: Up-shift of the CB signal at 300 K (red line) and 70 K (blue line) and a pump of 1.55 eV, with an incident fluence 2 mJ/cm^2.

(t=-1 ps). Unexpectedly, before the temporal up-shift a down-shift is also resolved at negative times. The overall movement at higher temperatures is clearly reduced and even a second down-shift is present, followed by a slower, linear reduction of the energy at higher times. In the 70 K data, the up-shifting feature settles at 1.80 eV and does not appear to change significantly after the initial time. To gather more information on this behavior, a more systematic fluence-dependent experiment at room temperature is presented in the next section.

5.4.4 *K point valence band dynamics*

The evolution of the K point CB and VB signals was studied as a function of the strength of the perturbation. To correctly measure the incident fluence, the pump spot size was measured ex-situ as described in Section 3.5, the transmission of the pump beam-line was measured behind the sample with a calibrated power-meter. The generated carrier density can be estimated from the dielectric function in Appendix A. For every time-resolved experiment, an EDC from the K point (width 0.02 Å^{-1}) was fitted as a function of time, following the same method described in Section 5.3.2.

Figure 95 shows a first set of measurements, containing incidend fluences from 40 up to 430 μJ/cm^2. For all data sets, the maximum of the signal in the replica bends was used as a zero for the time axis. The valence band signal now shows a sizable decrease close to temporal overlap: this is easily understood as the direct population transfer occurring from the top of the VB to the CB. The signal is normalized to its value at negative times: approximately a 10% reduction of the signal is measured at the maximum fluence. Correspondingly,

the area in the CB (here not normalized) increases linearly with the fluence.

The relative position of the VB and CB also scales linearly with the deposited energy and a closure of the gap of up to 30 meV is measured at the highest fluence. The up-shift in the CB has instead a remarkably stable behavior and is fluence-independent in the investigated range, except for the lowest fluence which appear moderately shifted by $\approx$ 20 meV to lower energies. Also in these fits, at the first negative times there is a initial down-shift in the energy.

The FWHM of the VB, as observed in the case of the UV pump (Section 5.3.2), is sensitive to the increased phase space for decay of the photo-hole. The relative broadening is calculated here as

$$\Delta FWHM = \sqrt{\Delta E_{VB}(t)^2 - \Delta E_{VB}(t \ll t_0)^2}, \tag{123}$$

where ΔE_{VB} is the fitted FWHM. For the NIR pump, the broadening is considerably less, even if the incident fluence is significantly higher. This supports the phase-space argument: the 3.1 eV pump reaches states 1.55 eV higher in the CB, accessing a greater phase space. The FWHM of the CB has a considerable spread at initial times, reflecting the weakness of the signal in the wings of the cross-correlation, after time-zero there is a general trend to increase toward later times, going from 200 meV to more than 300 meV.

At the excitonic resonance light absorption is very efficiency and population is easily transferred to the CB: an interesting question is whether is possible to saturate the transition. A second set of experiments explored the regime of the highest fluences, starting from 0.4 mJ/cm^2 and going up to 4 mJ/cm^2 (which was the limiting fluence for the experimental setup). The results for the very same analysis are shown in Figure 96. The system is close to population inversion at the K point at 3 mJ/cm^2, above this value the absorption saturates and the signal loss from 3.3 to 4.1 mJ/cm^2 is nearly the same. The intensity of the CB signal relative was normalized to the area of the VB at negative times: the intensity nearly saturates at 30% and then drops again. This analysis does not take into account the different matrix elements for photoemission between CB and VB, it is therefore not a surprise that the sum of the two signals is not equal to one. The position of the VB keep shifting also once saturation is reached, however the linear increase does not hold anymore. The CB starts always with an initial down-shift at negative times, followed by an up-shift. After the rise, as the fluence increases, quite interestingly the position undergoes a second decrease, more and more pronounced at saturation. The width of the VB also behaves in an anomalous way in the saturation area, exhibiting even a reverse trend where the highest fluences are less broadened than the one before saturation. The FWHM of the CB consistently increases as a function of time. These findings, will
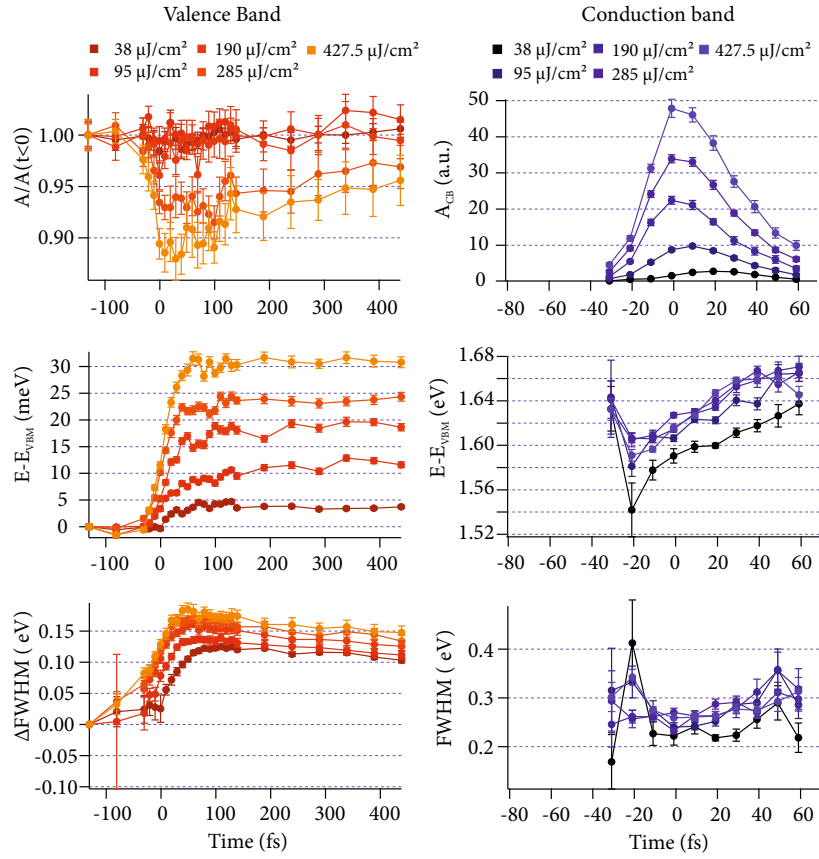
Figure 95: Fluence dependent VB and CB dynamics in 2H-WSe$_2$ at the K-point. The first column reports the fit results for the top valence band, the second the results for the CB. The top-left graph reports the area loss in the VB, relative to is value before photoexcitation. The top-right graph is the area of the CB, in arbitrary units. The second row reports the position of fitted peaks, expressed relative to the top VB before time zero. The bottom left graph reports the broadening ΔFWHM observed in the VB (see main text for the definition). The bottom right graph is the FWHM of the CB peak.
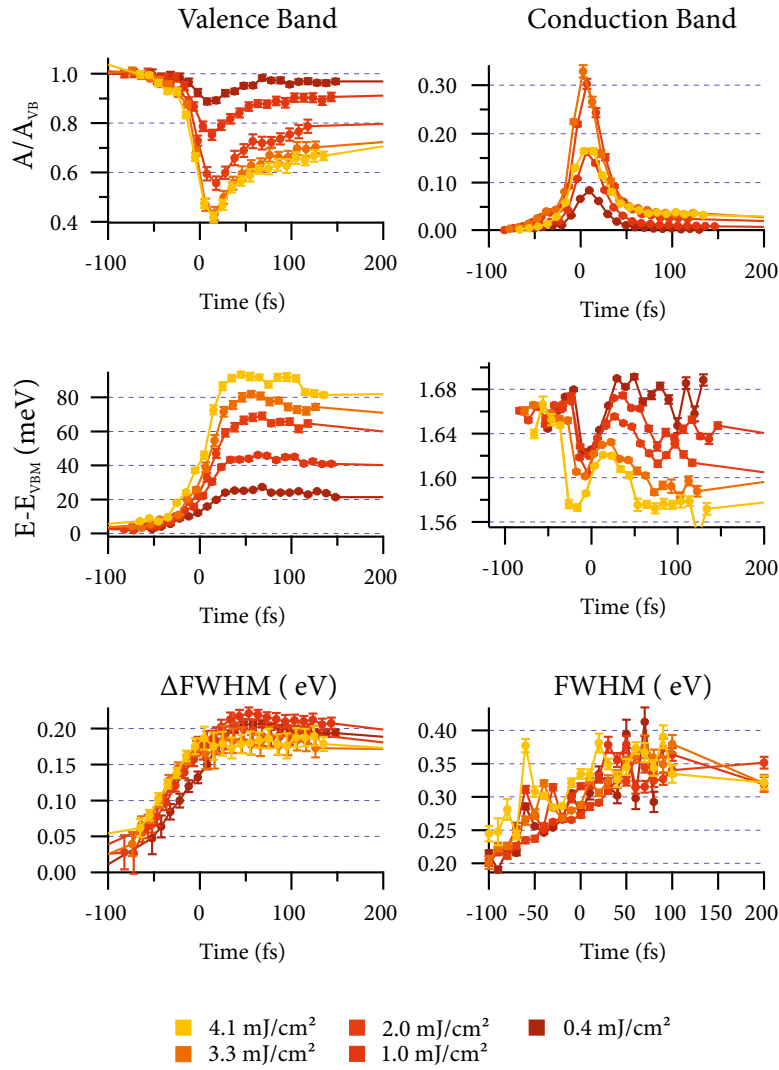
Figure 96: Fluence dependent VB and CB dynamics in 2H-WSe$_2$ at the K-point, high fluence case. See Figure 95 for a definition of the different quantities.

not be treated in detail in this work. However it is clear that at the highest fluences the field strength is sufficient to drive the inter-band transition in the nonlinear absorption regime. To correctly account for the findings in this range, optical Stark-shifts might have to be considered , as it was observed in TMDs monolayers [273]. In the following sections the lowest fluence of this last dataset will be studied in greater detail: at 0.4 μJ/cm^2 the excitation is still in a linear regime.

5.4.5 *k-resolved K-valley evolution*

Another effect, clearly seen in Figure 92, was so-far neglected: both the CB signal and the replica band dispersion initially seem to mimic the VB; as the system evolves, the feature flattens and after the pulse temporal overlap is lost, an electron-like dispersion is observed at the K valley. To quantify this evolution, in Figure 97 several neighbouring EDCs at the K point where fitted with a Gaussian function as a function of time. For every temporal delay, the extracted peak
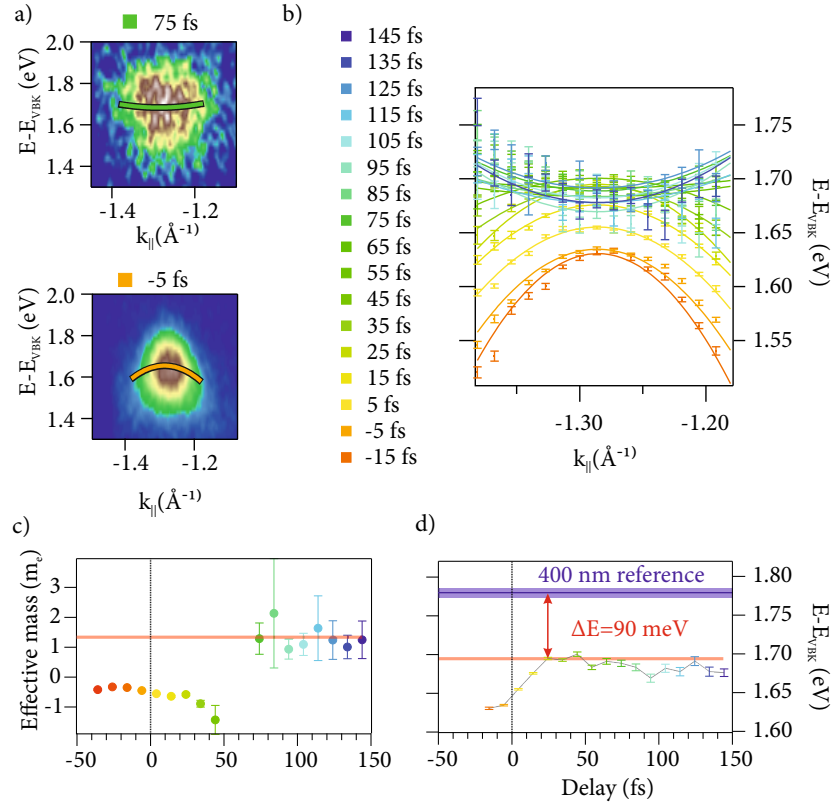

Figure 97: Fit of the excited state signal at the K point, for a fluence of 0.4 mJ/cm^2. a) Energy position for two representative delays, -5 fs and 75 fs b) Time-dependend fit results, together with a parabolic dispersion fit. c) Time evolution of the effective mass, in units of electron mass m_e d) Energy position of the parabolic band, together with the 400 nm CB position obtained with mapping at a delay of 100 fs.

positions were fitted with a function of the form:

$$E(k_\parallel, t) = E_0 + \frac{\hbar^2(k_\parallel - k_{\parallel,K})^2}{2m_{CB}(t)}, \tag{124}$$

here $m_{CB}(t)$ is the effective mass in units of the electron mass, E_0 is the energy position of the parabola and $k_{\parallel,K}$ represents the center parallel momentum. The fit was performed in a range of approximately 0.2 Å^{-1} around $k_{\parallel,K}$. The central position of the band was held fixed during the fit while the other two parameters were left unconstrained. Time delays below 20 fs could not be reliably fitted due to the weakness of the signal. The analysis allows to quantify the main effects, which are already visible from the raw data: the results of the fit are shown in Figure 97, c) and d). It must be stressed that at the effective mass concept, often used for describing electric transport properties, is used here only as a convenient measure of the observed band dispersion.

The fitted effective mass is shown in panel c): first, the excited states have a hole-like dispersion with an effective mass close[13] to -0.5 m_e. The mass continues to increase, until it diverges to a flat band (points outside the plot range) and assumes an electron-like dispersion with a rather constant behavior at positive delays. The end value for the mass does not coincide with the CB dispersion[14] and is slightly higher than 1 m_e.

Quite interestingly, the final effective mass is quite different than the 0.4 m_e reported for the CB, and is more comparable to the effective exciton mass of 0.91 m_e, measured with electron-energy loss spectroscopy (EELS) [265]. Unfortunately, the UV-pumped data cannot be fitted with the same reliability at later delays to appreciate an evolution of the effective mass in that case.

The fitted E_0 follow the trend reported for the central EDC in Section 5.4.4 and is compared in Figure 97 d) with the CB position from the mapping experiments. For the comparison, a single value from the mapping dataset is used, collected at 100 fs delay. After the initial rise, the energy stabilizes around 1.7 eV: this is approximately 90 meV lower than the mapping reference, a value greater than the bulk exciton's binding energy. After photoemission, the exciton is ionized and an hole is left behind. Following the energy conservation arguments described in the work of Weinelt et al. [260], the energy position of a photoelectron coming from an exciton, should approximately be equal to the energy of the conduction band from which it originates, minus the exciton's binding energy. It is tempting to assign the final value after rise to the position of the surface excitonic resonance, where the increase of binding energy as compared to the bulk might come from the different screening environment (Section 5.4.1).

---

13 The VB effective mass, before time zero was -0.5 m_e
14 The mapping results for the CB is 0.4 m_e (Section 5.2.1).

5.4.6 *Simulation of 2PPE based on optical-Bloch equations*

The signal in the CB follows a rather complex dynamics which in principle could be influenced by several factors: exciton formation, lattice response and optical Stark effects. A dynamical up-shift is present for all the measured fluences: a possible mechanism for an energy increase of the excited states is the break-up of excitons to finally produce free carriers in the CB. The magnitude of the upshift is indeed ≈ 60 meV at room temperature. From the known optical absorption, shown in Figure 84, it is pretty clear that the exciting pulses are not exactly on resonance with the A exciton peak; as soon as the band gap is further increased the energy excursion of the CB is even higher. At high detuning the excursion reaches up to 250 meV, suggesting an unrealistic increase of the exciton binding energy at lower T if the interpretation of the up-shift as exciton break-up would hold.

To gain insight in the observed dynamics, a model of two-color two-photon photoemission which allows for energy detuning is needed. A minimal model has to include at least three levels: the initial state i is the VB, the intermediate state n is populated by the pump photon and the final state belongs to a continuum of free states, corresponding to the photoemission from the second photon.

Femtosecond, two-photon photoemission where both photons are below the ionization potential is a well-established technique. One of the most widely studied systems are image-potential states at metal surfaces: these states reside in the immediate vicinity of the solid and are well decoupled, long-lived states, ideally suited to probe ultrafast microscopic scattering and dephasing mechanisms at surfaces. 2PPE can be described using the formalism of optical-Bloch equations [276]. The basic theoretical description is valid also for our experiments, under the simplifying assumption of a few-level system: the main equations are reported here, following closely the derivation in reference [35], where the interested reader can find further information. The analysis is based on the Liouville-Von Neumann equation 131:

$$\dot{\rho_{kl}} = \frac{1}{i\hbar}[\hat{H}_0 + \hat{V}, \hat{\rho_{kl}}] - \Gamma_{kl}\rho_{kl}.$$

(125)

The equation describes the evolution of the density matrix under a perturbation $\hat{V}$ for a system with an unperturbed Hamiltonian $\hat{H}_0$; to account for scattering and dephasing, a damping matrix Γ_{kl} is included:

$$\hat{\Gamma} = \begin{pmatrix} 0 & \Gamma_n/2 + \Gamma_n^* + \Gamma_i^* & \Gamma_i^* + \Gamma_f^* \\ \Gamma_n/2 + \Gamma_n^* + \Gamma_i^* & \Gamma_n & \Gamma_n/2 + \Gamma_n^* + \Gamma_f^* \\ \Gamma_i^* + \Gamma_f^* & \Gamma_n/2 + \Gamma_n^* + \Gamma_f^* & 0 \end{pmatrix},$$

here Γ_j and Γ_j^* are the decay and the pure dephasing rates for the j-th level, respectively. The initial and the final state are assumed to have an infinite lifetime, $\Gamma_i = \Gamma_f = 0$. The off-diagonal terms of Γ_{kl} are the dephasing rates, describing the decay of quantum coherence established by the photons between the various levels. The perturbing fields are described in the dipole approximation by the quantities $p_a(t) = \mathcal{E}_a(t) \langle i|D|n \rangle$ and $p_b(t) = \mathcal{E}_b(t) \langle n|D|f \rangle$, where the temporal envelope functions $\mathcal{E}(t)$ are both taken as Gaussian and D is the dipole operator. From Equation 131 one can derive a set of six coupled differential equation ($\hbar = 1$), the optical Bloch equations (OBE):

$$\dot{\rho}_{ii} = \mathbb{I}m(p_a^* \rho_{in}^{(1)}) \qquad (126)$$

$$\dot{\rho}_{nn} = -\mathbb{I}m(p_a^* \rho_{in}^{(1)}) + \mathbb{I}m(p_b^* \rho_{nf}^{(2)}) - \Gamma_{nn}\rho_{nn} \qquad (127)$$

$$\dot{\rho}_{ff} = -\mathbb{I}m(p_b^* \rho_{nf}^{(2)}) \qquad (128)$$

$$\dot{\rho}_{in}^{(1)} = -i\Delta_a \rho_{in}^{(1)} - \frac{i}{2}p_b^* \rho_{if}^{(3)} + \frac{i}{2}p_a(\rho_{nn} - \rho_{ii}) - \Gamma_{in}\rho_{in}^{(1)} \qquad (129)$$

$$\dot{\rho}_{nf}^{(2)} = -i\Delta_b \rho_{nf}^{(2)} + \frac{i}{2}p_a^* \rho_{if}^{(3)} + \frac{i}{2}p_b(\rho_{ff} - \rho_{nn}) - \Gamma_{nf}\rho_{nf}^{(2)} \qquad (130)$$

$$\dot{\rho}_{if}^{(3)} = -i(\Delta_a + \Delta_b)\rho_{if}^{(3)} + \frac{i}{2}p_a \rho_{nf}^{(2)} - \frac{i}{2}p_b \rho_{in}^{(1)} - \Gamma_{if}\rho_{if}^{(3)}. \qquad (131)$$

The energy detunings are defined as:

$$\Delta_a = \hbar\omega_a - (E_n - E_i) \qquad (132)$$

$$\Delta_b = \hbar\omega_b - (E_f - E_n). \qquad (133)$$

All the energy-dependent information are included in these two terms and an energy-resolved 2PPE spectrum can be obtained by allowing Δ_b to vary continuously. Here $\hbar = 1$ and the equations $\rho_{in}^{(1)}$ are defined as follows:

$$\rho_{in}^{(1)} = e^{-i\omega_a t}\rho_{in}$$

$$\rho_{nf}^{(2)} = e^{-i\omega_b t}\rho_{nf}$$

$$\rho_{if}^{(3)} = e^{-i\omega_b t}\rho_{if}.$$

A Matlab program was written to solve the coupled differential equations as a function of the detuning and temporal delay of the system. Here is reported a preliminary analysis ought to show how this three-level model can already describe some of the features observed in the experiment, and essentially shows that the apparent energy shifts can be explained by a slightly off-resonant excitation of the intermediate level. To simulate the observed dispersion in the experiment, the detuning Δ_a was varied, assuming an effective mass of the i and n levels matching the experimentally determined ones: $m_i = -0.5\,m_e$ and $m_n = 1.0\,m_e$, for the CB a value close to te results of Section 5.4.5 was

chosen, rather than the mapped CB. The pump pulse duration was set to 30 fs and probe pulse duration to 20 fs; the minimum pump detuning was chosen to be five times the energy width determined by the pump pulse duration ($\approx$ 40 meV): this translates in a 200 meV detuning, similar to the energy shift measured at low temperature in Figure 94. Both the decay and dephasing rate for initial and final states where chosen to be zero, while the lifetime $\tau_n = \hbar/\Gamma_n$ and $\tau_n^* = \hbar/\Gamma_n^*$ where arbitrary chosen to both be 50 fs.

The amplitude of the pump term p_a was chosen to achieve a signal decrease in the state i of approximately 10% , the probe amplitude was p_b instead chosen to be 0.1 times the pump one, further reduction did not change the results in a tangible way. The simulations results are plotted in Figure 98. The main features of the data are reproduced by the simplified model: snapshots at several delays are plotted in panel a) and the transition from hole-like to electron-like dispersion is clearly observed. An EDC as a function of time is shown in panel b), highlighting how traces from different k-vectors (and therefore detuning) show a delayed rise time. Finally the same analysis of Section 5.4.5 allow to reconstruct the central position and dispersion as a function of time. The similarity with Figure 97 is remarkable, showing both an energy rise and the correct evolution of the measured dispersion. The energy shift starts approximately from the detuning energy, the final position is somewhat detuned from the expected resonance position. The dispersion starts from the VB dispersion and ends on a value very close to the CB one.

5.4.7 *Ultrafast inter-valley scattering and electron-phonon coupling*

In Section 5.4.3, the ultrafast decay of the K valley was found to have a time-constant below 20 fs in a simplified fit with exponential decays. A more correct treatment, should consistently take into account the rise time of the signal in the Σ valley, and the observed cross-correlation signal measured in the band gap. The optical-Bloch equation model in the previous section was extended to include incoherent population transfer to an additional level (the Σ valley in this case) and the respective photoemission final state. The three time traces of Figure 91, panel c) where simultaneously fitted with the coupled differential equations of the model, to reliably extract the scattering rate of the K point, assuming that the only decay channel is the Σ valley. The results, shown in Figure 99, panel b), predict a time constant of $\tau_{K-\Sigma} = 15 \pm 1$ fs.

To explain this very fast scattering channel, a comparison with theory was attempted. The scattering toward the Σ point requires a suitable mechanism to conserve simultaneously momentum and energy: in a single-particle picture (without considering excitons), an electron can be scattered from the K valley to the Σ valley if in the VB a second
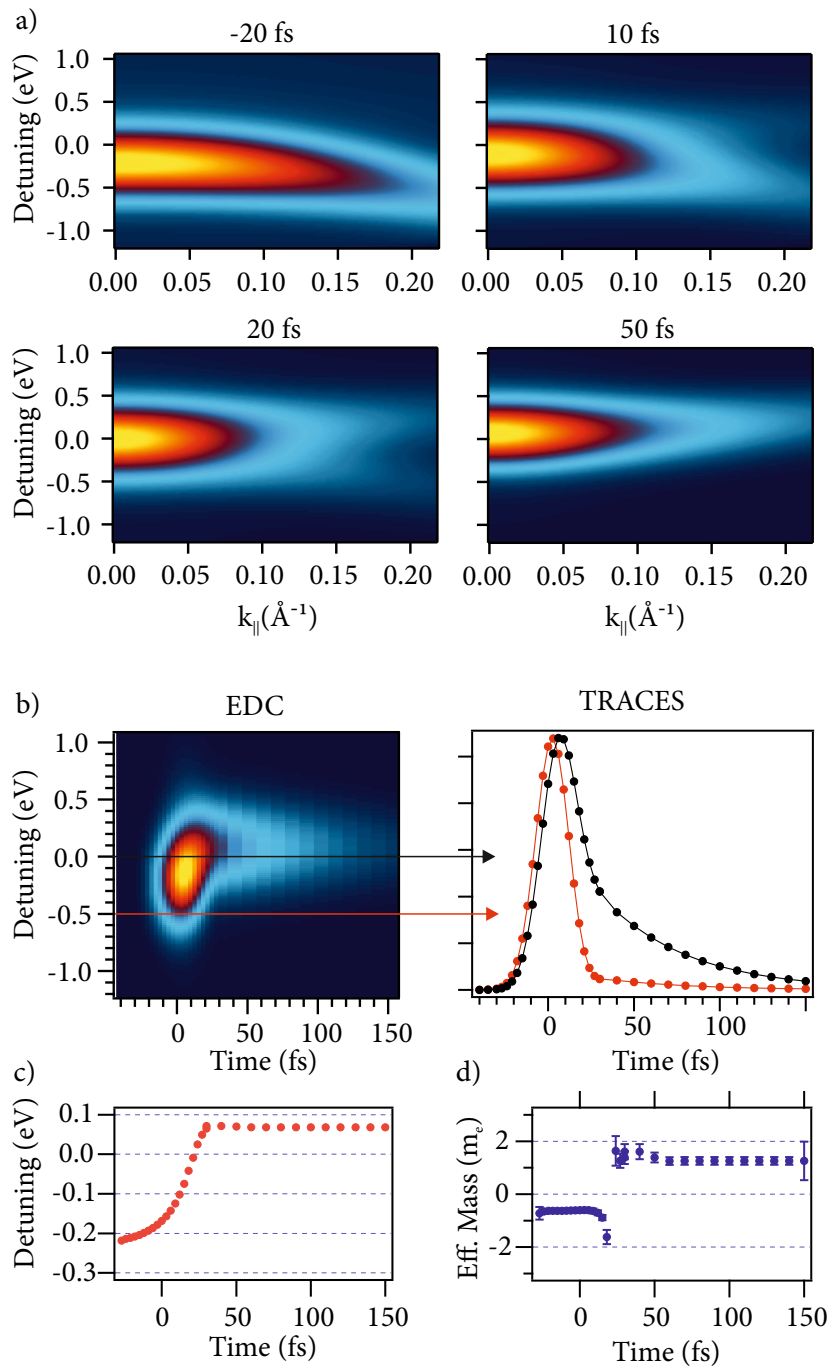
Figure 98: Optical Bloch Equations simulations results. a) Simulated 2PPE snapshots, for selected time delays b) Central EDC ($k = 0$) as a function of time, two line-cuts through the dataset are shown as time traces on the right graph. c) Energy position of the envelope as a function of delay d) Apparent effective mass as a function of delay.
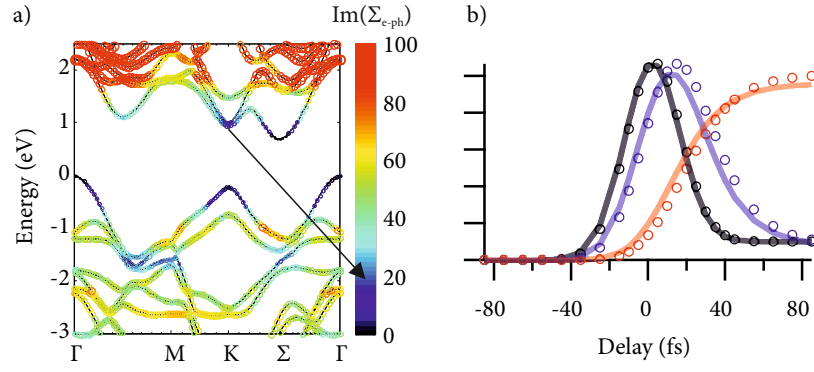
Figure 99: a) Calculated imaginary part of the self-energy for electron-phonon coupling in 2H-WSe$_2$: the arrow indicates that the $Im(\Sigma_{e-ph}) \approx 20$ meV at the K point. b) Optical-Bloch equation fit of the intervalley scattering. The round markers are the experimental points, shown already in Figure 91. The time traces are collected in the bandgap (black), at the K point (blue), at the Σ point (red); the lines represent the fitted values.

electron would gain the same amount of energy and momentum by filling one of the holes generated by the pump at the K point. This appears unlikely for the lack of a suitable state in the VB, as can be seen along the K-Σ direction in Figure 91, or in the high resolution data of Riley et al.[229].

The required momentum for the scattering can be provided by a suitable phonon. The natural question arising is whether the electron-phonon coupling is sufficiently strong to explain this fast scattering and how to relate the measured lifetime with theoretical calculations. As mentioned in Section 1.5.5, the single-particle lifetime τ_{sp} can be compared with the imaginary part of the calculated self-energy using the relation $2Im(\Sigma) = \hbar/\tau_{sp}$. tr-ARPES measures the lifetime of the excited population, which in general is not equivalent to single-particle lifetime [63]: for instance in Figure 86, the population lifetime at the KP is 0.7 ps, very different than the 15 fs lifetime measured with a 1.55 eV pump. The reason behind the discrepancy are the contributions of multiple electron-electron and electron-phonon scattering channels, which are present in the case of above band-gap pumping and which mask the true electron single-particle lifetime. In the 1.55 eV case, many of the additional scattering channels should be quenched by the reduced scattering-phase space. The simplified few-level model used to fit the temporal traces is in relatively good agreement with the data and it is interesting to compare the time constant with theory, assuming that it reflects a single-particle lifetime for an electron at the K point, which decays via electron-phonon scattering, in this case one can write:

$$2Im(\Sigma_{e-ph}) = \frac{\hbar}{\tau_{K-\Sigma}}. \tag{134}$$

Bernardi et al. [277] introduced an ab-initio method to calculate the imaginary part of the electron-phonon self-energy. The result of similar calculations (courtesy of Hannes Hübner, [278]) for the case of 2H-WSe$_2$ is shown in Figure 99, panel a). At the K point $Im(\Sigma_{e-ph}) \approx 13$ meV. This number is comparable with the fit result $1/2 \times \hbar/\tau_{K-\Sigma} \approx 22$ meV. The scattering rate extracted from the experiment is somewhat faster than what is predicted by the theory: the reason behind this discrepancy could be the electron-hole interaction, which is neglected in this calculations. The formula is no longer valid for the decay of a bound electron-hole pair into free conduction band states or into dark excitons.

These results indicates electron-phonon coupling is a possible mechanism for the observed ultrafast intervalley scattering, naturally explaining momentum conservation. Equilibrium calculations and tr-ARPES scattering rate are comparable in this case, although not in perfect agreement. The formalism is derived for single-particle states, if the addition of electron-hole interaction would affect the overall picture, explaining the faster decay observed in the experiment, is still an unanswered question.

5.4.8 *Conclusions*

High-repetition-rate tr-ARPES experiments can be successfully conducted with the new light source. The unprecedented combination of flux, energy resolution and the high photon energy enable new experimental possibilities.

The excited states of 2H-WSe$_2$ where successfully mapped throughout the Brillouin zone. This represent an unique k-resolved view of a semiconductor's bandgap, which can be used to interpret the results of other optical spectroscopies. The data was successfully compared with ab-initio DFT calculations, revealing that the Kohn-Sham energies are in reasonable agreement with the measured quasi-particle band structure also for the excited states. One future direction for these experiments will be to compare the data with higher-level theories, such as GW correction or td-DFT, to quantify the agreement of theory with the measured band-structure. Such a comparison is important as these calculations are routinely used for the interpretation of many experiments. The population dynamic is followed throughout the Brillouin zone and the energy relaxation rate in the Σ valley compared with time-resolved diffraction data. The experimental tr-ARPES timescale coincides with the one measured for the lattice. A band-gap renormalization is observed in the K valley, compatible with the formation of excitons after few hundreds of femtoseconds after photoexcitation.

By pumping the system below the bandgap, close to the A excitonic resonance, replica bands in the band gap and a complex energy

dynamic is observed. An up-shift in energy of the CB and the inversion of band dispersion can be resolved in the experimental data. Both effects can be reproduced by simulations based on optical Bloch equations. The replica bands can be seen as non-resonant two-photon photoemission features. The calculations seem to qualitatively reproduce the data, in the future a multi-dimensional fit of the tr-ARPES data might provide quantitative results for the scattering and dephasing time of the K valley signal.

The comparison of the two experiments supports the idea that with NIR pumping, bright excitons are created: the energy difference between the mapping data and the excited state after the pump pulse is approximately 90 meV, slightly higher than the bulk exciton energy of 55 meV. The difference can be potentially explained by the different screening environment for surface excitons.

The measured effective mass of the CB feature is considerably higher than the one observed for above-bandgap-pump data and is similar to the experimental values obtained with electron-energy loss spectroscopy, also suggesting that the state formed after the 1.55 eV pump are excitons in the K valley.

A very fast scattering transfers the population to the Σ valley: the scattering time constant was extracted by fitting the time traces with optical Bloch equations and was compared with the calculated imaginary part of the electron-phonon self-energy. The results agree in order of magnitude, highlighting how phonon emission can indeed lead to very short single-particle lifetimes. This is a promising step toward quantitative comparison of tr-ARPES data with many-body calculations. As a future direction, the electron-hole interaction needs to be include in the picture in a rigorous way.

Part III

APPENDIX

DIELECTRIC FUNCTION OF WSE$_2$ AND PUMP ABSORPTION

The dielectric function of a material completely determines the reflection and absorption coeffients. In the case of 2H-WSe$_2$, the complex dielectric function was retrieved by Kramers-Kronig analysis of the material's optical properties, from the visible to the VUV [268]. The dielectric function from reference [268] are shown in figure 100 a). Knowing both the real and imaginary part of ϵ, the reflection and absorption can be determined for both the wavelengths used to excite the system. This in turn can be used to give an estimate - in the linear regime - on what is the carrier density generated in the material. The refractive index n and the extinction coefficient k (related to the attenuation coefficient $\alpha = 4\pi k/\lambda$) are plotted in figure 100 b) and are approximately $k_{400} = 1.46$, $n_{400} = 3.55$ and $k_{800} = 0.57$, $n_{800} = 4.59$.
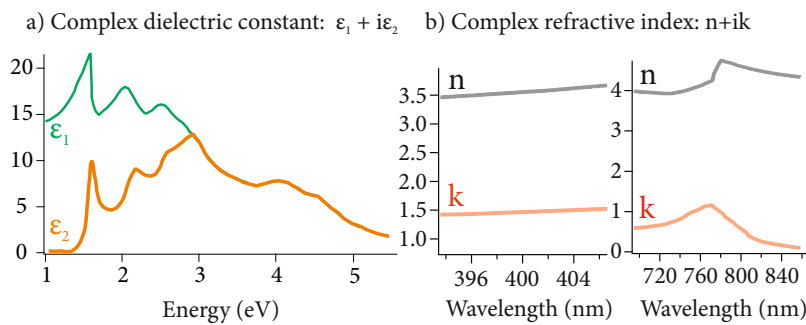

Figure 100: a) Complex dielectric function, from [268] b) Calculated complex refractive index, around 400 nm (left) and 800 nm (right).

Starting from the complex dielectric function, the absorbed fluence is calculated taking into account the Fresnel reflection from the surface: an angle of incidence of $10°$ was used for the plots in Figure 101, this is the geometry in which most of the time traces were collected. The exciton density is calculated in a slab of thickness of the first unit cell (that is, a bilayer of WSe$_2$). Classical electrodynamics might however be inaccurate in determining the carrier density on the atomic scale, i.e. in a single layer. The figures plot also the characteristic density a_0^{-2}, which can be thought as the density at which excitons start to overlap significantly: this can be used as a rough estimate of the Mott density, or the exciton density at which there is a transition between an exciton gas to an electron-hole plasma [272] (generally this is an overestimate [279]).

The surface exction radius is expected to lie somewhere in the range 1-2 nm (Section 5.4.1): the limit is reached for approximately
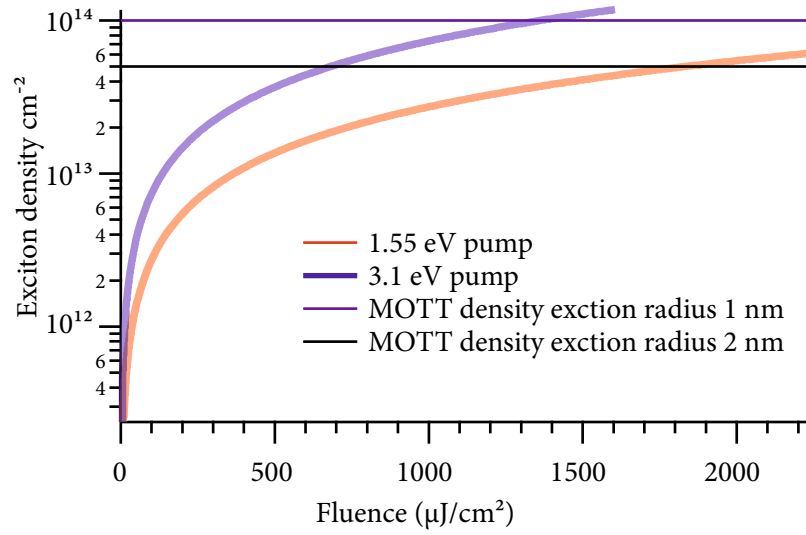
Figure 101: Calculated surface exciton density as a function of the incident optical fluence.

700 μJ/cm^2 incident fluence at 400 nm, and above 1.8 mJ/cm^2 in the case of an 800 nm pump.

BIBLIOGRAPHY

[1] I. Zutic, J. Fabian, and S. D. Sarma. Spintronics: Fundamentals and applications, apr 2004.

[2] M. Z. Hasan and C. L. Kane. Colloquium: Topological insulators. Rev. Mod. Phys., 82(4):3045–3067, 2010.

[3] D. Pesin and A. H. MacDonald. Spintronics and pseudospintronics in graphene and topological insulators. Nat. Mater., 11(5):409–416, apr 2012.

[4] X. Xu, W. Yao, D. Xiao, and T. F. Heinz. Spin and pseudospins in layered transition metal dichalcogenides. Nat. Phys., 10(5):343–350, apr 2014.

[5] A. D. Yoffe. Layer Compounds. Annu. Rev. Mater. Sci., 3(1):147–170, aug 1973.

[6] R. L. Withers and J. A. Wilson. An examination of the formation and characteristics of charge-density waves in inorganic materials with special reference to the two- and one-dimensional transition-metal chalcogenides. J. Phys. C: Solid State Phys., 19(25):4809–4845, sep 2000.

[7] K. S. Novoselov, D. Jiang, F. Schedin, T. J. Booth, V. V. Khotkevich, S. V. Morozov, and A. K. Geim. Two-dimensional atomic crystals. Proc. Natl. Acad. Sci. U.S.A., 102(30):10451–3, jul 2005.

[8] H. Zeng, J. Dai, W. Yao, D. Xiao, and X. Cui. Valley polarization in MoS2 monolayers by optical pumping. Nat. Nanotechnol., 7(8):490–493, jun 2012.

[9] A. K. Geim and I. V. Grigorieva. Van der Waals heterostructures. Nature, 499(7459):419–425, jul 2013.

[10] X. Hong, J. Kim, S.-F. Shi, Y. Zhang, C. Jin, Y. Sun, S. Tongay, J. Wu, Y. Zhang, and F. Wang. Ultrafast charge transfer in atomically thin MoS2/WS2 heterostructures. Nat. Nanotechnol., 9(9):682–686, 2014.

[11] A. Yoffe. Low-dimensional systems: quantum size effects and electronic properties of semiconductor microcrystallites (zero-dimensional systems) and some quasi-two-dimensional systems. Adv. Phys., 42(2):173–262, apr 1993.

[12] C. M. Heyl, J. Güdde, A. L'Huillier, and U. Höfer. High-order harmonic generation with μJ laser pulses at high repetition rates. J. Phys. B: At., Mol. Opt. Phys., 45(7):074020, apr 2012.

[13] H. Wang, Y. Xu, S. Ulonska, J. S. Robinson, P. Ranitovic, and R. A. Kaindl. Bright high-repetition-rate source of narrowband extreme-ultraviolet harmonics beyond 22 eV. Nat. Commun., 6(May):7459, 2015.

[14] C.-T. T. Chiang, A. Blättermann, M. Huth, J. Kirschner, and W. Widdra. High-order harmonic generation at 4 mhz as a light source for time-of-flight photoemission spectroscopy. Appl. Phys. Lett., 101(7):071116, 2012.

[15] P. Russbueldt, T. Mans, J. Weitenberg, H. D. Hoffmann, and R. Poprawe. Compact diode-pumped 1.1 kW Yb: YAG Innoslab femtosecond amplifier. Optic Letters, 35(24):4169–4171, dec 2010.

[16] T. Eidam, S. Hanf, E. Seise, T. V. Andersen, T. Gabler, C. Wirth, T. Schreiber, J. Limpert, and A. Tünnermann. Femtosecond fiber CPA system emitting 830 W average output power. Optic Letters, 35(2):94–6, jan 2010.

[17] J.-P. Negel, A. Voss, M. Abdou Ahmed, D. Bauer, D. Sutter, A. Killi, T. Graf, and M. A. Ahmed. 1.1 kW average output power from a thin-disk multipass amplifier for ultrashort laser pulses. Opt. Lett., 38(24):5442–5445, dec 2013.

[18] M. Krebs, S. Hädrich, S. Demmler, J. Rothhardt, A. Zaïr, L. Chipperfield, J. Limpert, and A. Tünnermann. Towards isolated attosecond pulses at megahertz repetition rates. Nat. Photonics, 7(7):555–559, 2013.

[19] M. Puppin, Y. Deng, O. Prochnow, J. Ahrens, T. Binhammer, U. Morgner, M. Krenz, M. Wolf, and R. Ernstorfer. 500 kHz OPCPA delivering tunable sub-20 fs pulses with 15 W average power based on an all-ytterbium laser. Opt. Express, 23(2):1491, 2015.

[20] S. Meskers, P. van Hal, A. Spiering, J. Hummelen, A. van der Meer, and R. Janssen. Generation and Evolution of Spin-, Valley-, and Layer-Polarized Excited Carriers in Inversion-Symmetric WSe2. Phys. Rev. B, 61(15):9917–9920, jun 2000.

[21] A. Damascelli. Angle-resolved photoemission studies of the cuprate superconductors. Rev. Mod. Phys., 75(April):473, 2003.

[22] S. Hüfner. Photoelectron spectroscopy : principles and applications. Springer, Berlin New York, 1996.

[23] S. Hüfner. Very high resolution photoelectron spectroscopy. New York Springer, Berlin, 2007.

[24] E. W. Plummer and W. Eberhardt. <u>Angle-Resolved Photoemission as a Tool for the Study of Surfaces</u>, pages 533–656. John Wiley and Sons, Inc., 1982.

[25] N. Ashcroft. <u>Solid state physics</u>. Saunders College Pub, Fort Worth, 1976.

[26] M. Seah and W. Dench. Quantitative Electron Spectroscopy of Surfaces :. <u>Surf. Interface Anal.</u>, 1(1):2–11, 1979.

[27] J. D. Koralek, J. F. Douglas, N. C. Plumb, J. D. Griffith, S. T. Cundiff, H. C. Kapteyn, M. M. Murnane, and D. S. Dessau. Experimental setup for low-energy laser-based angle resolved photoemission spectroscopy. <u>Rev. Sci. Instrum.</u>, 78(5):053905, may 2007.

[28] S. Moser. An experimentalist's guide to the matrix element in angle resolved photoemission. <u>J. Electron Spectrosc. Relat. Phenom.</u>, 214:29–52, 2017.

[29] N. Smith, P. Thirtym, and Y. Petroff. Photoemission Linewidth and quasiparticle lifetimes. <u>Phys. Rev. B</u>, 47(23):15476–15481, 1993.

[30] P. C. Yeh, W. Jin, N. Zaki, D. Zhang, J. T. Liou, J. T. Sadowski, A. Al-Mahboob, J. I. Dadap, I. P. Herman, P. Sutter, and R. M. Osgood. Layer-dependent electronic structure of an atomically heavy two-dimensional dichalcogenide. <u>Phys. Rev. B</u>, 91(4):1–6, 2015.

[31] U. Bovensiepen and P. S. Kirchmann. Elementary relaxation processes investigated by femtosecond photoelectron spectroscopy of two-dimensional materials, sep 2012.

[32] F. Krausz and M. Ivanov. Attosecond physics. <u>Rev. Mod. Phys.</u>, 81(1):163–234, feb 2009.

[33] U. Bovensiepen. <u>Dynamics at solid state surfaces and interfaces</u>. John Wiley distributor, Weinheim Chichester, 2010.

[34] X. Cui, C. Wang, A. Argondizzo, S. Garrett-Roe, B. Gumhalter, and H. Petek. Transient excitons at metal surfaces. <u>Nat. Phys.</u>, 10(7):505–509, 2014.

[35] M. Weinelt. Time-resolved two-photon photoemission from metal surfaces. <u>J. Phys.: Condens. Matter</u>, 14(43):R1099, 2002.

[36] H. Petek and S. Ogawa. Femtosecond Time-Resolved Two-Photon Photoemission Studies of Electron Dynamics in Metals. <u>Prog. in Surf. Sci.</u>, 56(4):239–310, 1997.

[37] P. Echenique, R. Berndt, E. Chulkov, T. Fauster, a. Goldmann, and U. Höfer. Decay of electronic excitations at metal surfaces. Surf. Sci. Rep., 52(7-8):219–317, may 2004.

[38] X.-Y. Zhu. Electron transfer at molecule-metal interfzces: a two-photon photoemission study. Annu. Rev. Phys. Chem., 53(4):221–247, 2002.

[39] I. Gierz, M. Mitrano, H. Bromberger, C. Cacho, R. Chapman, E. Springate, S. Link, U. Starke, B. Sachs, M. Eckstein, T. O. Wehling, M. I. Katsnelson, A. Lichtenstein, and A. Cavalleri. Phonon-pump extreme-ultraviolet-photoemission probe in graphene: Anomalous heating of dirac carriers by lattice deformation. Phys. Rev. Lett., 114(12):125503, mar 2015.

[40] R. Haight and D. Peale. Tunable photoemission with harmonics of subpicosecond lasers. Rev. Sci. Instrum., 65(6):1853–1857, 1994.

[41] W. S. Lee, I. M. Vishik, D. H. Lu, C. L. Smallwood, R. A. Kaindl, and A. Lanzara. A brief update of angle-resolved photoemission spectroscopy on a correlated electronsystem Ultrafast angle-resolved photoemission spectroscopy of quantum materials. EPL, 115(2):27001, 2016.

[42] L. Perfetti, P. a. Loukakos, M. Lisowski, U. Bovensiepen, H. Eisaki, and M. Wolf. Ultrafast Electron Relaxation in Superconducting $Bi_2Sr_2CaCu_2O_{8+\delta}$ by Time-Resolved Photoelectron Spectroscopy. Phys. Rev. Lett., 99(19):197001, nov 2007.

[43] W. Zhang, C. Hwang, C. L. Smallwood, T. L. Miller, G. Affeldt, K. Kurashima, C. Jozwiak, H. Eisaki, T. Adachi, Y. Koike, D.-H. Lee, and A. Lanzara. Ultrafast quenching of electron-boson interaction and superconducting gap in a cuprate superconductor. Nat. Commun., 5:4959, jan 2014.

[44] T. Rohwer, S. Hellmann, M. Wiesenmayer, C. Sohrt, A. Stange, B. Slomski, A. Carr, Y. Liu, L. M. Avila, M. Kalläne, S. Mathias, L. Kipp, K. Rossnagel, and M. Bauer. Collapse of long-range charge order tracked by time-resolved photoemission at high momenta. Nature, 471(7339):490–493, 2011.

[45] S. Hellmann, T. Rohwer, M. Kalläne, K. Hanff, C. Sohrt, A. Stange, A. Carr, M. M. Murnane, H. C. Kapteyn, L. Kipp, M. Bauer, and K. Rossnagel. Time-domain classification of charge-density-wave insulators. Nat. Commun., 3:1069, jan 2012.

[46] F. Schmitt, P. S. Kirchmann, U. Bovensiepen, R. G. Moore, L. Rettig, M. Krenz, J.-H. Chu, N. Ru, L. Perfetti, D. H. Lu, M. Wolf,

I. R. Fisher, and Z.-X. Shen. Transient electronic structure and melting of a charge density wave in TbTe3. Science (New York, N.Y.), 321(5896):1649–52, sep 2008.

[47] C. Monney, M. Puppin, C. W. Nicholson, M. Hoesch, R. T. Chapman, E. Springate, H. Berger, A. Magrez, C. Cacho, R. Ernstorfer, and M. Wolf. Revealing the role of electrons and phonons in the ultrafast recovery of charge density wave correlations in 1T:TiSe$_2$. Phys. Rev. B, 94(16):165165, oct 2016.

[48] L. Perfetti, P. Loukakos, M. Lisowski, U. Bovensiepen, H. Berger, S. Biermann, P. Cornaglia, a. Georges, and M. Wolf. Time Evolution of the Electronic Structure of 1T-TaS2 through the Insulator-Metal Transition. Phys. Rev. Lett., 97(6):067402, aug 2006.

[49] L. Rettig, R. Cortés, S. Thirupathaiah, P. Gegenwart, H. S. Jeevan, M. Wolf, J. Fink, and U. Bovensiepen. Ultrafast momentum-dependent response of electrons in antiferromagnetic EuFe$_2$As$_2$ driven by optical excitation. Phys. Rev. Lett., 108(9):1–5, 2012.

[50] L. Rettig, R. Cortés, H. S. Jeevan, P. Gegenwart, T. Wolf, J. Fink, and U. Bovensiepen. Electron-phonon coupling in 122 Fe pnictides analyzed by femtosecond time-resolved photoemission. New J. Phys., 15(8):083023, aug 2013.

[51] S. Yang, J. a. Sobota, D. Leuenberger, A. F. Kemper, J. J. Lee, F. T. Schmitt, W. Li, R. G. Moore, P. S. Kirchmann, and Z. X. Shen. Thickness-dependent coherent phonon frequency in ultrathin FeSe/SrTiO$_3$ films. Nano Lett., 15(6):4150–4154, 2015.

[52] G. Saathoff, L. Miaja-Avila, M. Aeschlimann, M. Murnane, and H. Kapteyn. Laser-assisted photoemission from surfaces. Phys. Rev. A, 77(2):022903, feb 2008.

[53] L. Miaja-Avila, J. Yin, S. Backus, G. Saathoff, M. Aeschlimann, M. M. Murnane, and H. C. Kapteyn. Ultrafast studies of electronic processes at surfaces using the laser-assisted photoelectric effect with long-wavelength dressing light. Phys. Rev. A, 79(3):1–4, 2009.

[54] Y. H. Wang, H. Steinberg, P. Jarillo-Herrero, and N. Gedik. Observation of Floquet-Bloch States on the Surface of a Topological Insulator. Science, 342(6157):453–457, 2013.

[55] F. Mahmood, C.-K. Chan, Z. Alpichshev, D. Gardner, Y. Lee, P. A. Lee, and N. Gedik. Selective scattering between Floquet-Bloch and Volkov states in a topological insulator. Nat. Phys., 12(January):1–6, 2015.

[56] N. V. Smith. Inverse photoemission. Rep. Prog. Phys., 51(9):1227–1294, 1988.

[57] J. a. Sobota, S. Yang, J. G. Analytis, Y. L. Chen, I. R. Fisher, P. S. Kirchmann, and Z.-X. Shen. Ultrafast Optical Excitation of a Persistent Surface-State Population in the Topological Insulator Bi_{2}Se_{3}. Phys. Rev. Lett., 108(11):117403, mar 2012.

[58] A. Grubišić Čabo, J. A. Miwa, S. S. Grønborg, J. M. Riley, J. C. Johannsen, C. Cacho, O. Alexander, R. T. Chapman, E. Springate, M. Grioni, J. V. Lauritsen, P. D. C. King, P. Hofmann, and S. Ulstrup. Observation of Ultrafast Free Carrier Dynamics in Single Layer MoS2. Nano Lett., 15(9):5883–5887, 2015.

[59] S. Ulstrup, A. G. Čabo, J. A. Miwa, J. M. Riley, S. S. Grønborg, J. C. Johannsen, C. Cacho, O. Alexander, R. T. Chapman, E. Springate, M. Bianchi, M. Dendzik, J. V. Lauritsen, P. D. C. King, and P. Hofmann. Ultrafast band structure control of a two-dimensional heterostructure. ACS Nano, 10(6):6315–6322, 2016.

[60] R. Wallauer, J. Reimann, N. Armbrust, J. Güdde, and U. Höfer. Intervalley scattering in MoS2 imaged by two-photon photoemission with a high-harmonic probe. Appl. Phys. Lett., 109(16):162102, 2016.

[61] P. Hein, A. Stange, K. Hanff, L. X. Yang, G. Rohde, K. Rossnagel, and M. Bauer. Momentum-resolved hot electron dynamics at the 2H-MoS$_2$ surface. Phys. Rev. B, 94(20):205406, 2016.

[62] M. Sentef, A. Kemper, B. Moritz, J. Freericks, Z.-X. Shen, and T. Devereaux. Examining Electron-Boson Coupling Using Time-Resolved Spectroscopy. Phys. Rev. X, 3(4):041033, dec 2013.

[63] S. L. Yang, J. a. Sobota, D. Leuenberger, Y. He, M. Hashimoto, D. H. Lu, H. Eisaki, P. S. Kirchmann, and Z. X. Shen. Inequivalence of Single-Particle and Population Lifetimes in a Cuprate Superconductor. Phys. Rev. Lett., 114(24):247001, 2015.

[64] A. McPherson, G. Gibson, H. Jara, U. Johann, T. S. Luk, I. a. McIntyre, K. Boyer, and C. K. Rhodes. Studies of multiphoton production of vacuum-ultraviolet radiation in the rare gases. Journal of the Optical Society of America B, 4(4):595, 1987.

[65] M. Ferray, A. L'Huillier, X. F. Li, L. A. Lompre, G. Mainfray, and C. Manus. Multiple-harmonic conversion of 1064 nm radiation in rare gases. J. Phys. B: At., Mol. Opt. Phys., 21(3):L31–L35, 1999.

[66] H. S. Karlsson, G. Chiaia, and U. O. Karlsson. A system for time- and angle-resolved photoelectron spectroscopy based on

an amplified femtosecond titanium:sapphire laser system. Rev. Sci. Instrum., 67(10):3610–3615, 1996.

[67] S. Mathias, L. Miaja-Avila, M. Murnane, H. Kapteyn, M. Aeschlimann, and M. Bauer. Angle-resolved photoemission spectroscopy with a femtosecond high harmonic light source using a two-dimensional imaging electron analyzer. Rev. Sci. Instrum., 78:083105, 2007.

[68] M. Bauer. Femtosecond ultraviolet photoelectron spectroscopy of ultra-fast surface processes. J. Phys. D: Appl. Phys., 38(16):R253–R267, 2005.

[69] S. Passlack, S. Mathias, O. Andreyev, D. Mittnacht, M. Aeschlimann, and M. Bauer. Space charge effects in photoemission with a low repetition, high intensity femtosecond laser source. J. Appl. Phys., 100:024912, 2006.

[70] J. Graf, S. Hellmann, C. Jozwiak, C. Smallwood, Z. Hussain, R. Kaindl, L. Kipp, K. Rossnagel, and A. Lanzara. Vacuum space charge effect in laser-based solid-state photoemission spectroscopy. J. Appl. Phys., 107(1):014912–014912, 2010.

[71] S. K. Sundaram and E. Mazur. Inducing and probing non-thermal transitions in semiconductors using femtosecond laser pulses. Nat. Mater., 1(4):217–224, 2002.

[72] L. P. Oloff, K. Hanff, A. Stange, G. Rohde, F. Diekmann, M. Bauer, and K. Rossnagel. Pump laser-induced space-charge effects in HHG-driven time- and angle-resolved photoelectron spectroscopy. J. Appl. Phys., 119(22), 2016.

[73] E. Carpene, E. Mancini, C. Dallera, G. Ghiringhelli, C. Manzoni, G. Cerullo, and S. De Silvestri. A versatile apparatus for time-resolved photoemission spectroscopy via femtosecond pump-probe experiments. Rev. Sci. Instrum., 80(5):055101, may 2009.

[74] C. L. Smallwood, C. Jozwiak, and A. Lanzara. An ultrafast angle-resolved photoemission apparatus for measuring complex materials. Rev. Sci. Instrum., 83(12):123904, 2012.

[75] J. Faure, J. Mauchain, E. Papalazarou, W. Yan, J. Pinon, M. Marsi, and L. Perfetti. Full characterization and optimization of a femtosecond ultraviolet laser source for time and angle-resolved photoemission on solid surfaces. Rev. Sci. Instrum., 83(4):043109, 2012.

[76] F. Boschini, H. Hedayat, C. Dallera, P. Farinello, C. Manzoni, A. Magrez, H. Berger, G. Cerullo, and E. Carpene. An innovative Yb-based ultrafast deep ultraviolet source for time-resolved photoemission experiments. Rev. Sci. Instrum., 85(12):1–9, 2014.

[77] G. L. Dakovski, Y. Li, T. Durakiewicz, and G. Rodriguez. Tunable ultrafast extreme ultraviolet source for time- and angle-resolved photoemission spectroscopy. Rev. Sci. Instrum., 81(7):073108, 2010.

[78] E. Turcu, E. Springate, C. Froud, C. Cacho, J. Collier, W. Bryan, G. Nemeth, J. Marangos, J. Tisch, R. Torres, and Others. Ultrafast science and development at the Artemis facility. Proceedings of SPIE, 746902:1–15, 2010.

[79] B. Frietsch, R. Carley, K. Döbrich, C. Gahl, M. Teichmann, O. Schwarzkopf, P. Wernet, and M. Weinelt. A high-order harmonic generation apparatus for time- and angle-resolved photoelectron spectroscopy. Rev. Sci. Instrum., 84(7):075106, 2013.

[80] S. Plogmaker, J. A. Terschlüsen, N. Krebs, M. Svanqvist, J. Forsberg, U. B. Cappel, J. E. Rubensson, H. Siegbahn, and J. Söderström. Helios - a laboratory based on high-order harmonic generation of extreme ultraviolet photons for time-resolved spectroscopy. Rev. Sci. Instrum., 86(12):123107, 2015.

[81] G. Rohde, A. Hendel, A. Stange, K. Hanff, L.-P. Oloff, L. X. Yang, K. Rossnagel, and M. Bauer. Time-resolved ARPES with sub-15 fs temporal and near Fourier-limited spectral resolution. Rev. Sci. Instrum., 87(10):103102, 2016.

[82] J. Ojeda, C. A. Arrell, J. Grilj, F. Frassetto, L. Mewes, H. Zhang, F. van Mourik, L. Poletto, and M. Chergui. Harmonium: A pulse preserving source of monochromatic extreme ultraviolet (30-110 eV) radiation for ultrafast photoelectron spectroscopy of liquids. Structural Dynamics, 3(2), 2016.

[83] F. Frassetto and L. Poletto. Grating monochromators for the spectral selection of femtosecond extreme-ultraviolet pulses. Nucl. Instrum. Methods Phys. Res., Sect. A, 635(1 SUPPL.):S75–S79, apr 2011.

[84] J. Norin, K. Osvay, F. Albert, D. Descamps, J. Yang, A. Lhuillier, and C.-G. Wahlström. Design of an extreme-ultraviolet monochromator free from temporal stretching. Appl. Opt., 43(5):1072–81, 2004.

[85] S. Eich, A. Stange, A. Carr, J. Urbancic, T. Popmintchev, M. Wiesenmayer, K. Jansen, A. Ruffing, S. Jakobs, T. Rohwer, S. Hellmann, C. Chen, P. Matyba, L. Kipp, K. Rossnagel, M. Bauer, M. M. Murnane, H. C. Kapteyn, S. Mathias, and M. Aeschlimann. Time- and angle-resolved photoemission spectroscopy with optimized high-harmonic pulses using frequency-doubled

Ti:Sapphire lasers. J. Electron Spectrosc. Relat. Phenom., 195:231–236, may 2014.

[86] C.-T. T. Chiang, M. Huth, A. Trützschler, F. O. Schumann, J. Kirschner, and W. Widdra. Efficient and tunable high-order harmonic light sources for photoelectron spectroscopy at surfaces. J. Electron Spectrosc. Relat. Phenom., 200:15–21, 2015.

[87] C.-T. Chiang, M. Huth, A. Trützschler, M. Kiel, F. O. Schumann, J. Kirschner, and W. Widdra. Boosting laboratory photoelectron spectroscopy by megahertz high-order harmonics. New J. Phys., 17(1):13035, 2015.

[88] Y. Ishida, T. Togashi, K. Yamamoto, M. Tanaka, T. Kiss, T. Otsu, Y. Kobayashi, and S. Shin. Time-resolved photoemission apparatus achieving sub-20-meV energy resolution and high stability. Rev. Sci. Instrum., 85(12), 2014.

[89] R. Trebino. Frequency-Resolved Optical Gating: The Measurement of Ultrashort Laser Pulses. Springer US Imprint Springer, Boston, MA, 2000.

[90] J.-C. Diels and W. Rudolph. Ultrashort laser pulse phenomena : fundamentals, techniques, and applications on a femtosecond time scale. Elsevier/Academic Press, Amsterdam London, 2006.

[91] B. Saleh. Fundamentals of photonics. Wiley-Interscience, Hoboken, N.J, 2007.

[92] Z. Chang. Fundamentals of attosecond optics. CRC Press, Boca Raton, 2011.

[93] R. Boyd. Nonlinear optics. Academic Press, Amsterdam Boston, 2008.

[94] Y. Wang, B. Luther-Davies, Y. H. Chuang, R. S. Craxton, and D. D. Meyerhofer. Highly efficient conversion of picosecond Nd laser pulses with the use of group-velocity-mismatched frequency doubling in KDP. Optic Letters, 16(23):1862–4, dec 1991.

[95] J. Reintjes. Nonlinear Optical Parametric Processes in Liquids and Gases. Elsevier Science, Oxford, 1984.

[96] W. Silfvast. Laser fundamentals. Cambridge University Press, Cambridge New York, 2004.

[97] D. Strickland and G. Mourou. Compression of amplified chirped optical pulses. Opt. Commun., 56(3):219–221, 1985.

[98] P. Maine, D. Strickland, P. Bado, M. Pessot, and G. Mourou. Generation of Ultrahigh Peak Power Pulses By Chirped Pulse Amplification. IEEE J. Quantum. Electron., 24(2):398–403, 1988.

[99] E. B. Treacy. Optical Pulse Compression With Diffraction Gratings. IEEE J. Quantum. Electron., 5(9):454–458, 1969.

[100] R. Fork, O. Martinez, and J. Gordon. Negative dispersion using pairs of prisms. Optic Letters, 9(5):150–152, 1984.

[101] O. E. Martinez. 3000 times grating compressor with positive group velocity dispersion: application to fiber compensation in 1.3-1.6 μm region, 1987.

[102] S. Backus, C. G. Durfee, M. M. Murnane, and H. C. Kapteyn. High power ultrafast lasers. Rev. Sci. Instrum., 69(3):1207, 1998.

[103] R. D. Boyd, J. a. Britten, D. E. Decker, B. W. Shore, B. C. Stuart, M. D. Perry, and L. Li. High-efficiency metallic diffraction gratings for laser applications. Appl. Opt., 34(10):1697–1706, 1995.

[104] M. Rumpel, M. Moeller, C. Moormann, T. Graf, and M. Abdou Ahmed. Broadband pulse compression gratings with measured 99.7% diffraction efficiency. Opt. Lett., 39(2):323–6, 2014.

[105] H. Kaptyen and M. M. Murnane. Femtosecond Lasers: the next generation. Optics and Photonics News, page 20, 1994.

[106] S. Rausch, T. Binhammer, A. Harth, J. Kim, R. Ell, F. X. Kärtner, and U. Morgner. Controlled waveforms on the single-cycle scale from a femtosecond oscillator. Opt. Express, 16(13):9739–9745, 2008.

[107] I. Matsushima, H. Yashiro, and T. Tomie. 10 kHz 40 W Ti: sapphire regenerative ring amplifier. Opt. Lett., 31(13):2066–2068, 2006.

[108] X. Zhang, E. Schneider, G. Taft, H. Kaptyen, M. Murnane, and S. Backus. Multi-microjoule, MHz repetition rate Ti:sapphire ultrafast regenerative amplifier system. Opt. Express, 20(7):7015–21, mar 2012.

[109] S. Nolte. Ultrashort pulse laser technology : laser sources and applications. Springer, Cham, 2015.

[110] P. Russbueldt, T. Mans, G. Rotarius, J. Weitenberg, H. D. Hoffmann, and R. Poprawe. 400 W Yb:YAG Innoslab fs-amplifier. Opt. Express, 17(15):1013–1023, 2009.

[111] J. Limpert, F. Röser, T. Schreiber, and A. Tünnermann. High-power ultrafast fiber laser systems. IEEE Journal on Selected Topics in Quantum Electronics, 12(2):233–244, 2006.

[112] T. a. Birks, J. C. Knight, and P. S. Russell. Endlessly single-mode photonic crystal fiber. Opt. Lett., 22(13):961–3, jul 1997.

[113] L. Lavenu, M. Natile, F. Guichard, Y. Zaouter, M. Hanna, E. Mottay, and P. Georges. High-energy few-cycle Yb-doped fiber amplifier source based on a single nonlinear compression stage. Opt. Express, 25(7):7530, 2017.

[114] S. Hädrich, M. Krebs, A. Hoffmann, A. Klenke, J. Rothhardt, J. Limpert, and A. Tünnermann. Exploring new avenues in high repetition rate table-top coherent extreme ultraviolet sources. Light: Science & Applications, 4(8):e320, 2015.

[115] T. Mans, J. Dolkemeyer, P. Russbüldt, and C. Schnitzler. Highly flexible ultrafast laser system with 260 W average power. Proceedings of SPIE, 7912(2):79120M, 2011.

[116] B. W. Tilma, M. Mangold, C. A. Zaugg, S. M. Link, D. Waldburger, A. Klenner, A. S. Mayer, E. Gini, M. Golling, and U. Keller. Recent advances in ultrafast semiconductor disk lasers. Light: Science & Applications, 4(7):e310, 2015.

[117] H. Fattahi, H. G. Barros, M. Gorjan, T. Nubbemeyer, B. Alsaif, C. Y. Teisset, M. Schultze, S. Prinz, M. Haefner, M. Ueffing, A. Alismail, L. Vámos, A. Schwarz, O. Pronin, J. Brons, X. T. Geng, G. Arisholm, M. Ciappina, V. S. Yakovlev, D.-E. Kim, A. M. Azzeer, N. Karpowicz, D. Sutter, Z. Major, T. Metzger, and F. Krausz. Third-generation femtosecond technology. Optica, 1(1):45, 2014.

[118] M. Schulz, R. Riedel, A. Willner, S. Düsterer, M. J. Prandolini, J. Feldhaus, B. Faatz, J. Rossbach, M. Drescher, and F. Tavella. Pulsed operation of a high average power Yb:YAG thin-disk multipass amplifier. Opt. Express, 20(5):5038–43, 2012.

[119] R. Sutherland. Handbook of nonlinear optics. Marcel Dekker, New York, 2003.

[120] K. Kato, N. Umemura, and T. Mikami. Sellmeier and thermo-optic dispersion formulas for β-Ba$_2$O$_4$ (revisited). Proceedings of SPIE, 7582:75821L–1, feb 2010.

[121] K. Kato. Second-harmonic generation to 2048 Å in β-Ba$_2$O$_4$. IEEE J. Quantum. Electron., 22(7):1013–1014, July 1986.

[122] G. Cerullo, S. De Silvestri, S. D. Silvestri, and S. De Silvestri. Ultrafast optical parametric amplifiers. Rev. Sci. Instrum., 74(1):1, 2003.

[123] R. C. Eckardt, H. Masuda, Y. X. Fan, and R. L. Byer. Absolute and relative nonlinear optical coefficients of KDP, KD*P,

BaB$_2$O$_4$, LiIO$_3$, MgO:LiNbO$_3$, and KTP measured by phase-matched second-harmonic generation. IEEE J. Quantum. Electron., 26(5):922–933, 1990.

[124] C. C. Wang and G. W. Racette. Measurement of Parametric Gain Accompanying Optical Difference Frequency Generation. Appl. Phys. Lett., 6(8):169, 1965.

[125] B. C. Stuart, M. D. Feit, S. Herman, A. M. Rubenchik, B. W. Shore, and M. D. Perry. Nanosecond-to-femtosecond laser-induced breakdown in dielectrics. Phys. Rev. B, 53(4):1749–1761, 1996.

[126] M. Mero, J. Liu, W. Rudolph, D. Ristau, and K. Starke. Scaling laws of femtosecond laser pulse induced breakdown in oxide films. Phys. Rev. B, 71:1–7, 2005.

[127] J. Rothhardt. High power ultra-short pulse lasers based on fiber driven OPCPA. PhD thesis, Friedrich-Schiller Universität Jena, 2010.

[128] D. Brida, G. Krauss, A. Sell, and A. Leitenstorfer. Ultrabroadband Er:fiber lasers. Laser & Photonics Reviews, 8(3):409–428, may 2014.

[129] T. Lang, A. Harth, J. Matyschok, T. Binhammer, M. Schultze, and U. Morgner. Impact of temporal, spatial and cascaded effects on the pulse formation in ultra-broadband parametric amplifiers. Opt. Express, 21(1):949–59, jan 2013.

[130] M. J. Prandolini, R. Riedel, M. Schulz, a. Hage, F. Tavella, D. Jena, H. Höppner, and F. Tavella. Design considerations for a high power, ultrabroadband optical parametric chirped-pulse amplifier. Opt. Express, 22(2):1594, jan 2014.

[131] J. Matyschok, T. Lang, T. Binhammer, O. Prochnow, S. Rausch, M. Schultze, A. Harth, P. Rudawski, C. L. Arnold, A. L'Huillier, and U. Morgner. Temporal and spatial effects inside a compact and CEP stabilized, few-cycle OPCPA system at high repetition rates. Opt. Express, 21(24):29656–65, dec 2013.

[132] A. Dubietis, G. Jonusauskas, and A. Piskarskas. Powerful femtosecond pulse generation by chirped and stretched pulse parametric amplification in BBO crystal. Opt. Commun., 88(4-6):437–440, 1992.

[133] R. Butkus, R. Danielius, A. Dubietis, A. Piskarskas, and A. Stabinis. Progress in chirped pulse optical parametric amplifiers. Appl. Phys. B: Lasers Opt., 79(6):693–700, 2004.

[134] A. Vaupel, N. Bodnar, B. Webb, L. Shah, and M. Richardson. Concepts, performance review, and prospects of table-top, few-cycle optical parametric chirped-pulse amplification. Opt. Eng., 53(5):051507, dec 2013.

[135] S. Witte and K. S. E. Eikema. Ultrafast optical parametric chirped-pulse amplification. IEEE Journal on Selected Topics in Quantum Electronics, 18(1):296–307, 2012.

[136] M. Bradler and E. Riedle. Sub-20 fs μJ-energy pulses tunable down to the near-UV from a 1 MHz Yb-fiber laser system. Opt. Lett., 39(9):2588–91, may 2014.

[137] H. Pires, M. Baudisch, D. Sanchez, M. Hemmer, and J. Biegert. Ultrashort pulse generation in the mid-IR. Prog. Quantum Electron., 43:1–30, 2015.

[138] S.-W. Huang, G. Cirmi, J. Moses, K.-H. Hong, S. Bhardwaj, J. R. Birge, L.-J. Chen, E. Li, B. J. Eggleton, G. Cerullo, and F. X. Kärtner. High-energy pulse synthesis with sub-cycle waveform control for strong-field physics. Nat. Photonics, 5(8):475–479, 2011.

[139] S. Witte, R. Zinkstok, W. Hogervorst, and K. Eikema. Generation of few-cycle terawatt light pulses using optical parametric chirped pulse amplification. Opt. Express, 13(13):4903–8, jun 2005.

[140] F. J. Furch, S. Birkner, F. Kelkensberg, A. Giree, A. Anderson, C. P. Schulz, and M. J. J. Vrakking. Carrier-envelope phase stable few-cycle pulses at 400 kHz for electron-ion coincidence experiments. Opt. Express, 21(19):22671, 2013.

[141] S. Prinz, M. Haefner, C. Y. Teisset, R. Bessing, Y. Lee, X. T. Geng, S. Kim, D. E. Kim, M. Schultze, K. Michel, Y. Lee, X. T. Geng, S. Kim, D. E. Kim, T. Metzger, and M. Schultze. CEP-stable, sub-6 fs, 300-kHz OPCPA system with more than 15 W of average power. Opt. Express, 23(2):1388–1394, 2015.

[142] M. Schultze, T. Binhammer, A. Steinmann, G. Palmer, M. Emons, and U. Morgner. Few-cycle OPCPA system at 143 kHz with more than 1 microJ of pulse energy. Opt. Express, 18(3):2836–41, feb 2010.

[143] M. Schultze, T. Binhammer, G. Palmer, M. Emons, T. Lang, and U. Morgner. Multi-μJ, CEP-stabilized, two-cycle pulses from an OPCPA system with up to 500 kHz repetition rate. Opt. Express, 18(26):27291–27297, 2010.

[144] H. Höppner, A. Hage, T. Tanikawa, M. Schulz, R. Riedel, U. Teubner, M. J. Prandolini, B. Faatz, and F. Tavella. An optical

parametric chirped-pulse amplifier for seeding high repetition rate free-electron lasers. New J. Phys., 17(5):53020, 2015.

[145] C. Y. Teisset, N. Ishii, T. Fuji, T. Metzger, S. Köhler, R. Holzwarth, A. Baltuška, A. M. Zheltikov, and F. Krausz. Soliton-based pump-seed synchronization for few-cycle OPCPA. Opt. Express, 13(17):140–142, 2005.

[146] A. Steinmann, A. Killi, G. Palmer, T. Binhammer, and U. Morgner. Generation of few-cycle pulses directly from a MHz-NOPA. Opt. Express, 14(22):10627–10630, 2006.

[147] A. Killi, A. Steinmann, G. Palmer, U. Morgner, H. Bartelt, and J. Kobelke. Megahertz optical parametric amplifier pumped by a femtosecond oscillator. Opt. Lett., 31(1):125–7, jan 2006.

[148] J. Rothhardt, S. Hädrich, F. Röser, J. Limpert, and a. Tünnermann. 500 MW peak power degenerated optical parametric amplifier delivering 52 fs pulses at 97 kHz repetition rate. Opt. Express, 16(12):8981–8, jun 2008.

[149] S. Hädrich, J. Rothhardt, F. Röser, T. Gottschall, J. Limpert, and A. Tünnermann. Degenerate optical parametric amplifier delivering sub 30 fs pulses with 2GW peak power. Opt. Express, 16(24):19812–20, nov 2008.

[150] J. Dudley, G. Genty, and S. Coen. Supercontinuum generation in photonic crystal fiber. Rev. Mod. Phys., 78(4):1135, 2006.

[151] M. Bradler, P. Baum, and E. Riedle. Femtosecond continuum generation in bulk laser host materials with sub-uJ pump pulses. Appl. Phys. B: Lasers Opt., 97(3):561–574, 2009.

[152] T. V. Andersen, O. Schmidt, C. Bruchmann, J. Limpert, C. Aguergaray, E. Cormier, and A. Tünnermann. High repetition rate tunable femtosecond pulses and broadband amplification from fiber laser pumped parametric amplifier. Opt. Express, 14(11):4765–4773, 2006.

[153] J. Nillon, O. Crégut, C. Bressler, and S. Haacke. Two MHz tunable non collinear optical parametric amplifiers with pulse durations down to 6 fs. Opt. Express, 22(12):14964–74, jun 2014.

[154] M. Emons, A. Steinmann, T. Binhammer, G. Palmer, M. Schultze, and U. Morgner. Sub-10-fs pulses from a MHz-NOPA with pulse energies of 0.4 microJ. Opt. Express, 18(2):1191–6, 2010.

[155] C. Homann, C. Schriever, P. Baum, and E. Riedle. Octave wide tunable UV-pumped NOPA: pulses down to 20 fs at 0.5 MHz repetition rate. Opt. Express, 16(8):5746–56, apr 2008.

[156] C. Schriever, S. Lochbrunner, P. Krok, and E. Riedle. Tunable pulses from below 300 to 970 nm with durations down to 14 fs based on a 2 MHz ytterbium-doped fiber system. Optic Letters, 33(2):192–4, jan 2008.

[157] M. Schulz, R. Riedel, a. Willner, T. Mans, C. Schnitzler, P. Russ-bueldt, J. Dolkemeyer, E. Seise, T. Gottschall, S. Hädrich, S. Du-esterer, H. Schlarb, J. Feldhaus, J. Limpert, B. Faatz, a. Tünner-mann, J. Rossbach, M. Drescher, and F. Tavella. Yb:YAG Innos-lab amplifier: efficient high repetition rate subpicosecond pum-ping system for optical parametric chirped pulse amplification. Opt. Lett., 36(13):2456–8, jul 2011.

[158] R. Riedel, A. Stephanides, and M. Prandolini. Power scaling of supercontinuum seeded megahertz-repetition rate optical pa-rametric chirped pulse amplifiers. Opt. Lett., 39(6):1422–1424, 2014.

[159] M. Puppin, Y. Deng, O. Prochnow, J. Matyschok, T. Binhammer, U. Morgner, M. Wolf, and R. Ernstorfer. Fiber-Slab-Pumped OP-CPA for XUV-Based Time-Resolved Photoelectron Spectroscopy at 500 kHz Repetition Rate. In 19th International Conference on Ultrafast Phenomena, OSA Technical Digest (online), page 09.Wed.P3.53, Okinawa, 2014. Optical Society of America.

[160] M. Pergament, M. Kellert, K. Kruse, J. Wang, G. Palmer, L. Wis-smann, U. Wegner, and M. J. Lederer. High power burst-mode optical parametric amplifier with arbitrary pulse selection. Opt. Express, 22(18):22202, sep 2014.

[161] R. Alfano. The supercontinuum laser source : fundamentals with updated references. Springer, New York, 2006.

[162] T. Brabec and F. Krausz. Intense few-cycle laser fields: Frontiers of nonlinear optics. Rev. Mod. Phys., 72(2):545–591, 2000.

[163] S. L. Chin, S. A. Hosseini, W. Liu, Q. Luo, F. Théberge, N. Akö-zbek, A. Becker, V. P. Kandidov, O. G. Kosareva, and H. Schroe-der. The propagation of powerful femtosecond laser pulses in opticalmedia: physics, applications, and new challenges. Can. J. Phys., 83(9):863–905, 2005.

[164] A.-L. Calendron, H. Çankaya, G. Cirmi, and F. X. Kärtner. White-light generation with sub-ps pulses. Opt. Express, 23(11):13866, 2015.

[165] F. Tavella. Multiterawatt few-cycle pulse OPCPA for applications in high-field physics. PhD thesis, Ludwig-Maximilians Universität München, 2007.

[166] R. Riedel, M. Schulz, M. J. Prandolini, A. Hage, H. Höppner, T. Gottschall, J. Limpert, M. Drescher, and F. Tavella. Long-term stabilization of high power optical parametric chirped-pulse amplifiers. Opt. Express, 21(23):28987, 2013.

[167] J. Moses and S. Huang. Conformal profile theory for performance scaling of ultrabroadband optical parametric chirped pulse amplification. Journal of the Optical Society of America B, 28(4):812–831, 2011.

[168] J. Moses, C. Manzoni, S.-W. Huang, G. Cerullo, and F. X. Kärtner. Temporal optimization of ultrabroadband high-energy OPCPA. Opt. Express, 17(7):5540–55, mar 2009.

[169] J. A. Fülöp, Z. Major, B. Horváth, F. Tavella, A. Baltuška, and F. Krausz. Shaping of picosecond pulses for pumping optical parametric amplification. Appl. Phys. B: Lasers Opt., 87(1):79–84, 2007.

[170] M. Guardalben, J. Keegan, L. Waxer, V. Bagnoud, I. Begishev, J. Puth, and J. Zuegel. Design of a highly stable, high-conversion-efficiency, optical parametric chirped-pulse amplification system with good beam quality. Opt. Express, 11(20):2511–2524, 2003.

[171] J. Rothhardt, S. Demmler, S. Hädrich, J. Limpert, and A. Tünnermann. Octave-spanning OPCPA system delivering CEP-stable few-cycle pulses and 22 W of average power at 1 MHz repetition rate. Opt. Express, 20(10):10870–8, may 2012.

[172] J. Bromage, J. Rothhardt, S. Hädrich, C. Dorrer, C. Jocher, S. Demmler, J. Limpert, A. Tünnermann, and J. D. Zuegel. Analysis and suppression of parasitic processes in noncollinear optical parametric amplifiers. Opt. Express, 19(18):16797–808, aug 2011.

[173] J. Rothhardt, S. Demmler, S. Hädrich, T. Peschel, J. Limpert, and A. Tünnermann. Thermal effects in high average power optical parametric amplifiers. Opt. Lett., 38(5):763–5, mar 2013.

[174] F. Wise, a. Chong, and W. Renninger. High-energy femtosecond fiber lasers based on pulse propagation at normal dispersion. Laser & Photonics Review, 2(1-2):58–73, apr 2008.

[175] A. Chong, J. Buckley, W. Renninger, and F. Wise. All-normal-dispersion femtosecond fiber laser. Opt. Express, 14(21):10095, 2006.

[176] M. Schultz, H. Karow, D. Wandt, U. Morgner, and D. Kracht. Ytterbium femtosecond fiber laser without dispersion com-

pensation tunable from 1015nm to 1050nm. *Opt. Commun.*, 282(13):2567–2570, jul 2009.

[177] J. Rothhardt, T. Eidam, S. Hädrich, F. Jansen, F. Stutzki, T. Gottschall, T. V. Andersen, J. Limpert, and A. Tünnermann. 135 W average-power femtosecond pulses at 520 nm from a frequency-doubled fiber laser system. *Optic Letters*, 36(3):316–8, feb 2011.

[178] R. Haight, J. Silberman, and M. I. Lilie. Novel system for picosecond photoemission spectroscopy. *Rev. Sci. Instrum.*, 10598(April):1941–1946, 1988.

[179] P. Corkum. Plasma perspective on strong field multiphoton ionization. *Phys. Rev. Lett.*, 71(13):1994–1997, 1993.

[180] M. Lewenstein, P. Balcou, M. Y. Ivanov, A. L'Huillier, and P. B. Corkum. Theory of high-harmonic generation by low-frequency laser fields. *Phys. Rev. A*, 49(3):2117–2132, 1994.

[181] M. V. Ammosov, N. B. Delone, and V. P. Krainov. Tunnel ionization of complex atoms and of atomic ions in an alternating electromagnetic field. *Sov. Phys. JETP*, 64(December 1986):1191–1194, 1986.

[182] G. Yudin and M. Ivanov. Nonadiabatic tunnel ionization: Looking inside a laser cycle. *Phys. Rev. A*, 64(1):4, 2001.

[183] T. Popmintchev, M.-C. Chen, D. Popmintchev, P. Arpin, S. Brown, S. Alisauskas, G. Andriukaitis, T. Balciunas, O. D. Mucke, a. Pugzlys, a. Baltuska, B. Shim, S. E. Schrauth, a. Gaeta, C. Hernandez-Garcia, L. Plaja, a. Becker, a. Jaron-Becker, M. M. Murnane, and H. C. Kapteyn. Bright Coherent Ultrahigh Harmonics in the keV X-ray Regime from Mid-Infrared Femtosecond Lasers. *Science*, 336(6086):1287–1291, 2012.

[184] K. Varjú, Y. Mairesse, B. Carré, M. B. Gaarde, P. Johnsson, S. Kazamias, R. López-Martens, J. Mauritsson, K. J. Schafer, P. Balcou, A. L'huillier, and P. Salières. Frequency chirp of harmonic and attosecond pulses. *J. Mod. Opt.*, 52(2-3):379–394, 2005.

[185] X. He, M. Miranda, J. Schwenke, O. Guilbaud, T. Ruchon, C. Heyl, E. Georgadiou, R. Rakowski, A. Persson, M. B. Gaarde, A. L'Huillier, and A. L'Huillier. Spatial and spectral properties of the high-order harmonic emission in argon for seeding applications. *Phys. Rev. A*, 79(6):1–7, jun 2009.

[186] C.-J. Lai, G. Cirmi, K.-H. Hong, J. Moses, S.-W. Huang, E. Granados, P. Keathley, S. Bhardwaj, and F. X. Kärtner. Wavelength Scaling of High Harmonic Generation Close to the Multiphoton Ionization Regime. *Phys. Rev. Lett.*, 111(7):073901, aug 2013.

[187] E. Constant, D. Garzella, P. Breger, E. Mével, C. Dorrer, C. Le Blanc, F. Salin, and P. Agostini. Optimizing High Harmonic Generation in Absorbing Gases: Model and Experiment. Phys. Rev. Lett., 82(8):1668–1671, feb 1999.

[188] C.-J. Lai and F. X. Kärtner. The influence of plasma defocusing in high harmonic generation. Opt. Express, 19(23):22377, 2011.

[189] D. Popmintchev, C. Hernandez-Garcia, F. Dollar, C. Mancuso, J. A. Perez-Hernandez, M.-C. Chen, A. Hankla, X. Gao, B. Shim, A. L. Gaeta, M. Tarazkar, D. A. Romanov, R. J. Levis, J. A. Gaffney, M. Foord, S. B. Libby, A. Jaron-Becker, A. Becker, L. Plaja, M. M. Murnane, H. C. Kapteyn, and T. Popmintchev. Ultraviolet surprise: Efficient soft x-ray high-harmonic generation in multiply ionized plasmas. Science, 350(6265):1225–1231, 2015.

[190] A. Bideau-Mehu, Y. Guern, R. Abjean, and A. Johannin-Gilles. Measurements of refractive indexes of gases extended in the vacuum ultraviolet and revised values for krypton. Opt. Commun., 16(1):186–189, 1976.

[191] A. L'Huillier, X. F. Li, and L. A. Lompré. Propagation effects in high-order harmonic generation in rare gases. Journal of the Optical Society of America B, 7(4):527, 1990.

[192] J. Rothhardt, M. Krebs, S. Hädrich, S. Demmler, J. Limpert, and A. Tünnermann. Absorption-limited and phase-matched high harmonic generation in the tight focusing regime. New J. Phys., 16(3):033022, mar 2014.

[193] S. M. Teichmann, F. Silva, S. L. Cousin, M. Hemmer, and J. Biegert. 0.5-keV Soft X-ray attosecond continua. Nat. Commun., 7(May):1–6, 2016.

[194] E. A. Gibson, A. Paul, N. Wagner, R. Tobey, D. Gaudiosi, S. Backus, I. P. Christov, E. M. Gullikson, D. T. Attwood, and M. Murnane. Coherent Soft X-ray Generation in the Water Window with Quasi-Phase Matching. Science, 302(October):95–98, 2003.

[195] C. M. Heyl, H. Coudert-Alteirac, M. Miranda, M. Louisy, K. Kovacs, V. Tosa, E. Balogh, K. Varjú, A. L'Huillier, A. Couairon, and C. L. Arnold. Scale-invariant nonlinear optics in gases. Optica, 3(1):75–81, 2016.

[196] H. Christoph. High-order harmonic generation at 100 kHz repetition rate for time-resolved two-photon photoemission. PhD thesis, Phillips-Universität Marburg, 2010.

[197] C. Heyl, J. Güdde, U. Höfer, and a. L'Huillier. Spectrally Resolved Maker Fringes in High-Order Harmonic Generation. Phys. Rev. Lett., 107(3):3–6, jul 2011.

[198] F. Lindner, W. Stremme, M. Schätzel, F. Grasbon, G. Paulus, H. Walther, R. Hartmann, and L. Strüder. High-order harmonic generation at a repetition rate of 100 kHz. Phys. Rev. A, 68(1):013814, jul 2003.

[199] M.-C. Chen, M. R. Gerrity, S. Backus, T. Popmintchev, X. Zhou, P. Arpin, X. Zhang, H. C. Kapteyn, and M. M. Murnane. Spatially coherent, phase matched, high-order harmonic EUV beams at 50 kHz. Opt. Express, 17(20):17376–83, sep 2009.

[200] S. Hädrich, J. Rothhardt, M. Krebs, F. Tavella, A. Willner, J. Limpert, and A. Tünnermann. High harmonic generation by novel fiber amplifier based sources. Opt. Express, 18(19):20242–50, sep 2010.

[201] A. A. Cabasse, G. Machinet, A. Dubrouil, E. Cormier, and E. Constant. Optimization and phase matching of fiber-laser-driven high-order harmonic generation at high repetition rate. Opt. Lett., 37(22):4618–4620, nov 2012.

[202] J. Boullet, Y. Zaouter, J. Limpert, S. Petit, Y. Mairesse, B. Fabre, J. Higuet, E. Mével, E. Constant, and E. Cormier. High-order harmonic generation at a megahertz-level repetition rate directly driven by an ytterbium-doped-fiber chirped-pulse amplification system. Optic Letters, 34(9):1489–91, may 2009.

[203] J. Rothhardt, S. Hädrich, A. Klenke, S. Demmler, A. Hoffmann, T. Gotschall, T. Eidam, M. Krebs, J. Limpert, and A. Tünnermann. 53 W average power few-cycle fiber laser system generating soft x-rays up to the water window. Opt. Lett., 39(17):5224–7, sep 2014.

[204] M. Zürch, J. Rothhardt, S. Hädrich, S. Demmler, M. Krebs, J. Limpert, a. Tünnermann, a. Guggenmos, U. Kleineberg, and C. Spielmann. Real-time and sub-wavelength ultrafast coherent diffraction imaging in the extreme ultraviolet. Sci. Rep., 4:7356, 2014.

[205] S. Hädrich, A. Klenke, J. Rothhardt, M. Krebs, A. Hoffmann, O. Pronin, V. Pervak, J. Limpert, and A. Tünnermann. High photon flux table-top coherent extreme-ultraviolet source. Nat. Photonics, 8(September), sep 2014.

[206] J. Rothhardt, S. Hädrich, Y. Shamir, M. Tschnernajew, R. Klas, A. Hoffmann, G. K. Tadesse, A. Klenke, T. Gottschall, T. Eidam, J. Limpert, A. Tünnermann, R. Boll, C. Bomme, H. Dachraoui, B. Erk, M. Di Fraia, D. A. Horke, T. Kierspel, T. Mullins, A. Przystawik, E. Savelyev, J. Wiese, T. Laarmann, J. Küpper, and D. Rolles. High-repetition-rate and high-photon-flux 70 eV

high-harmonic source for coincidence ion imaging of gas-phase molecules. Opt. Express, 24(16):18133, 2016.

[207] A. Vernaleken, J. Weitenberg, T. Sartorius, P. Russbueldt, W. Schneider, S. L. Stebbings, M. F. Kling, P. Hommelhoff, H.-D. Hoffmann, R. Poprawe, F. Krausz, T. W. Hänsch, and T. Udem. Single-pass high-harmonic generation at 20.8 MHz repetition rate. Optic Letters, 36(17):3428–30, sep 2011.

[208] I. Pupeza, S. Holzberger, T. Eidam, H. Carstens, D. Esser, J. Weitenberg, P. Rußbüldt, J. Rauschenberger, J. Limpert, T. Udem, a. Tünnermann, T. W. Hänsch, a. Apolonski, F. Krausz, and E. Fill. Compact high-repetition-rate source of coherent 100Å eV radiation. Nat. Photonics, 7(8):608–612, jul 2013.

[209] H. Pauly. Atom, molecule, and cluster beams I : basic theory, production and detection of thermal energy beams. Springer Berlin Heidelberg, Berlin, 2000.

[210] G. Scoles. Atomic and molecular beam methods. Oxford University Press, New York, 1988.

[211] F. Johannes. A 500 kHz high harmonics generation XUV light source for photoelectron spectroscopy. PhD thesis, Ludwig-Maximilians Universität München, 2016.

[212] E. Palik. Handbook of optical constants of solids. Academic Press, San Diego, 1998.

[213] R. Doering. Handbook of semiconductor manufacturing technology. CRC Press, Boca Raton, 2008.

[214] D. L. Windt. IMD - Software for modeling the optical properties of multilayer films. Computers in Physics, 12(4):360–370, 1998.

[215] J. Végh. The Shirley background revised. J. Electron Spectrosc. Relat. Phenom., 151(3):159–164, may 2006.

[216] S. Mcdonnell, A. Azcatl, R. Addou, C. Gong, S. Chuang, K. Cho, A. Javey, and R. M. Wallace. Hole Contacts on Transition Metal Dichalcogenides : Interface Chemistry and Band Alignments Hole Contacts on Transition Metal Dichalcogenides : Interface Chemistry and Band Alignments. ACS Nano, 8(6):6265–6272, 2014.

[217] J. A. Wilson and A. D. Yoffe. The transition metal dichalcogenides discussion and interpretation of the observed optical, electrical and structural properties. Adv. Phys., 18(73):193–335, 1969.

[218] H. Cercellier, C. Monney, F. Clerc, C. Battaglia, L. Despont, M. G. Garnier, H. Beck, P. Aebi, L. Patthey, H. Berger, and L. Forró. Evidence for an excitonic insulator phase in 1T-TiSe$_2$. Phys. Rev. Lett., 99(14):146403, oct 2007.

[219] Q. H. Wang, K. Kalantar-Zadeh, A. Kis, J. N. Coleman, and M. S. Strano. Electronics and optoelectronics of two-dimensional transition metal dichalcogenides. Nat. Nanotechnol., 7(11):699–712, nov 2012.

[220] K. F. Mak and J. Shan. Photonics and optoelectronics of 2D semiconductor transition metal dichalcogenides. Nat. Photonics, 10(4):216–226, 2016.

[221] K. F. Mak, K. He, J. Shan, and T. F. Heinz. Control of valley polarization in monolayer MoS2 by optical helicity. Nat. Nanotechnol., 7(8):494–498, jun 2012.

[222] A. Chernikov, T. C. Berkelbach, H. M. Hill, A. Rigosi, Y. Li, O. B. Aslan, D. R. Reichman, M. S. Hybertsen, and T. F. Heinz. Exciton Binding Energy and Nonhydrogenic Rydberg Series in Monolayer WS2. Phys. Rev. Lett., 113(7):076802, mar 2014.

[223] S. Ulstrup, A. G. Čabo, D. Biswas, J. M. Riley, M. Dendzik, C. E. Sanders, M. Bianchi, C. Cacho, D. Matselyukh, R. T. Chapman, E. Springate, P. D. C. King, J. A. Miwa, and P. Hofmann. Spin and valley control of free carriers in single-layer WS 2. Phys. Rev. B, 95(4):041405, jan 2017.

[224] X. Zhang, Q. Liu, J.-W. Luo, A. J. Freeman, and A. Zunger. Hidden spin polarization in inversion-symmetric bulk crystals. Nat. Phys., 10(5):387–393, 2014.

[225] S.-W. Yu, T. Lischke, R. David, N. Müller, U. Heinzmann, C. Pettenkofer, A. Klein, A. Perlov, E. Krasovskii, W. Schattke, and J. Braun. Spin resolved photoemission spectroscopy on WSe2. J. Electron Spectrosc. Relat. Phenom., 101-103:449–454, jun 1999.

[226] J. M. Riley, F. Mazzola, M. Dendzik, M. Michiardi, T. Takayama, L. Bawden, C. Granerød, M. Leandersson, T. Balasubramanian, M. Hoesch, T. K. Kim, H. Takagi, W. Meevasana, P. Hofmann, M. S. Bahramy, J. W. Wells, and P. D. C. King. Direct observation of spin-polarized bulk in an semiconductor bulk inversion-symmetric. Nat. Phys., 10(11):835–839, 2014.

[227] W. J. Schutte, J. L. De Boer, and F. Jellinek. Crystal structures of tungsten disulfide and diselenide. J. Solid State Chem., 70(2):207–209, 1987.

[228] T. Straub, K. Fauth, T. Finteis, M. Hengsberger, R. Claessen, P. Steiner, S. Hufner, and P. Blaha. Valence-band maximum

in the layered semiconductor WSe2: Application of constant-energy contour mapping by photoemission. Phys. Rev. B, 53(24):16152–16155, 1996.

[229] J. M. Riley, F. Mazzola, M. Dendzik, M. Michiardi, T. Takayama, L. Bawden, C. Granerod, M. Leandersson, T. Balasubramanian, M. Hoesch, T. K. Kim, H. Takagi, W. Meevasana, P. Hofmann, M. S. Bahramy, J. W. Wells, and P. D. C. King. Direct observation of spin-polarized bulk bands in an inversion-symmetric semiconductor. Nat. Phys., 10(11):835–839, 2014.

[230] I. Tanabe, T. Komesu, D. Le, T. B. Rawal, E. F. Schwier, M. T. Zheng, Y. Kojima, H. Iwasawa, K. Shimada, T. S. Rahman, and P. A. Dowben. The symmetry-resolved electronic structure of 2H-WSe2(0001). Journal of Physics-Condensed Matter, 28(34):10, 2016.

[231] T. Finteis, M. Hengsberger, T. Straub, K. Fauth, R. Claessen, P. Auer, P. Steiner, S. Hüfner, P. Blaha, M. Vögt, M. Lux-Steiner, and E. Bucher. Occupied and unoccupied electronic band structure of WSe_{2}. Phys. Rev. B, 55(16):10400–10411, 1997.

[232] J. M. Riley, W. Meevasana, L. Bawden, M. Asakawa, T. Takayama, T. Eknapakul, T. K. Kim, M. Hoesch, S.-K. Mo, H. Takagi, T. Sasagawa, M. S. Bahramy, and P. D. C. King. Negative electronic compressibility and tunable spin splitting in WSe2. Nat. Nanotechnol., 10(12):1043–1047, 2015.

[233] B. S. Kim, J.-W. Rhim, B. Kim, C. Kim, and S. R. Park. Determination of the band parameters of bulk 2H-MX$_2$ (M = Mo, W; X = S, Se) by angle-resolved photoemission spectroscopy. Sci. Rep., 6(October):36389, 2016.

[234] P. Giannozzi, S. Baroni, N. Bonini, M. Calandra, R. Car, C. Cavazzoni, D. Ceresoli, G. L. Chiarotti, M. Cococcioni, I. Dabo, A. D. Corso, S. de Gironcoli, S. Fabris, G. Fratesi, R. Gebauer, U. Gerstmann, C. Gougoussis, A. Kokalj, M. Lazzeri, L. Martin-Samos, N. Marzari, F. Mauri, R. Mazzarello, S. Paolini, A. Pasquarello, L. Paulatto, C. Sbraccia, S. Scandolo, G. Sclauzero, A. P. Seitsonen, A. Smogunov, P. Umari, and R. M. Wentzcovitch. QUANTUM ESPRESSO: a modular and open-source software project for quantum simulations of materials. J. Phys.: Condens. Matter, 21(39):395502, 2009.

[235] J. P. Perdew and A. Zunger. Self-interaction correction to density-functional approximations for many-electron systems. Phys. Rev. B, 23(10):5048–5079, may 1981.

[236] Y. Zhang, M. M. Ugeda, C. Jin, S. F. Shi, A. J. Bradley, A. Martín-Recio, H. Ryu, J. Kim, S. Tang, Y. Kim, B. Zhou, C. Hwang,

Y. Chen, F. Wang, M. F. Crommie, Z. Hussain, Z. X. Shen, and S. K. Mo. Electronic Structure, Surface Doping, and Optical Response in Epitaxial WSe$_2$ Thin Films. Nano Lett., 16(4):2485–2491, 2016.

[237] R. G. Parr. Density Functional Theory of Atoms and Molecules, pages 5–15. Springer Netherlands, Dordrecht, 1980.

[238] R. O. Jones and O. Gunnarsson. The density functional formalism, its applications and prospects. Rev. Mod. Phys., 61(3):689–746, jul 1989.

[239] J. P. Perdew. Density functional theory and the band gap problem. Int. J. Quantum Chem., 28(S19):497–523, 2009.

[240] F. Aryasetiawan and O. Gunnarsson. The GW method. Rep. Prog. Phys., 61(3):237, 1998.

[241] E. E. Salpeter and H. A. Bethe. A Relativistic Equation for Bound-State Problems. Phys. Rev., 84(6):1232–1242, dec 1951.

[242] G. Onida, L. Reining, and A. Rubio. Electronic excitations: Density-functional versus many-body Green's-function approaches. Rev. Mod. Phys., 74(2):601–659, jun 2002.

[243] U. De Giovannini, H. Hübener, and A. Rubio. Monitoring Electron-Photon Dressing in WSe$_2$. Nano Lett., 16:7993–7998, 2016.

[244] U. De Giovannini, H. Hübener, and A. Rubio. A First-Principles Time-Dependent Density Functional Theory Framework for Spin and Time-Resolved Angular-Resolved Photoelectron Spectroscopy in Periodic Systems. J. Chem. Theory Comput., 13:265–273, 2016.

[245] A. R. Beal and W. Y. Liang. Excitons in 2H-WSe 2 and 3R-WS 2. J. Phys. C: Solid State Phys., 9(12):2459, 1976.

[246] A. Arora, M. Koperski, K. Nogajewski, J. Marcus, C. Faugeras, and M. Potemski. Excitonic resonances in thin films of WSe2 : from monolayer to bulk material. Nanoscale, 7(23):10421–10429, 2015.

[247] R. Roldán, J. A. Silva-Guillén, M. P. López-Sancho, F. Guinea, E. Cappelluti, and P. Ordejón. Electronic properties of single-layer and multilayer transition metal dichalcogenides MX2 (M = Mo, W and X = S, Se), 2014.

[248] H. Jiang. Electronic Band Structures of Molybdenum and Tungsten Dichalcogenides by the GW Approach. The Journal of Physical Chemistry C, 116(14):7664–7671, 2012.

[249] J. He, K. Hummer, and C. Franchini. Stacking effects on the electronic and optical properties of bilayer transition metal dichalcogenides MoS_2, $MoSe_2$, WS_2, and WSe_2. Physical Review B, 89(7):1–11, 2014.

[250] C. Kittel. Introduction to solid state physics. Wiley, Hoboken, NJ, 2005.

[251] C. Kuper and G. Whitfield. Polarons and Excitons. Plenum Press, 1963.

[252] P. Yu. Fundamentals of semiconductors : physics and materials properties. Springer, Berlin London, 2010.

[253] A. R. Beal, J. C. Knights, and W. Y. Liang. Transmission spectra of some transition metal dichalcogenides. II. Group VIA: trigonal prismatic coordination. J. Phys. C: Solid State Phys., 5(24):3540–3551, 1972.

[254] M. Selig, G. Berghäuser, A. Raja, P. Nagler, C. Schüller, T. F. Heinz, T. Korn, A. Chernikov, E. Malic, and A. Knorr. Excitonic linewidth and coherence lifetime in monolayer transition metal dichalcogenides. Nat. Commun., 7:13279, nov 2016.

[255] M. Selig, G. Berghäuser, M. Richter, R. Bratschitsch, A. Knorr, and E. Malic. Dark and bright exciton formation, thermalization, and photoluminescence in monolayer transition metal dichalcogenides. ArXiv e-prints, mar 2017.

[256] R. A. Kaindl, M. A. Carnahan, D. Hägele, R. Lövenich, and D. S. Chemla. Ultrafast terahertz probes of transient conducting and insulating phases in an electron-hole gas. Nature, 423(6941):734–738, 2003.

[257] C. Poellmann, P. Steinleitner, U. Leierseder, P. Nagler, G. Plechinger, M. Porer, R. Bratschitsch, C. Schüller, T. Korn, and R. Huber. Resonant internal quantum transitions and femtosecond radiative decay of excitons in monolayer WSe2. Nat. Mater., 14(9):889–893, 2015.

[258] P. Steinleitner, P. Merkl, P. Nagler, J. Mornhinweg, C. Schüller, T. Korn, A. Chernikov, and R. Huber. Direct Observation of Ultrafast Exciton Formation in a Monolayer of WSe_2. Nano Lett., 17(3):1455–1460, 2017.

[259] X. Y. Zhu. Photoemission from excitons in organic semiconductors. J. Electron Spectrosc. Relat. Phenom., 204:75–79, 2015.

[260] M. Weinelt, M. Kutschera, T. Fauster, and M. Rohlfing. Dynamics of exciton formation at the Si(100) c(4 × 2) surface. Phys. Rev. Lett., 92(12):126801–1, 2004.

[261] T. Y. Jeong, B. M. Jin, S. H. Rhim, L. Debbichi, J. Park, Y. D. Jang, H. R. Lee, D. H. Chae, D. Lee, Y. H. Kim, S. Jung, and K. J. Yee. Coherent Lattice Vibrations in Mono- and Few-Layer WSe2. ACS Nano, 10(5):5560–5566, 2016.

[262] A. Rettenberger, P. Leiderer, M. Probst, and R. Haight. Ultrafast electron transport in layered semiconductors studied with femtosecond-laser photoemission. Phys. Rev. B, 56(19):12092–12095, 1997.

[263] A. Steinhoff, M. Florian, M. Rösner, M. Lorke, T. O. Wehling, C. Gies, and F. Jahnke. Nonequilibrium Carrier Dynamics in Transition Metal Dichalcogenide Semiconductors. 2D Mater., 3:031006, 2016.

[264] C. Ruppert, A. Chernikov, H. M. Hill, A. F. Rigosi, and T. F. Heinz. The Role of Electronic and Phononic Excitation in the Optical Response of Monolayer WS2 after Ultrafast Excitation. Nano Lett., 17(2):644–651, 2017.

[265] R. Schuster, Y. Wan, M. Knupfer, and B. Büchner. Nongeneric dispersion of excitons in the bulk of WSe2. Phys. Rev. B, 94(8):1–5, 2016.

[266] J. J. Hopfield and D. G. Thomas. Fine structure and magneto-optic effects in the exciton spectrum of cadmium sulfide. Phys. Rev., 122(1):35–52, apr 1961.

[267] W. Y. Liang. Optical anisotropy in layer compounds. J. Phys. C: Solid State Phys., 6(3):551–565, 1973.

[268] A. R. Beal, W. Y. Liang, and H. P. Hughes. Kramers-Kronig analysis of the reflectivity spectra of 3R-WS$_2$ and 2H-WSe$_2$. Journal of Physics C, 89:2449, 1976.

[269] A. V. Stier, N. P. Wilson, G. Clark, X. Xu, and S. A. Crooker. Probing the Influence of Dielectric Environment on Excitons in Monolayer WSe2: Insight from High Magnetic Fields. Nano Lett., 16(11):7054–7060, 2016.

[270] Q. N. Cui, F. Ceballos, N. Kumar, and H. Zhao. Transient Absorption Microscopy of Mono layer and Bulk WSe2. ACS Nano, 8(3):2970–2976, 2014.

[271] P. Dey, J. Paul, Z. Wang, C. E. Stevens, C. Liu, A. H. Romero, J. Shan, D. J. Hilton, and D. Karaiskaj. Optical Coherence in Atomic-Monolayer Transition-Metal Dichalcogenides Limited by Electron-Phonon Interactions. Phys. Rev. Lett., 116(12):1–6, 2016.

[272] A. Chernikov, C. Ruppert, H. M. Hill, A. F. Rigosi, and T. F. Heinz. Population inversion and giant bandgap renormalization in atomically thin WS2 layers. Nat. Photonics, 9(7):466–470, 2015.

[273] E. J. Sie, J. W. McIver, Y.-H. Lee, L. Fu, J. Kong, and N. Gedik. Valley-selective optical Stark effect in monolayer WS2. Nat. Mater., 14(3):290–294, 2014.

[274] E. J. Sie, C. H. Lui, Y.-H. Lee, L. Fu, J. Kong, and N. Gedik. Large, valley-exclusive Bloch-Siegert shift in monolayer WS2. Science, 13(4):1852–1857, 2017.

[275] H. Sahin, S. Tongay, S. Horzum, W. Fan, J. Zhou, J. Li, J. Wu, and F. M. Peeters. Anomalous Raman spectra and thickness-dependent electronic properties of WSe2. Phys. Rev. B, 87(16):1–6, 2013.

[276] M. Wolf, A. Hotzel, E. Knoesel, and D. Velic. Direct and indirect excitation mechanisms in two-photon photoemission spectroscopy of cu(111) and co/cu(111). Phys. Rev. B, 59:5926–5935, Feb 1999.

[277] M. Bernardi, D. Vigil-Fowler, J. Lischner, J. B. Neaton, and S. G. Louie. Ab initio study of hot carriers in the first pico-second after sunlight absorption in silicon. Phys. Rev. Lett., 112(25):257402, jun 2014.

[278] L. Waldecker, R. Bertoni, H. Hübener, T. Brumme, T. Vasileiadis, D. Zahn, A. Rubio, and R. Ernstorfer. A momentum-resolved view on electron-phonon coupling in multilayer WSe$_2$. ArXiv e-prints, mar 2017.

[279] C. F. Klingshirn. Semiconductor optics. Springer, Berlin New York, 2005.

ACKNOWLEDGEMENTS

SELBSTSTÄNDIGKEITSERKLÄRUNG GEMÄSS DER PROMOTIONSORDNUNG

Sämtliche verwendeten Hilfsmittel, Hilfen und Quellen sind an der entsprechenden Stelle angegeben. Ich versichere, dass ich auf dieser Grundlage diese Arbeit selbstständig verfasst habe. Diese Arbeit wurde bisher weder in gleicher noch ähnlicher Form einer anderen Prüfungskomission vorgelegt oder veröffentlicht.

Berlin, Juni 2017

Michele Puppin, 27.06.2017

List of Publications

September 12, 2018

Articles in peer reviewed journals

[1] R. Bertoni, C. W. Nicholson, L. Waldecker, H. Hübener, C. Monney, U. De Giovannini, M. Puppin, M. Hoesch, E. Springate, R. T. Chapman, C. Cacho, M. Wolf, A. Rubio, and R. Ernstorfer. "Generation and Evolution of Spin-, Valley-, and Layer-Polarized Excited Carriers in Inversion-Symmetric WSe_2". In: *Phys. Rev. Lett.* 117 (27 2016), p. 277201. DOI: `10.1103/PhysRevLett.117.277201`.

[2] C. Monney, M. Puppin, C. W. Nicholson, M. Hoesch, R. T. Chapman, E. Springate, H. Berger, A. Magrez, C. Cacho, R. Ernstorfer, and M. Wolf. "Revealing the role of electrons and phonons in the ultrafast recovery of charge density wave correlations in 1T-$TiSe_2$". In: *Physical Review B* 94.16 (2016), p. 165165. DOI: `10.1103/PhysRevB.94.165165`.

[3] C. W. Nicholson, C. Berthod, M. Puppin, H. Berger, M. Wolf, M. Hoesch, and C. Monney. "Dimensional Crossover in a Charge Density Wave Material Probed by Angle-Resolved Photoemission Spectroscopy". In: *Phys. Rev. Lett.* 118 (20 2017), p. 206401. DOI: `10.1103/PhysRevLett.118.206401`.

[6] M. Puppin, Y. Deng, O. Prochnow, J. Ahrens, T. Binhammer, U. Morgner, M. Krenz, M. Wolf, and R. Ernstorfer. "500 kHz OPCPA delivering tunable sub-20 fs pulses with 15 W average power based on an all-ytterbium laser". In: *Optics Express* 23.2 (2015), p. 1491. DOI: `10.1364/OE.23.001491`.

Conference Proceedings

[4] M. Puppin, Y. Deng, O. Prochnow, J. Matyschok, T. Binhammer, U. Morgner, M. Wolf, and R. Ernstorfer. "Fiber-Slab-Pumped OPCPA for XUV-Based Time-Resolved Photoelectron Spectroscopy at 500 kHz Repetition Rate". In: *Ultrafast Phenomena*. 2014, pp. 6–7. DOI: `10.1364/UP.2014.09.Wed.P3.53`.

[5] M. Puppin, Y. Deng, C. Nicholson, C. Monney, M. Krenz, O. Prochnow, J. Ahrens, T. Binhammer, U. Morgner, M. Wolf, and R. Ernstorfer. "500 kHz OPCPA-Based UV-XUV Light Source For Time-Resolved Photoemission Spectroscopy". In: *CLEO: 2015*. OSA Technical Digest (online). San Jose, California: Optical Society of America, 2015, SF2M.4. DOI: `10.1364/CLEO_SI.2015.SF2M.4`.